Nanopropulsion by biocatalytic self-assembly

Joy Susan Leckie

Thesis submitted to the University of Strathclyde for the degree of Doctor of Philosophy

Department of Chemical & Process Engineering

University of Strathclyde

2015

Declaration

This thesis is the result of the author's original research. It has been composed by the author and has not been previously submitted for examination which has led to the award of a degree.

Signed:

Date:

Acknowledgments

I would like to acknowledge those who have supported me throughout the project; firstly my supervisors Mark and Rein for giving me the opportunity to undertake this research project and for all of their help and guidance through every stage of the research, but also for inspiring me and allowing freedom to communicate my research to public audiences. I would also like to show my appreciation to Alastair (my unofficial third supervisor) for his assistance with the operation of his microscope but also for his useful input into the research project. I also thank Gail McConnell for her help.

I show my gratitude to members of the Department of Chemical and Process Engineering for helpful discussions but also for making my time in the Department a pleasurable and memorable experience. I particularly thank, Sandy for his advice and support using MATLAB and for making the office environment more colourful. I have many great memories thanks to Scott D, Paul, Stewart, David, Javier, Craig and the twins: Claire (my office neighbour) and Carol. I am also grateful for the support and guidance given to me by the secretarial and technical staff in the Department.

I give many thanks to Ulijn Group members, past and present, for their support and friendship. I would like to acknowledge the support of Sangita not only for her friendship but for many helpful discussions. I also thank Sisir for his support throughout my research, particularly for synthesising peptides for the use in this project and Meghan for obtaining Cryo-TEM images. I'd like to show gratitude to Isabel Scott for her kind support throughout my time in the group.

My PhD studies would not have been the same without Krystyna for being a great friend and always being there for a chat; Scott F for making the office more… interesting, especially for his, sometimes controversial, 'Scott quotes'; Daniela for her always late arrival and her colourful Italian 'phrases' in the office and Babis (The Hero) for being great company during our walks home.

I would like to show my appreciation to all of those who helped out with public engagement activities, there are too many to mention, but with your help we've managed to hopefully inspire hundreds of children (and adults) about nano-science!

Finally and most importantly I would like to thank all of the special people in my life, my amazing boyfriend for putting up with me over the years, for all of his patience and for painstakingly proof reading all 200+ pages of my thesis. To my mum and dad (and Jock) for their constant love and support throughout my life. To friends and family who have helped me through many ups and downs: my big cousin Sarahjane for being like a sister to me, my aunties Irene, Carol, and Margaret; and friends Jenn, Laura, Mairi and Nicola, for just being there. Not forgetting my second family, the Peeks, for their additional support throughout. Lots of love goes to the newest member of the family, Abigail, for her ability to instantly cheer me up and bring much happiness and laughter.

The author

Publications

- **J. Leckie,** A. Hope, M. Hughes, S. Debnath, S. Fleming, A.W. Wark, R.V. Ulijn and M.D. Haw, Nanopropulsion by Biocatalytic Self-assembly, *ACS Nano*, 2014, 8, 9580-9589 (first author).
- S. Bai, C.G. Pappas, S. Debnath, P.W.J.M. Frederix**, J. Leckie**, S. Fleming and R.V. Ulijn, Stable Emulsions Formed by Self-Assembly of Interfacial Networks of Dipeptide Derivatives, *ACS Nano*, 2014, 8, 7005-7013 (co-author).
- J.W. Sadownik, **J. Leckie** and R.V. Ulijn, Micelle to Fibre Biocatalytic Supramolecular Transformation of an Aromatic Peptide Amphiphile, *Chem. Commun*., 2011, 47, 728-730 (co-author).

Presentations

- ACS Dallas 2014 conference (Poster) – 'Nanopropulsion by biocatalytic self-assembly.'
- Directed Assembly of Functional Nanomaterials Conference 2013, Strathclyde (Talk) – 'Self-assembly-driven enzyme motion using dipeptide derivative 'fuel' molecules.'
- Nanopeptide 2012 conference, Manchester (Poster) – 'Self-assembly driven enzyme motion.'
- Bionanotechnology III: from biomolecular assembly to applications 2012 conference, Cambridge (Poster) – 'Self-assembly driven enzyme motion.'

Awarded grants

- Bridging the Gap (BTG) – for interdisciplinary research and collaboration
- EPSRC Pathways to Impact – for Ulijn group public engagement activities
- RSC travel grant – for ACS Dallas Conference
- Physical Chemistry Departmental (University of Strathclyde)travel grant - for ACS Dallas Conference
- PEG group funding – for Really Small Science group public engagement activities

Contributions to public engagement

- Social networking for Ulijn group and Really Small Science
- Articles and newsletters *e.g.* articles for the monthly Engineering Newsletter
- Really Small Science group co-ordinator (April 2014-present)
- 'Meet the expert' at Glasgow Science Centre (September 2014)
- Dunoon Primary School P3-4 – Really Small science workshops (September 2014)
- Bionano research educational movie on Youtube (August 2014)
- Gowdie afterschool club – Really Small Science workshops (August 2014)
- 'Meet the expert' at Glasgow Science Centre (August 2014)
- Early years – play scheme jelly activities (July 2014)
- STEM Ambassador induction (June 2014)
- School Engagement event at Biocity Scotland (June 2014)
- Glasgow Science Festival – Nanojelly Stall (June 2014)
- Public engagement introductory session for the Department of Chemical and Process Engineering – organisation and delivery (June 2014)
- Bellahouston Academy S4 class – Nanojelly workshop (May 2014)
- 'Meet the expert' at Glasgow Science Centre (May 2014)
- Skills-Sharing for Early Years... BIG Ideas for Little People, Edinburgh (May 2014)
- 'Meet the expert' at Glasgow Science Centre (October 2013)
- Inspire and Challenge Training by Glasgow Science Centre (August 2013)
- 'The Science of Jelly' – educational movie on Youtube (July 2013)
- Glasgow Science Festival – Science of Jelly Stall (June 2013)
- University of Strathclyde research day – Science of Jelly Stall (June 2013)
- Busby Primary School P6 class – Science of Jelly workshop (March 2013)

Abbreviations

2D – Two dimensional

3D – Three dimensional

ADF – Actin depolymerising factor

ADP – Adenosine diphosphate

AFM – Atomic force microscopy

AP – Alkaline phosphatase

APS – Ammonium persulfate

ARF 1 – ADP-ribosylation factor 1

ATP – Adenosine triphosphate

BOD – Bilirubin oxidase

BSA – Bovine serum albumin

BTEE – N-Benzoyl-L-tyrosine ethyl ester

CCD – Charged coupled device

CIAP – Calf intestinal alkaline phosphatase

CNT – Carbon nanotube

DMF - Dimethylformamide

DNA – Deoxyribonucleic acid

DLS – Dynamic light scattering

EDC – 1-Ethyl-3-(3-dimethylaminopropyl)carbodiimide

EDTA – Ethylenediaminetetraacetic acid

EMCCD – Electron multiplying charged coupled device

FITC – Fluorescein isothiocyanate

Fmoc – 9-Fluorenylmethoxycarbonyl

GFP – Green fluorescent protein

GOx – Glucose oxidase

GTP – Guanosine-5'-triphosphate

HMM – Heavy meromyosin

HPLC – High performance liquid chromatography

HRP – Horseradish peroxidase

LED – Light emitting diode

MSD – Mean square displacement

MT – Microtubule

MWCO – Molecular weight cut-off

NA – Numerical aperture

Nap – Naphthalene

NHS – N-Hydroxysuccinimide

NP – Nanoparticle

PAH – Polycyclic aromatic hydrocarbon

PBS – Phosphate buffered saline

PDB ID – Protein database identification number

PDMS – Polydimethylsiloxane

PEDOT – Poly(3,4-ethylenedioxythiophene)

Pi – Inorganic phosphate

PMMA – Poly(methyl methacrylate)

PNP – p-nitrophenyl phosphate

PSS – Poly(sodium styrene sulfonate)

PTFE – Polytetrafluoroethylene

QD – Quantum dot

QD-AP – Quantum dot-alkaline phosphatase conjugate

QD_{525}-AP – 525 nm emitting quantum dot-alkaline phosphatase conjugate

QD_{525}-Therm – 525 nm emitting quantum dot-thermolysin conjugate

QD_{655}-AP – 655 nm emitting quantum dot-alkaline phosphatase conjugate

QD_{655}-Chym – 655 nm emitting quantum dot-chymotrypsin conjugate

ROMP – Ring opening metathesis polymerisation

sCMOS – Scientific complementary metal–oxide–semiconductor

SDS – Sodium dodecyl sulfate

Sw-CNT – Single-walled carbon nanotube

TCA – Trichloroacetic acid

TEM – Transmission electron microscopy

TEMED – Tetramethylethylenediamine

ThT – Thioflavin T

TMS - Tetramethylsilane

TMCS – Trimethylsilyl chloride

UV-Vis – Ultra violet-visible

WASP – Wiskott-Aldrich syndrome protein

Abstract

In nature, a number of organisms and organelles are capable of self-propulsion at the micro- and nano-scale. Inspired by biological motors, this investigation aims to induce self-propulsion of an enzyme, by the biocatalytic self-assembly of aromatic peptide amphiphile molecules into supramolecular fibre structures. The individual motion of enzymes is measured directly using fluorescence microscopy, by the covalent attachment of alkaline phosphatase to fluorescing quantum dots. Enzyme-quantum dot conjugates represent nanoparticulate 'vehicles' transported by the enzyme 'motor'. Two aromatic peptide substrate 'fuels', initially assembled in a micellar form, are studied for their ability to propel enzyme-quantum dot conjugates, by biocatalytic dephosphorylation causing self-assembly into one-dimensional fibres. The effect of the 'fuel' on conjugate motion is compared with controls consisting of no fuel, a non-self-assembling substrate and a non-directional self-assembling substrate (*i.e.* one that assembles into spheres, but not fibres).

Significant quantities of data were obtained for each substrate scenario and speed distribution plots revealed that enzyme-conjugates exhibit faster transport with the fibre forming system, compared to controls. Further to this, upon increasing the concentration of the fibre-forming fuel, the average speed of the conjugates increases, although directionality remains random. An initial investigation for directional control is carried out using 'fuel' reservoirs consisting of substrate saturated polyacrylamide gels. Substrates diffuse from the gel into surrounding motility medium creating a concentration gradient, which the enzyme-motors are proposed to travel along in a directional manner.

The proposed propulsion model for self-assembly-driven motion of enzyme-conjugates is that short bursts of fibre growth provides linear propulsion which increases the diffusion rate of the enzyme-conjugate. Simultaneous visualisation of self-assembled fibres and enzyme-quantum dot conjugates is attempted, using extrinsic and intrinsic fluorescent methods, to investigate the mechanism proposed for fibre-propulsion.

Finally, enzymes thermolysin and α-chymotrypsin are investigated as a step toward generalising the method for other enzymes and for their potential use in a multi-enzyme/multi-coloured quantum dot system for future applications in nano-separation of enzymes.

Contents

– Chapter 1 –

Introduction

1.1. Motion at the micro- and nano-scale

Motion is a fundamental physical property of all matter. Everything around us moves, from subatomic to macroscopic scales. Motion is defined as the displacement of an object over a period of time. This thesis will focus on motion at the colloidal or nano- to micron-scale range *i.e.* 1-1000 nanometres. This size range lies between atomic or single molecule dimensions and macroscopic objects that are visible to the human eye.[1] Within a colloidal system particles of one 'phase' are dispersed in a medium of another phase, for example a solid micron-sized particle suspended in water.

At colloidal dimensions, gravity is negligible over short timescales and so colloidal particles will not quickly sediment but remain suspended in the surrounding medium. While suspended, colloidal particles will exhibit random or Brownian motion, named after the botanist Robert Brown, who was the first to measure microscopic erratic motion of pollen grains in water.[2,3] The random motion exhibited by a colloidal particle is the result of the suspended particles being bombarded by the molecules of the surrounding fluid, causing the particle to become displaced from its original position. When followed over a period of time, the particle's trajectory will reveal the random nature of its movement, referred to as a random walk. Therefore motion at the nano- to micro-scale is different to macroscale motion due to thermal Brownian effects. For a particle undergoing a random walk, displacement or distance travelled is not proportional to time (as with linear ballistic motion *e.g.* $d = vt$), instead is proportional to the square root of time.

The mean square displacement (MSD) is a measure of how far a Brownian particle has moved from its starting position over a certain period of time.[2] The MSD is related to the size of the colloidal particle (hydrodynamic radius) by the diffusion coefficient (D), which is a measure of the migration characteristics of a particle. The diffusion of a particle is dependent on the particle radius and also the surrounding medium viscosity and

temperature. According to the Stokes-Einstein equation below (equation 1), a particle with a larger hydrodynamic radius (R_H) will have a smaller value for diffusion coefficient (D).[4]

$$\boldsymbol{R_H = \frac{k_B T}{6\pi\eta D}} \quad \textbf{or} \quad \boldsymbol{D = \frac{k_B T}{6\pi\eta R_H}} \qquad \textbf{Equation 1}$$

Where R_H is the hydrodynamic radius; k_B is the Boltzmann constant (1.38×10^{-23} $m^2 kg\ s^{-2} K^{-1}$); T = absolute temperature (Kelvin); η = viscosity of the medium and D is the diffusion coefficient.

For a one dimensional random walk, *i.e.* where a particle can either move in one direction or the other along the *x* axis, in a given time period (t), the probability for each scenario is 1/2.

For two and three dimensional random walk, motion is in the *x* and *y*, or *x, y*, *z* directions, respectively. Motion in each direction is statistically independent of the others for example:

$$\langle x^2 \rangle = 2Dt; \quad \langle y^2 \rangle = 2Dt; \quad \text{and } \langle z^2 \rangle = 2Dt$$

For two dimensional diffusion (which is measured in this study) the square of the displacement (*x, y*) from the origin (0, 0) is given by:

$MSD_{xy} = x^2 + y^2$ and therefore: $< \boldsymbol{MSD_{xy}} >= \boldsymbol{4Dt}$ **Equation 2**

(or in three dimensions $MSD_{xyz} = x^2 + y^2 + z^2$, $< MSD_{xyz} > = 6Dt$)

As well as translational diffusion, a particle will experience rotational diffusion ($\boldsymbol{D_R}$), which is a measure of the orientation of a particle. The rotational diffusion can be expressed by the following Stokes-Einstein equation[5]:

$$\boldsymbol{D_R = \frac{k_B T}{8\pi\eta R^3}} \qquad \textbf{Equation 3}$$

Particles with a smaller hydrodynamic radius will have faster rotational diffusion than larger particles, so a characteristic rotational time ($\boldsymbol{\tau_R}$) can be defined as the inverse of the diffusion coefficient:

$$\boldsymbol{\tau_R}^{-1} = \boldsymbol{\frac{k_B T}{8\pi\eta R^3}} \qquad \textbf{Equation 4}$$

Therefore, taking into account both the translational and rotational diffusion the MSD of a particle can be expressed as:

$$< MSD_{xy} >= 4D\Delta t + \frac{V^2 {\tau_R}^2}{2}\left[\frac{2\Delta t}{\tau_R} + e^{-2\Delta t/\tau_R} - 1\right] \qquad \textbf{Equation 5}$$

At short times ($\Delta t < \tau_R$) the particle trajectory is given by the quadratic relationship illustrated by the following equation: $<MSD_{xy}> = v^2 t^2 + 4D\Delta t$ (where v is the average velocity).[6] This also show by a curved MSD versus lag time plot **Figure 1A**.[7] At longer times (compared to the rotational diffusion time ($\Delta t > \tau_R$)), translational diffusion will dominate[6,8] and equation 5 reduces to:

$$< MSD_{xy} >= \left(4D\Delta t + V^2 {\tau_R}^2\right)\Delta t - \frac{V^2 {\tau_R}^2}{2} \qquad \textbf{Equation 6}$$

For the purposes of this project which, studies nanoscale motion we will be focussing on the $4D\Delta t$ term of Equation 6 , which can be shown by a linear MSD versus lag time plot **(Figure 1B).**

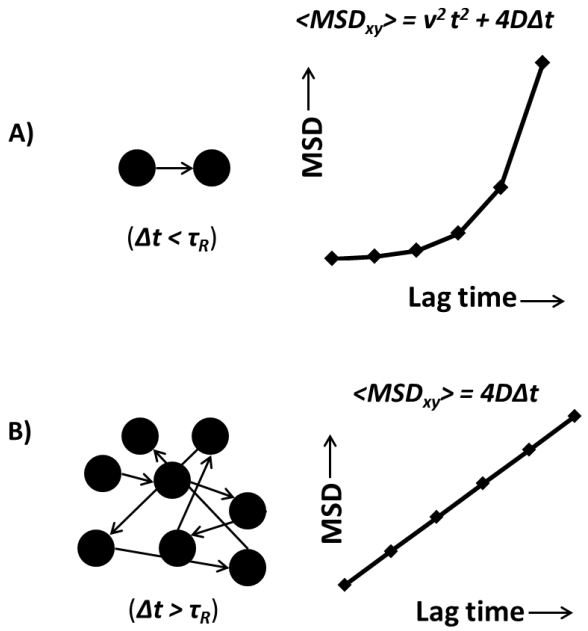

Figure 1 - Scheme representing (A) short and (B) long time frames compared to rotational time (τ_R) with corresponding MSD versus lag time plots.

For this study, involving nano-sized particles, rotational diffusion was not measured due to the typically much faster rotational diffusion compared to translational diffusion, compared to micro-sized objects. However rotational diffusion is included here for completeness. The key parameters measured for this study are frame-to-frame speed distributions to indicate enhanced diffusion, as well as with diffusion coefficient values. For studies which attempt directed motion, the shape of the MSD plot is studied alongside average frame-to-frame speeds and angle of trajectory.

1.2. Research aim

The ultimate aim of this research is to engineer a nanoscale motor propelled by biocatalytically induced self-assembly (see scheme in **Figure 2**). Our approach is inspired by biological nanoscale motion, for example the protein kinesin which converts ATP to ADP producing walking motion along a track.

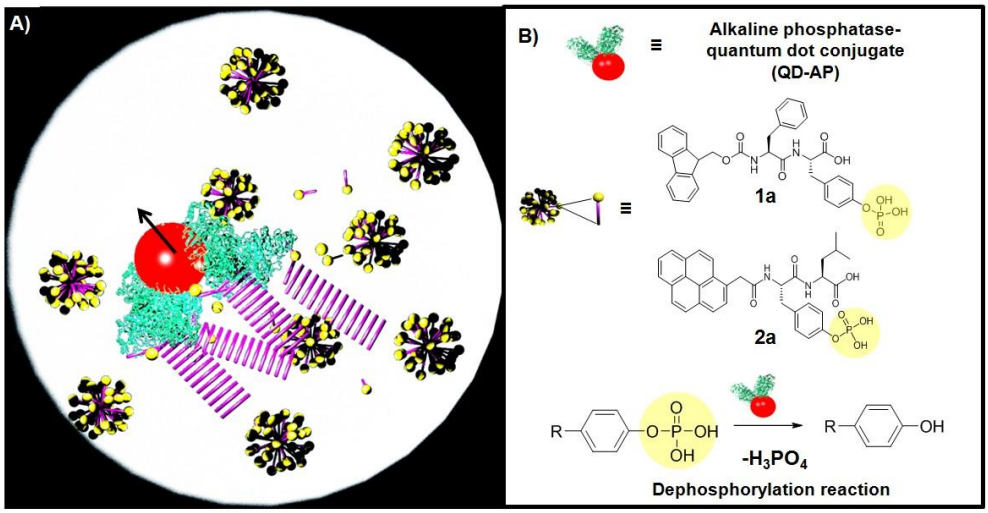

Figure 2 – A) Scheme of proposed nanomotor design propelled by biocatalytic self-assembly. B) The enzyme nanomotor (alkaline phosphatase-quantum dot conjugate) is propelled as the enzyme converts micelle fuel (**1a** or **2a**) into fibres.

There are three key factors to take into account when designing a nano-sized motor. Firstly a chemical fuel is required that is converted by the motor to produce mechanical energy. Secondly, asymmetry is important whether it is inherently built into the motor design or whether symmetry breakage occurs during fuel conversion *e.g.* due to the release of 'spent fuel' or the creation of a fuel concentration gradient. Finally, thermal fluctuations

(Brownian motion) must be overcome to achieve transport or enhanced motion beyond expected diffusion.

A hypothetical nanomotor in a fluid environment, without fuel or a propulsive force will diffuse in a random walk manner. With the addition of a chemical fuel there are a number of possible scenarios that the nanomotor could encounter. For example the conversion of fuel could provide little or no propulsive effect on the motor, over and above thermal fluctuations, therefore having no observable effect *i.e.* motor would continue to diffuse randomly. Another possibility is that the conversion of fuel to mechanical motion is non-directional resulting in faster or enhanced nanomotor diffusion but motion remains directionally erratic. Lastly, if the fuel is converted and released asymmetrically from the surface of the motor or a fuel gradient arises, the motor would move linearly *i.e.* following a ballistic trajectory, on a timescale associated with how long the asymmetry or gradient persists for.

An enzyme molecule capable of self-propulsion by the conversion of a substrate fuel to self-assembled linear fibre structures, has the potential for enhanced transport of the enzyme *i.e.* fibre growth exhibits a propulsive effect on the enzyme. Therefore the objective of this work is to design and engineer an enzyme nanomotor suitable for single molecule tracking in order to determine the diffusive properties of the motor (*i.e.* whether enhanced and/or directed propulsion is achievable), with the addition of a 'fuel' that is converted into one-dimensional self-assembled fibrous structures by the enzyme motor.

1.3. Layout of thesis

In Chapter 2, a literature review serving as the detailed background for the thesis is given. Part 1, describes the biological inspiration for motion at the micro- and nano-scale, followed by a review of historical and key examples of biologically inspired micro- and nano-motors, engineered from purely artificial components or from hybrids containing biological and synthetic elements. Motors are classified into three main groups according to their propulsion mechanism: those propelled linearly by catalysis due to a gradient; motors with added asymmetry causing rotational motion and motors capable of walking motion. The second part of the review describes self-assembly; specifically, biocatalytic self-assembly of aromatic dipeptide amphiphiles will be discussed for a potential route to nanopropulsion.

Chapter 3 details materials and methods employed for the bioconjugation of enzyme molecules to fluorescent nanoparticles, including characterisation and development of a number of self-assembling aromatic dipeptide 'fuel' systems. Experimental set-up and motility assay design will be described as well as methods towards the simultaneous visualisation of enzyme-conjugates and self-assembled structures.

Chapter 4 describes the techniques used for the development of methods to achieve enzyme nanomotors propelled by biocatalytic self-assembly. Part 1 details the bioconjugation method chosen to visualise enzyme 'motors' and the fundamental electronic properties of semiconductor nanoparticles used for bioconjugation. Part 2 summarises fluorescent spectroscopic methods for the detection of self-assembled structures *via* intrinsic and extrinsic staining techniques. Part 3 focuses on techniques for the visualisation of single enzyme-conjugate 'motors' and self-assembled structures, with an in depth discussion of the microscope configuration capable for this purpose.

In Chapter 5, the bioconjugation and characterisation of alkaline phosphatase-quantum dot conjugates are discussed, including a consideration of batch variation and long term stability.

Chapter 6 looks at the biocatalytically induced self-assembled systems studied for their potential as fuels for enzyme-quantum dot motors. Two micelle-to-fibre and one sphere-to-

sphere assembling systems are characterised initially with unconjugated enzyme, before repeating the study with enzyme-quantum dot conjugates.

Chapter 7 details how enzyme-quantum dot motors observed using fluorescence microscopy can be tracked providing speed, trajectory, and mean square displacement data. Here, 'motor' motion is compared with different self-assembling substrate 'fuels' and initial attempts at directed motion are discussed.

Chapter 8 describes methods used towards the simultaneous visualisation of enzyme-quantum dot motors alongside resulting self-assembled structures to gain further information on the propulsion mechanism.

Chapter 9 shows how the bioconjugation techniques used for alkaline phosphatase could be used for other enzymes towards a multi-enzyme/multi-fluorophore system. This chapter discusses how bioconjugation to QDs can be applied to thermolysin and chymotrypsin. Potential self-assembling substrate fuels are investigated towards other possible enzyme-quantum dot motors propelled by enzymatically induced self-assembly.

Finally the overall conclusions are summarised and suggestions for future work are provided in chapter 10.

– Chapter 2 –

Literature review Part 1: Micro- and nano-scale propulsion

2.1. Introduction: Biological Inspiration

Biological systems employ a number of strategies for controlling the motion of individual cells for example by changing shape; and for the intracellular transportation of vital components. Within the cell, filaments composed of polymerised monomeric proteins, can lengthen or shorten by polymerisation and depolymerisation, respectively. This lengthening and shortening is the mechanism for the 'crawling' movement of a cell along a surface, where the growth of the filament pushes the membrane promoting cell mobility. [9–11]

Filaments similar to those used for cell crawling are also employed by nanosized motor proteins inside the cell. Motor proteins use filaments such as actin or microtubules as tracks to 'walk' along and in some cases to transport 'cargo' around the cell.

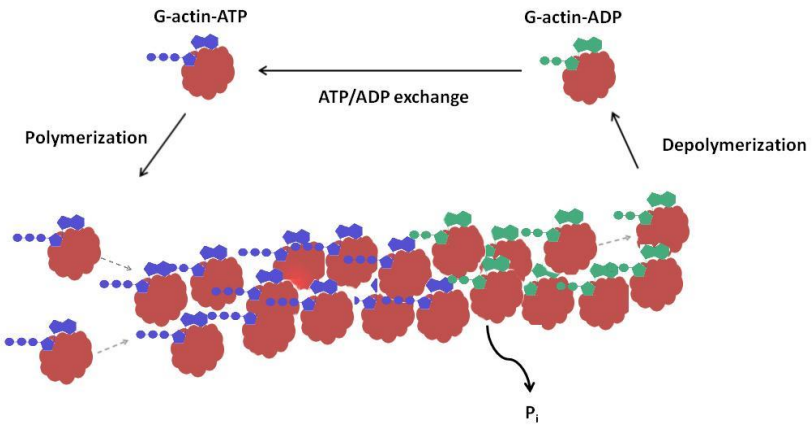

Figure 3 - Actin Polymerisation - G-actin with bound ADP exchanged with ATP. Polymerisation occurs preferentially at the barbed (+ve) end of the filament by association of ATP-actin monomers. Enzymatic cleavage of phosphate from ATP-actin within the filament releases inorganic phosphate. Depolymerisation occurs preferentially from the pointed (-ve) end by disassociation of actin-ADP.

Intracellular polymerised actin filaments consist of a double chain of subunits of actin monomers (diameter 6 nm).[12] At one end of the filament polymerisation is more rapid than depolymerisation and at the other end depolymerisation occurs at a greater rate. These ends are termed the barbed/positive and pointed/negative ends respectively (see **Figure 3**).[10] Each actin monomer has an adenosine binding site, capable of binding either adenosine triphosphate (ATP) or adenosine diphosphate (ADP).[10] The form of the nucleotide bound will influence the kinetics of the monomer, for example monomers containing ATP are found more frequently at the polymerising end of the filament and the ADP-bound actin at the end which is depolymerising.[13] Polymerised actin containing ATP is readily hydrolysed by the addition of water, transforming the bound nucleotide to ADP and inorganic phosphate (P_i).[10] The resulting filaments are dynamic as the polymerisation is a reversible process, in which actin monomers essential for microfilament growth are supplied by the disassembly of the filament from another region.

Motor proteins which utilise filamentous tracks for example kinesin and myosin catalyse the conversion of chemical fuel to mechanical energy for motion. Motor proteins are involved in intracellular transport, cell division and muscle contraction[14] and enable the transportation of 'cargo' along a fuel concentration gradient to a target location within the cell.[15] Myosin, the motor protein associated with actin is present within the majority of eukaryotic cells and its main function is for the contraction of skeletal muscle. Muscle myosin is composed of two polypeptide chains that come together to form a structure with two globular head groups attached to a long tail section.[10] The head groups of myosin have binding sites for ATP or ADP. The tail is a coiled-coil structure of the two polypeptide chains twisted together and connected to the head groups by a 'neck' segment. There are also smaller polypeptide chains that help to strengthen the neck so it can successfully act as a molecular lever. The head groups can bind independently with actin subunits; only one head unit binds to actin at a time and changes in protein conformation with ATP hydrolysis, allow the myosin head to bind, release and then rebind to the actin filament at a different position, resulting in a walking motion.[16]

Another motor protein-filament combination is the kinesin/microtubule system. Microtubules are fibrous networks found within the cytoskeleton of the cell. Like actin, microtubules can assemble and disassemble resulting in a stimuli responsive change in the

shape of the cell.[10] Dimers associate in an end-to end fashion to form short linear fibres called protofilaments. These protofilaments come together in a side-by-side alignment with an element of curvature to form a hollow tubule (diameter 25 nm).[17] Similar to actin filaments, microtubules are classified at each end according to the polymerisation kinetics. The positive end extends at a faster rate, as dimers prefer to attach at this end. Disassembly occurs at both ends but is found to be more rapid at the negative end. The dynamic nature of microtubules is controlled by proteins that either encourage or inhibit polymerisation.[10,18]

The motor protein kinesin has a similar structure to myosin with two globular heads attached to a coiled-coil tail. Each head in this case has a tubulin and nucleotide binding site. Kinesin is capable of transporting vesicles as 'cargo', towards the positive end of the microtubule by step-wise movements along a single protofiliament.[10] It has been reported that the net movement of a kinesin step while carrying cargo is ~80 Å which is roughly the length of one dimer unit.[9,10]

2.2. Artificial micro- and nano- propulsion examples

In order to achieve artificial propulsive motion at the micro- and nano-scale, the design of the motor is crucial. The motor design influences the resulting propulsion mechanism *e.g.* the catalyst employed, the type of motion exhibited, and also possible applications.

The following sections will review recent (and historical) examples of micro- and nano-scale motors. The examples are classified under the following headings: 'catalytic/gradient propulsion'; 'rotational motion' and 'walking motion'. Within each section fully artificial examples will be discussed, followed by examples which make use of biological molecules not normally associated with biological motor ability. Finally biological systems known for motor ability will be discussed, *i.e*. taking advantage of actin polymerisation, rotary ATPase enzymes and walking motor proteins.

Each subsection will discuss motor/fuel design, asymmetry, motility, propulsion mechanism, methods of directional and speed control, and resulting applications.

2.2.1. Gradient/Catalytic Propulsion

The first artificial catalytic motor was reported by Whitesides *et al.* using millimetre sized plates propelled asymmetrically, at the air/water interface, by the decomposition of hydrogen peroxide on a platinum coated surface.[19] This larger scale catalytic motor subsequently inspired small scale (micro- to nano-metre) sized motors.

Catalytic propulsion of an object typically requires the asymmetric attachment of a catalyst to the surface of the object being propelled. The catalyst converts chemical fuel in the surrounding local environment, to products. Products released asymmetrically from the surface of the catalyst result in a propulsion effect. By far the most reported catalytic reaction for propulsion is the decomposition of hydrogen peroxide fuel to water and oxygen by platinum. Albeit the most studied system, there is much controversy as to the mechanism of propulsion and also the terminology used including: local bubble formation[20–31]; electrocatalysis[32–38]; and interfacial tension[39,40] propulsion mechanisms.

Other approaches take advantage of biological catalysts, for example enzymes such as catalase[14,37,41] or glucose oxidase.[14,42] The biological catalysts play the same role as the artificial catalysts, by converting chemical fuel to mechanical energy for movement.

2.2.1.1. Artificial catalytic propulsion

Artificial catalytic motors can be classified according to the propulsion mechanism but also how asymmetry is achieved. This review classifies the following examples under the heading of propulsion *via* generation of product gradient *i.e.* oxygen concentration, proton, or monomer/polymer gradients. There are also three obvious classifications for achieving asymmetry: firstly, Janus particles are colloids with two different faces, for example bimetallic rods or asymmetric spheres. Next, striped or multi-metallic rod examples are discussed, showing that by incorporating additional metals, for example nickel, the motor directionality can be magnetically controlled. Finally, rolled up multi-metallic tubes containing active catalyst on the interior surface, are shown to release product from one end of the tube resulting in propulsion. These examples are discussed from the most simple to more complex where relevant, highlighting unique features of each system and finally discussing speed and directionality control.

Firstly the three main propulsion mechanisms (electrochemical, interfacial tension and oxygen bubble gradients) are discussed using the extensively studied bimetallic Pt/Au artificial rods as examples (see **Figure 4**). This will be followed by an overview of different motor designs employed to achieve asymmetry.

2.2.1.2. Bimetallic rods

In 2004, Sen and co-workers[39] were the first to report nano-sized gold/platinum Janus rods propelled autonomously in a hydrogen peroxide solution (see **Table 1** entry 1). The same system was also studied more recently in 2010 by Posner, Wheat and Moran[32] (see **Table 1** entry 4). Both systems show similar motion in which the rod-shaped particles move towards the platinum end however different mechanisms are proposed; Sen *et al.* describe nanorod motion by an interfacial tension gradient propulsion mechanism,[39] whereas Posner, Wheat and Moran describe the movement by an electrochemical propulsion mechanism,[32] illustrating the controversy involved in determining a common propulsion mechanism. So far three different hypotheses have been proposed.

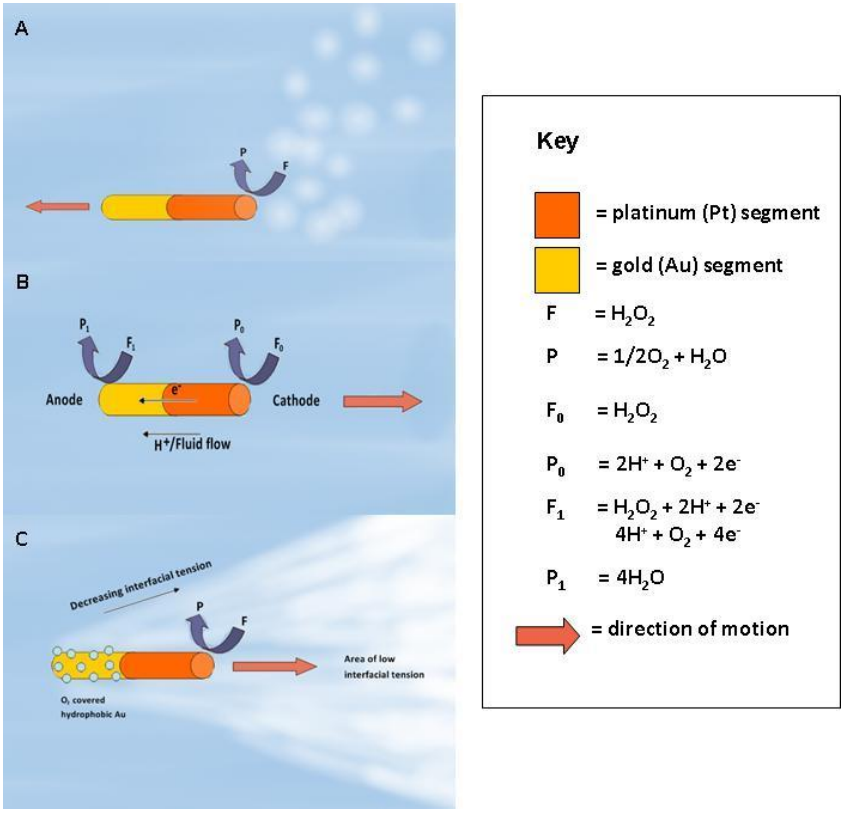

Figure 4 - Mechanisms for catalytic propulsion of Au/Pt bimetallic rods in hydrogen peroxide solution. (A) Oxygen bubble propulsion, (B) Electrochemical propulsion, and (C) Interfacial tension gradient propulsion.

2.2.1.2.1. Electrochemical propulsion

The electrochemical propulsion mechanism describes motion *via* a redox reaction occurring at the opposite ends of a bimetallic rod. Oxidation takes place at the platinum segment of the rod releasing oxygen, protons and electrons. The electrons and protons flow from the platinum anode to the gold cathode. The generated proton gradient results in a force capable of 'pushing' against the surrounding fluid, resulting in propulsion of the motor towards the platinum anode, in the opposite direction to that of the fluid flow (and also electron and proton flow) (see **Figure 4B**). The protons and electrons produced at the platinum anode combine with hydrogen peroxide and oxygen at the gold cathode to produce water. Electrochemical reactions can be enhanced by the incorporation of carbon nanotubes into the motor design as a supply of extra electrons,[33,43] and the addition of redox enhancing additive hydrazine to the motility medium (see **Table 1** entries 3 and 10).[33,43]

2.2.1.2.2. Interfacial tension gradient

A second propulsion mechanism is attributed to the disruption of the local interfacial tension, caused by oxygen generation and subsequent diffusion from the platinum surface. The interface described here is the solid/liquid interface between the bimetallic rod and the surrounding solution containing fuel.[44] The release of oxygen into an aqueous environment disrupts the hydrogen bonding of the water, resulting in decreased interfacial tension. This mechanism of propulsion propels the object with the platinum end leading (as with electrochemical propulsion) (see **Figure 4C**). The direction, however can be reversed if the gold segment is polar or hydrophilic. The interfacial tension increases and the direction of motion will be towards the gold segment. Conversely, if the gold is non-polar or hydrophobic, the rods move toward the platinum segment due to a decrease in interfacial tension.[45] Therefore the propulsion proposed for this mechanism is due to the generation of an interfacial tension gradient along the length of the rod, caused by the generation of a concentration gradient, which in turn produces a net axial force, propelling the rod.[44,45]

2.2.1.2.3. Oxygen bubble propulsion

The 'oxygen bubble propulsion' mechanism describes motor propulsion *via* the asymmetric release of oxygen bubbles from the platinum surface. Platinum decomposes hydrogen peroxide to release water and oxygen, but instead of oxygen dissolution, oxygen bubbles grow from the surface of the platinum and eventually break-free due to buoyancy force (see **Figure 4A**).[46] Water quickly enters the space that the oxygen bubble once occupied and this flow of water is the force responsible for the propulsion of the object.[46] Interestingly in contrast with other proposed propulsion mechanisms, the direction of motion, due to local oxygen bubble production is towards the gold segment of the rod. The reason as to why, in some cases, oxygen bubbles form preferentially (rather than dissolve) resulting in propulsion towards the gold end, is unclear. However it can be hypothesised that there is a relationship between the direction of motion and the catalytic conversion rate. Higher catalytic conversion will produce oxygen at a faster rate on the platinum surface. This oxygen may not be able to fully dissolve but instead forms into bubbles. As the bubbles grow and subsequently break free from the surface, the detachment process generates enough force to propel the rod towards the gold segment, overcoming any interfacial or electrochemical effects.

Further investigation is required to determine the distinguishing factors affecting whether oxygen dissolves or forms bubbles at the platinum surface, giving an insight into how to control which propulsion mechanism will dominate. More of a challenge however, is distinguishing between interfacial and electrochemical propulsion, where perhaps the propulsion observed is in fact a combination of more than one mechanism.

2.2.1.3. Designing a bimetallic rod system

The design of a bimetallic rod system is not confined to gold and platinum, other combinations of metals have been investigated, including Pt, Pd, Ni, Au, Ru and Rh.[37] In this investigation, fifteen combinations of bimetallic nanorods were studied and the predicted direction of motion was confirmed for each. It was found that rotational and translational motion could be achieved by all bimetallic combinations, where rotational motion was only observed for motors with extra asymmetry. Measuring the potential difference between the two metals within the rods revealed that a greater potential difference results in faster

motor speed. The direction of propulsion of a bimetallic rod relies on the combination of metals due to the flow of electrons, protons and water.

Other fuel systems have also been investigated with catalytic platinum/copper bimetallic motors, in motility media containing bromine or iodine. Copper acts as an anode and the platinum end catalytically reduces the halogen fuel. Propulsion occurs *via* an electrochemical mechanism, due to redox reactions occurring at each end of the rod. Directionality in this case was towards the copper section and motors were observed to move faster in I_2 compared with the same concentration of Br_2, with speeds of 12 and 7 μm/s, respectively. The motor's lifetime in this case is limited due to the copper segment being consumed during propulsion.[47]

Improved speeds are achieved by incorporating carbon nanotubes into the platinum section of a Pt/Au nanorod *via* electrodeposition (see **Table 1** entry 3).[33] The added CNTs assist in the redox reactions resulting in an increase in the average speed of the motor from 7.2 μm/s to 51 μm/s (based on approximately 50 nanorods). The reason for this is still unknown, but could be due to a supply of additional electrons by CNTs. Speeds can be accelerated further by the fuel additive hydrazine, which speeds up the oxygen reduction reaction at the gold segment.[33,48,49] It has also been shown that hydrazine is decomposed in the presence of hydrogen peroxide at a catalytic carbon surface.[33,50] According to example trajectories of nanorods and accelerated nanorods containing CNTs, bursts of linear motion along with changes in direction is observed.

These highly accelerated artificial motors can exceed the speed of most biological motors and motors not containing CNTs, with motion occurring towards the platinum region as seen with previous electrochemically propelled Pt/Au examples. The driving force for motion of the CNT-Pt/Au motors is thought to be *via* electrochemical propulsion (explained in section 2.2.1.2.1).[33]

2.2.1.4. Controlling directionality

In the previous motor examples, although they are directional to a certain extent, (*i.e.* towards one end of the rod), different motors still move in different directions, since their individual orientations at any moment is random. Sen and Velegol report the first artificial

chemotaxis of platinum-gold rods in hydrogen peroxide (see **Table 1** entry 2).[34] Chemotaxis is a term usually used to describe the movement of a living organism, towards or away from a local chemical stimulus. Here the movement of the Pt/Au rods can be compared to biological systems which move according to chemical gradients, despite the two systems being completely different. The fuel in this study is localised within a hydrogel 'depot' allowing it to diffuse from the gel into the surrounding solution generating a fuel concentration gradient. The fluid immediately surrounding the 'depot' will have the greatest concentration of H_2O_2, and at increasing distances from the gel the fuel concentration decreases. Diffusion of the fuel from the gel was estimated using diffusion theory. The rods actively diffuse towards higher concentrations of hydrogen peroxide along a fuel concentration gradient towards the hydrogel. The 'chemotaxis' exhibited by the rods is attributable to a combination of electrochemical propulsion and Brownian rotation giving the movement a random walk appearance (a combination of directed and random fluctuations). Other motors have also been reported to exhibit 'chemotaxis' behaviour.[51,52]

2.2.1.4.1. Spherical Janus Particles

Spherical catalytic motors can be produced by asymmetrically coating spherical objects on one hemisphere, in this case with a catalyst/metal (sometimes referred to as Janus particles). Gibbs and Zhao report propulsion of spherical particles by the oxygen bubble propulsion mechanism described in section 2.2.1.2.3 (see **Table 1** entry 7).[20] This system utilises the well-studied hydrogen peroxide/platinum system but instead of a bimetallic rod, oxygen bubbles develop from the surface of the spherical silica/Pt colloidal particles. In the same way that bimetallic rods are propelled, bubbles form on the catalytic (Pt) surface until they break free, driving the particles away from the platinum region. The speed of the motor is dependent on the concentration of fuel and it is reported that the propulsion of the particle is influenced by the surface tension of the motility medium, demonstrated by the addition of varying amounts of sodium dodecyl sulfate (SDS).

Howse *et al*. report the motion of polystyrene spheres, coated with platinum on one hemisphere.[6] As observed with other Pt/H_2O_2 systems, the hydrogen peroxide is decomposed by the platinum face of the sphere. For individual spheres, ballistic (straight line) motion is observed, but at longer times the directional motion reverts to a more diffusive random motion with changes in direction, referred to as a 'random walk', as discussed in chapter 1.1, due to perception of time compared to rotational time, τ_R (see

equation 5). The characteristics of this system's motion can be compared to the 'run and tumble' motion displayed by some types of bacteria.[5]

Other spherical Al-Ga and Mg based Janus motors have been fuelled by water[53] and sea water,[54] respectively. Propulsion is achieved by the breakdown of the water at a catalytic surface, generating hydrogen bubbles.

2.2.1.4.2. Laser/light driven motion

Not all gradient driven motion is generated by chemical gradients; light gradients or light induced chemical gradients can also be employed to promote motor motion.[36,38,55–57]

Velegol, Sen and co-workers investigated photocatalytic spherical micro-motors driven by an asymmetric gradient of light (see **Table 1** entry 5).[58] A number of spherical particles, and sometimes Janus particles[56] have been functionalised by photo responsive moieties, for example azobenzene.[57] Other approaches use light responsive catalysts to produce a chemical gradient. One example involves a catalytic silver/hydrogen peroxide system, where instead of the decomposition of H_2O_2 by Pt, UV light initiates a photolysis reaction with silver, producing Ag^+ and OOH^- ions, which in turn creates a chemical gradient. Propulsion is said to be *via* a self-diffusiophoresis mechanism, whereby the particles move away from the generated ion gradient created by UV illumination.[58]

2.2.1.4.3. Hollow tubular motors

A popular design employed by a number of research groups is a hollow tube-shaped motor.[13, 17, 18, 19, 20, 21, 22, 32] This type of motor contains the catalytic surface on the interior of a tubular support. In fuel rich environments, catalytic reaction products produced inside the tube, are released asymmetrically as fuel is taken in from one end, bubbles evolve from the other, resulting in propulsion of the motor.

Several examples report catalytic Pt on the inner surface of the tube; titanium on the outer surface and an intermediate layer of either Cr, Co or Fe.[25,26,27,28] Other designs incorporate an inner catalytic surface with thermoresponsive polymeric tubes, which roll and unroll with changes in temperature.[59] Many tubular motors are propelled at the air-liquid interface of the motility medium containing H_2O_2 fuel, due to buoyancy created by oxygen bubbles.[25] The intermediate layer can be useful for directional control by incorporating Co

and Fe; the motors can be magnetically controlled, with added guidance employed by using micro-channels.[26] In addition tubular motors are capable of transporting polymer beads as model cargo.[26]

2.2.1.4.4. Conical motors

Bimetallic conical motors function in a similar way to the tubular motors, such that there is a catalytic inner surface for example Pt. Conical-shaped (rather than tubular) motors have been designed to direct catalytic products produced on the inner surface, to emerge from only one end, due to a shape and pressure difference within the conical motor.[29,30] The motors move *via* the oxygen bubble propulsion mechanism where bubbles are released from the larger opening. It is thought that the size of the larger end of the cone affects the overall speed of the motor, where smaller openings lead to decreased speeds.[30] An intermediate magnetic layer, such as nickel can be incorporated between the inner and outer surfaces for added control, and to aid in the loading and transportation of cargo.[29]

Table 1 – Summary of artificial catalytic motors propelled *via* gradient generation. *ROMP – ring opening metathesis polymerisation (see section 2.2.1.5).

	Description	Size (μm) Length/ diameter	Asymmetry	Catalysis	Fuel	Average Speed (μm/s)	Reference
1	Au/Pt rods	1000/ 370	Half Pt	Decomp. of H_2O_2	H_2O_2	~10.0	Paxton[39]
2	Au/Pt rods	2/0.37	Half Pt	Decomp. of H_2O_2	H_2O_2	0.1-0.6	Hong[34]
3	Au/CNT-Ptrods	2/0.22	Half Pt	Decomp. of H_2O_2	H_2O_2	50.0-60.0	Laocharoensuk[33]
4	Au/Pt rods	2/0.37	Half Pt	Decomp. of H_2O_2	H_2O_2	2.0-30.0	Moran[32]
5	SiO_2-Ag spheres	NA/2.34	Half coated in Ag	Photolysis reaction between Ag and H_2O_2	H_2O_2	Not stated	Sen[58]
6	Polystyrene-Pt spheres	NA/1	Half Pt	Decomp. of H_2O_2	H_2O_2	~0.5-3.0	Howse[6]
7	SiO_2-Pt spheres	NA/2.01	Half coated in Pt	Decomp. of H_2O_2	H_2O_2	~1.0-6.0	Zhao[20]
8	Au/SiO_2-Grubbs' spheres	NA/0.96	Hemisphere coated in catalyst	ROMP*	Norborene	0.24-0.31	Pavlick[51]
9	Pt/Ni/Au/Ni /Au rods	1.5/0.4	Terminal Pt	Decomp. of H_2O_2	H_2O_2	~2.4-3.1	Kline[40]
10	Au/Ni/Au/Pt -CNT	2/cargo 1.3 +4.3	Terminal Pt	Decomp. of H_2O_2	H_2O_2	4.0-15.0	Burdick[43]
11	Ti/Fe/Pt tubes	50/cargo 10-15	O_2 released from one terminal of tube	Decomp. of H_2O_2	H_2O_2	60.0	Sanchez[21]
12	Pt-NP coated vesicles	NA/ vesicles 1-25, (Pt NPs 9nm)	'non-uniform' Pt coating	Decomp. of H_2O_2	H_2O_2	2.5-3.0	Kumar[60]
13	Pt/Ni/Au-Ag-HRP wires	0.25/NA	Terminal Pt	Pt decomp. of H_2O_2 and polymerisation by HRP	H_2O_2 and aniline	~12.0	Manesh[61]

2.2.1.5. Other examples of artificial catalytic propulsion

A current hot topic of research is the fabrication of simple, artificial cell mimics. These must include features such as a permeable wall, fibrous skeletal interior and a means of movement. Kumar *et al*. report propulsion of self-assembled spherical vesicles, by catalytic Pt on the surface of the 'protocell' (see **Table 1** entry 12).[60] As seen with previous artificial systems, hydrogen peroxide fuel is decomposed by Pt, and directed propulsion results *via* a

diffusion gradient mechanism. This simple system is a step closer to mimicking the complex structure of living cells using artificial Pt catalysis as a means of propulsion; however this is very different to cell locomotion mechanisms such as actin polymerisation.

The skeletal interior is achieved by the biocatalytic self-assembly of the amino acid derivative, Fmoc-phospho-tyrosine, into fibres by dephosphorylation using alkaline phosphatase. (This self-assembling system has been reported previously[62]). The resulting fibre network, which forms within the vesicle, is a simple mimic of the cell's cytoskeleton. More simplified versions were reported for hollow capsules partially coated in platinum nanoparticles[63] and platinum loaded stomatocytes.[64]

The vast majority of catalytic-gradient propelled motors rely on the H_2O_2/Pt catalysis combination, however not all gradient propulsion mechanisms involve the decomposition of hydrogen peroxide. A simple and artificial mimic to actin polymerisation-based propulsion has recently been accomplished by Sen *et al.* (see **Table 1** entry 8).[51] This example illustrates the first polymerisation powered micro-motor reported outside biological systems. The motor is a Janus particle, half coated with Grubbs' catalyst, which is propelled by the generation of a fuel/product concentration gradient. The catalytic polymerisation reaction involves ring-opening metathesis polymerisation (ROMP) of the monomeric fuel norborene. A similar ROMP propulsion method has also been employed recently for the motion of molecular nanosized 'cars'.[65] The propulsion mechanism is thought to be due to osmophoresis, in which the substrate is catalysed to polymerize on one hemisphere of the particle. The polymer product is 'released', creating an osmotic force on the particle, leading to a net flow of the fluid from the uncoated-hemisphere. Unexpectedly, the particle is thought to move in the direction of polymerisation, opposite to fluid flow. The polymerisation-powered motor also shows chemotaxis, similar to the previously mentioned example by Sen and Velegol.[34] Motors show an increase in aggregation or motion towards an acrylamide gel 'depot' containing the monomer fuel norborene. Motors move along a concentration gradient of norborene, caused by the fuel leaching from the gel. The diffusion rate is shown to increase as the motors move along the gradient towards increasing norborene concentration.

Depolymerisation reactions have also been reported for the propulsion of micromotors, thought to be due to depolymerisation products inducing a surface tension gradient.[66]

2.2.1.6. Controlling speed

Artificial catalytic motor speed can be controlled in a number of ways such as increasing the fuel concentration,[12,16,17,21,22,25,38,39] increasing temperature[28,67] or by the presence of additives *e.g*. hydrazine[33,43] or surfactant.[20,26,29,30] Other speed control measures involve the overall design of the motor such as the size and shape; and also the location and type of catalyst used. An investigation into the relationship between motor speed of bimetallic Au/Ni nanorods and catalytic surface area was reported in 2009 by Ozin and co-workers.[22] A larger surface area was found to promote accelerated decomposition of fuel, resulting in greater motor speeds. By controlling the motor catalytic surface roughness, the overall speed of the resulting nanomotor can, in turn, be controlled.

Studies of spherical Janus particles, have shown that by altering the platinum overlap of Pt/Au coated spheres, the motor speed was affected.[35] Motors with larger gold surface areas resulted in greater motor speeds. The motors are thought to be propelled *via* electrochemical propulsion mechanism but only when the gold and platinum surfaces are in contact with each other, in the presence of fuel.

2.2.1.6.1. External speed control

Externally controlling the speed of nanomotors involves methods which affect the speed indirectly for, in some cases, a more precise speed control without the need for an inbuilt mechanism such as chemical fuel. For example Wang *et al*. report electrochemical speed control of Pt/Au nano-motor motion in hydrogen peroxide fuel.[44] An 'on/off' switch mechanism was incorporated by alternating the applied potential where increased motor velocities are experienced when the system is switched 'on' *i.e.* a negative potential (compared to when switched 'off' where motion is due to Brownian fluctuations only). Enhanced speed caused by a more negative potential, is thought to be due to the reduction of oxygen. This effect can be explained for the interfacial tension gradient propulsion mechanism where at positive potential, the concentration of oxygen is high causing the hydrogen peroxide concentration gradient at the platinum segment to decrease, in turn reducing the overall speed of the motor. The opposite effect is seen at a negative potential, as a low oxygen concentration results therefore the fuel concentration gradient and the motor speed are increased.[44]

Similar ‘on/off’ behaviour was reported for bimetallic rods, in which increasing the solution temperature resulted in acceleration of the nanorod.[67] Thermal pulsing (increasing and decreasing motility medium temperature) is thought to cause rod acceleration at higher temperatures *e.g.* 65°C, due to a combination of decreased water viscosity and an increased rate of electrochemical reactions occurring.

2.2.1.7. Other applications

The examples above display enhanced motion compared to Brownian diffusion, however most systems lack a precise means of controlling directionality, which is key in developing motors for example that can transport cargo to specific locations. As touched upon briefly, one method of externally controlling the direction the motor travels, is the introduction of a magnetic component into the motor design,[26,29,40,68–70] which can be further applied for pick-up and transportation of cargo.[26,29,71] Other methods of motor control include using ultrasound for propulsion.[72]

For magnetically controlled motion, the design of the catalytic motor encompasses ferromagnetic regions by layering between the catalytic surface metals. For example, multi-metallic striped rods or tubes composed of layers of Pt, Ni or Fe and Au/Ti are catalytically propelled by the decomposition of hydrogen peroxide, and directional control is achieved magnetically.[21,40,52] When a magnetic field is applied to the rods, most align themselves with the catalyst end forward and in a perpendicular manner to the field, thought to be a similar mechanism used by magnetotactic bacteria.[40,73] Added control can be employed with the use of microfluidic channels in addition to magnetic guidance.[43]

One magnetically controlled motor, uses a nanoparticle self-assembly method resulting in a motor with both catalytic Pt and ferromagnetic nanoparticles.[68]

Besides transportation applications, motors can potentially be used to perform specific tasks such as drug delivery[74,75] and nano-motor writing on microsurfaces.[61] Enzyme-functionalised Pt/Ni/Au-Ag nano-wires are capable of ‘writing’ on gold surfaces *via* an enzymatic polymerisation reaction. Under external magnetic control, the enzyme facilitates the polymerisation of aniline in the presence of hydrogen peroxide, which is deposited or ‘written’ on a gold microsurface. This nanomotor is primarily propelled by the decomposition of hydrogen peroxide fuel *via* the platinum present within the nanowire; however the enzymatic polymerisation reaction, involving horseradish peroxidase (HRP),

may also have an effect on the motion of the overall system and should also be taken into account.

2.2.1.8. Summary

By far the most studied artificial catalytic motors, involve platinum catalysis of hydrogen peroxide fuel with three main propulsion mechanisms being reported: surface tension gradient, electrochemical and oxygen bubble propulsion. It is clear there is still some debate as to which mechanism best describes the platinum catalysed motor motion, and perhaps it is not as simple as there being only one explanation. It is more likely that the propulsion mechanism of these systems is more complex and involves a combination of forces and effects and depending on the experimental conditions; one mechanism may be more prevalent.

Controlled directionality, surface writing and transportation of simple motors has been illustrated by the addition of ferromagnetic components to allow for magnetic guidance, cargo pick-up, transportation and specific release of cargo such as artificial particles and even biological cells. These systems have the potential for nano-scale transportation *in vivo*, however much work is still needed to ensure they are not only biocompatible but the propulsion mechanism is fully controllable and well understood.

More complex systems aim to mimic highly efficient biological motility, as seen above with the simple-cell mimic that was achieved by the formation of fibre-containing vesicles. The vesicles are essentially much simplified versions of biological cells containing cytoskeletal-like fibre networks enclosed in a permeable membrane. The means of movement however, is far from biological cell locomotion. Controlled, directional and localised fibre growth or extension, as opposed to platinum-based catalysis to achieve motion, would bring this motor closer to a simple cell-mimic. All in all, the advances show a promising way forward for the fabrication of simple and controllable colloidal motors.

2.3. Making use of Biology for motion

Biohybrid motors make use of highly efficient biological catalysts such as enzymes, for the propulsion of simple artificial objects, towards the construction of biocatalytic analogues of artificial catalytic motors reviewed above. (Bio-) catalysts offer an accelerated pathway from reactants to products, with lowered activation energies, for example it is thought that

the decomposition of hydrogen peroxide occurs at lower activation energy with the biological catalyst catalase, compared to catalytic metals such as platinum.[76] The comparable decomposition rates are dependent on type of catalase and concentration of catalysts used.[77] In most cases the biocatalytic motors are propelled by asymmetric distribution of an enzyme, for the catalysis of a reaction, which in turn generates the release of products from near the surface of the motor, resulting in overall propulsion of an object.

2.3.1. Bioelectrochemical propulsion

Bioelectrochemical propulsion of carbon fibres containing a glucose oxidizing anode and an oxygen reducing cathode was reported by Mano and Heller.[42] As current flows through the fibre, ions are transported resulting in motor movement at the air-water interface (see **Table 2** entry 1).The design of the fibre includes a hydrophobic section to allow it to float at the air/water interface; and hydrophilic electrode segments for contact with the electrolytic solution (see **Figure 5**). Glucose oxidase is coated onto one end of the wire for the oxidation of glucose, and on the other end of the fibre oxygen is reduced by the enzyme bilirubin oxidase (BOD). The propulsion mechanism can be explained using the electrochemical mechanism, in which electrons, protons and fluid flow are in the direction of anode (GOx) to cathode (BOD) resulting in motion of the fibre in the opposite direction towards the anode. The ratio of each enzyme can be optimised to control the motion, for example a small excess of glucose oxidase resulted in a spiral trajectory whereas a large excess produced rotational motion.

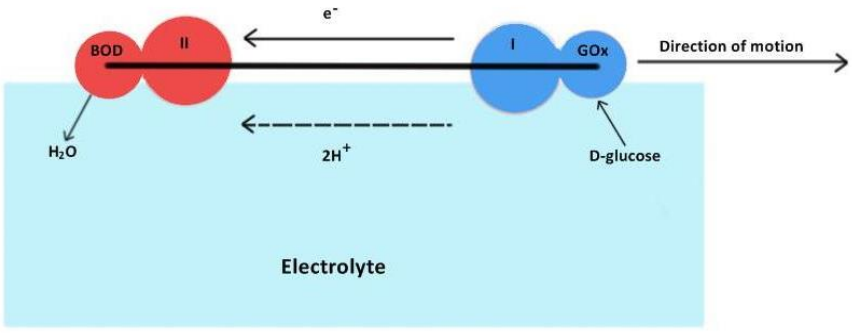

Figure 5 - Carbon fibre with GOx and BOD attached in addition of redox polymers I and II

2.3.1.1. Enzymatic oxygen bubble propulsion

The enzymes catalase and glucose oxidase were attached covalently to carbon nanotubes resulting in autonomous propulsion of the motor, in aqueous glucose fuel.[14] This biohybrid motor involves a similar mechanism to platinum based catalytic motors reviewed in previous sections.[19,33,62,78–80] The primary fuel, glucose, is enzymatically converted to hydrogen peroxide, which is then finally decomposed by catalase resulting in propulsion of the nanotubes (see **Figure 6**). Breaking down the concerted enzymatic reaction, first of all the glucose oxidase facilitates the conversion of glucose to gluconolacton and molecular oxygen, producing hydrogen peroxide. The catalase then decomposes the hydrogen peroxide into water and oxygen which forms bubbles (rather than dissolution). The latter stage is analogous to oxygen bubble propelled platinum based motors seen in previous examples (shown in **Table 1**). The multi-walled carbon nanotubes (MWNTs) tend to bundle together and the resulting aggregates are propelled at various velocities (see **Table 2** entry 2) depending on the size of aggregate formed. Motor movement and directionality is dependent on the nanotube aggregation size and shape formed, however there appears to be no control measure in place for the aggregation process.

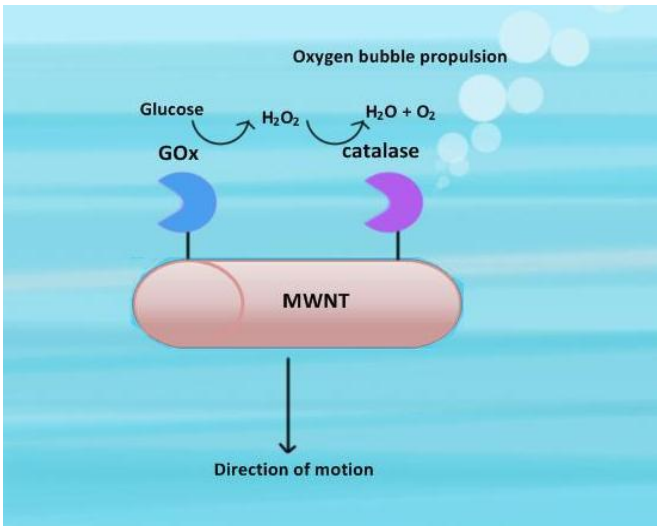

Figure 6 - GOx and catalase attached to multi-walled carbon nanotubes (MWNTs) for oxygen bubble propulsion.

Schmidt *et al*. published work on biocatalytic micro-motors composed of hollow tubes (see **Table 2** entry 3),[41] similar to the above mentioned artificial catalytic tubular motor by

Sanchez.[21] Instead of the interior surface of the rolled up Ti/Au tube being platinum based, this motor contains the enzyme catalase (see **Figure 7**). When placed in aqueous hydrogen peroxide, catalase produces oxygen bubbles which emerge from the tube's opening, as with the platinum example. The release of the oxygen bubbles applies a viscous drag force resulting in propulsion of the micro-motors at the air-water interface. Changes in direction and circular motion are induced by torque produced by the growth and release of the oxygen bubbles.

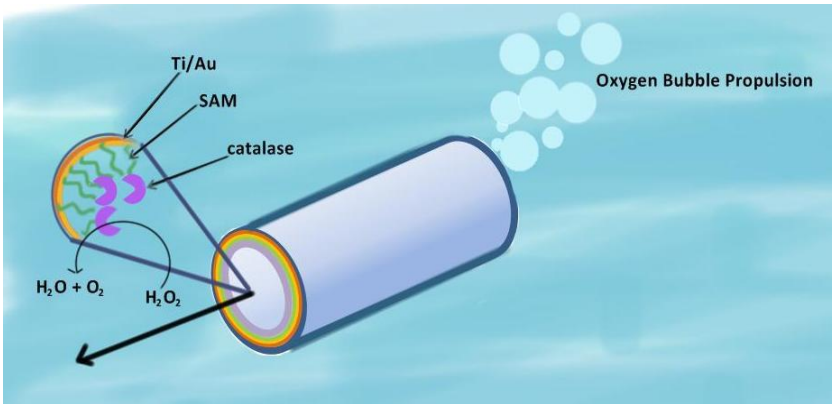

Figure 7 - Ti/Au rolled up tubes with an inner SAM for catalase attachment.

Systems which use biocompatible components such as enzymes are desirable for many applications including *in vivo* transportation. One such application reports the detection of aqueous pollutants using conical catalase micromotors (**Table 2** entry 4).[81] In a polluted environment, catalase is inhibited resulting in reduced release of oxygen bubbles and hence slower motion.

Making use of biological catalysis to produce biohybrid motors, could lead to more effective motors. However it is clear from the smaller number of reported biohybrid motors, that there is much room for expansion and improvement on the already reported systems.

Table 2 – Summary of motors which make use of biological catalysts for motion.

	Description	Size (µm) Length/ Diameter	Asymmetry	Catalysis	Fuel	Average Speed	Reference
1	GOx-Fibre-BOD	0.5-1 cm/7	Different enzyme on each terminal	GOx – oxidises glucose, BOD – reduces oxygen	Glucose (and O_2)	1 cm/s	Mano[42]
2	Catalase-, GOx-CNT	Various	Localised release of O_2 bubbles	GOx – oxidises glucose, catalase – decomposes H_2O_2	Glucose	0.2-0.8 cm/s	Pantarotto[14]
3	Ti/Au-Catalase tubes	50/NA	O_2 bubbles emerge from one end	Decomp. of H_2O_2	H_2O_2	167.4 µm/s (max)	Sanchez[41]
4	Catalase-Au/(PEDOT) conical tubes	2/NA	O_2 bubbles emerge from one end	Decomp. of H_2O_2	H_2O_2	Various	Wang[81]

2.3.2. Making use of biological polymerisation for motion

The actin polymerisation-driven motion of bacterial cells has inspired many groups to investigate actin polymerisation for the propulsion of artificial objects. This section will briefly describe some key examples of artificial objects being propelled by actin polymerisation – termed as actin 'swimmers'. The polymerisation reaction occurring generates a monomer/product gradient and propulsive force on the object. Most of the studies published on actin 'swimmers' are aimed at gaining more knowledge of physiological actin polymerisation, rather than designing a novel motor powered by polymerisation; however as shown with artificial polymerisation powered motors this type of propulsion is effective at transporting artificial objects (see section 2.1 for actin-polymerisation description).

2.3.2.1. Actin 'swimmer' biological components

Actin cell motility relies on a number of proteins being present at localised regions on the surface of the cell. In addition pathogens are known to enter host cells and promote actin polymerisation at the cell's surface for motion.[82] The mechanism of actin polymerisation within certain cells is thought to rely on the protein family WASP (Wiskott-Aldrich

syndrome protein) for the activation of the Arp2/3 complex, which subsequently catalyses the growth of an actin filament.[82,83] There are also WASP mimics such as the protein ActA.[82] In addition the pathogen *Rickettsia* promotes actin polymerisation by the protein RickA.[82] Physiological actin motility requires a complex protein cocktail in order for the nucleating protein to function correctly and for the regulation of other processes including capping; promotion of depolymerisation and cross-linking. In order to replicate or mimic biological actin-driven motility, the motility medium must contain the most essential proteins; by either making use of cell extracts which already contain these proteins or determining the proteins required, isolating them and combining, to replicate a cell extract.

2.3.2.2. Asymmetry

One of the key features with actin polymerisation-powered motors is that asymmetry required for propulsion occurs spontaneously from an initially symmetrical motor. Upon addition of a symmetrically nucleating protein-coated object, to a medium containing fluorescently labelled actin monomers, actin polymerisation occurs around the entire surface of the object. A fluorescent 'cloud' is observed which also grows symmetrically to a given thickness, over a given period of time, depending on a number of factors. These factors may include surface density of active protein, actin monomer concentration or the size of the object being propelled. The development of the initial actin cloud is then followed by a spontaneous symmetry breakage and the formation of an asymmetric tail shaped extension of actin filaments (see **Figure 8** overleaf). The reason why symmetry breakage occurs on a symmetrically coated sphere is unclear, but could be due to a small defect on the particle surface or slightly more monomers adding to one side of the particle over time. This asymmetric distribution of actin polymerisation near to (or on) the surface of the object drives it forward in the direction away from polymerisation (without actin tail formation the object exhibits Brownian motion). The direction of movement contradicts that of the artificial polymerising motors reported by Sen. [51] It may be important to determine how and where the monomers in each case add to the polymer to attribute how directionality is achieved.

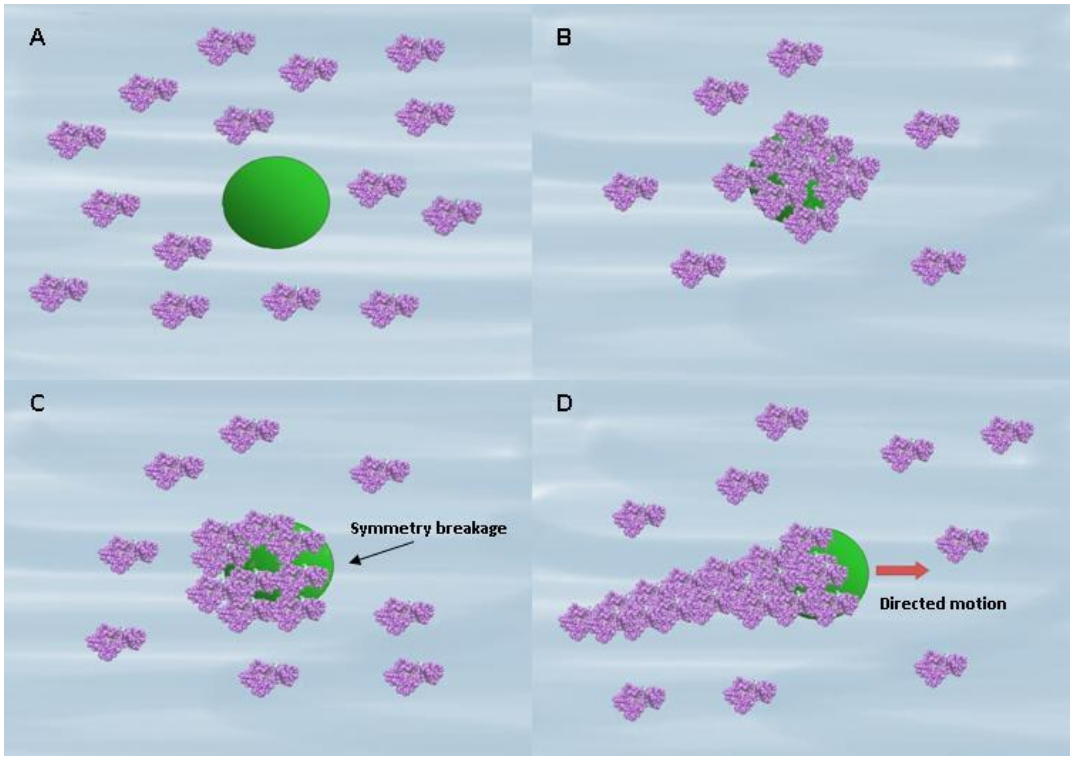

Figure 8 - Actin 'swimmer' mechanism. (A) Artificial object/bead (green) coated uniformly with an actin polymerisation-promoting protein in a solution containing G-actin monomers (purple). (B) Actin polymerisation begins to occur (in the presence of ATP) uniformly around the bead surface forming an actin 'cloud'. (C) Symmetry breakage occurs. (D) Actin tail formation begins to propel the bead away from polymerisation. This shows a very simplified representation of the process, where molecular detail is not included as this varies depending on the polymerisation promoting protein used.

One of the first artificial objects driven by actin polymerisation was reported in 1999 by Theriot *et al*.[84] The study involved symmetrically coating beads (0.5µm i.d.) and asymmetrically coating larger micro-beads (1µm i.d.), with the protein ActA. Larger beads were only driven when an asymmetrical coating was employed with speeds comparable to that of the bacterial cell *L. monocytogenes*[84] (see **Table 3** entry 1). Symmetrically coated beads exhibit Brownian motion until symmetry breakage occurs, caused by actin tail formation; therefore promoting directed motion, in the opposite direction of the comet tail. This study confirmed that initial asymmetry of the nucleating protein was not essential for polymerisation driven directional motion of small beads but by introducing an asymmetric distribution of ActA on the motor, enhanced speeds can be achieved and larger beads can be propelled.

The symmetry breakage stage was studied further using polystyrene beads coated uniformly with the active region of the WASP protein family (see **Table 3**).[83,85] Results

showed actin 'cloud formation',[86] followed by initial signs of symmetry breakage made apparent by a small 'hole' forming in the actin cloud. The 'hole' increases in size until it is large enough for the bead to move through it. The study also showed that actin cloud size and the time taken for symmetry to be disrupted were related to the size of the bead.

Schwartz *et al*. take a slightly different approach to actin polymerisation propulsion, rather than spheres, they uniformly coated both sides of polystyrene disks with ActA (see **Table 3** entry 4).[11] As observed with the spherical objects, areas of actin polymerisation initially develop around the entire ActA coated disk and eventually form into two elastic tails on either side of the disk (flat regions only). It is also reported that flat disks can achieve enhanced velocities compared with curved or spherical beads, possibly due to the dual tail formation working cooperatively to push the disc, in the direction away from actin polymerisation.[11,87]

A simulated model representing disks asymmetrically coated with the Arp2/3complex on only one side has been studied.[9] In this model actin filaments grow exclusively on the side with the activated polymerisation-promoting protein, resulting in asymmetric polymerisation which pushes the disk away from the growing polymer as seen experimentally with previous examples.

2.3.2.3. Controlling actin tail formation

A study was performed in 2010 by Kang *et al*. which showed that actin polymerisation could be controlled by the addition of bovine serum albumin (BSA) and/or ADF/cofilin (see **Table 3** entry 3).[85] Polystyrene beads were coated uniformly with the actin nucleating protein VCA. The additive BSA functioned to prevent unwanted adsorption of proteins, in particular monomeric actin. ADF (actin depolymerising factor) was added to promote actin depolymerisation, in turn supplying more monomers into the surrounding solution available to take part in polymerisation.

2.3.2.4. Liposome-cargo transportation

Actin polymerisation can be employed for the transportation of cargo, for example ARF1-mediated actin-polymerisation has been shown to transport vesicles (see **Table 3** entry 6).[79] ARF1 (ADP-ribosylation factor 1) is a guanosine-5'-triphosphate (GTP) binding protein, involved in a cascade of reactions leading to the promotion of actin polymerisation.

Artificial liposomes bound with ARF1 were prepared as simple vesicle mimics and in motility medium, actin clouds were observed around the liposome, increasing in thickness over time, as seen previously with bead motility examples. 'Cloud' formation was followed by either collapse of the liposome or actin tail formation, only resulting in movement in the latter case. Only liposomes that were less than two micrometres in size exhibited actin tails and motion, therefore the ability to control the size of the liposome is a key factor for achieving motility.[79]

Table 3 – Summary of actin 'swimmers'. In all cases the catalysis is the hydrolysis of ATP and actin polymerisation, with ATP and G-actin monomers as fuel molecules.

	Description	Size (µm i.d.)	Asymmetry	Average Speed (µm/min)	Reference
1	ActA coated polystyrene beads	1	Asymmetric ActA coating	6.00	Cameron[84]
2	VCA coated polystyrene beads	6	Asymmetric actin tail formation	0.50	van der Gucht[86]
3	VCA coated polystyrene beads	1 and 2	Asymmetric actin tail formation	0.086	Kang[85]
4	ActA coated disks	5 (0.8 µm thick)	Asymmetric actin tail formation	0.37	Schwartz[11]
5	WASP coated beads	1	Asymmetric actin tail formation	0.20	Yarar[88]
6	ARF1 coated vesicles	1-20	Asymmetric actin tail formation	0.52	Heuvingh[79]
7	RickA coated beads	0.5	Asymmetric actin tail formation	3.20	Jeng[82]
8	ActA coated beads	0.5	Asymmetric actin tail formation	7.20	Van Oudenaarden[80]

2.3.2.5. Summary

In summary, the examples described above have proved that artificial objects can be successfully propelled, making use of biological actin-polymerisation. There are many theories proposed for the actin-based propulsion mechanism but here the propulsion is

classified as a gradient induced mechanism. As the monomer is converted to polymer, the area directly surrounding the surface of the 'motor' contains an immediately high concentration of monomer, which decreases along the length of the resulting actin tail. Actin 'swimmers' make use of a variety of polymerisation promoting proteins which have comparable mechanisms and speeds. Interestingly, the need for the motor to initially be asymmetric, seen for some artificial and biohybrid motor systems, is not crucial for actin polymerisation-driven motility. Asymmetry or symmetry breakage is however important for the overall motility of the object, where actin tail formation acts as the trigger to the motion. As mentioned previously, these studies were aimed at understanding actin polymerisation further and the focus was not on polymerisation powered motion. Perhaps if this was the primary goal, actin 'swimmers' could be engineered to be highly efficient with improved 'swimming' speeds, making use of the most optimal actin-polymerising proteins and additives.

2.3.3. Rotational movement

For the scope of this review, the focus is on directional ballistic motion, therefore rotational motion will only be briefly discussed with the use of key examples of artificial and biohybrid rotary systems (see **Table 4**).

As demonstrated in the previous section, a number of micro- and nano-motors aim to achieve linear motion, however a number of recent efforts have been inspired by nature's rotary motors, such as ATPase. The process of rotation involves the circular movement of an object about a fixed point or axis where rotational motion occurs preferentially over translational motion, for objects which have extra built in asymmetry within their design. Research groups have successfully reported rotary motion by purely artificial means. There are a variety of ways to design artificial catalytically driven motors with additional asymmetry and hence rotational motion, such as bimetallic rods,[89] spherical rotational motors, [90, 78] L- or spring shaped rotors,[91] and multi-metallic rods. [92,93]

Generally clock-wise and anti-clockwise rotation is reported with no apparent control over the direction[89,92,93] and for one example rotary motion is only observed in viscous solutions such as glycerol.[78] In most cases motors are not restricted to rotational motion but translational, circular and 'rolling' motion have also been reported. [90,89,91] Further to this, and depending on the motor shape, rotationally induced translational motion is possible.

As with translational motors, external control can be accomplished magnetically by an added ferromagnetic layer within the motor design. [94,95] In one case a silica helix is coated with cobalt and by applying a magnetic field rotation occurs, resulting in rotationally induced translational motion.[94]

Ferromagnetic nickel nanowires are capable of magnetically induced rotational (and in turn translational) motion, when the motor comes into close proximity with a vertical boundary.[94] Cargo pick-up and transportation is also possible through magnetic control of Ni nanowires.[94]

Table 4 – Summary of artificial rotary motors. All examples catalyse the decomposition of hydrogen peroxide.

	Description	Size (μm) Length/ diameter	Asymmetry	Average Speed (rad/s)	Reference
1	Mn catalytic rotor on SiO_2 spheres	NA/80	Local O_2 bubble formation	1.55 x10^{-2}	Vicario[78]
2	Au/Ni rods	2.5/NA	Ni at one terminus	1.5	Fournier-Bidoz[89]
3	Au-Pt rods	5/0.36	Au/Cr bilayer half coating rod	2.5	Qin[92]
4	Pt-polystyrene spheres	NA/2	Half of sphere coated with Pt	0-1.3	Ebbens[90]
5	Si/Pt and Si/Ag rod, L- and spring- shaped nanomotors	Various	Asymmetric Pt coating	Various	He[91]
6	Au-Ru rods coated in trilayer	3.5/NA	Half coated in trilayer with Pt outer surface	18.8	Wang[93]

An alternative approach to mimicking biological rotational motion is to make use of biological motors capable of producing rotary torque. The rotary motor ATPase is an enzyme that hydrolyses ATP in living organisms. Hydrolysis of three ATP molecules by the enzyme generates a net torque to drive rotation. ATPase has been attached to artificial objects to gain knowledge of the rotational motion under physiological conditions,[16,96] but for the purposes of this review they are classified for their use in rotational propulsion of artificial objects.

2.3.3.1. Summary

It is clear from the above examples that it is challenging to control whether rotational or translational motion occurs, especially for motors that are not anchored to a stator or

surface. In many cases both types of movement can be achieved by applying different conditions, for example increasing the solution viscosity or allowing aggregation of the motors. Other motors exhibit motion somewhere in between or a combination of rotational and translational *i.e.* 'tumbling' or rotary induced translation motion.[91] The key factor in ensuring rotary motion is the structural asymmetry of the object being propelled. The motor must be fabricated in a way to precisely control the asymmetry and the resulting motion. Many of the rotational motors arise accidentally due to surface defects[78,89] or interactions with other components in the system.[90,93] Other methods involve physically anchoring one section of the motor to a surface or designing the motor carefully to ensure asymmetric distribution of reaction products.

Examples which take advantage of the biological rotary motor ATPase appear to have exclusively rotational motion and in one of the previously mentioned examples, only one direction of rotation is observed.[96] The built in biological design of the motor provides a highly specific and efficient rotary torque to ensure controlled rotational motion.

2.4. Walkers

Walking motion is defined as a motor containing two or more 'legs' or appendages which alternate for forward (or backward) motion. Ultimately biological motor proteins capable of 'walking' at the nanoscale have inspired artificial molecular walkers. Specific details of walkers will not be described in this review, however for completeness molecular artificial walkers are mentioned briefly with reference to recent papers and reviews in the area.[61,73,97]

2.4.1. Making use of DNA for walking motion

Biology's information carrying molecule, deoxyribonucleic acid (DNA), has been employed for the development of biological molecular motors capable of walking motion. As a system normally associated for carrying genetic information, many DNA walkers take advantage of specific complementary base pairing, therefore using biological functionality not normally used for motion in nature.

There are two major DNA walker systems reported in literature. The first involves the walker molecule that is capable of cleaving sites on a DNA track *via* cleavage enzymes, [98–102] forcing the walker onward to new sites.[98,99]

The second method, termed 'strand displacement', uses hybridisation of strands that are not exactly complementary.[100–105] By adding a strand with a better match, the first strand will be displaced, leading to walking motion along a predetermined DNA sequence track. The direction of motion can be controlled by altering the fuel strand that is added to the system.[106] Smart systems have been developed that are responsive to stimuli such as pH,[107] and DNA molecular walkers have even been employed for cargo transportation.[107]

2.4.2. Making use of motor proteins for walking motion

Directed walking motion along a surface has been studied with the use of biological motor proteins and their corresponding self-assembled filamentous tracks (as discussed in section 2.1). The most commonly used pairs of motor proteins and filaments are the kinesin-microtubule and myosin-actin systems.

In nature, motor proteins walk along the corresponding filaments in a directed fashion to one end of the track and are capable of transporting vesicles along these tracks within cells.[10] A number of groups have taken advantage of this type of motion by immobilising filaments ('fixed filament') onto a surface which motor proteins walk along using the filaments as tracks.

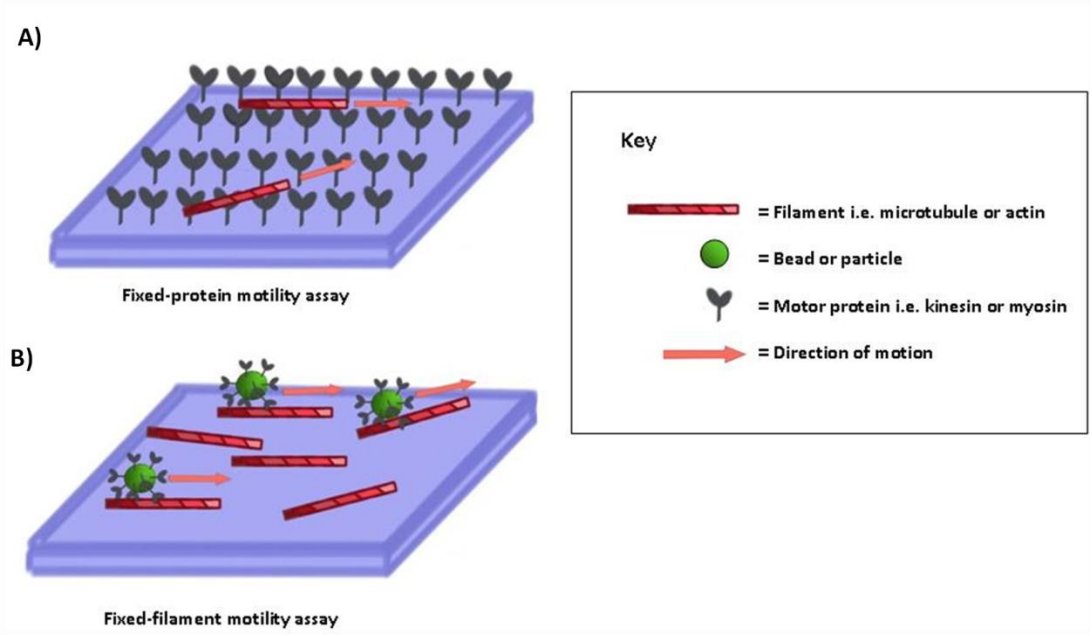

Figure 9 – Walking motor protein/filament motility assay arrangements. (A) 'Fixed protein'; for example myosin is attached to a glass surface and actin filaments glide over in presence of ATP. (B) 'Fixed filament'; *e.g.* actin filaments are fixed to the surface and an artificial object is coated with myosin. When combined the object is transported along the length of the filament in the presence of

ATP fuel. The direction of motion is dependent upon the motor protein and conditions used in each individual assay.

Another, more popular method of motion along a surface turns the previous system around and instead of immobilising the filaments the motor proteins are attached to the surface ('fixed motor protein'). The filaments are then added to the system and glide along the carpet of motor protein molecules.

Further studies have investigated not only the directed motion of the filaments but also their ability to transport cargo. As a result many artificial objects including beads,[108] liposomes[109] and quantum dots (QDs)[110] have been successfully transported either by the motor proteins themselves or by being attached to the gliding filaments, depending on the motility assay being used; 'fixed filament' or 'fixed motor protein' respectively (see **Figure 9** on previous page). This review will describe examples of the myosin-actin systems only with both 'fixed-filament' and 'fixed-motor protein' arrangements, first of all introducing the general features of the devices. In addition there are a number of review papers summarising motor protein *in vitro* motility assays for further information.[111,112]

2.4.2.1. Motility assay design

The general design of a motor protein motility assay involves making a simple flow cell around the chosen motility surface, to which the motility medium is added which contains essential components for motor protein function in an *in vitro* environment.[109,113,114] Other additives can be included to minimise photo-bleaching and photo-oxidation.[109,115–117] The most important addition to the motility buffer is the chemical fuel ATP which powers motion and in some examples the fuel can be released in a controlled manner.[118]

Another important aspect of the device is the underlying surface which can be lithographically patterned with a variety of substances to create tracks for motor protein guidance.[113–115,119–121] Many groups have dedicated studies investigating the interactions occurring between the motor protein and the surface to which it adsorbs ('Fixed motor protein' arrangement).[122–124] These studies have found that surface hydrophobicity is an important factor for motor protein interaction, where a more hydrophobic surface encourages adsorption. In most studies of actin-myosin motility assays, heavy meromyosin (HMM) is used instead of the full motor molecule.[114] This molecule is simply the myosin

head region minus the tail fragment.[125,126] After motor protein adsorption to the substrate, an inert protein such as casein or bovine serum albumin (BSA) is added to coat the free surface, preventing unwanted adsorption of the filaments. Once the surface and motility medium is prepared within a flow cell, the filaments can be added.

In order to visualise movement, filaments are usually labelled with a fluorescent tag for imaging, for example actin labelled with rhodamine-phalloidin.[113] Most studies record the velocity of the filaments and gliding speeds have been shown to be dependent on fuel concentration,[127,128] pH,[112,128] ionic strength[128] and temperature[109,119,128] with speeds ranging from a few tens of nanometres per second up to 20 μm/s (see **Table 5**). Some devices incorporate elements of external control *e.g.* electrical,[118,119,129] and magnetic.[130,131]

Table 5 - Summary of myosin-actin motility assays.

	ATP concentration (mM)	Speed (μm/s)	Myosin	Cargo	Tracks/surface	Track Width (nm)	Reference
1	1	0.5-1.3	Rabbit skeletal HMM	None	PTFE	10-100	Suzuki[113]
2	1	4.0-10.0	HMM myosin II	None	TMCS/O_2 plasma PMMA	150-500	Sundberg[114]
3	7.5	0-20.0	Not stated	None	PMMA	1000	Riveline[129]
4	2	2.9 and 2.5	Rabbit skeletal HMM	None	PDMS on PAH/PSS	micro	Jaber[115]
5	1	4.0-5.0	HMM myosin II	None	PMMA	100-700	Bunk[120]
6	Not stated	2.5-6.5	Rabbit skeletal HMM	None	sw-CNT/ODT or cysteamine	nano-micro	Byun[121]
7	500nM, 2 and 5 μM	21.0, 49.0, 116.0 (nm/s)	myosin V and X	None	N/A	None	Arsenault[108]
8	Not stated	16.8 (max)	Rabbit skeletal HMM	None	Nitrocellulose	None	Mihajlović[119]
9	2	0-8.0	Rabbit skeletal HMM	None	Nitrocellulose	None	Gordon[116]
10	1	0-1.2	Rabbit skeletal HMM	None	Range of surfaces	None	Albet-Torres[122]
11	2	0-3.3	Rabbit skeletal HMM	None	PMMA and AAPO	None	Nicolau[124]
12	1	8.4	Rabbit skeletal HMM	None	graphene/Py-NH_2	None	Byun[118]
13	1	5.0-7.0	Rabbit skeletal HMM	QD	Nitrocellulose or TMS	None	Månsson[110]
14	1.5	1.7-2.4	HMM myosin II	Liposomes and *E.coli* cells	Nitrocellulose	None	Takatsuki[109]

2.4.2.2. Controlling motion and cargo transportation

The use of polymer patterned surfaces is employed to introduce an element of spatial confinement within the motility assay, and offer a way of controlling walking or gliding speeds.[113,114,115,120] Alternatively actin guidance can be accomplished using carbon nanotube (CNT) patterned surfaces.[121] Actin filaments gliding in a controlled manner can then be

employed to transport cargo, such as fluorescent quantum dots,[110] liposomes,[109] and even cells can be transported by actin filament bundles.[109]

External control of walking motion has been reported by the application of external electric fields. One example shows directional control over negatively charged actin filaments gliding toward positive electrodes.[129] Others show electrochemically controlled thermal acceleration/deceleration of actin filaments, taking advantage of increased reaction rate trends at higher temperature.[119] 'On/off' motility can also be controlled through electrically controlled release of ATP fuel. [118]

2.4.2.3. Kinesin-microtubule motility assays

As with the actin-myosin walkers, equivalent work has been published for kinesin and microtubule (MT) walking systems. These systems feature similar ideas and so will be briefly summarised and the reader is directed to some recent review papers on the topic.[132–136] The 'fixed filament' [137–143]and 'fixed protein'[144–164,] arrangements are also reported for MT and kinesin motility assays. Walker motion can be controlled by a variety of techniques including the use of predetermined tracks for guidance[139,144,149,151,152] and the external application of electric[162,163] or magnetic fields.[130,131,144] Start-stop motion can also be achieved using thermoresponsive[117] or photoresponsive materials.[146]

Kinesin molecules or microtubules can be loaded with cargo in the 'fixed filament' and 'fixed protein' arrangements, respectively. A number of different cargos have been reported to be transported, such as micro- and nano- sized particles,[139,141,144,154,164,165,] quantum dots,[140,143,144,148,152,154] oil droplets,[137] liposomes,[145] vesicles[142] and biomolecules[140,144,150] for example DNA.[156] More complex systems have incorporated loading and unloading of cargo, with the use of DNA hybridisation.[145,164] Applications of such devices have included nano-separation or sorting,[137,149] drug delivery[137] and biosensing.[158]

2.5. Summary

In conclusion it can be seen that self-propelled micro- and nano- motion can be achieved in multiple ways. Artificial self-propelled motors have been widely studied with three main proposed propulsion mechanisms: oxygen bubble, electrochemical and interfacial tension

propulsion. There is some debate as to which of these mechanisms best describes the propulsion of catalytic motors.

Catalytic biohybrid motors are becoming a popular area of research, with the incorporation of highly efficient biomolecules with artificial objects for motion. The propulsion mechanisms described for artificial systems can also be applied for biohybrid motors. Overall the three main propulsion strategies for catalytic motors can be classified as the formation of a gradient, whether it is a chemical, bubble or electrical gradient.

Overall it can be seen that asymmetry is key to designing directed propulsion at the micro- and nano-scale. In all of the above examples asymmetry or symmetry breakage is required to overcome or enhance Brownian diffusion. It is yet unknown whether permanent asymmetry is required to enhance the motion of a nanomotor. It may in fact be possible for semi-permanent 'pulses' of asymmetrical catalysis to push or drive propulsion, resulting in Brownian yet enhanced diffusion.

Actin polymerisation powered motor examples have shown that initial asymmetry is not necessary and that spontaneous symmetry breakage is observed, initiating motor movement, however further studies are required to fully understand the mechanism of symmetry breakage.

Inspiration from biology's walking motor proteins has led to the development of artificial molecular walkers, walkers that take advantage of biological components such as DNA and also the use of motor proteins for walking motion along artificial surfaces.

The investigation and development of such motors can reveal properties of movement at such a small scale and how to overcome Brownian fluctuations to achieve propulsion. In addition micro- and nano- motors could be used for the loading, transportation and unloading of cargo; separation or construction and also for biosensing applications.

For statistical comparison, the total amount of data measured by many of the micro- and nano- motor examples discussed here is unclear. Realistically it would be beneficial to track large numbers of particles or motors to achieve reliable results.

To date there have been no known reports of propulsion *via* biocatalytic self-assembly. Therefore this project aims at developing a new method for nano-propulsion using

biocatalysis for the self-assembly of aromatic dipeptide amphiphile molecules into fibre structures.

Literature review Part 2: Self-assembly

Self-assembly is the spontaneous and potentially reversible self-association of two or more molecules into higher ordered structures, held together by supramolecular interactions. There are many examples of self-assembled systems in nature, for example nucleic acids, phospholipids and amino acids are all natural building blocks capable of self-assembling into more complex systems by non-covalent interactions to make up the DNA double helix, membranes and the three dimensional structure of protein molecules, respectively.[166,167] Such biological self-assembled structures rely on weak, compared to chemical bonds, non-covalent interactions such as hydrogen bonds and electrostatic, hydrophobic, aromatic and van der Waals interactions.[168,169]

2.6. Supramolecular interactions

A typical covalent bond can range in strength from 350-940 kJ mol^{-1} however biological systems and supramolecular self-assembling systems employ generally much weaker supramolecular interactions ranging from 2 kJ mol^{-1} for van der Waals interactions to 250 kJ mol^{-1} for ion-ion interactions. The length scale between interacting groups of a non-covalent 'bond' can be in the range of 10 Å, compared to a shorter interatomic distance of 2 Å for atoms bonded in a covalent bond.[170] Individually supramolecular interactions are weak but with the combination of many interactions dynamic and reversible structures are seen widely, for example in biological systems such as those mentioned above.[171]

2.6.1. Hydrogen bonding

A hydrogen bond arises when a hydrogen atom possesses a small positive charge, due to being covalently bonded to an electronegative atom *i.e.* oxygen or nitrogen. The bond then occurs between the hydrogen and an electron withdrawing atom (see **Figure 10** overleaf). The type of donor and acceptor groups and the bond geometry influences the overall strength and length scale of a hydrogen bond, where a typical hydrogen bond can range in strength from 4-120 kJ mol^{-1}.[172] The surrounding solvent will have an effect on a hydrogen bond, if the solvent is a good donor or acceptor such as water this can weaken hydrogen bonds.[171] Hydrogen bonding is an important interaction in biological assemblies, as hydrogen bond donors and acceptors occur between for example nucleic acids within the

DNA double helix and amino acids of a protein molecule, leading to tertiary and quaternary structures.[172]

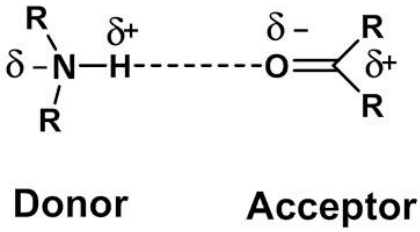

Figure 10 - A carbonyl group acting as an acceptor for a hydrogen atom from an amine donor group.

2.6.2. Electrostatic interactions

Ionic (and dipolar) interactions occur between oppositely charged groups and atoms *i.e.* negative and positive charges. Electrostatic interactions can be grouped into three main classes: i) ion-ion interactions; ii) ion-dipole interactions and iii) dipole-dipole interactions, where the strongest interaction is seen for ion-ion interactions (see **Figure 11**). The strength of individual ionic interactions depends on the atoms or species involved, however ionic species will result in stronger interactions (strength typically between 200-300 kJ mol^{-1}) than dipolar species (5-50 kJ mol^{-1}) due to ions possessing a greater charge density.[172] Biological systems make use of electrostatic interactions for a variety of recognition processes, for example the interaction between an enzyme active site and a substrate.[172]

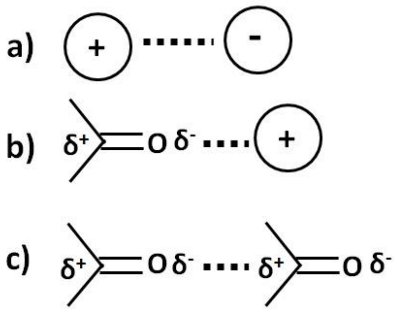

Figure 11 - Electrostatic interactions (a) ion-ion, (b) ion-dipole and (c) dipole-dipole.[171]

2.6.3. Hydrophobic interactions

The hydrophobic effect arises from the exclusion of hydrophobic or non-polar molecules from aqueous environments. The driving force for this type of interaction is that water

molecules interact *via* hydrogen bonds with other water molecules or polar groups.[172] Therefore molecules that are unable to take part in hydrogen bonding with water disrupt the local structure of the water and result in hydrophobic molecules grouping together in order to reduce the free energy of the system.[173] Hydrophobic interactions are important for membrane lipids owing to the fluid properties of membranes.[169]

2.6.4. Aromatic interactions

π-interactions occur between aromatic rings, usually where one ring constituent is electron rich and another is electron poor. Attractive forces arise between the negatively charged π-electron-cloud of the ring and a positive σ-frame of another aromatic group.[172]

There are thought to be two main types of π- π interactions: i) *face-to-face* where parallel aromatic rings interact in such a way that the centre of one ring interacts with a corner of another; and ii) *edge-to-face* interactions occur between the hydrogen atom of a ring perpendicular to the centre of another aromatic group (shown using benzene as an example in **Figure 12**).[172] The aromatic amino acids phenylalanine, tyrosine and tryptophan, are capable of participating in π-interactions, for the folding of proteins into their three-dimensional structures. The DNA double helix also maintains its structural stability through aromatic interactions between base-pairs.[172,174]

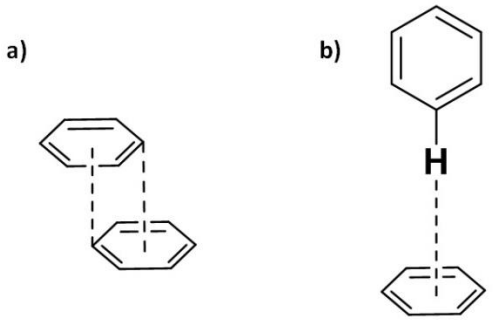

Figure 12 - π-π interactions (a) face-to-face and (b) edge-to-face conformations.

2.6.5. van der Waals interactions

van der Waals (or London) interactions occur between overall uncharged atoms, molecules or particles with fluctuating electron distributions which result in temporary dipole moments. A temporary dipole moment of one atom will induce a corresponding opposite dipole moment in another atom, if the atoms are in close enough proximity, resulting in

attraction between the two atoms. The interaction strength depends on other atoms in the molecule and how polarisable the atoms involved are.[172,173]

2.7. Peptide self-assembly

Self-assembled structures usually exist due to a combination of the above described supramolecular interactions. The self-assembling building blocks can be designed to interact in specific orientations with each other. Vast arrays of artificial materials are capable of self-assembly but for the purposes of this project only peptide self-assembly will be reviewed.

Peptides are biological polymers containing two or more amino acids, linked in a chain-like fashion *via* peptide bonds *i.e.* the bond formed between the carboxyl group and amino group of neighbouring amino acids in the chain. Peptide sequences can be designed specifically using the twenty naturally occurring amino acids (see **Figure 13**) as well as artificial amino acids and functional groups not found in nature.[175] The inbuilt design of the peptide sequence can produce specific 'artificial' self-assembled structures, inspired by biologically assembled structures. A vast library of possible peptide sequences can be achieved by altering the chain length, primary sequence, and by modifying the amino acid side chains or termini.

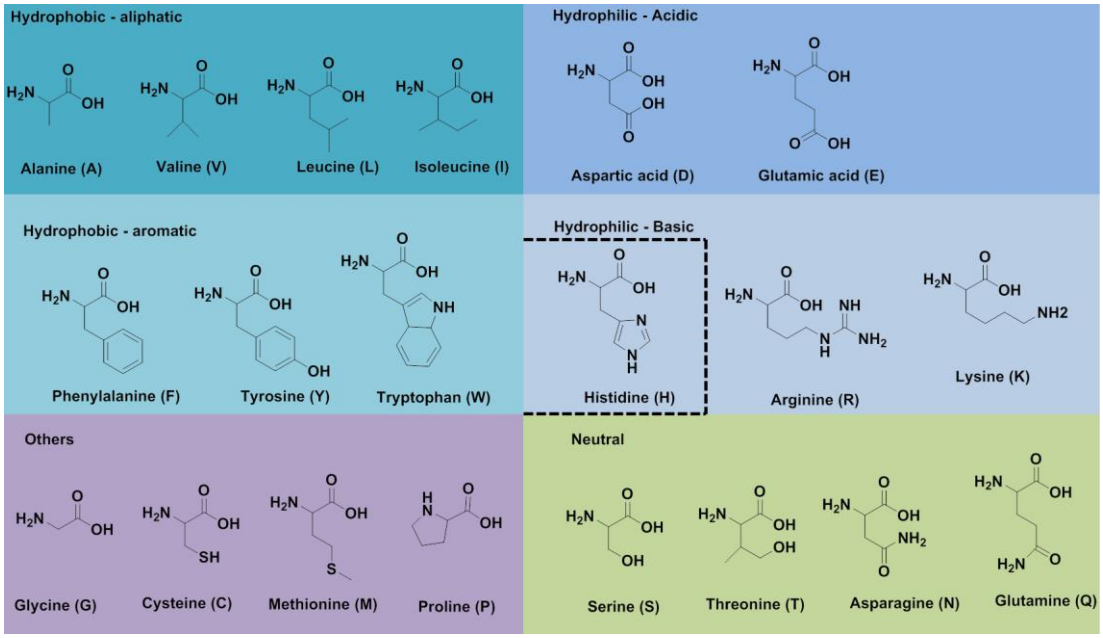

Figure 13 - Naturally occurring amino acids.

Inspired by biology, peptide sequences have been designed to self-assemble to mimic the commonly found biological architectures, such as helices/coiled-coils,[176,177] sheets,[178,179] tubes,[180,181] fibres[182,183] and amphiphilic assembles,[184,185] *via* supramolecular interactions such as electrostatic, aromatic and H-bonding interactions (as mentioned in section 2.6). In many cases self-assembled structures extend hierarchically to larger length scales, to produce, for example, fibrous networks capable of entrapping water, resulting in self-supporting hydrogels.[186]

2.7.1. Applications of peptide nano-materials

Possible applications for self-assembled peptide materials depend on the structures formed, for example fibrous hydrogels can be used as synthetic mimics for the three dimensional environment of the cell, for uses in cell culture applications.[187] Hydrogels have potential in drug delivery, by trapping drug molecules and releasing in response to external stimuli.[188,189]

Amphiphilic peptides designed to self-assemble into vesicles or spherical aggregates have potential as drug carriers. Amphiphilic assemblies of nanotubes and vesicles have been used for the delivery of DNA using a positively charged peptide amphiphile to trap positively charged DNA.[169]

Nanomaterials for specific applications often require stimuli responsive self-assembled materials, *i.e.* the capability to 'switch on' assembly using some external control. Peptide sequences can be designed to display self-assembly in response to specific external factors such as pH,[188,190] temperature,[182] light,[191] sound,[192–194] salts[195] and biocatalysts.[62,196,197] For the purpose of this project, biocatalytically triggered self-assembly will be discussed further, with a particular focus on enzyme responsive aromatic dipeptide amphiphiles. Recent review articles summarise biocatalytic conversion of peptides to self-assembled structures.[198–200]

2.8. Biocatalytic self-assembly of aromatic dipeptide amphiphiles

Peptide sequences can be designed not only to influence self-assembly but also to act as substrates for biological catalysts, such that catalysis initiates assembly. Enzyme responsive

self-assembly has been reported over recent years, with a variety of enzymes and peptidic substrates. The enzymes convert the peptide substrates to another form, capable of self-assembling into supramolecular structures.[198,201]

Aromatic dipeptide amphiphiles offer an attractive platform for biocatalytic self-assembly. As they contain only two amino acids, they can be easily synthesised and functionalised with groups recognised by specific enzymes.

Aromatic dipeptides are defined as the simplest peptide sequence (two residues), with an aromatic functional group, usually at the N-terminus.[197] Therefore for a peptide sequence to be classified as an *aromatic peptide amphiphile* it must contain an aromatic moiety as well as both hydrophilic and hydrophobic regions. Such peptides can aggregate or assemble above a critical aggregation concentration into ordered structures due to the hydrophobic effect, by the exclusion of water in aqueous environments. In the case of aromatic peptide amphiphiles, aromatic regions also take part in aromatic interactions and also offer added hydrophobicity to the molecule.

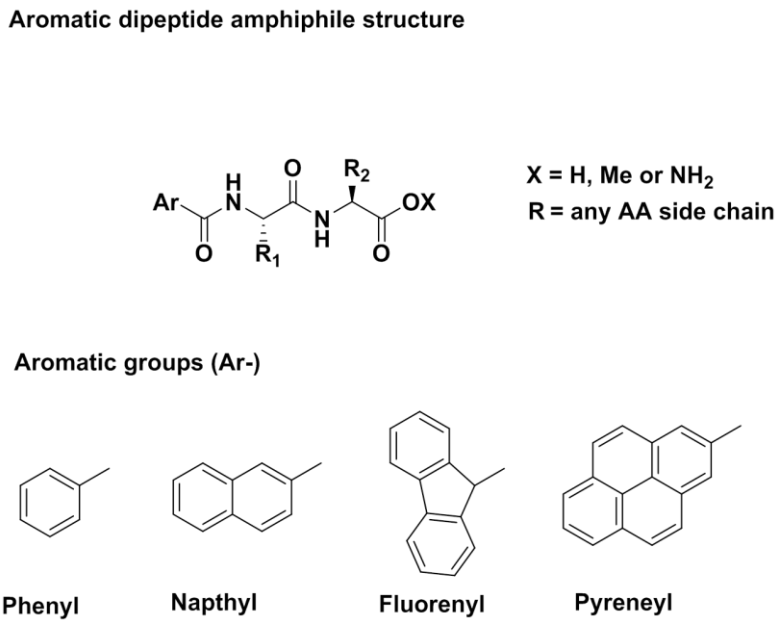

Figure 14 – General structure of an aromatic dipeptide amphiphile composed of two amino acids (AA) and possible N-terminal aromatic groups (Ar-).

Aromatic groups are commonly used to modify dipeptide sequences and add to the hydrophobicity of the molecule. Functionalisation of the peptide termini can be achieved using fluorenyl, pyrene, naphthalene, or phenyl groups (see **Figure 14**).[197,202–205] Aromaticity

can also be incorporated within the dipeptide sequence using aromatic amino acids tyrosine, phenylalanine or tryptophan.

Hydrophilic regions can be designed by the incorporation of charged amino acids such as the positively charged histidine, lysine and arginine; or negatively charged aspartic acid and glutamic acid. Phosphorylated amino acid side chains *i.e.* phospho-tyrosine, serine or threonine, can also offer hydrophilicity within the amino acid dipeptide sequence, due to the polar phosphate group. [206–208]

For an aromatic dipeptide amphiphile to be enzyme responsive, the design of the sequence must incorporate an enzyme cleavable or recognisable group. Examples include C-terminal methyl esters (-OMe) hydrolysed by subtilisin[209,210] or thermolysin;[203,211] dephosphorylation of phosphorylated residues *e.g*. tyrosine by phosphatases[203,206–208,212,213] and hydrolysis/reversed hydrolysis of peptide bonds by thermolysin,[203,209,211] chymotrypsin[214] and lipase.[215] Enzyme responsive systems of aromatic dipeptide amphiphiles are summarised in **Table 6**.

The terminology we use to name an aromatic dipeptide amphiphile, for example Fmoc-F*p*Y-OH, which reads from the N- to C-terminus of the sequence *i.e.* from left to right, contains an N-terminal fluorenyl group (Fmoc) (see **Figure 14**). Other N-terminal groups include pyrene or Nap (naphthalene). The amino acid sequence is named according to the one letter code (see amino acid table in **Figure 13**), for example 'F' stands for phenylalanine and 'Y' for tyrosine. Letter p's in italic, such as *p*Y, refer to a phosphorylated side chain of the amino acid to the right of the *p* (in this case phospho-tyrosine). The C-terminus is named due to the functionality it possesses *i.e.* carboxyl (-OH), amine ($-NH_2$) or methyl (-OMe).

Table 6 - Summary of biocatalytic self-assembling (SA) aromatic dipeptide amphiphile (PA). See **Figure 111** Appendix A for full chemical structures of PA precursors.

Enzyme	Aromatic PA precursor	Product	SA structure
Alkaline phosphatase	Fmoc-F*p*Y-OH[207,208,212,213]	Fmoc-FY-OH	Micelle to fibre
	Fmoc-F*p*Y-OH+ FmocS/T/RGD[206]	Fmoc-FY-OH + FmocS/T/RGD	Micelle to fibre (co-assembly)
	Fmoc-*p*YT-OH[208]	Fmoc-YT-OH	Fibres
	Fmoc-*p*YS-OH[208]	Fmoc-YS-OH	Fibres
	Fmoc-*p*YN-OH[208]	Fmoc-YN-OH	Fibres
	Fmoc-*p*YQ-OH[208]	Fmoc-YQ-OH	Spheres
	Pyrene-*p*YL-OH[203]	Pyrene-YL-OH	Fibres
Subtilisin (ester hydrolysis)	Fmoc-YL-OMe[216]	Fmoc-YL-OH	Fibres
	Fmoc-YT-OMe[210]	Fmoc-YT-OH	Fibres
	Fmoc-YS-OMe[210]	Fmoc-YS-OH	Fibres
	Fmoc-YN-OMe[210]	Fmoc-YN-OH	Fibres
	Fmoc-YQ-OMe[210]	Fmoc-YQ-OH	Spheres
Thermolysin (ester hydrolysis)	Fmoc-SF-OMe[203,211]	Fmoc-SF-OH	Nanosheets
	Fmoc-TL-OMe[203,211]	Fmoc-TL-OH	Short twisted fibres
	Fmoc-SL-OMe[211]	Fmoc-SL-OH	Nanobelts
	Fmoc-TF-OMe[211]	Fmoc-TL-OH	Extended twisted fibres
Thermolysin (reverse hydrolysis)	Fmoc-S/F-OMe[179]	Fmoc-SF-OMe	Sheets
Chymotrypsin (reverse hydrolysis)	Nap-Y-OMe/Y-NH_2[214]	Nap-YY-NH_2	Fibres

2.8.1. Phosphatase responsive self-assembly of aromatic dipeptide amphiphiles

A number of groups have investigated phosphorylated aromatic dipeptide amphiphiles and the ability for phosphatase enzymes to recognise synthetic phospho-peptides as substrates.[203,206–208,217] In most cases alkaline phosphatase (AP) is employed, however acid phosphatase has been used to initiate self-assembly, for example in the conversion of Fmoc-*p*Y to Fmoc-Y.[217,218]

The design of an AP responsive peptide must include an amino acid capable of functionalisation with a phosphate group. Commonly phospho-tyrosine residues (and serine or threonine) are incorporated within the amino acid sequence. The remaining amino acid in the dipeptide sequence, can be interchanged for any other amino acid, and a number of variations have been studied, for example phenylalanine, leucine, glutamine, giving rise to various nanostructures.[208] An N-terminal aromatic group is usually required to encourage self-assembly through π-stacking interactions, such as fluorenyl[206–208,212,213] or pyrene[203] groups.

Fmoc-F*p*Y has been investigated previously as a switchable self-assembling micelle to fibre system.[206,207] The phosphorylated form has been reported to form spherical micelle-like aggregates[206,207] but at higher concentrations assembles into nanorods.[213] The molecule (Fmoc-F*p*Y) exhibits a C-terminal polar region due to phosphorylated tyrosine and negatively charged carboxyl terminus. At the N-terminus, phenylalanine is functionalised with Fmoc. The combination of the two aromatic groups results in the N-terminal region being overall hydrophobic in nature. Hydrophobic (and aromatic) interactions occur between the hydrophobic 'tail' regions of the molecule, excluding water molecules as the hydrophobic sections gather together, protected within a central hydrophobic core (see **Figure 15** overleaf). The polar 'head' C-terminal region of the peptide is capable of hydrogen-bonding with water and so forms the outer surface of the aggregate (**Figure 15**). The initial self-assembled structures of Fmoc-F*p*Y (*i.e.* before enzyme addition) have been proposed to be spherical micelles, confirmed by critical aggregation measurements, dynamic light scattering,[207] and microscopic techniques.[206] Similar observations have been reported for the single amino acid analogue Fmoc-*p*Y.[44]

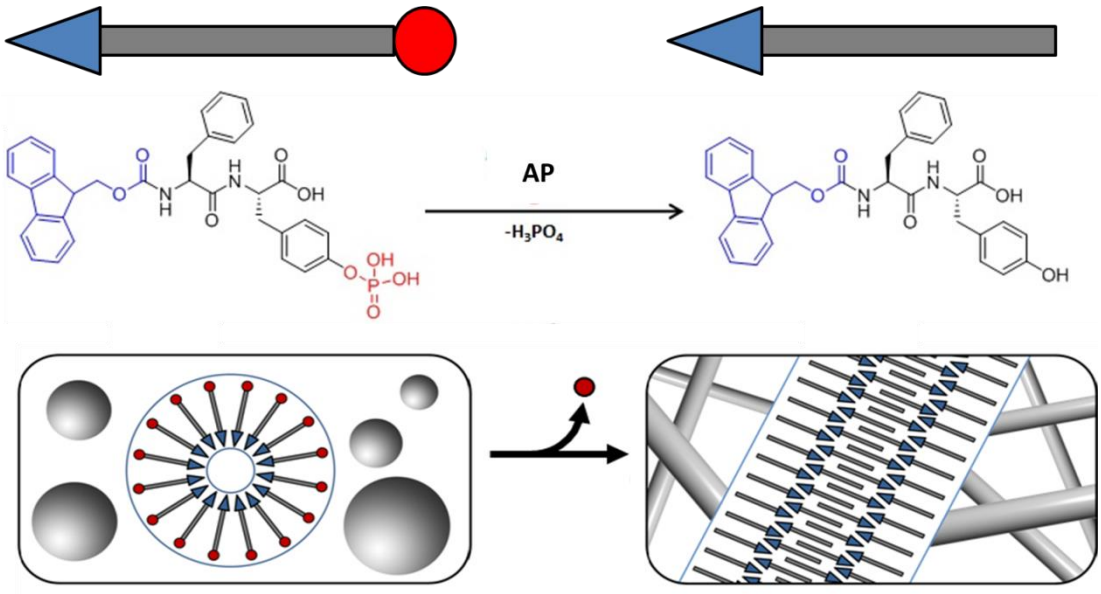

Figure 15 – AP catalysed dephosphorylation of Fmoc-F*p*Y-OH (micellar structures) to Fmoc-FY-OH (fibrous assemblies). The aromatic Fmoc-group is represented in blue and the polar phosphate is highlighted in red.[207]

Upon addition of alkaline phosphatase to a solution containing Fmoc-F*p*Y, the phosphate group is enzymatically cleaved from the tyrosine side chain, resulting in a hydroxyl moiety (**Figure 15**). The molecules are now driven to form a stacking array, due to hydrophobic and π-π interactions between the aromatic groups, as well as hydrogen bonding between dipeptide chains.[221–223] Fmoc-FY is thought to stack in a β-sheet arrangement however it is unclear whether the parallel or anti-parallel conformation is prevalent.[208]

The stacking of fluorenyl groups extends *via* self-assembly until fibrous networks form, and at high enough conversion, result in hydrogel formation. The overall system therefore represents an example of biocatalytic micelle to fibre transformation of aromatic dipeptide amphiphiles. By altering the amino acid sequence and the aromatic group of an aromatic dipeptide, the resulting supramolecular structures can be controlled, for example by changing one amino acid in the sequence Fmoc-*p*Y**N** to Fmoc-*p*Y**Q**,[208] fibres or spheres are produced respectively as summarised in **Table 6**.

Structure switching systems similar to the micelle to fibre transformation have been reported, for example nanotubes going to vesicles by dilution[224,225] and nanotubes switching to microspheres by a change in pH;[226] however the biocatalytic route to structural switching offers mild physiological conditions, biocompatibility and also a wide toolbox of possible selective catalysts that can either break or form bonds, to trigger self-assembly of a

peptide substrate.[227] To illustrate this, different amino acid sequences and aromatic functionalities have been employed for self-assembled fibrous or spherical structures. [196,203,208,212]

Going a step further, multi-enzyme systems have been used to switch between phosphorylated/dephosphorylated forms of a naphthalene functionalised penta-peptide derivative using a kinase/phosphatase switch, resulting in a gel/sol/gel transition.[196] Others combine phosphatase/tyrosinase to initiate a concerted enzymatic reaction. In this case a solution of phospho-peptide (Ac-YYY*p*Y-OMe) was converted to a hydrogel of Ac-YYYY-OMe by phosphatase and finally back to a solution, using the enzyme tyrosinase to convert the hydroxyl groups of the tyrosine residues to quinone.[228]

2.9. Summary

In conclusion, it has been illustrated that enzyme responsive aromatic dipeptides have the potential to self-assemble into a number of different supramolecular structures. In addition several examples of phosphatase responsive self-assembling structures of phospho-tyrosine-containing peptide substrates have been studied as the aromatic nature of tyrosine also contributes π-interactions within the supramolecular assemblies. Additionally, phospho-serine or threonine residues could be incorporated which would broaden the library of phosphatase responsive sequences and structures available. Studying phosphatase responsive systems, could lead to future advances in the detection and treatment of disease states that cause an over- or under-expression of phosphatase.[201]

Here, the ultimate aim is to use biocatalytic fibre formation to drive enhanced motion of the enzyme (and cargo). Aromatic dipeptide amphiphile substrates act as the enzyme-motor 'fuel', and the study of fibre and sphere forming systems will be compared to determine whether a relationship exists between the resulting self-assembled structure, and the ability to enhance the motion of the enzyme-motor.

– Chapter 3 –

Materials and Methods

3.1. Introduction

This section describes the materials and methods used throughout the investigation. The way in which the methods were employed will be discussed in detail later in results and discussions chapters 5-9.

3.2. Materials

All reagents were purchased from commercial sources (*e.g.* Sigma Aldrich, Bachem, Rathburn) at the highest purity and were used as supplied, unless stated otherwise in the experimental procedures. High performance liquid chromatography (HPLC) grade water (Rathburn) was used throughout the study unless stated otherwise. Alkaline phosphatase (*Escherichia coli*) was purchased from Sigma Aldrich and quantum dots from Invitrogen (Q21321MP Lot: 891174 and 1252823). Fmoc-F*p*Y (**1a**) was purchased from CS Bio Co., Pyrene-*p*YL (**2a**) and Fmoc-*p*YQ (**3a**) were synthesised by Sisir Debnath (see **Figure 16** for chemical structures). Fmoc-FY used for QD quenching studies was synthesised by Sangita Roy.

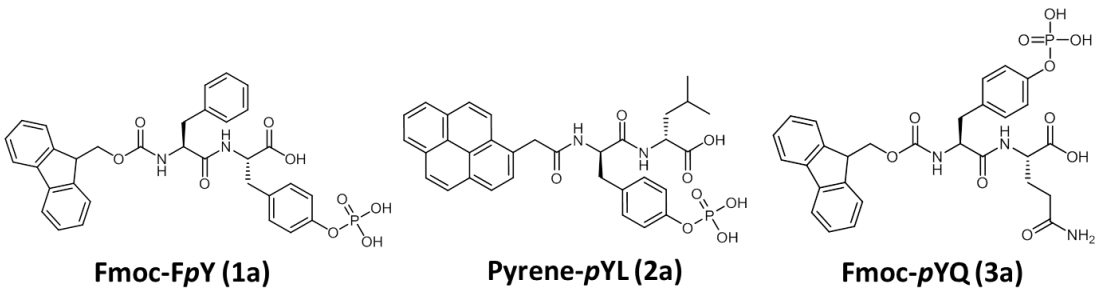

Figure 16 - Chemical structures of Fmoc-F*p*Y (**1a**), Pyrene-*p*YL (**2a**) and Fmoc-*p*YQ (**3a**).

3.3. Experimental methods

3.3.1. FITC labelling – method development using bovine serum albumin (BSA)

Fluorescein isothiocyanate (FITC) was used for the fluorescent labelling of proteins – as discussed in section 5.3. A 10 mg/mL solution of FITC isomer 1 (Sigma Aldrich) in DMF was prepared (1 mg in 100 µL DMF) and wrapped in foil. A 1mg/ml BSA sample was prepared in buffer and a 24 molar excess of FITC was added (compared to BSA). 14 µL of FITC stock solution was added to the 1mg/ml BSA solution and left to react for 1 hour at room temperature on a blood rotator.

Excess FITC was removed by dialysis using Slide-A-Lyzer(R) dialysis cassettes (3 ml, 20K molecular weight cut-off (MWCO)) purchased from ThermoScientific (Perbio). A 0.5-3 mL Slide-A-Lyzer(R) dialysis cassette was hydrated in phosphate buffered saline (PBS) solution (1 PBS tablet per 200 mL water to make 0.01 M, 0.0027 M potassium chloride and 0.137 M sodium chloride at pH 7.4) for 2 minutes at room temperature. The FITC/BSA reaction mixture was injected into the cassette using a syringe and excess air was removed from the cassette. A polystyrene 'float' was attached to the cassette and the cassette was submerged in a beaker containing 300 mL PBS and a stirrer bar. The reaction mixture was dialysed with fresh PBS buffer every hour for four hours. The FITC-BSA sample was removed using a syringe after the fourth buffer exchange. During labelling and dialysis all FITC-containing samples were covered in foil.

Dialysis was monitored by measuring the fluorescence emission spectra of each buffer exchange. 1 mL of each buffer exchange was added to a cuvette for fluorescence spectroscopy measurements, using the following parameters: excitation 495 nm, emission range 300-600 nm, slit width 1 nm.

3.3.2. FITC labelling of calf intestinal alkaline phosphatase (CIAP)

A 10 mg/mL solution of FITC isomer 1 (Sigma Aldrich) in DMF was prepared (1 mg in 100 µL DMF) and wrapped in foil (see section 5.3). A 1 mg/ml enzyme solution was prepared of

alkaline phosphatase from calf intestinal mucosa (CIAP) (Sigma Aldrich P6772-10 KU, 2,000-4,000 DEA units/mg* of protein, 25-45 % protein, 8.15 mg solid, 1228 units/mg of solid, 3721 units per mg/protein) and a 24 molar excess of FITC was added (compared to CIAP). 5.835 µL of FITC stock solution was added to 1 mg/mL AP solution and left to react overnight. Excess FITC was removed by dialysis using Slide-A-Lyzer(R) dialysis cassettes as described for BSA method development. 1 mL of FITC-CIAP was added to a cuvette for fluorescence spectroscopy measurements, using the fluorescence parameters as described for FITC-BSA.

3.3.3. Bioconjugation of AP to QDs

A 10 mM pH 7.4 borate buffer was prepared by dissolving 763 mg of borax (sodium tetraborate NaB_4O_7) in 30 mL H_2O. The pH was adjusted to pH 7.4 using 0.2 M boric acid, before adjusting the volume to 200 mL with water.

A 50 mM pH 8.3 borate buffer was prepared by dissolving 3.81 g of borax (sodium tetraborate - NaB_4O_7) in 30 mL H_2O. The pH was adjusted to pH 8.3 using 0.2 M boric acid, before adjusting the volume to 200 mL with water.

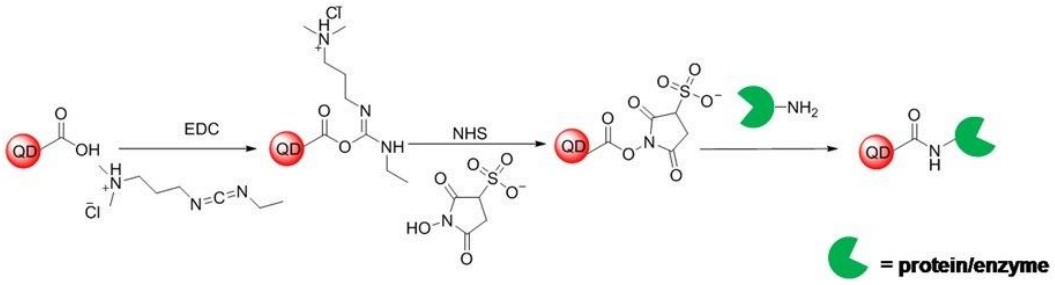

Figure 17 - Alkaline phosphatase bioconjugation reaction with quantum dots *via* an EDC/NHS coupling method.

The alkaline phosphatase-quantum dot (QD-AP) conjugation method was adapted from the Invitrogen bioconjugation method (see **Figure 17**).[229] A 0.85 µM 655 nm emitting quantum dot (QD_{655}) solution was prepared in 10mM pH 7.4 borate buffer. A reaction mixture was prepared by combining EDC activated quantum dots, with alkaline phosphatase from

---

* *An enzyme unit (U) is defined as the amount of enzyme that converts 1 µmol of substrate per minute within specific condition such as temperature and pH. Substrate and conditions are dependent on the enzyme.*

Escherichia coli (Sigma Aldrich P5931 lyophilized powder, 30-60 units/mg protein (in glycine buffer)) and NHS at a molar ratio of 1:13:1500:6500 (QDs:AP:EDC:NHS). The reaction mixture was left to react on a blood rotator for 2 hours at room temperature. The conjugate was filtered through a 0.2 µm PES syringe filter into an Amicon Ultra centrifugal ultrafiltration unit with a 100 kDa cutoff (Millipore), and then diluted with 2.5 mL of 10 mM pH 7.4 borate buffer. The conjugates were centrifuged in an Eppendorf centrifuge 5415R at 10, 000 rpm for 5 minutes and then washed with 50 mM borate buffer pH 8.3 up to 12 times (until no catalytic activity was measured in the wash), whilst retaining each of the wash samples for further analysis. The purity of the conjugate was determined by the addition of 50 µL of each wash sample into a sample containing 0.003 M *p*-nitrophenyl phosphate in 1.5 M pH 8 Tris buffer. The dephosphorylation reaction was monitored by UV-VIS (Jasco V660 spectrophotometer) by recording the absorbance at 410 nm over 10 minutes (method also used for activity assay of pure conjugate). After the wash sample absorbance resembled that of the negative control the conjugate was deemed 'pure'. The QD-AP conjugate was then transferred and filtered through a 0.2 µm syringe filter and diluted by the addition of 4 mL of 50 mM pH 8.3 borate buffer. The final conjugate solution was stored at 4 °C (see sections 5.6, 5.7 and 5.8).

Batches 1 and 2 were prepared for method development purposes using only EDC coupling. Batches 3-6 were prepared using the method described above *i.e.* EDC/NHS coupling. Batch 5 was prepared using QDs which had expired and were therefore not used for any tracking experiments. All experimental tracking results were therefore obtained using batches 3, 4 and 6. QD_{525}-AP conjugates prepared as method described above.

3.3.4. QD_{525}-Thermolysin bioconjugation

The enzyme-QD conjugation method was adapted from the Invitrogen bioconjugation method[229] as mentioned previously. A 0.8 µM 525 nm emitting quantum dot (QD_{525}) solution was prepared in 10mM pH 7.4 borate buffer. A reaction mixture was prepared by a combing EDC activated quantum dots, with thermolysin from *Bacillus thermoproteolyticus rokko* and NHS at a molar ratio of 1:40:1500:6500 (QDs:Thermolysin:EDC:NHS). The reaction mixture was left to react on a blood rotator for 2 hours at room temperature. The conjugate was filtered through a 0.2 µm PES syringe filter into an Amicon Ultra centrifugal filtration unit with a 100 kDa cutoff (Millipore), and then diluted with 2.5 mL of 10 mM pH 7.4 borate buffer. The reaction mixture was centrifuged in an Eppendorf centrifuge 5415R

at 10, 000 rpm for 5 minutes and then washed with 50 mM borate buffer pH 8.3 up to 12 times (until no catalytic activity was measured in the wash), whilst retaining each of the wash samples for further analysis (see section 9.4.1).

3.3.5. QD_{655}-α-chymotrypsin bioconjugation

α-chymotrypsin (from bovine pancreas) was conjugated to 655 nm emitting QDs as per method described above for QD_{525}-Thermolysin *i.e.* reaction mixture prepared with molar ratio of 1:40:1500:6500 (QDs: α-chymotrypsin:EDC:NHS). Purification was as per previous conjugation methods (see section 9.4.3). *(Performed alongside Sisir Debnath).*

3.3.6. Dynamic Light Scattering (DLS)

DLS was performed on an AVL/LSE-5004 light scattering electronics and multiple tau digital correlator. Solutions (4 mL) of QDs, free AP and QD-AP conjugates *etc.* were filtered, using a 0.2 µm syringe filter, into glass tubes and analysed using a DLS instrument at a temperature of 295 K, with an angle of 90° and wavelength of 632 nm.

3.3.7. Transmission electron microscopy (TEM)

Carbon-coated copper grids (200 mesh) were glow discharged in air for 30 seconds. 20 µL of sample was transferred to the support film, left for 30 seconds and blotted using filter paper. Negative stain (20 µL, 1 % aq. Methylamine vanadate obtained from Nanovan; Nanoprobes) was applied and the mixture blotted again with filter paper to remove excess. The dried specimens were then imaged using a LEO 912 energy filtering transmission electron microscope operating at 120 kV fitted with 14 bit/2K Proscan CCD camera. *(Samples imaged by Margaret Mullin at Glasgow University).*

3.3.8. Cryo-TEM

Three microlitres of the sample was transferred onto a thin film grid of 100-200 nm. The grid was then plunged into liquid ethane (temperatures below -170 °C) and transferred to a GATAN 626 cryoholder and imaged using a JEOL 2100 transmission electron microscope fitted with a GATAN 4K Ultra scan camera. *Cryo TEM analysis was carried out at Unilever, Bedford by Meghan Hughes.

3.3.9. Atomic force microscopy (AFM)

20 µL sample was placed on a trimmed, freshly cleaved mica sheet attached to an atomic force microscopy (AFM) support stub, which was left to air-dry overnight in a dust-free environment, prior to imaging. The images were obtained by scanning the mica surface in air under ambient conditions using a Veeco MultiMode with NanoScope IIID Controller Scanning Probe Microscope (Digital Instruments, Santa Barbara, CA, USA; Veeco software Version 6.14r1) operated in tapping mode. The AFM measurements were obtained using a sharp silicon probe (TESP; nominal length (lnom) = 125 µm, width (wnom) = 40 µm, tip radius (Rnom) = 8 nm, resonant frequency (nom) = 320 kHz, spring constant (knom) = 42 N m^{-1}; Veeco Instruments SAS, Dourdan, France), and AFM scans were taken at 512 x 512 pixels resolution. Typical scanning parameters were as follows: tapping frequency 308 kHz, integral and proportional gains 0.3 and 0.5, respectively, set point 0.5 – 0.8 V and scanning speed 1.0 Hz. The images were analysed using Veeco Image Analysis software Version 6.14r1.

3.3.10. Fluorescence spectroscopy

Fluorescence emission spectra were measured on a Jasco FP-6500 spectrofluorometer with light measured orthogonally to the excitation light. 1-2 mL of sample is required in a cuvette for measuring the fluorescence emission spectra of the sample.

For **Fmoc**-containing dipeptide systems *i.e.* **1a** and **3a**, the excitation wavelength was 295 nm and the emission detection range was 300-600nm.

For fluorescence studies using **pyrene** as a probe or dipeptides functionalised with pyrene *i.e.* **2a**, the excitation wavelength was 334 nm and the emission range was 390-600 nm, with band widths set to 10 and 3 nm.

For samples containing **QDs or QD-enzyme conjugates** excitation was typically 435 nm unless stated otherwise, with an emission range of 450-700 nm. For QD-AP quenching studies the fluorescence intensity of QD-AP (λ_{max} – 655 nm) was monitored over time in the presence of a number of materials *e.g.* Fmoc-F*p*Y **1a**, Fmoc-FY **1b**, alkaline phosphatase and/or 0.6 mM phosphate buffer.

For **Thioflavin T** assay studies the excitation wavelength was 442 nm and the emission range was 450-600nm. The bandwidth was 3 nm.

3.3.11. Ultra violet-visible spectroscopy (UV-Vis)

A Jasco V660 UV-Vis spectrophotometer was used for all absorbance and spectral measurements. 1-2 mL samples were measured in PMMA cuvettes (Fisher Scientific).

3.3.12. Alkaline phosphatase activity assay

0.003 M *p*-nitrophenyl phosphate solution was prepared by dissolving 11.14 mg of PNP in 10 mL of water. Each sample contained: 1 mL 1.5 M Tris.Cl pH 8; 500 µL 0.003M PNP and 50 µL of sample or wash. Immediately after the addition of the sample, the absorbance at 410 nm was measured every 30 seconds for 9-10 minutes. The same activity assay was used to monitor the removal of unconjugated AP from QD-AP conjugates by measuring the absorbance as a function of time for each conjugate wash. A QD-AP conjugate life time study was undertaken for QD-AP batch 4, in which the activity *i.e.* absorbance at 410 nm every 30 seconds for 9 minutes, was measured once every week for 8 weeks.

3.3.13. Thermolysin activity assay

Prior to activity measurement a number of reagent solutions and standards were prepared:

Reagent A – 50 mM potassium phosphate buffer pH 7.5 at 37˚C

Reagent B – 0.65% (w/v) casein solution, heated gently to 80-90˚C for 10 minutes with stirring

Reagent C – 110 mM trichloroacetic acid (TCA)

Reagent D – Folin and Ciocalteu's phenol reagent, 10 mL diluted with 40 mL distilled water

Reagent E – 500 mM sodium carbonate solution

Reagent F – 10 mM sodium acetate with 5 mM calcium acetate

Reagent G – 1.1 mM L-tyrosine standard, solution heated gently on a hot plate for a few minutes

Reagent H – Thermolysin solution (0.1-0.2 units/mg)

A calibration curve was prepared by the preparation of 4 standard solutions composed of 1 mL reagent D, 5 mL reagent E and 0, 50, 100, 200 or 400 µL of reagent G (standard). Each

sample was adjusted to a final volume of 8 mL with distilled water. The absorbance at 660 nm was measured for each standard sample and a blank (reagent E + distilled water). The following calculation was used to calculate a corrected absorbance value:

$$\Delta A_{660nm}\ \boldsymbol{Standard} = A_{660nm}\ \boldsymbol{Standard} - A_{660nm}\ \boldsymbol{Blank}$$

Thermolsyin and blank samples were prepared by addition of 2.5 mL reagent B (casein) with 0.5 mL Reagent H (thermolysin) added to sample 1 only, followed by incubation at 37˚C for 10 minutes then the addition of 2.5 mL reagent C to each sample and 0.5 mL reagent H to sample 2 only. Both samples were mixed by swirling and incubated for a further 30 minutes at 37˚C. After incubation samples were filtered through a 0.2 µm syringe filter, of which the filtrate was used for colour development.

Colour development was achieved by combining 400 µL of either thermolysin sample or blank to a mixture containing 1 mL reagent E and 200 µL reagent D. The samples were mixed by swirling and incubated for 30 minutes at 37˚C. After incubation the samples were allowed to cool to room temperature. Solutions were then filtered through 0.2 µm syringe filters immediately before measuring the absorbance of each sample at 660 nm. This activity assay was also used to measure the activity of QD-Therm conjugates as well as conjugation wash samples to monitor removal of the free enzyme.

3.3.14. α-chymotrypsin activity assay

A typical activity assay reaction combined 1.5 mL 0.08 M Tris.HCl buffer (pH 8) containing 0.1 M calcium chloride; 1.4 mL 0.00107 M benzoyl-L-tyrosine ethyl ester (BTEE) in 50% w/w methanol and 100 µL enzyme, conjugate or wash sample. The absorbance at 256 nm was monitored every 30 seconds for 5.5 minutes. *α*-chymotrypsin positive control sample was prepared at 1 mg/ml in 0.001 N HCl then diluted in HCl to 20 µg/mL. (*Performed alongside Sisir Debnath).*

3.3.15. QD fluorescence calibration

A number of QD (655 nm) samples were prepared: 0.08, 0.05, 1, 2, 4, 6 and 8 nM by diluting the 8 µM stock solution supplied by Invitrogen. The fluorescence emission spectrum of each concentration was obtained as described previously. A plot of the λ_{max} fluorescence intensity versus concentration shows a linear relationship which can be used to determine

an unknown QD concentration within samples of QD-enzyme conjugates, assuming the optical properties of the QDs are unaffected by conjugation.

A number of QD-enzyme dilutions were prepared *i.e.* 5, 10, 25, 32, 50, 100 and 200 µL/mL 0.6 M phosphate buffer. The fluorescence emission spectrum of each concentration was obtained as described previously.

3.3.16. Calculation to determine QD:AP ratio

A *p*-nitrophenyl phosphate colorimetric activity assay monitored by UV-Vis was used to estimate the effective activity of the enzyme after conjugation (**Figure 114** Appendix D) relative to free enzyme by measuring the change in absorbance at 410 nm with time for different AP concentrations.

The fluorescence calibration curve of QDs was used to estimate the QD concentration in a given conjugate solution *i.e.* 32 µL/mL (**Figure 113** Appendix C). For the same volume/mL of QD-AP an activity assay was performed and compared to the activity of free AP, to give an estimated QD-AP conjugate effective activity approximately equivalent to a free enzyme concentration of 0.37 nM (equivalent to approximately 7.0 x10^{-4}U *i.e.* 43.68 U/mg protein and 19.9 U/mg of solid, as per manufacturer). Note that this represents an upper limit of enzyme concentration, assuming that all protein in the commercial preparation is enzyme. The two calibrations are then combined to determine an approximate ratio of QDs to AP in a QD-AP sample for batches 3 and 6.

Calculation:

1mg/mL AP solution (MW 94 kDa) – stock solution 1

$$c_{\text{stock 1}} = \frac{1\text{x}10^{-3}}{94000}\text{x } 1000 = 1.06\text{x}10^{-5}\text{M}$$

Stock 2 - 1µL of stock 1 in 1 mL buffer = 1.06x10^{-8}M

35 µL of stock 2, in 1mL was used for assay

$$C_1V_1 = C_2V_2$$

$$1.06\text{x}10^{-8}\text{x}35\mu\text{L} = C_2\text{x}1000\mu\text{L}$$

$C_2 = 3.71x10^{-10}M = \mathbf{0.37\ nM}$ **– QD-AP(3)**

For **QD-AP(6)** the gradient representing activity is 2.4 times less than QD-AP(3) *i.e.* 0.37/2.4 = 0.15 nM (see Appendix D).

QD-AP - 50µL in 1.55 mL = 32 µL/mL

Equation of line (**Figure 114** Appendix D):

$y = 3.8629x - 60.388$ – **Equation 3a QD-AP(3)**

$y = 6.5938x - 6.3659$ – **Equation 3b QD-AP(6)**

If x = 32 µL/mL then:

QD-AP(3) *y* (intensity) = 63.2 au by substituting *x* into equation 3a

QD-AP(6) *y* (intensity) = 204.6 au by substituting *x* into equation 3b

Using the values calculated for y *i.e.* 63.2 au and 204.6 au. The equation of the QD calibration plot (**Figure 113** Appendix C) can be used to estimate the QD concentration in a given volume of QD-AP of both batches (3 and 6).

By substituting y = 63.2 or 204.6 into $y = 147.81x - 90.845$ – **Equation 4**

x (QD concentration) = **1.04 nM QD-AP(3)**

x (QD concentration) = **2.00 nM QD-AP(6)**

Therefore to estimate the ratio of QDs to enzyme molecules for a 32 µL/mL solution of QD-AP: 1.04/0.37 nM = 2.8:1.0 and QD-AP 6: 2.00/ (0.37/2.4) nM = 13.0:1.0

Ratio of QD:AP = **2.8:1.0 QD-AP(3)**

Ratio of QD:AP **= 13.0:1.0 QD-AP(6)**

3.3.17. Biocatalytic self-assembly method with AP and QD-AP

A typical reaction of **1a**, **2a** or **3a** with AP or QD-AP involves dissolving the dipeptide powder (6.3 mg **1a**; 6.2 mg **2a** or 6.2 mg **3a** to make 10 mM, 1 mL final volume) in 980 µL or 968 µL 0.6 M phosphate buffer (pH 9) before the addition of 20 µL *E. Coli* AP (4 U) or 32 µL QD-AP conjugate solution, respectively. For chemical structures of **1a**, **2a** and **3a** see **Figure 16**. The

peptide/enzyme(conjugate)mixtures were left to react at room temperature in a darkened environment (or covered in foil) for up to 4 weeks for samples containing QD-AP. For samples containing $7x10^{-4}$ U AP, aromatic dipeptides were dissolved in 996.5 µL 0.6 M phosphate buffer followed by the addition of 3.5 µL diluted AP solution (1mg/mL AP solution diluted by the addition of 1 µL in 1 mL of buffer). Samples were then mixed by ultrasonication and vortexing after the addition of AP or QD-AP.

3.3.18. Pyrene and 2a doping of 1a

A 10 mM **1a** solution was prepared (6.3 mg in 1 mL final volume). Pyrene was added to the solution of **1a** to make a final pyrene concentration of 100 nM or 0.5 µM. The mixture was then mixed by ultrasonication and vortexing before the addition of 4 U AP (as described above).

For coassembly of **1b** with **2b** converted by AP, 10 mM **1a** and 1 mM **2a** were combined and dissolved in 980 µL phosphate buffer (0.6M pH 9), before the addition of 20 µL AP (final concentration 0.2 mg/ml, 4U). The samples were then mixed by ultrasonication and vortexing then left to react at room temperature (see section 8.5).

3.3.19. High performance liquid chromatography (HPLC)

A Dionex P680 HPLC system equipped with a Macherey-Nagel C18 column of 250 mm length, 4.6 mm internal diameter and 5mm particle size was used to analyse the mixtures of peptide derivatives. The gradient used was a linear exchange between 40% acetonitrile in water at 4 min to 100% acetonitrile at 31 min using a flow rate of 0.7 ml/min and detection wavelength of 301 nm (for the detection of aromatic groups such as Fmoc functionalised dipeptide derivatives). Sample preparation: 20µl of sample plus acetonitrile/water (1.5 ml, 50:50 v/v mixture) containing 0.1% trifluoroacetic acid. For samples containing QD-enzyme conjugates, these were filtered through Amicon Ultra centrifugal ultrafiltration unit with a 100 kDa cutoff (Millipore) before being injected into the HPLC column.

3.3.20. Motility assay

Optical tracking motility experiments were performed using 35 mm glass bottom dishes (Ibidi®). 60 µL of 0.6 M pH 9 phosphate buffer was added to the well, containing QD-AP conjugates with Fmoc-FpY **1a**, pyrene-pYL **2a**, Fmoc-*p*YQ **3a,** *p*-nitrophenol phosphate **4a** or

no fuel. A glass coverslip (22x22 mm, No. 1.5 thickness: 0.16-0.19 mm) was placed over the well and immersion oil was added to the coverslip for use with 100x oil immersion objective (see section 4.3.3.6). Each experiment was repeated up to 4 times allowing for repeatability analysis.

For fuel reservoir experiments 4x4 mm substrate saturated polyacrylamide gels were placed in one quadrant of the glass bottom dish prior to addition of QD-AP conjugated in buffer (see section 7.7).

3.3.21. Optical imaging

Video acquisition was performed using a fluorescence microscope (Nikon Eclipse LV100) with a 100x oil immersion 0.5-1.3 NA objective (Nikon Plan Fluor) WD 0.6, ∞ 0.17, combined with an Andor iXon+ 897 EMCCD camera fitted with 650/60 nm and 536/40 nm single band optical filters (Semrock) to capture the signals from the 655 nm and 525 nm emitting quantum dots respectively. The camera shutter was permanently open during video acquisition. Video capture is achieved by the detector using a detector chip which has an area exposed to the sample and another that is used as a storage area (not exposed to the sample). The storage area stores the image information temporarily before processing, while the camera (exposed area of the chip) acquires the next image. Excitation of quantum dots was performed by a LV-UEPI halogen lamp (50 W) combined with a 435/40 nm optical filter (Semrock) and UV-LED driver LEDDI Thorlabs, CW full power, Imax = 700 mA and LED (Thorlab fitted with a 365 s M365L2-C1, S/N M00268758) combined with a DAPI filter set containing excitation optical filter 365 nm (Carl Zeiss 0424-879, G365), 395 nm dichroic filter and 420 nm long pass filter. Videos were obtained in kinetic acquisition mode with typically 23 frames s^{-1}. A Thorlabs optical table was used to minimise vibrations during motility measurements.

Optical imaging of ThT stained fibres of **1b** was achieved by the use of 482/35 nm single band optical filter for detection of 480 nm fluorescence emission upon ThT binding to β-sheet assemblies (excitation at 435 nm). Simultaneous QD-AP (655 nm emitting) and ThT stained **1b**, used corresponding optical filters *e.g.* 650 and 482 nm respectively, which were fitted in turn.

For **2b** fibre visualisation, a 417/60 nm single band optical filter was fitted for detection of pyrene emission. Similarly for simultaneous fibre and QD-AP detection, optical filters (650

and 417 nm) were exchanged according to the fluorophore *e.g.* QD-AP or **2b** fibres respectively.

For samples containing a mixture of QD_{525}-AP and QD_{655}-AP, optical filters were switched between 536/40 nm and 650/60 nm for detection conjugates, respectively.

3.3.22. Gel reservoir preparation

10% polyacrylamide gel was prepared by the addition of: 1.25 mL 40% acrylamide mix, 1.25 mL Tris.Cl pH 8, 50 µL SDS and 2.00 mL H_2O. Followed by the addition of 50 µL 10% APS and 15 µL TEMED, before the entire mixture was immediately added between two clamped glass plates. After polymerisation was complete the gel was cut into squares approximately 4x4x1 mm. Gel squares were then placed in solution containing 5 mM **1a**, **2a** and **4a** and left to saturate overnight at room temperature.

3.3.23. Gel diffusion study

Substrate saturated gel squares containing **1a** and **2a** were separately placed in cuvettes containing 1 mL 0.6 M phosphate buffer. The fluorescence emission spectra for each were recorded every 5 minutes for 1 hour. Fluorescence parameters for **1a** and **2a** are as described previously.

3.3.24. Sample preparation for fibre visualisation by fluorescence microscopy

Simple flow cells were prepared by the deposition of 20 µL liquid or gel sample onto a glass slide, followed by the addition of 22x22 mm glass coverslip which was finally sealed in place with clear nail polish. Dried samples were prepared by depositing 20-50 µL liquid or gel sample onto a glass slide. The slide(s) were left to dry overnight in the dark environment. For samples containing fibres of **1b** 0.1 or 1 µM ThT was added either to the sample prior to drying or added to the slide, left to dry before washing away excess ThT with water and drying for a final time before imaging.

3.3.25. 2-photon microscopy

Sample preparation for 2-photon microscopy consisted of adding 20 µL of sample onto a glass slide and adding a 22x22 mm glass coverslip over the sample, before finally sealing

with clear nail polish. A Leica SP S Multi-photon scanning microscope with Leica DFC 360 FX was used to image samples. An excitation wavelength of 740 nm was employed, operating at either 40 or 80% power corresponding to 27.2 and 59.6 mW respectively. Detection ranges for pyrene containing samples was 400-500 nm and for samples containing QD-AP, the detection range was 600-700nm. 100x 1.4NA and 10x 0.3 NA objectives were employed for image capture. Images obtained were 2048 x 2028 pixels and 1 pixel is equal to 72.11 nm. Background noise reduction was achieved by averaging over 10 scans. *Performed alongside Gail McConnell.

3.3.26. Thermolysin fuel system method development: FmocTF-OMe

A mixture of 10 mM Fmoc-T-OH and 40 mM F-OMe was prepared by dissolving 7.2 mg and 17.3 mg in 2 mL final volume of 0.1 M phosphate buffer pH 8. Mixing was achieved by ultrasonication and vortexing before and after addition of thermolysin (final concentration of 0.5 mg/mL) or 600 µL QD_{525}-Thermolysin.

3.3.27. α-chymotrypsin fuel system method development: Pyrene-YY-NH_2

A mixture of 20 mM pyrene-Y-OMe and 20 mM YNH2 was prepared in 0.1 M phosphate buffer pH 8. Mixing was achieved by ultrasonication and vortexing before and after addition of α-chymotrypsin (final concentration of 1mg/mL) or 25 µL/mL QD_{655}-Chymotrypsin (*performed alongside Sisir Debnath*).

– Chapter 4 –

Techniques – Part 1

4.1. Spectroscopic techniques for the analysis of self-assembled structures

4.1.1. Fundamentals of fluorescence spectroscopy

Fluorescence is the emission of photons (or light) from fluorophore molecules which are excited to higher energy levels by a fixed and appropriate wavelength of light (usually in the ultra-violet (UV) region).[230] Initially light is absorbed by the fluorophore molecule in the form of a photon and the resulting species becomes excited by the promotion of electrons from the ground state (S_0) to higher energy levels, for example S_0 to S_1 (see **Figure 18**).

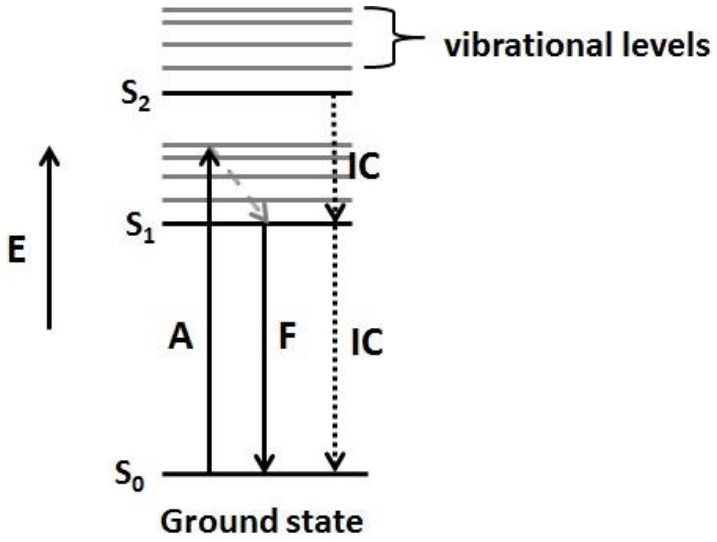

Figure 18 – Energy state diagram for fluorophore excitation and relaxation.

Excited molecules lose energy or 'relax' as the promoted electron descends down vibrational energy levels to the first singlet excited state (S_1). The excited singlet state fluorophore *i.e.* S_1 returns to the ground state (S_0) by the radiative or non-radiative processes, fluorescence (F) or internal conversion (IC), respectively – see **Figure 18**.[230] Fluorescence excitation and emission is characteristic to the molecule. Due to vibrational

relaxation prior to emission of a photon, energy is lost therefore resulting in a shift in the wavelength with regards to the excitation wavelength, commonly called the Stokes or red shift.[230]

4.1.2. Fluorescence spectroscopy using intrinsic fluorescence

Spectroscopy can be used as a tool to probe the self-assembly modes of aromatic dipeptide amphiphiles. In particular fluorescence spectroscopy can be used for systems involving aromatic moieties such as Fmoc or pyrene, as their fluorescent spectral properties can indicate aromatic orientations and interactions occurring. A change in the local environment due to molecular association or solvent polarity will result in changes in fluorescence emission characteristics.

Fluorenyl containing peptides are typically excited at around 300 nm and display characteristic 'monomer' fluorescence emission spectra, with a λ_{max} of 320 nm for Fmoc.[206,207,219] The presence or absence of certain spectral peaks, can give clues as to how the molecules are organised within a supramolecular structure and also the polarity of the local environment. For example with Fmoc-F*p*Y, a characteristic shoulder at 370-380 nm is indicative of micelle-like assemblies in which Fmoc groups make up the hydrophobic core of the micelle in aqueous environments (see **Figure 19**). Alkaline phosphatase converts the dipeptide derivative to a more neutral Fmoc-FY, resulting in a diminished spectral shoulder (370-380nm) as the micelle structures are disrupted and the 'new' molecules are driven to align in a different orientation.[206–208]

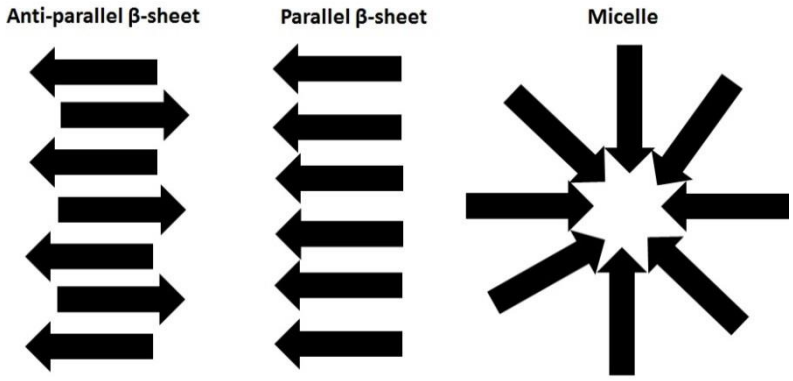

Figure 19 - Schematic representation of different orientations of self-assembly *i.e.* anti-parallel, parallel β-sheets and micellar structures.

Subsequent self-assembly of Fmoc-FY into aromatic stacked arrangements *i.e.* parallel or anti-parallel β-sheets (**Figure 19**), can also be detected using fluorescence spectroscopy. A red shift in the 320 nm Fmoc peak is observed with some systems indicating Fmoc excimers[†],[204,221] and a peak at 400 nm can suggest Fmoc or phenyl J-aggregates[‡] forming.[62,221,231,232]

Pyrene functionalised peptides are excited at 334 nm and 'monomer' spectra contain multiple emission peaks at 375, 380, 385, 398 and 410-418 nm, representing the major vibrational bands I, II, III, IV and V respectively.[205,233–235] The spectral peaks are due to $\pi \rightarrow \pi^*$ transitions of monomeric pyrene, where the third vibrational state (385 nm) can be used to monitor the environment polarity.[235] As with the Fmoc-system, self-assembly of pyrene-functionalised peptides into fibrous structures is indicated by a change in the emission spectra, where excimer peaks become more intense compared to those associated with the 'monomer'. Typically unstructured bands arise at longer wavelengths (between 425-550 nm).[235] A red-shift of a peak can indicate aromatic stacking interactions; however the fluorescence emission spectrum of a pyrene-containing peptide is more complex (compared to fluorenyl functionalised peptide) due to the different pyrene orientations available. For example, the fluorescence emission spectra of self-assembled pyrene-YL, exhibits a broad less-defined profile, accompanied by quenching of peaks associated with monomers.[205]

4.1.3. Fluorescence spectroscopy using extrinsic fluorescence

As well as an inbuilt chemical fluorescent probe, *i.e.* pyrene or Fmoc, extrinsic fluorescent probes can be added to peptide solutions, in order to gain more information about the self-assembled structures and resulting local environments.

[†] *An excimer originates from the words 'excited' and 'dimer' and relates to associated molecules which are stable and exist in an excited state.*

[‡] *J-aggregates are species which exhibit bathochromic shifts (a shift to longer wavelengths) in the spectral band during the association of molecules.*

Free pyrene can be used to determine critical micelle concentration (CMC) of peptides suspected of forming micelles (see **Figure 20** for the molecular structure of pyrene). The free pyrene fluorescence signal depends on the solvent environment of the molecule, therefore upon encapsulation by micellar aggregates the fluorescence signal alters according to the hydrophobic environment. Below the CMC pyrene experiences a polar aqueous environment and as the concentration of surfactant or amphiphilic peptide increases, pyrene becomes more solubilised within the hydrophobic micellar core. The environmental change from polar to more hydrophobic can be monitored by comparing the ratio of fluorescence emission intensity values of the first and third vibrational peaks (I_I/I_{III}). In a hydrophobic environment band III increases compared to band I (the opposite effect is seen in polar environments).[235] In the presence and absence of micelles the ratio between the two bands is high or low respectively.[236,237] By plotting the ratio value against surfactant (or peptide amphiphile) concentration, the resulting curve can be used to determine a value of CMC *i.e.* where there is a sharp change in the curved profile.[237]

The fluorescence method of determining the CMC using pyrene can be employed for peptides which are not already functionalised at the N-terminus by pyrene. For example, the CMC of Fmoc-F*p*Y has been previously determined to be 5 mM using free pyrene as a probe.[207]

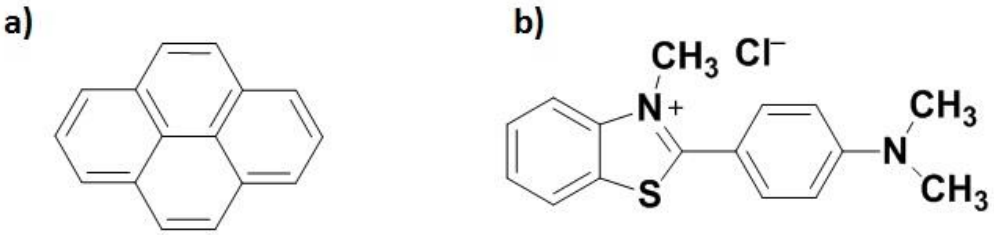

Figure 20 - Chemical structures of (a) pyrene and (b) Thioflavin T.

Thioflavin T (ThT) is a fluorescent probe that can indicate β-sheet structures (**Figure 20**), and is typically used to detect β-rich amyloid fibrils associated with protein misfolding diseases such as Alzeimer's.[238,239] ThT binds to β-structures and so can be used to detect self-assembled peptide structures suspected of forming β-sheets. There is debate as to the mechanism by which ThT non-covalently binds to β-rich amyloid fibrils, where some suggest that aromatic and hydrophobic amino acid residues provide a recognition site for

ThT binding.[239,240] Alternatively, it is thought that ThT forms micellar structures capable of binding to β-rich fibrils[241] or that size specific cavities are present in β-structures for the dye to penetrate.[241–243]

The fluorescence emission characteristics of ThT allow for the detection of β-sheet structures (exciting at 442 nm), due to a shift in the emission maxima from 445 to 480 nm and an increase in fluorescence emission at 480 nm in the presence of β-rich structures.[240,242,244–246] The shift and subsequent increase in fluorescence emission is a result of changes in the local environment where it is thought that steric restriction prevents rotation of the dye molecule about the benzothiazole and benzene ring (see **Figure 20**), leading to an increased quantum yield and fluorescence output.[238,240,246–248]

Techniques – Part 2

4.2. Visualisation of proteins using bioconjugation to fluorescent nanoparticles

Single biomolecule tracking has led to the understanding of how many molecular motors move *in vivo* and *in vitro*.[249–251] Biomolecules however, can prove difficult to visualise using fluorescence microscopy techniques, with the exception of naturally fluorescing proteins such as the green fluorescent protein.[252,253] Proteins exhibit a natural intrinsic fluorescence for sequences containing aromatic residues tryptophan, tyrosine or phenylalanine. However, this fluorescence intensity is weak and in the low nanometre wavelength range (200-350nm), so is generally unsuitable for visualising proteins by fluorescence microscopy.[247] Therefore, methods to visualise and track single molecules and proteins require the attachment of a fluorophore or particle to allow for visualisation. Strategies currently in place for protein observation and tracking include labelling with an organic fluorophore,[254–257] genetically fusing to a fluorescent protein,[254,258] conjugating to fluorescing or metallic nanoparticles[259,260] and attaching to the surface of micron sized particles.[261–264]

Single biomolecule observation can be achieved by modification with organic molecular fluorophores, only if the fluorescence signal is sufficiently greater than the background noise. In most cases organic fluorophores have low fluorescence emission intensity and cannot offer sufficient time resolution for single molecule tracking.[265] Conjugation to larger micron-sized particles is more convenient in terms of visualisation, but the larger size, compared to nanoparticles, presents an increased load on the biomolecule. This in turn causes a decrease in the diffusion coefficient of the overall conjugate and therefore could potentially prevent realistic tracking of the attached biomolecule. Nanoparticles (NPs) are comparable in size to many proteins. NPs composed of metals *e.g.* gold or silver are ideal for dark-field microscopy as they are highly contrasting.[259,265]

Visualisation of the enzyme alkaline phosphatase is essential in order to track individual molecules. In this investigation we firstly label the enzyme with an organic fluorophore

(fluorescein) and also conjugate to fluorescent nano-sized quantum dots (see Chapter 5). Quantum dot-enzyme conjugates were utilised for all subsequent tracking investigations therefore here we focus on the fundamental properties of semi-conductor quantum dots.

4.2.1. Quantum dots

Quantum dots (QDs) are highly fluorescent semiconductor nanocrystals, which offer attractive optical properties for the conjugation and tracking of biomolecules. QDs range in size from 2-20 nm in diameter, with around 200-10,000 atoms per crystal.[250,251,266] The general structure of a core-shell QD comprises of a primary semiconductor core such as CdSe plus an optional layer of different semiconductor for example ZnS (**Figure 21**).[267] The outer semiconductor shell functions as a protective layer against oxidation and it also enhances the quantum yield of the QD.[266,268] An additional coating of polymer or ligands allows for solubilisation of QDs in either organic or aqueous environments.[266] It is essential for biological applications that the outer surface of the QD is hydrophilic for use in aqueous solutions.

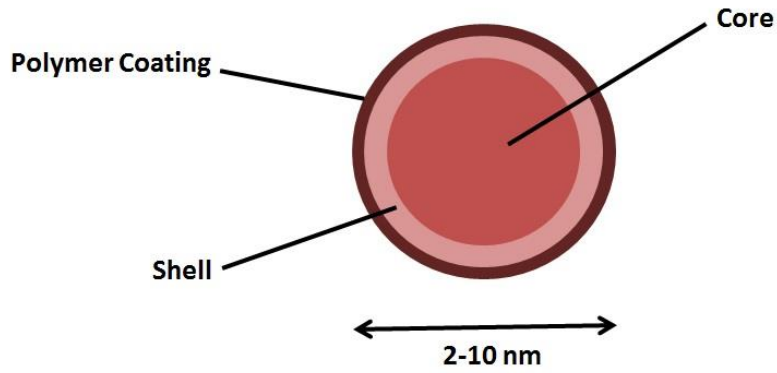

Figure 21 - Structure of a core-shell quantum dot, with semiconductor core and shell *e.g.* CdSe and ZnS respectively. In some cases polymer coatings are added for solubilisation purposes.

4.2.1.1. Electronic properties

Semiconductor nanocrystals are named quantum dots due to the quantum confinement of their electrons by a potential barrier.[269] QDs differ from bulk semiconductors in such a way that the electronic properties become more like those of a molecule, where continuous valence and conduction bands exist in bulk semiconductors and discrete bonding and anti-bonding molecular orbitals are found in QDs (see **Figure 22** overleaf).[267] As a result of QDs

having discrete energy levels, the bandgap of a quantum dot nanocrystal is greater than the bulk semiconductor of the same material.[267]

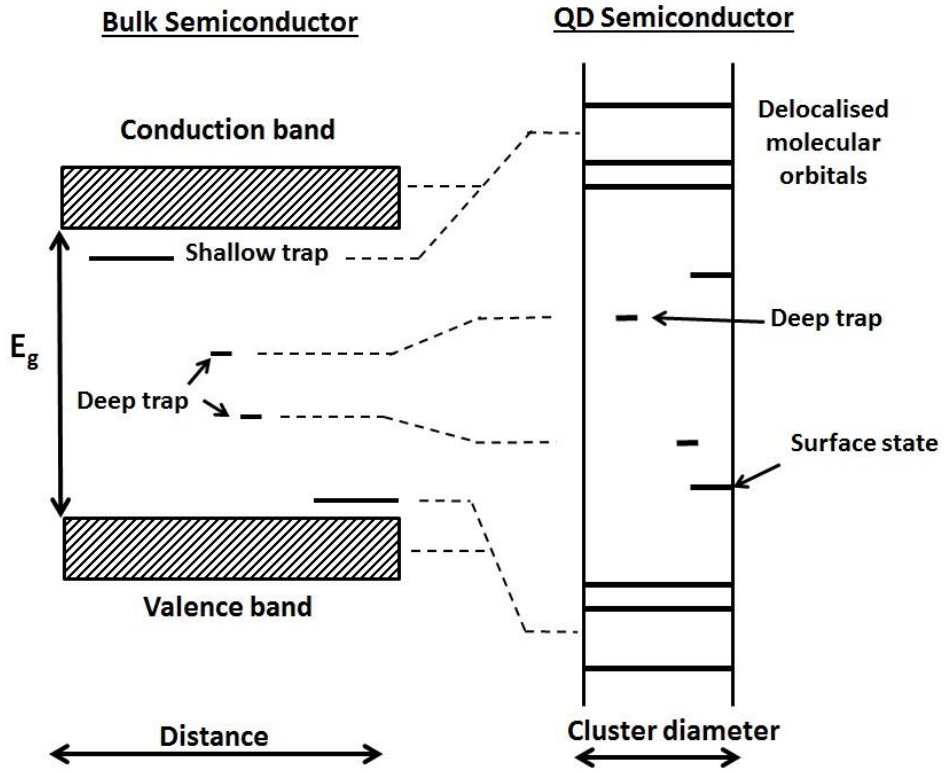

Figure 22– Electronic state schematic diagram comparing bulk semiconductors and quantum dots.[270]

QDs absorb energy in the form of photons, when the excitation energy is greater than the bandgap. Upon excitation, electrons occupy higher energy levels, similar to the promotion of an electron from the valence to the conduction band in a bulk semiconductor.[271] Emission of light then arises due to the recombination of electron-hole pairs from the discrete energy levels, as in bulk semiconductors where electron-hole pairs are recombined in the shallow and deep traps caused by defects.[267]

The size of the QD influences the spacing or band gap between the discrete energy levels. By changing the size and composition of the QD nanocrystal, the band gap is affected therefore influencing the optical properties of the QD.[269] As a result, the wavelength of light emitted by a particular type of semiconductor nanocrystal is controlled by the bandgap and therefore by the size of the crystal.[269]

4.2.1.2. Optical properties

As mentioned previously, the QD fluorescence emission wavelength is dependent on the size of the nanocrystal, with a range of light being emitted from ultraviolet to infrared regions of the electromagnetic spectrum.[249–251,272] As the size of the QD decreases, the band gap increases, where smaller sized nanocrystals *i.e.* 2 nm QDs emit blue/green light, whereas larger 5 nm QDs emit in the red region.[251,268,273]

QDs have a number of advantages for microscopy imaging applications, compared to organic fluorophores and fluorescent proteins. QDs are 10-100 times brighter due to their large molar extinction coefficients between 0.5-5x10^6 M^{-1} cm^{-1} (compared to 7x10^4 M^{-1} cm^{-1} for FITC).[249,250,272,274] They are generally highly photostable allowing them to be used for long-term tracking applications.[249–251,272–275] Organic fluorophores, on the other hand, can experience considerable photobleaching after only a few minutes illumination, due to permanent photochemical destruction.[249]

QDs have narrow, symmetrical fluorescence emission spectra with broad adsorption bands allowing simultaneous excitation of multiple coloured QDs.[249–251,268,272,274] Organic fluorophores have narrow adsorption and broad emission spectra that tend to overlap and are less symmetrical.[249,251,268]

Disadvantages of using QDs for biomolecule tracking, include size restrictions where a QD can be larger than the biomolecule being conjugated, therefore affecting the realistic diffusion of that molecule.[274] QDs also suffer from blinking (alternation between emission and non-emission), thought to be caused by the crystals diffusing in close proximity to a surface.[251,268] This blinking effect can make single particle tracking difficult.

4.2.2. Bioconjugation

Despite the downsides of QDs for single biomolecule tracking, there have been a number of reported examples of successful conjugation and subsequent microscopic imaging,[272–274,276] or tracking of a variety of biomolecules.[143,258,277–281] The observation of enzymes conjugated with QDs moving along and cleaving a DNA extension was reported.[260] Motor proteins carrying QDs as cargo have been successfully tracked 'walking' along microtubule tracks.[143] Other single molecule tracking studies include bioconjugation of QDs to: viruses,[278] wheat

germ agglutinin proteins,[281] prion proteins[280] and mRNA for tracking within cells.[279,268] QD nanocrystals have never to our knowledge been reported for tracking biocatalysts involved in self-assembly processes.

As mentioned, a variety of biomolecules have been successfully attached to semiconductor nanocrystals and there are a number of strategies for bioconjugation to QDs including electrostatic; thiol; streptavidin-biotin conjugation techniques and also amide bond formation or silane chemistry, and these are summarised as:

(i) Electrostatic conjugation - QDs with negatively charged surfaces are able to electrostatically bind to positively charged biomolecules.[250,268,271,276,282,283] Biomolecules can also be engineered with positively charged hexahistidine tags to enable electrostatic interactions with negatively charged QDs.[284]

(ii) Thiol conjugation - Coupling of maleimide-activated QDs to thiols of biomolecules is achieved by either engineering the molecule with free thiol groups or taking advantage of any thiol-containing cysteine residues within the sequence.[250,251,268,271,276,283] This strategy however has a few downsides, for example thiols can be sensitive to oxidation and free thiols are rarely found in native proteins as they are usually bound within disulphide bridges.[274] The ZnS-thiol bond is relatively weak and therefore proteins attached in this way can detach.[251]

(iii) Amide bond formation between COOH and NH_2 - EDC and sulfo-NHS can be used for the activation and coupling of the carboxyl group on the surface of QDs to amino groups of the biomolecule to form a stable amide bond.[251,271,276,283,285–288] This type of conjugation can also be used for coupling amino (PEG) QDs and carboxyl groups on the biomolecule.[289]

(iv) Silica coating and silane chemistry - Some QDs have a silica coating that can be modified using silane chemistry for the attachment of a number of functional groups on biomolecules.[250,271]

(v) Streptavidin-biotin conjugation - QDs conjugated with streptavidin may be used to bind molecules labelled with biotin, taking advantage of the naturally strong affinity streptavidin and biotin have for each other.[110,250,268,276,281,283,290–293]

A handful of alternative methods have also been reported, such as the direct adsorption of serum albumins to the surface of water soluble QDs.[251] One example illustrates a one-step incorporation of BSA by adding the protein to the precursors used for QD preparation.[294]

Taking into consideration the current strategies in place for bioconjugation to QDs, the amide bond formation *via* carbodiimide activation and coupling was chosen to attach alkaline phosphatase to QDs. Amide bond formation is more stable compared to thiol binding or electrostatic interactions and the biomolecule/QDs do not have to be engineered or modified prior to conjugation as with streptavidin-biotin or silane strategies.

A protein model of *Escherichia coli* alkaline phosphatase was visualised using VMD software from the crystal structure obtained from Protein Data Bank – 3TG0 (see **Figure 39** for model).[295] From the three-dimensional model it can be seen that there are a sufficient number of amino groups (*i.e.* 56 lysine residues; of which 32 are available on the surface of the enzyme). Therefore carboxyl functionalised QDs were chosen for conjugation to alkaline phosphatase *via* the EDC coupling strategy (see section 3.3.3 for conjugation information).

Techniques – Part 3

4.3. Single particle tracking microscopy technique and method development

4.3.1. Introduction

Here the fluorescence microscopy techniques employed to track single fluorescent enzyme-quantum dot conjugates will be discussed. The microscope configuration will be highlighted along with the major challenges posed for single particle tracking of nanosized species. Challenges such as achieving sufficient resolution and excitation will be covered with a final statement about the development of a suitable solution sample holder for tracking.

In addition, a proposal for future simultaneous two-fluorophore detection and tracking will be presented, as a natural step beyond this study would be to track QD-AP conjugates as well as self-assembling fibrous structures.

An overview is also given as to how the tracking program identifies particles from single frames of a video and subsequently pieces together the movements over a number of frames, resulting in single particle trajectories, from which data can be obtained about the diffusion characteristics of single conjugates (and entire populations of conjugates).

4.3.2. Microscope Configuration

Visualising and tracking the motion of single particles in a three-dimensional environment can prove challenging, particularly when tracking single nanosized species in a potentially optically turbid environment, for example in the presence of fluorescent fuel molecules and other scatterers. QD-enzyme conjugates exhibit Brownian diffusion characteristics as explained in section 1.1, therefore for real time visualisation of single QD-AP conjugates, the microscope configuration is important to accurately track motion at nanoscale resolution, as calculated in section 4.3.3.1.

Fluorescence microscopy is one of the most common methods for tracking single fluorescent or fluorescently labelled particles. Tracking generally relies on gathering a series

of images for a period of time.[296] Intense spots captured in each image can be assigned as a single particle, which due to its position will have individual coordinate values.[296] The position of a particle will be assigned according to the centre of the intensity distribution as described in 4.3.4.1.[296]

As described in section 4.2, the chosen method for labelling alkaline phosphatase was to conjugate to fluorescent nanosized quantum dots, for visualisation using epi-fluorescence microscopy (see **Figure 23** overleaf for microscopy configuration). Once a method of labelling was developed, there were a number of parameters which required development before single particle tracking was achieved.

Conventional wide-field fluorescence microscopes operate by illuminating the sample with the chosen excitation wavelength, and the sample can be observed through oculars or a camera set-up (**Figure 23** overleaf).[297] The environment that the microscope is set up in must have low light levels such as an appropriate dark room and the room temperature is usually controlled in order to control the performance of electronics such as EMCCD cameras.[297]

The microscope configuration for imaging QD-AP (emission 655 nm) is shown in Figure 23. Depending on the wavelength of light required for illumination, either a halogen lamp or UV-LED was coupled to the microscope. Filter combinations to direct and detect light at specific wavelengths, corresponding to the sample excitation and emission, can be incorporated either after the light source or as part of an optical filter cube (see **Figure 23** overleaf). Emission filters for capturing the sample signal can be placed before the camera or within a filter cube.

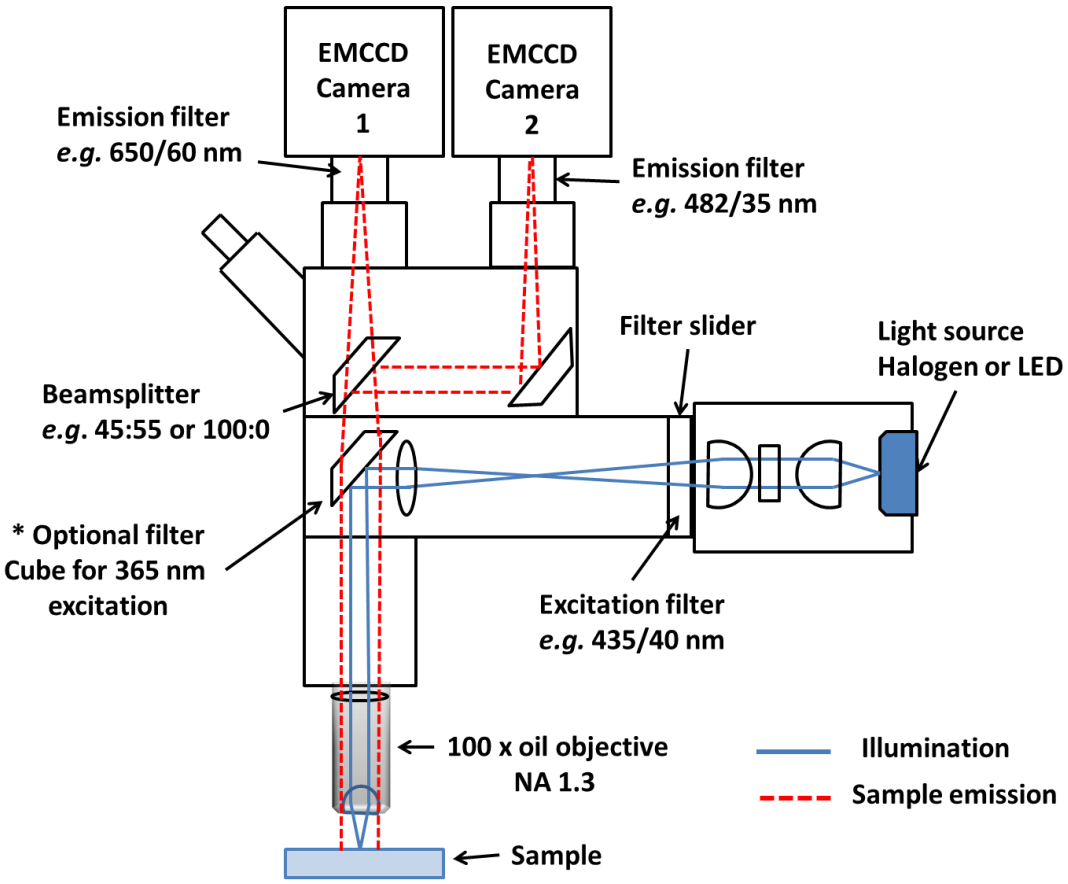

Figure 23 – Schematic of wide-field epi-fluorescence microscope set-up (with optional two-camera set-up). The light sources used were switched between halogen and UV-LED lamps, depending on the required sample excitation wavelength. The filter set-up here explores different filter combinations tailored to the sample requirement. Commercially available standard filter cubes are used only for 365 nm excitation (dichroic 395, long pass 420 nm). For 435 nm illumination, individual excitation and emission filters are employed (after the light source and fitted before the camera, respectively). For applications in imaging a two-fluorophore system such as QD-enzyme conjugates and self-assembled fibres, a beam splitter is employed to direct light between two cameras, each fitted with optical filters corresponding to the emission wavelength range of the fluorophores being tracked *e.g.* 650/60 nm and 482/35 nm single band filters for 655 nm emitting QDs and 480 nm emitting ThT-stained fibres, with band widths of 60 and 35 nm, respectively.

4.3.2.1. Simultaneous enzyme and fibre visualisation

For visualisation of enzyme-QD conjugates and self-assembled fibres simultaneously, the microscope design must be altered accordingly. Enzyme-QD conjugates can be visualised using a combination of optical filters which correspond to the excitation and emission properties of the QD. For the visualisation of self-assembled structures, two techniques can be employed: extrinsically staining the self-assembled structure with a fluorescent probe

i.e. Thioflavin T (section 4.1.3) or incorporating an intrinsic fluorescent moiety into the self-assembling aromatic dipeptide derivative *e.g.* pyrene (section 4.1.2).

In order to truly track and visualise a two fluorophore system such as fluorescent enzyme-QD conjugates and intrinsic or extrinsically fluorescent self-assembled fibres, the excitation and emission wavelengths should be compared. Ideally excitation wavelengths should be similar or the same. Conveniently QDs, have broad absorption bands, which allow for some degree of flexibility, regarding excitation wavelength. Ultimately the chosen dye or fluorophore molecule responsible for illuminating the self-assembled structure is the defining factor for deciding the excitation wavelength.

To obtain digital video data of each fluorophore *i.e.* conjugates and self-assembled fibres, the microscope design would incorporate a dual camera set-up and beamsplitter to ensure light is passed to each camera (**Figure 23**). For a one camera set-up the beamsplitter would direct 100% of the sample emission to camera 1 and for a two camera system, the signal would be split between the two cameras (45:55 ratio), as shown in **Figure 23**. Each camera would be fitted with an optical emission filter corresponding to the emission wavelength of either the QDs or the self-assembled structures. For example a system containing 655 nm emitting QD-conjugates and thioflavin T stained fibres (emission wavelength 480 nm – see section 4.1.3); 650nm and 482 nm optical filters would be fitted respectively (see **Figure 24** overleaf). Dichroic filters in this case are not required as the emission optical filters only pass light of a certain wavelength range or band, preventing light at the excitation wavelength from entering the detector. For an optical filter combination capable of detecting fluorescence emission from intrinsically fluorescent fibres of **2b** and QD-AP conjugates see Appendix B.

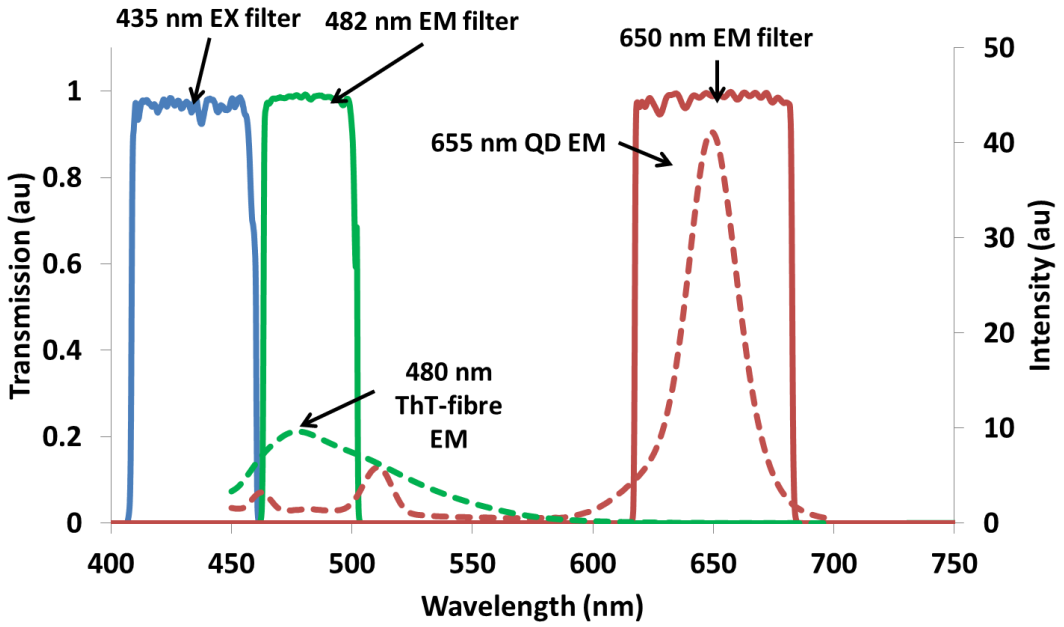

Figure 24 - Example plot of optical filter combination required to capture fluorescence signal for a two fluorophore system of 655 nm emitting QDs and 480 nm emitting Thioflavin T-stained fibres (used here to detect β-sheet structures in Fmoc-FY fibres – see section 4.1.3).

4.3.3. Challenges of tracking at the nanoscale by fluorescent microscopy

There are a number of potential challenges or factors worth contemplating when imaging fluorescent nano-sized objects in motion, such as choosing the correct objective, light source and optical filters to achieve suitably resolved images for tracking.

4.3.3.1. Selection of objective

Choosing an appropriate objective for applications such as imaging single particles, is important in order to achieve suitable resolution. The resolution obtained through optical microscopy is inherently restricted due to the properties of light *e.g.* diffraction (see equation 7 below). Problems may arise when resolving between two particles which are close together due to them appearing inflated in size by diffraction. In wide field microscopy, resolution in the x-y plane is typically 200 nm.[3,297]

The numerical aperture (NA) of an objective gives an indication of the light acceptance angle of the objective and determines the light collection, resolution and depth of field. High numerical aperture objectives (NA = 1.45-1.65) are capable of improved signal collection, but at the same time with an increased collection of noise.[297] To achieve a higher NA value, objectives can be designed to function in other media such as water or oil. Specific objectives are designed for use with fluorescence microscopes, as they transmit light in the UV and visible regions. Objectives with a higher NA value are favoured for fluorescence applications *i.e.* for the collection of low levels of light. The working distance of an objective is defined as the distance between the objective lens and the sample. Typically as the magnification increases the working distance decreases.

$$\boldsymbol{d = \frac{\lambda}{2n\,sin\theta}} \qquad \textbf{Equation 7}$$

Where d is the resolvable feature size, λ is the wavelength of emission light, n is the refractive index of the medium between the objective and the sample, θ is the half-angle of the inverted cone of light entering objective and $n \bullet sin\theta = NA$ of the objective (see **Figure 25**).[298] An alternative equation is simply: $d = \lambda/2NA$, which can be used to estimate the optical resolution of the set-up used to image fluorescent QD-enzyme conjugates *e.g.* for a species emitting light at 650 nm (QDs) and an objective with an NA of 1.3, has a theoretical resolution of 250 nm.

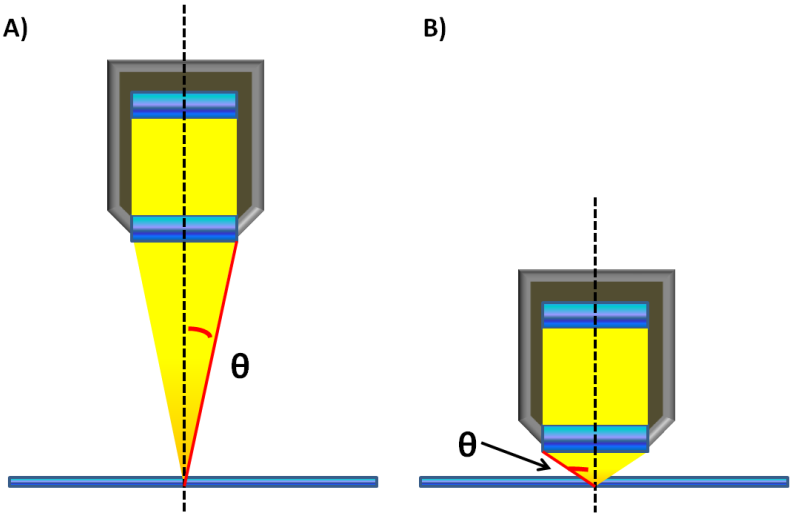

Figure 25 - Scheme representing objectives with different numerical aperture (NA) values. (B) has a larger NA value than (A) due to the light cone increasing in which in turn increases the angular aperture.

The axial resolution or depth of field must also be taken into account, especially for tracking particles in a liquid sample well. The depth of field also relies on the numerical aperture of the objective where low and high NA objectives can be compared in **Figure 26**. The depth of focus or image depth relies on the magnification and NA of the objective. Higher NA (and magnification) objectives usually have a larger depth of focus.

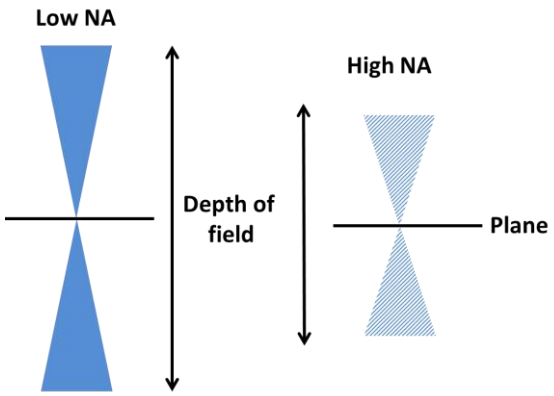

Figure 26 - Depth of field comparison of an objective with low or high numerical aperture (NA).[298]

For this study, a number of objectives were tested for the best resolution of QD-AP conjugate samples (50x air, 60x water immersion and 100x oil immersion). The objective chosen was a Nikon Plan Fluor objective with 100x magnification, oil immersion, with an adjustable NA between 0.5-1.3 (used at 1.3 NA) and a working distance of 0.6 mm. This

objective was chosen to enable as much sample signal to enter the camera and detector as possible.

4.3.3.2. Light source

The light source used will depend on the excitation wavelength required. The absorption spectra of QDs are broad and therefore offer a wide range of excitation wavelengths. To ensure high signal to noise, the correct light source for sample illumination is important.[297] For studies which illuminate at wavelengths of 350-450 nm, glass equipment such as slides and cover-slips may supply added background fluorescence to the system.

In this case two light sources were investigated: Halogen and LED lamps (see **Figure 27** overleaf). A UV-LED was investigated to increase the illumination light intensity for single particle tracking as well as excitation in the UV wavelength range for more efficient excitation of the sample. Particle tracking requires higher incident power compared to fluorescence imaging of immobilized samples, which can be achieved with longer integration times and frame averaging. Halogen lamps operate at wavelengths in the visible region *e.g.* >400 nm which may not be suitable for all samples and other light sources such as mercury lamps are not sufficiently powerful in the UV region for single QD tracking applications. Although many single particle tracking studies employ lasers for illumination, high power LED light sources are available in a range of wavelengths from UV-IR and so offer an alternative light source, in many cases, to exposed laser beams.

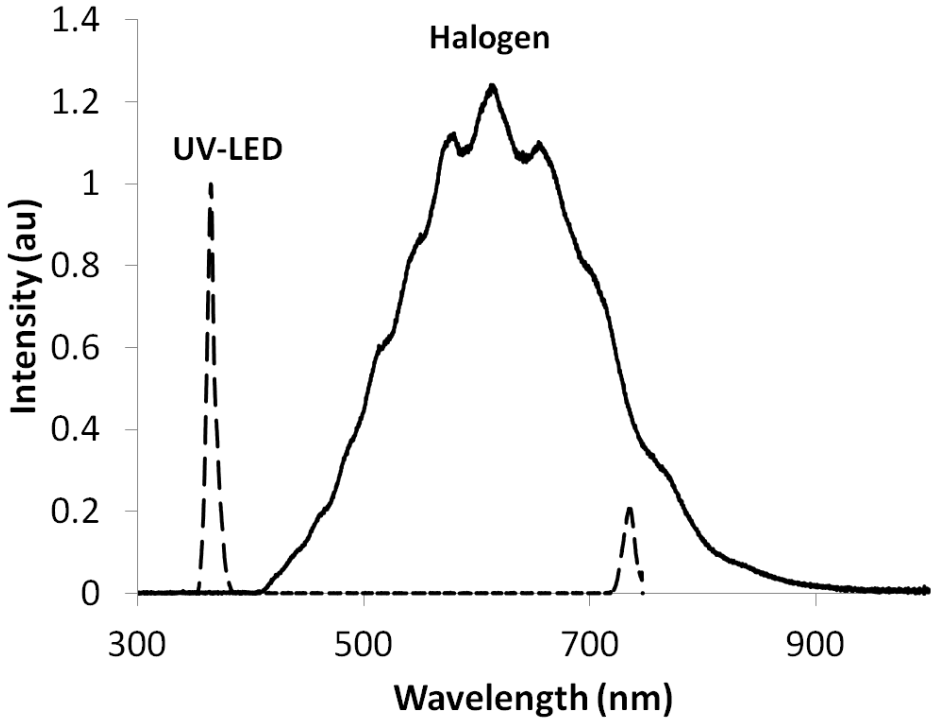

Figure 27 – Spectra of UV-LED and halogen lamps used for this study.

4.3.3.3. Optical filters

Optical filters operate by removing unwanted wavelengths of light but at the same time, allow the target wavelength to pass through the microscope system. There are generally three types of filters employed in a fluorescence microscope: excitation, emission and dichromatic filters.

The excitation optical filter functions to pass wavelengths of light required to excite the fluorescent sample. Emission optical filters allow wavelengths of light from the sample pass to the output *i.e.* camera. The dichromatic beamsplitter filters rely on interference to reflect certain wavelength ranges and transmit others, to direct the excitation wavelength to the sample.

An excitation filter should be chosen with the optimum excitation wavelength of the sample in mind. For this study quantum dots were chosen to conjugate with enzyme molecules. Due to the broad absorption profile of QDs, the excitation wavelength range is relatively broad also *i.e.* from UV to low visible region. Two excitation filters were chosen

for this study: 365/25 and 435/40 nm (central wavelength/ band width). It is also important when choosing an optical filter, particularly for low levels of fluorescence, to ensure the transmission is high which in turn enables optimum light capture. For this reason Semrock filters were selected which have transmission values close to 100%.

The emission optical filter selected to detect the signal of 655 nm emitting quantum dots, was a single band 650 nm filter. A single band filter passes light within a certain wavelength range *i.e.* a 650/60nm filter allows 650 nm light to pass with 30 nm each side of 650 nm (a range of 620-680 nm), as shown in **Figure 28**.

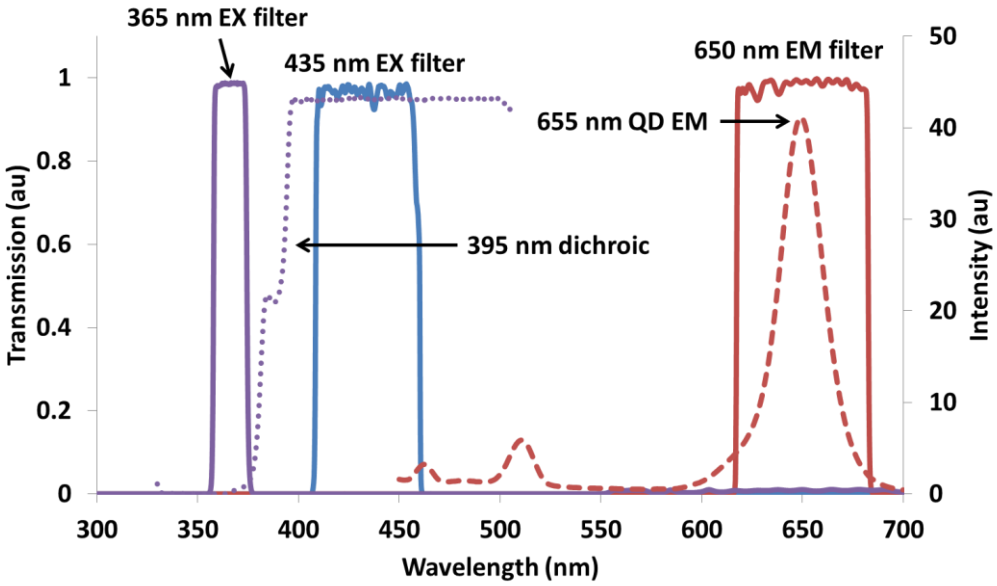

Figure 28 - Optical filter combination for 365 or 435 nm illuminated sample of 655 nm emitting QDs, collected using 650 nm emission filter (primary axis – transmission (%)). Dashed plot represents QD fluorescence emission spectrum (secondary axis – Intensity (au)) and dotted plot represents 395 nm dichroic filter employed with 365 nm excitation only. EX = excitation, EM = emission.

4.3.3.4. Image capture

To obtain images or video data of nanoparticles a suitable camera was necessary to detect and record the signal of individual particles. Typically, charged coupled device (CCD) cameras are employed for tracking single fluorescent particles, due to the high quality and low noise images produced. A CCD camera is an optical detector that converts light to a voltage output *i.e.* photoelectrons, which are amplified and converted from analogue to digital *via* a detector chip.[297] Amplification can be achieved before or after the production

of photoelectrons by intensified CCDs (ICCDs) or electron-multiplying CCDs (EMCCDs), respectively.

EMCCDs have solid state detectors that amplify the photoelectrons from the sample after they hit the detector chip. The chip in an EMCCD camera is usually thermoelectrically cooled to temperatures down to -100^{o}C which helps minimise noise, however dark noise may be amplified as well as signal. Methods to improve image contrast can include reducing the noise or increasing the sample brightness. Using a higher NA objective can increase the brightness of the sample, however noise is equally detected. Noise can be reduced by controlling unwanted light *i.e.* all light except the excitation wavelength range of the sample. Sources of unwanted light include light from nearby computer equipment, lamps or light from the external environment. In addition the sample will emit light in all dimensions, therefore light emitted in directions other than the detector or camera will be seen as background light.

For this study an EMCCD camera was chosen as it is suitable for single particle tracking applications due to less effects from noise (compared to other types of camera), and is particularly suited to conditions with low levels of fluorescence. Alternatively sCMOS cameras offer higher frame rates compared to CCD cameras, beneficial for the accurate tracking of nano-sized particles, however lack sensitivity compared to EMCCDs.[299]

4.3.3.5. Microscopy calibration

In order to determine distances for data analysis of tracked particles each objective used in the study was calibrated using a reference. An AFM/optical reference (Pacific Nanotechnology) with SiO square features was used to calibrate the objectives (**Figure 29**). Using ImageJ software the images were analysed to calculate the number of microns per pixel for each objective as follows:

50x 0.55 objective: 10 μm =35.251 pixels; 0.283 microns per pixel

100x oil immersion objective: 10 μm = 62.354 pixels; 0.160 microns per pixel

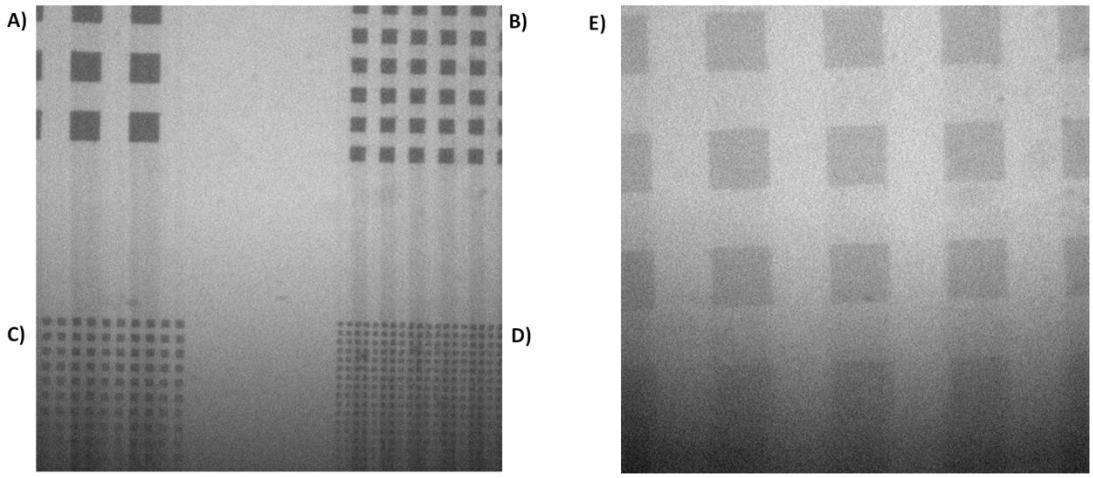

Figure 29 – 50x magnification of optical reference used to calibrate microscopic objectives. (A) 10 micron square/20 micron pitch, (B) 5 micron square/10 micron pitch, (C) 2.5 micron square/ 5 micron pitch, and (D) 1.5 micron square/3 micron pitch. (E) 100x magnification of 10 micron squares.

4.3.3.6. Solution sample holder design

In order to allow fluorescent particles (in this case enzyme-quantum dot conjugates) to move freely, the sample cell is important. A sealed cell is required to reduce evaporation of the liquid sample, as flow induced by evaporation would affect conjugate motility. There are a number of cells capable of holding liquid samples with the ability to seal, for example glass capillaries, glass bottom dishes and simple handmade cells (see **Figure 30** overleaf). Choosing the correct sample holder depends on a number of factors such as the objective specificity (NA and magnification), wavelength of illumination and the need for an oil or water immersion objective. As previously discussed, the objective chosen for this study is an oil immersion objective, therefore the sample holder was required to be compatible with the addition of oil and contain a suitably flat surface for contact with the objective.

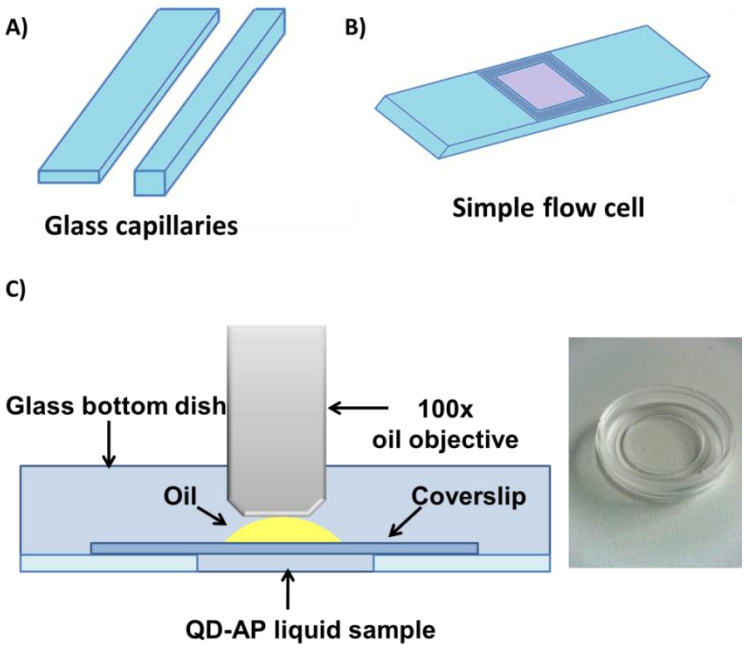

Figure 30 - Schematic representation of flow cells (A) glass capillary tubes with rectangular and square cross-sections, (B) Simple flow cell with sample sandwiched between glass slide and cover-slip and (C) Glass bottom dish with sample secured in a well with glass cover-slip, for use with oil immersion objective. Inset – image of a glass bottom dish.

The sample cells shown in **Figure 30** were evaluated for *in-situ* imaging of enzyme-QD conjugates, where glass capillary tubes offered simple sample loading through capillary action and were plugged at each end using glue to prevent evaporation. Although, samples once loaded, were not easily recovered from the tube due to the permanent sealant used. Capillary tubes are available in a range of sizes and cross-sectional design such as circular, square or rectangular (see **Figure 30 (A)**). Square or rectangular capillary tubes offered a flat surface for use with an oil immersion objective, however required extra stabilisation by securing the tube to a glass slide to reduce unwanted movement.

Simple cells prepared by sandwiching the liquid sample between a glass slide and a cover-slip, were sealed using glue around all edges of the glass cover-slip (**Figure 30 (B)**). This sample preparation technique was simple and materials are readily available, however evaporation was observed if the sample wasn't sufficiently sealed.

Glass bottom dish sample holders are purposefully designed for imaging cells using an inverted microscope *i.e.* the objective is positioned below the sample. For single particle tracking applications glass bottom dishes can be used with epi-fluorescence microscopy

where the objective is positioned above the sample. The dishes incorporate a well, capable of holding liquid samples. For use with an oil immersion objective the liquid sample was sealed within the well by the addition of a cover-slip over the well (**Figure 30 (C)**). The cover-slip offered a semi-permanent method of sealing the sample, as it was removed after observation and the sample was easily recovered for further analysis.

The sample cell chosen for this investigation was therefore a glass bottom dish, for use with epi-fluorescence microscopy, as it provided simple sample loading and recovery and was compatible with oil immersion objectives, without the need to permanently secure the sample.

As the liquid sample contains fluorescent particles in suspension other important factors were taken into account during the method development stage of the study, for example the concentration of QDs or enzyme-conjugates was investigated to achieve the optimum concentration for imaging *i.e.* enough QDs to image but not too many as to create background fluorescence issues or crowding. The volume and depth of focus (mentioned above) also played a key role in ensuring particles were freely diffusing in the centre of the sample well and not near glass surfaces of the sample holder. By using an oil immersion objective (rather than a water immersion), the top glass cover-slip was used as a reference to focus initially and then focus further into the sample to ensure tracked particles were freely diffusing.

4.3.4. MATLAB data analysis

Individual enzyme-QD conjugate motion is recorded in a digital video using an EMCCD camera. The frame rate and length of video can be controlled by manipulating the exposure time of the camera. A typical experiment recorded videos 300 or 600 frames long with a frame rate of 23 fps and an exposure time (the amount of time each frame is exposed for) of 0.01 seconds. Videos obtained using specialised camera software are required to be converted to TIFF file format for subsequent tracking and data analysis. It is worth noting that the conversion of files to other formats can, in some cases, cause compression of the file, and subsequent loss of information.

Video frames are composed from individual pixels arranged in a two-dimensional grid *i.e.* 512 x 512, with a video consisting of a number of frames in sequence, recorded at specific time intervals. The camera view could be reduced to achieve higher frame rates, however when working with highly diffusive nanoparticles, it was concluded that gathering as many particle tracks as possible was more important for this study, therefore 512 X 512 pixels and 23 fps were used.

For particle tracking applications each pixel is assigned an intensity value according to the brightness (fluorescence intensity) signal of the sample at each time point. Single particle tracking software is available commercially however MATLAB programs, based on an original IDL code by John Crocker and David Grier,[300] can be altered for specific systems. For this study, an in-house modified MATLAB program was used to obtain data on conjugate motion using three main stages of data analysis: pre-tracking, tracking and analysis.[§]

Other tracking programmes such as Nanosight are commercially available; however in this case were not be suitable for video acquisition using the available microscope/camera set-up, as it did not allow for the detection of low levels of fluorescence. Alternatively the raw data videos recorded using the EMCCD camera set-up could in theory be analysed using Nanosight, however the video (frame) dimensions would require to be altered and dimensions reduced to match the specifications of the Nanosight programme, resulting in loss of information.

4.3.4.1. Pre-tracking

The pre-tracking stage identifies particles with specific characteristics chosen by the operator such as intensity and size. Each frame or individual image of a video is analysed separately and based on the size and intensity of the features recorded, particles or intense features are assigned coordinates (**Figure 31** overleaf). A minimum diameter cut-off is required (*e.g.* 6 pixels) and a 'mass cut-off' (integral of the intensity/area of the particle) value of 1000 au, eliminates noise being mistaken for diffusing particles.

[§] *Development of MATLAB tracking programs performed by Alexander Hope, originally developed for algae tracking and modified for enzyme-QD tracking applications.*

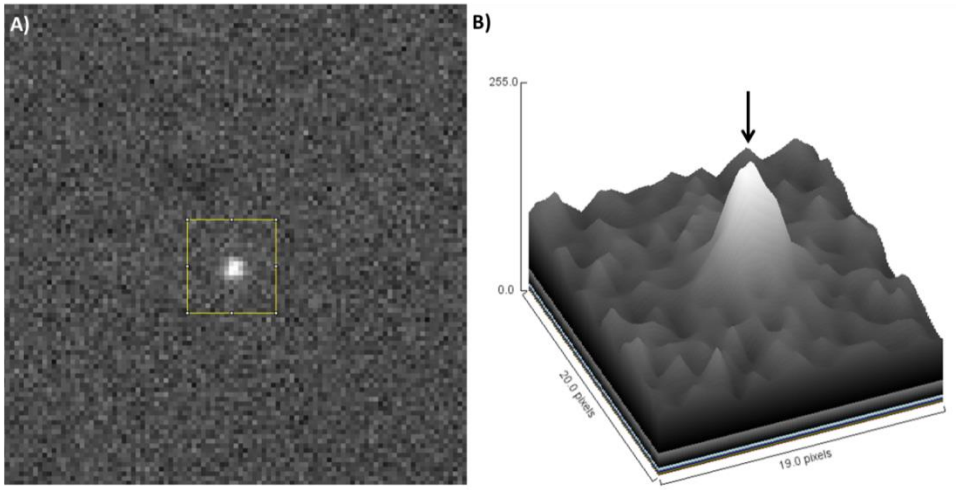

Figure 31 - (A) Snapshot image of a particle in one frame. (B) The corresponding 3D intensity profile of the particle used to identify particles.

4.3.4.2. Tracking

Tracking relies on information recorded from the pre-tracking stage *i.e.* positional coordinates. Particles in neighbouring frames which are in close proximity are compared and identified as either being the same particle or different particles, depending on a maximum distance value that a particle can travel from one frame to the next. Each particle is assigned an individual identification number allowing coordinate data, originally separated into single frames in the primary stage, to be joined together into sequences of coordinates over time, resulting in particle tracks as shown in **Figure 32** overleaf.

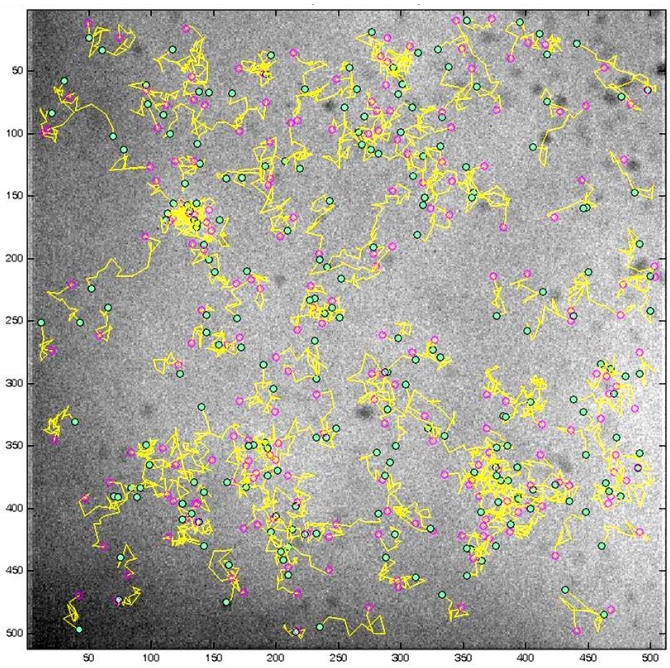

Figure 32 - Particle tracks for a 300 frame long example video. Tracks are made by combining individual coordinates of particles (assigned per frame). Image dimensions: 512 x 512 pixels. Green corresponds to the start of a track and magenta is the end of a track (see **Figure 64** for example trajectories).

The tracking program requires a number of parameters such as the maximum displacement, minimum duration of track and the memory. The maximum displacement used for this study was 15 pixels (2.4 µm). This is the maximum distance in pixels that a particle can travel between frames before being 'treated' as another particle. Calculating the distance travelled by the fastest particle tracked (assuming linear displacement) with a speed of 27.1 µm, over the time period of 1 video frame (0.04 seconds) this particle would have travelled 1.2 µm (if ballistic). Therefore according to the calculation only particles which have displacements >2.4 µm, should be 'new' particles and so will be assigned an individual particle identification number. The minimum duration of track (*e.g.* 10 frames) is the minimum number of frames in length a particle track should be before it will be disregarded. The memory or maximum number of dropped frames, in this case 5 frames, is the maximum number of frames a particle can be undetected *e.g.* going out of the focal plane and re-entering, before being given a new identification number.

4.3.4.3. Analysis

The analysis stage measures how parameters *e.g.* coordinates, of each particle alter with time *i.e.* over a certain time or frame interval. The analysis MATLAB program processes information gained from previous data handling stages and relies on the frame rate of the camera (typically 23 fps) and the microns per pixel value (0.16) calculated by calibrating the microscope objective (see 4.3.3.5). The analysis program takes particle coordinates to produce the speed of each particle, the mean squared displacement (MSD) (and diffusion coefficient) for individual particles, but also population averages; and angle of trajectory (see chapter 1.1).

The speed of an individual particle is defined as the 'frame-to-frame' speed, which is measured over a 10 frame interval *i.e.* frames 1-10; 2-11; 3-12 *etc.*, to reduce errors in identifying the centre of a particle due to QDs, for example exhibiting a halo effect associated with the particle being out of the focal plane.

The two dimensional mean square displacement is a measure of the square of the mean distance (from a starting point with x and y coordinates) that a particle has travelled in a given time.

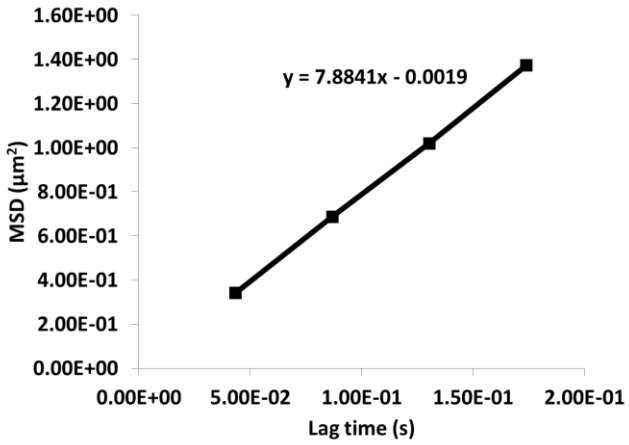

Figure 33 - MSD *vs.* lag time plot for an example video of QD-AP conjugates. The gradient of the plot can be used with equation 2 to calculate the diffusion coefficient.

The MSD plot can reveal how a particle or population of particles are diffusing, for example a linear MSD versus lag time plot is indicative of normal random diffusion ($\langle MSD_{xy} \rangle = 4D\Delta t$), where D is the diffusion coefficient, as discussed in section 1.1. However, directed motion is

shown by a quadratic relationship illustrated by the following equation: $\langle MSD_{xy} \rangle = v^2 t^2 + 4D\Delta t$ (where v is the average velocity) and a curved MSD plot.[7] From an MSD plot (for example **Figure 33**), the diffusion coefficient can be determined using the gradient of the line (MSD_{xy}) and the following equation:

$$\boldsymbol{MSD_{xy} = 4D\Delta t} \qquad \textbf{(Equation 2)}$$

The angle of trajectory of an individual particle is determined by assigning the starting position (x and y coordinates) of a particle with imaginary axes (see **Figure 34**), which are used to measure the angle between the original and 'new' coordinates of a particle over a certain period of time (*e.g.* over 10 frames as described above for speed).

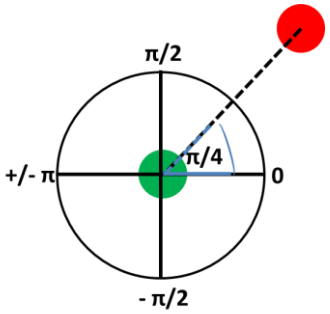

Figure 34 – Radian argand diagram representing a particle at position 1 (green) which over a given time has displaced to position 2 (red). The angle of trajectory is a measure of the angle from starting position to the new position of the particle according to the imaginary axis values.

A possible source of error, which could arise during particle tracking, is the precision in the initial particle identification 'pretracking' stage. A maximum error at this stage would occur if the centre of the particle was measured incorrectly at a distance equal to the radius of the particle's intensity profile (see **Figure 31**). Additionally errors can occur in which the acquisition time of the camera could be long therefore particle positions could be missed *i.e.* the particle could have moved multiple steps in the time it takes for the camera to acquire the next image/frame of the video and these would not have been recorded. Here, we analyse the frame-to-frame speed distributions for large amounts of particle data for statistical stability, and we then compare with a measured distribution. By analysing distributions data for a population of particles we give a full picture, compared to quoting solely an average speed value. Additionally, data is acquired and analysed using the same techniques for all experiments to ensure results are directly comparable.

– Chapter 5 –

Towards visualisation of single alkaline phosphatase molecules - Part 1

5.1. Objectives

To engineer an enzyme nanomotor capable of single molecule tracking, enzyme molecules must be modified to enable single molecule visualisation. Therefore the first objective was to develop a method to modify alkaline phosphatase molecules for visualisation and tracking by fluorescence microscopy using organic labelling and covalent attachment to fluorescent nanoparticles. Secondly, fluorescently 'labelled' enzymes are characterised to confirm successful 'labelling', as well as enzymatic activity studies to determine whether the enzyme remains active after fluorescent 'labelling'. Finally the enzyme source was investigated to determine whether mammalian or bacterial alkaline phosphatase would be preferential for this study.

5.2. Introduction

Alkaline phosphatase (AP) (EC 3.1.3.1) was chosen for this study as it non-specifically hydrolyses phosphate monoester moieties, such as the natural substrate inorganic pyrophosphate (PP_i) of mammalian AP.[301] Phosphatases exist in a variety of unicellular and multicellular organisms; from bacteria to humans, functioning for the regulation of protein activity and signal transduction.[201] Furthermore expression levels of phosphatases in certain organisms can be affected by diseases such as diabetes, cancer and multiple sclerosis.[201] Therefore elevated or decreased levels of phosphatase can be used to detect certain diseases. Here we use AP, and take advantage of its relatively non-specific behaviour towards phosphate containing substrates, for the dephosphorylation of short aromatic dipeptide amphiphiles and to consequently trigger molecular self-assembly (see section 2.8). The overall aim is to visualise and analyse the motion of individual AP molecules during the biocatalytic self-assembly of aromatic dipeptide molecules into supramolecular structures.

5.3. Labelling alkaline phosphatase with an organic fluorophore

In an attempt to investigate if molecular labelling could facilitate the visualisation and tracking of individual enzyme molecules, the organic fluorophore: fluorescein isothiocyanate (FITC) was chosen to label alkaline phosphatase. The optical properties of FITC for example, excitation and emission maximum wavelengths of 494/518 nm[256] respectively, allow for potential visualisation using a fluorescent microscope fitted with a FITC optical filter set. Labelling biomolecules with FITC relies on reactivity with amine groups such as lysine side chains, and also the N-terminal region of the protein (see **Figure 35**).[257]

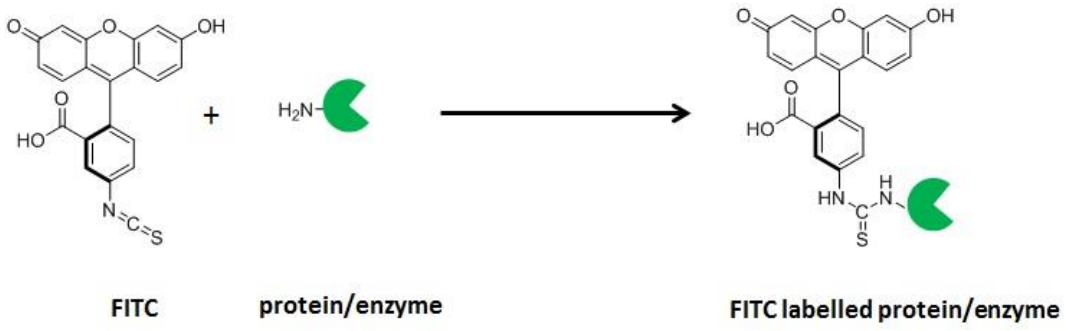

Figure 35 - FITC labelling of a protein or enzyme by the reactive isothiocyanate group of FITC with primary amines of proteins to produce the thio urea product.

The FITC labelling method was tested first of all using the less expensive protein, bovine serum albumin (BSA). The labelling method required an excess of FITC to BSA, therefore extensive purification was required, after labelling, to remove unreacted FITC. Purification was achieved by dialysis and was monitored by fluorescence spectroscopy, by measuring the fluorescence emission of FITC (520 nm) for each buffer exchange. Dialysis wash steps were continued until the buffer wash contained little or no fluorescence signal for FITC, indicating that the labelled enzyme was free of unreacted FITC. As expected the fluorescence emission measured at 520 nm decreased with each buffer exchange. However, it can be seen from **Figure 36** overleaf, that even after four dialysis wash steps, the fluorescence emission of FITC can still be detected; therefore further wash steps would be required.

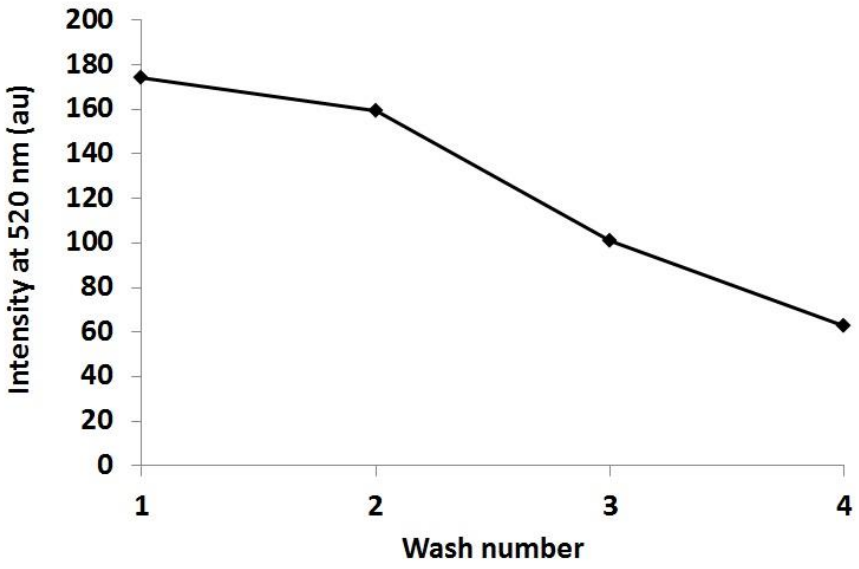

Figure 36 - FITC-BSA purification monitored by fluorescence spectroscopy.

For FITC labelling of alkaline phosphatase from calf intestinal mucosa (CI-AP), one main issue arose: the full amino acid sequence of the bovine form of the enzyme is unknown therefore possible sites for labelling cannot be determined *i.e.* sites on the surface of the enzyme molecule with amine groups. Despite this, labelling was attempted by reacting FITC and CI-AP. Free/unlabelled dye was removed by dialysis against water, using the method developed with BSA. The fluorescence emission spectra of FITC and FITC-AP were compared with a resulting red shift in the emission maximum of FITC, from 520 to 547 nm, after labelling to AP, suggesting successful attachment (**Figure 37** overleaf). The spectral shift could be a result of a change in the immediate environment of FITC molecules. A red shift in FITC emission has previously been reported upon covalent attachment to silica particles,[302] as more FITC molecules become localised in a given area, interactions can occur between neighbouring FITC molecules resulting in a shift towards longer wavelengths. The lower fluorescence intensity displayed by FITC-AP (shown by secondary axis scale in **Figure 37** over leaf), could be partly due to this effect but is thought to be mainly caused by a dilution effect, during purification *i.e.* the excess unreacted FITC is washed away and only FITC attached to the enzyme is detected.

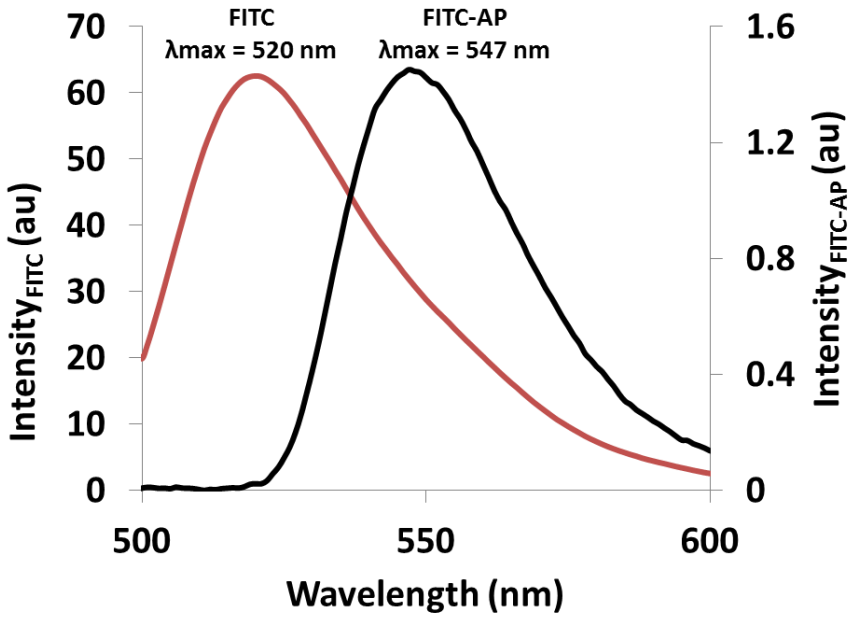

Figure 37 - Fluorescence emission spectra of FITC and FITC-AP, excited at 495 nm. Primary axis illustrates the intensity (au) of FITC compared to a lower intensity of FITC-AP (secondary axis).

A solution of FITC-labelled CI-AP was subjected to fluorescence microscopy to determine whether single molecules of labelled enzymes could be visualised in combination with a FITC optical filter set. However, the fluorescence of FITC-AP was low and the camera set-up available was not capable of detecting single molecules in suspension.

Overall the method of conjugation and purification was partly successful. The purification by dialysis required multiple buffer exchanges and large volumes of buffer, which proved time consuming and ineffective at removing all of the unreactive fluorophore. The presence of unreacted FITC prevented single molecule tracking due to significant fluorescence background issues (results not included).

5.3.1. *Escherichia coli* alkaline phosphatase

It became apparent from the attempt to label CI-AP with FITC, that it was important to determine possible conjugation sites on the surface of a molecule of alkaline phosphatase.

From this point on, alkaline phosphatase from the bacterium *Escherichia coli* replaced CI-AP, as the full amino acid sequence is known[303] and possible conjugation sites can be predicted.

When comparing CI-AP with *E.coli* AP, the major differences are thought to be that CI-AP is a glycoprotein and exists bound to the cell membrane whereas *E.coli* AP is present unbound, within the periplasmic space of the bacterial cell. Membrane proteins have proven difficult to establish amino acid sequences and therefore structures, due to difficulties in expression, purification and crystallisation.[304] The primary structures of CI-AP and *E.coli* AP are therefore different but sequence similarities have been reported, for example the common serine residue involved in the active site. The overall enzymatic reaction occurring in each case is thought to be the same.[305]

Alkaline phosphatase from *E.coli* was first studied between 1959-60 by Horiuchi, Torriani and co-workers; followed later by its preparation and characterisation by Levinthal and Garen.[306] The enzyme exists as a dimer containing one active site per monomer. The dimeric structure is thought to be vital to the activity of the enzyme, where the monomeric form has been proven inactive.[307] Each monomeric polypeptide chain is composed of 449 amino acids with a mass of 47 kDa per monomer (dimer mass is 94 kDa).[308]

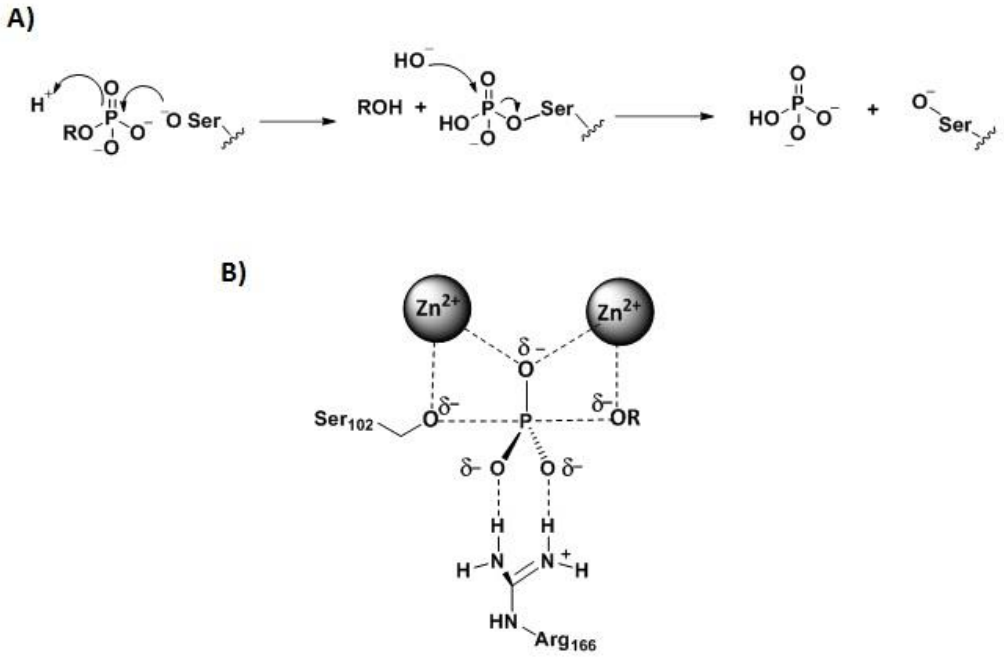

Figure 38 – (A) The mechanism for phosphate ester hydrolysis by alkaline phosphatase. The reaction involves nucleophilic attack by the active serine residue on the phosphate ester to form a phosphoserine intermediate. The alkoxide leaving group then requires a proton from solution to form the alcohol. (B)The expected transition state during dephosphorylation of a substrate by *E.coli* AP.[309,310]

As mentioned previously, the active site in each monomer of alkaline phosphatase contains an active serine residue,[311–313] which is present at position 102 of the amino acid sequence in *E.coli* AP.[303] During the hydrolysis reaction involving the phosphate ester of the substrate, the active serine residue is phosphorylated. The resulting phospho-enzyme complex can then react with an alcohol to form a phosphate ester which then dissociates from the enzyme (**Figure 38 A**)).[305] The dephosphorylation step is dependent on pH and also the presence of metal ions at the active site.[303] The optimum pH for AP is found to be around pH 8 and the isoelectric point at pH 4.5.[303] One magnesium and two zinc atoms are required at each active site.[311–313] The guanidinium group of arginine (position 166 in *E.coli* AP) is also thought to play an important role during phosphate binding and substrate alignment at the active site (**Figure 38 B**)).[310]

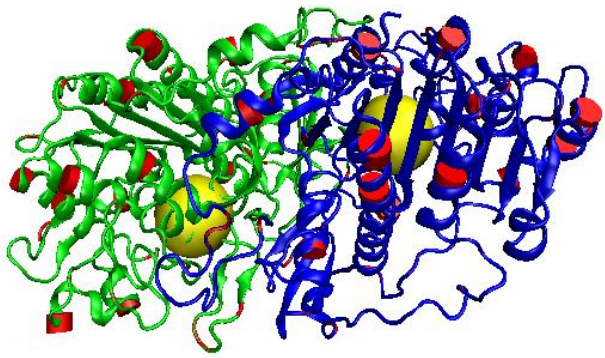

Figure 39 - *Escherichia coli* alkaline phosphatase model (PDB-ID 3TG0) with chain A and B in blue and green respectively. Basic residues (lysine and arginine) are highlighted in red and active sites illustrated by yellow spheres.

The crystal structure of *E.coli* AP in the presence of vanadate provides a suitable model for the proposed transition state during the catalytic reaction at the active site.[314] Vanadate is isostructural and isoelectronic with phosphate therefore is used as a substitute for the interaction and release of phosphate at the active site. The structural dimensions of an *E.coli* AP dimer is found to be 100 x 50 x 50 Å (10 x 5 x 5 nm) with the two active sites in each monomer being 30 Å (3 nm) apart.[314] The dimeric *E.coli* AP (PDB ID – 3TG0) structure, in terms of labelling or conjugation, has 56 lysine residues; 32 of which are available on the surface, with the potential to conjugate to amine reactive molecules or particles (**Figure 39**).

5.4. Summary

In summary, attempts at labelling the enzyme with an organic fluorophore (FITC), proved unsuitable for single molecule visualisation and tracking due issues with removal of unreacted FITC and subsequent background fluorescence experienced by fluorescence microscopy (results not shown). Therefore the most attractive method to enable visualisation of individual biomolecules by fluorescence microscopy is to conjugate with fluorescent nanoparticles.

Initial tests with CI-AP demonstrate the importance of knowing the full primary structure of the enzyme for the purpose of reacting with a fluorescent molecule or particle. For this reason *E.coli* alkaline phosphatase was chosen allowing the number of available reactive sites per molecule to be established.

Towards visualisation of single alkaline phosphatase molecules - Part 2

5.5. Introduction

Quantum dots are highly fluorescent semiconductor nanocrystals which can be modified with a number of biocompatible surface functionalities for conjugation to protein molecules. Here we investigate the bioconjugation of alkaline phosphatase with 655 nm emitting quantum dots towards the visualisation and tracking of single enzyme molecules.

5.6. Bioconjugation of alkaline phosphatase to quantum dot nanoparticles

AP from *E. coli* was conjugated to carboxyl functionalised CdSe/ZnS quantum dots (emission wavelength 655 nm) *via* EDC/NHS coupling (**Figure 40** overleaf). Common QD bioconjugate methods use EDC alone for coupling, however NHS has been shown to stabilise activated carboxyl reactive groups for a longer period of time, therefore allowing for a more efficient coupling reaction.[315] EDC activated carboxyl functionalised QDs can couple to free amines available on the AP molecule. As mentioned a dimeric molecule of AP from *E.coli* has 32 lysine residues available on the surface, with the potential to conjugate to carboxyl

functionalised QDs.[295] Having a number of possible attachment sites, leads to a variety of conjugation confirmations, therefore cluster formation is expected. A cluster for this type of QD-enzyme conjugate is defined as multiple QDs and/or enzymes involved in a single cluster, in contrast to a 1:1 ratio of enzyme to QD. Conjugate clusters in the context of this project may be advantageous for visualisation purposes and conjugate enzymatic activity may be enhanced if more than one active enzyme is present per conjugate.

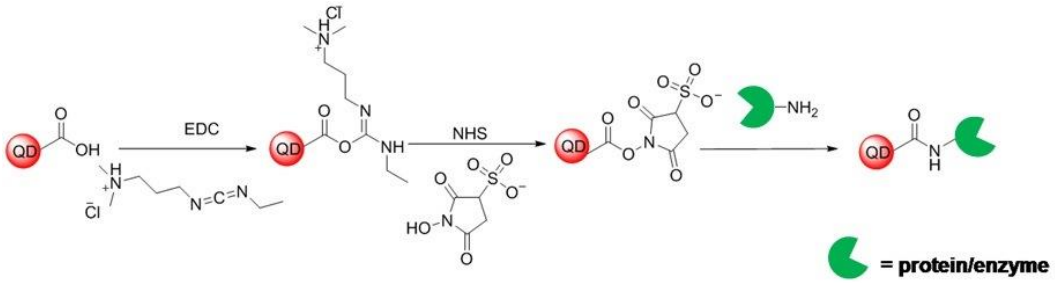

Figure 40 - Alkaline phosphatase bioconjugation reaction with quantum dots *via* an EDC/NHS coupling method.

5.7. Bioconjugate purification

Due to the large excess of reagents compared to QDs required during the coupling reaction, it is vital that the complete removal of all unconjugated enzyme and reactants is achieved, as the true activity of the conjugate is required without interference from free unconjugated enzyme. Purification of the conjugate is possible due to the difference in size of the conjugate compared to the unreacted QDs and enzyme molecules, for example the conjugate is expected to be larger in size compared to free QDs and AP (as demonstrated by DLS **Figure 43**). This is accomplished using a filtration unit capable of retaining the conjugate but allowing the unconjugated enzyme and reagents to pass through (**Figure 41**).

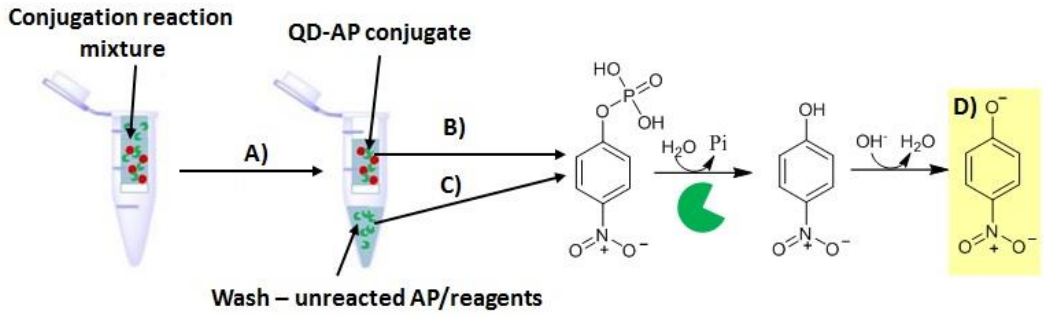

Figure 41 - (A) QD-AP purification *via* filtration and centrifugation with a number of wash steps to remove unreacted enzyme. The resulting conjugate is analysed using a *p*-nitrophenyl phosphate colorimetric assay (B) which gives a yellow colour change (D). The wash samples are also analysed (C) using the colorimetric assay to determine purity of the conjugate *i.e.* when free enzyme no longer exists in the filtration wash samples.

To ensure all free/unreacted enzyme molecules were removed from the conjugate, multiple filtration and centrifugation wash steps were performed and the purification wash samples were retained and subjected to a colorimetric activity assay (**Figure 41**). The substrate *p*-nitrophenyl phosphate is dephosphorylated by any alkaline phosphatase remaining in the wash, resulting in a yellow colour change which can be monitored by measuring the absorbance at 410 nm by UV-Vis spectroscopy. After 8-12 washes the absorbance at 410nm is reduced to the negative control value of buffer only, indicating that all unreacted alkaline phosphatase had been removed (**Figure 42**).

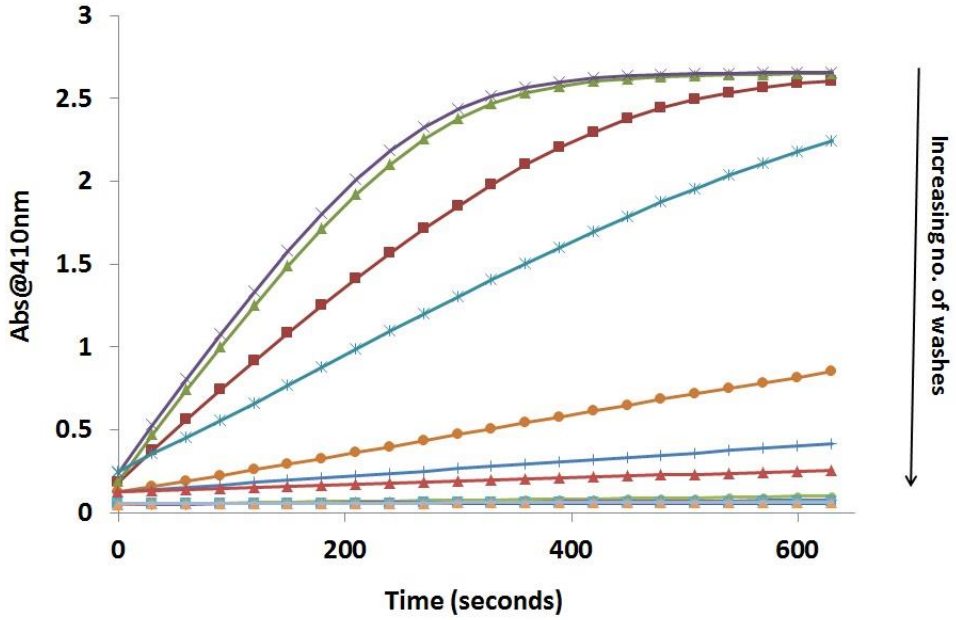

Figure 42 - Each QD-AP purification wash was analysed (as shown in **Figure 41 (C)**) by UV-VIS in the presence of *p*-nitrophenyl phosphate. The absorbance at 410 nm was monitored over time for each wash, revealing that after 8 washes the absorbance at 410 nm had reduced to the negative control, therefore indicating that all free (unconjugated) AP had been washed away.

5.8. Bioconjugate characterisation

The purified conjugate solution was characterised by dynamic light scattering (DLS) to obtain size distribution information. Before conjugation the average hydrodynamic diameter of AP molecules and QDs in suspension were found to be approximately 8 nm and 10 nm respectively, (compared to theoretical dimensions for alkaline phosphatase 10 x 5 x 5 nm[314] and 12 x 6 nm for free QDs, as quoted by manufacturer). Analysis of the purified conjugates (QD-AP) by DLS revealed a larger size distribution with a hydrodynamic radius centred around 17 nm (*i.e.* diameter of 34 nm), indicating successful conjugation (**Figure 43** overleaf).

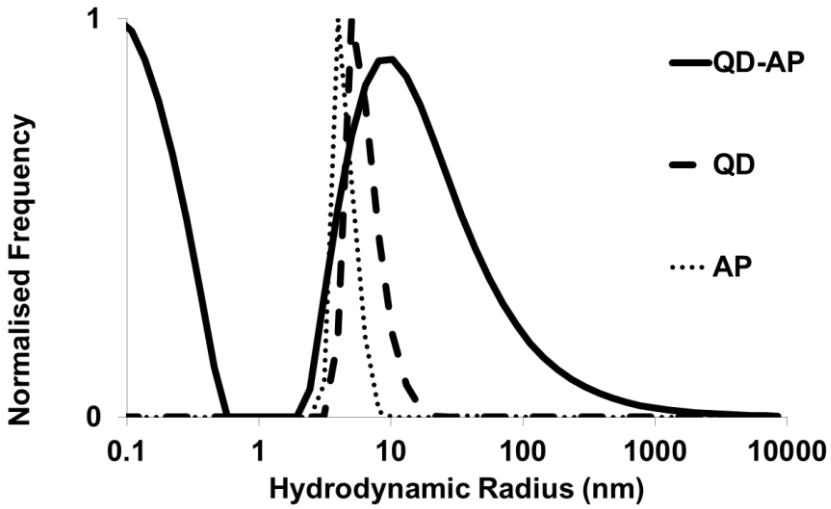

Figure 43 - Size distribution plot of QDs, AP and QD-AP conjugates by dynamic light scattering (size distributions observed below 1 nm are attributed to an artefact commonly observed using the DLS instrument).

In order to visualise QD-AP conjugates, atomic force microscopy (AFM) and transmission electron microscopy (TEM) techniques were used. It can be seen from **Figure 44** that QD-AP conjugates are larger in size compared to unconjugated QDs. It can be seen after conjugation that larger clusters are observed compared to single QDs **Figure 44** (A) and (B)/(C), respectively.

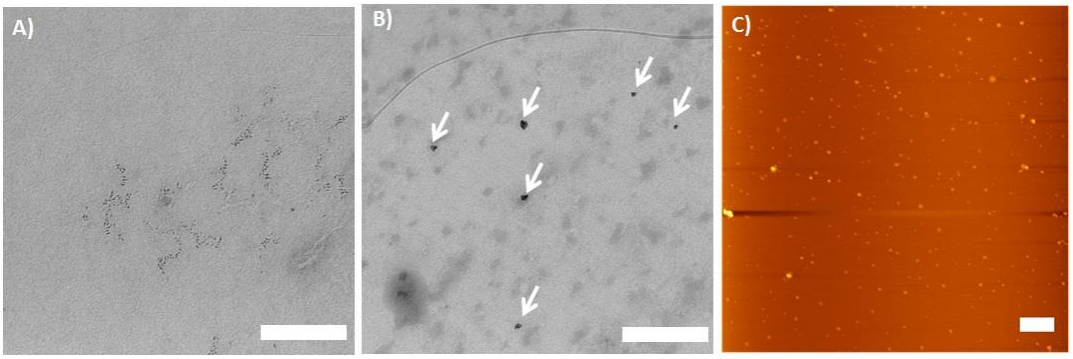

Figure 44 – (A) TEM image of unconjugated QDs (scale bar 200nm); (B) TEM image of QD-AP conjugate clusters (scale bar 200 nm); and (C) AFM image of QD-AP conjugates (scale bar 2 µm).

For the successful visualisation and detection of enzyme-QD conjugates by fluorescence techniques, enzyme-QD attachment must be achieved without hindering the fluorescence emission properties of the QDs. Equally, it is important that the enzyme remains active after conjugation. The absorption and fluorescence emission spectra of QDs (0.8 nM) before and after conjugation (100 µL of conjugate per millilitre of buffer) were compared,

to show that the emission maximum at 650 nm was unaffected by the conjugation and the absorption profile of QD-AP resembled the free QD spectrum (**Figure 45**). The lower fluorescence intensity of the conjugate is due to dilution during the conjugation and purification steps.

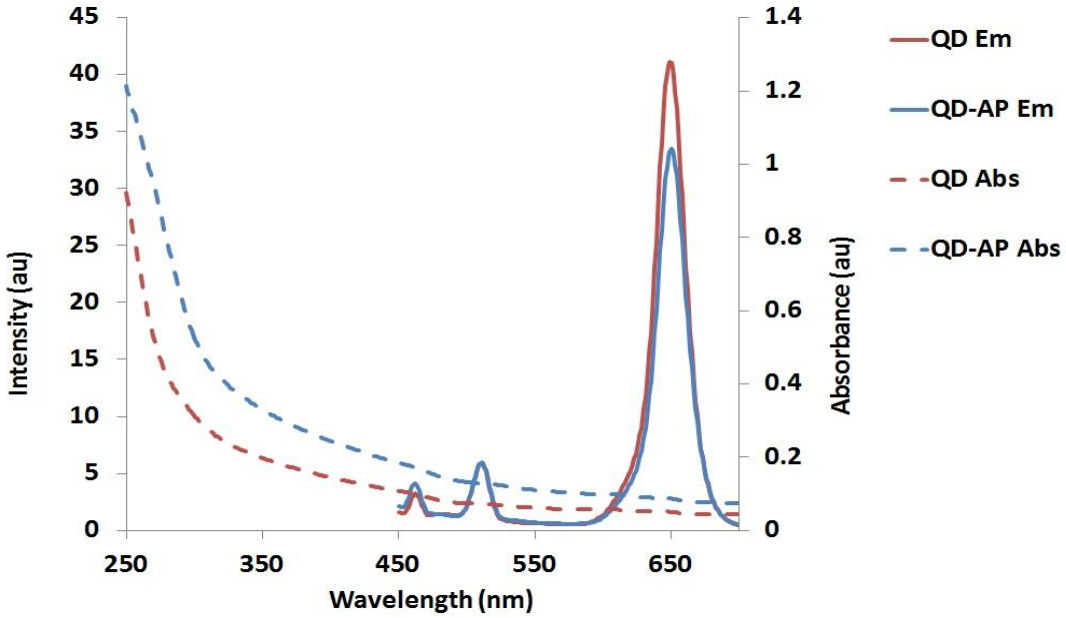

Figure 45 - Fluorescence emission spectra of QDs (red solid line) and QD-AP conjugates (blue solid line) – primary axis. The corresponding absorbance spectra are plotted on the secondary axis with QDs (red dotted line) and QD-AP (blue dotted line).

5.9. Estimation of QD and AP concentration in a given volume of conjugate

After conjugation the resulting conjugate contains unknown enzyme and QD concentrations. In order to assess the enzymatic activity and fluorescence intensity of the conjugate a number of calibration steps were performed. First, a fluorescence calibration curve was obtained by measuring the fluorescence emission intensity for a range of QD concentrations, used ultimately to estimate unknown QD concentrations of QD-AP solutions (**Figure 46** overleaf). Using the equation of the line for the calibration curve (**Figure 46**), a fluorescence emission intensity value of a conjugate solution can be substituted into the equation to calculate a concentration of QDs (see section 3.3.16 for full calculation). It can be seen from **Figure 46** that there is a detection limit of the fluorimeter below a QD concentration of 1 nM, and the plot does not cross through zero. However for

the purpose of this study, a number of assumptions are already in place, for the estimation of QD and AP in a given volume of conjugate, such as enzyme activity and fluorescence properties are unaffected by conjugation

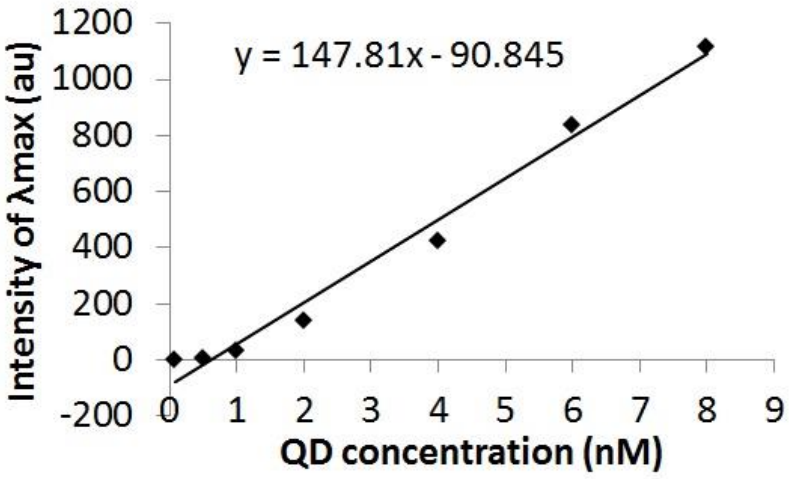

Figure 46 - Calibration curve to estimate the concentration of QDs present in an unknown conjugate solution.

Next, an activity assay calibration was performed to determine a similar activity of free enzyme compared to a given volume of QD-AP conjugate. The activity assay also served to confirm enzyme activity had been retained after conjugation (**Figure 47** overleaf). The *p*-nitrophenyl phosphate colorimetric assay was used to analyse the activity of the purified conjugate. Negative and positive controls were also analysed; consisting of free unconjugated QDs and a variety of known concentrations of free enzyme, respectively. It was identified that a dilution of 32 µl/mL of QD-AP conjugate in buffer had similar activity to $7x10^{-4}$ U of free enzyme with an estimated upper concentration limit of 0.37 nM. Whereas, the enzyme is supplied as: 43.68 U/mg protein and 19.9 U/mg of solid as per manufacturer. (see section 3.3.16 for calculation).

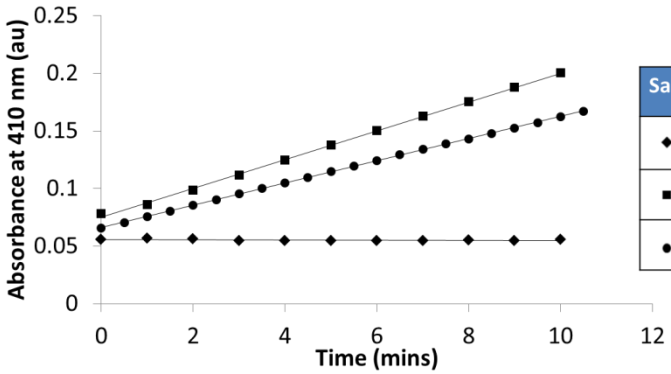

Sample	Gradient (x10^{-3})
◆ Control	0.1
■ AP (0.37 nM)	12.5
● QD-AP (3) (32 µL/mL)	9.6

Figure 47 - Calibration for the estimation of enzyme concentration in a given volume of QD-AP conjugate solution (32µl/mL). The table lists line gradients for each sample illustrating the rate of substrate (*p*-nitrophenyl phosphate) turnover.

Using the information gained from the enzyme activity calibration and the fluorescence calibration of QD emission, it can be estimated that there is 1.04 nM QDs and an upper limit of 0.37nM AP in a diluted QD-AP solution (32µl/mL). This translates to a 2.8:1.0 ratio of QD to enzyme in the QD-AP conjugate (batch 3), assuming that the activity of the enzyme and the fluorescence emission intensity of the QDs are unaffected by the conjugation reaction (see calculation – section 3.3.16). It has been shown with streptavidin conjugated QDs, that as many as twenty protein molecules can be present per conjugate and there are a variety of possible spatial conformations for protein attachment.[276,284]

In addition, an activity lifetime study showed that, the rate of *p*-nitrophenyl phosphate dephosphorylation (the increase in absorbance at 410 nm over time) remains relatively steady, over at least eight weeks (**Figure 48** overleaf). This implies that the conjugates remain at a constant activity level for at least this time duration (8 weeks).

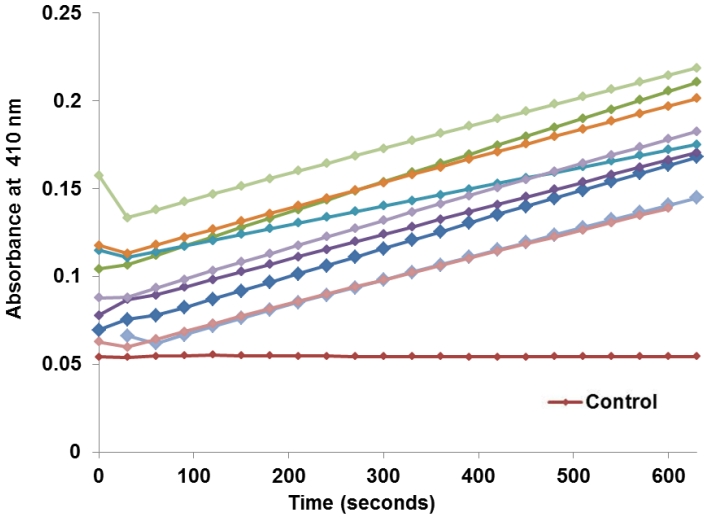

Time (weeks)	Gradient (x10^{-4})
0	1.6
1	1.7
2	1.4
3	1.0
4	1.4
5	1.4
6	1.4
7	1.3
8	1.6

Figure 48 - QD-AP conjugate lifetime study. An activity assay was performed every week for 8 weeks, to determine the effective lifetime of the conjugates. The plot is accompanied by a table of corresponding gradients.

5.10. Enzyme-quantum dot conjugate batch comparison

A number of batches of enzyme-QD conjugates were prepared throughout the entire study, of which the first two batches (1 and 2) were used for method development and were therefore not used for final enzyme tracking experiments; batches 4 and 5 were disposed of due to issues with QDs that were used for conjugation having passed the recommended date of use. Overall batches 3 and 6 were used for all of the data acquisition therefore characterisation was performed for both batches for comparison of the enzymatic activity, fluorescence properties of QDs and size distribution of conjugates. In **Figure 49** (overleaf) it can be seen that QD-AP conjugates vary in terms of fluorescence emission intensity and peak maxima (λ_{max}) but also the size distribution plots show some variation between batches.

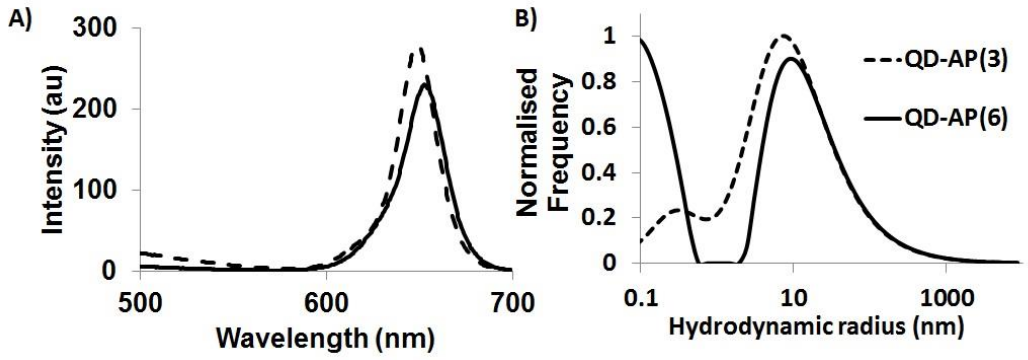

Figure 49 – (A) Fluorescence emission spectra of QD-AP batch 3 (dashed line) and 6 (solid line). (B) size distribution of QD-AP batches measured by dynamic light scattering.

For each batch of enzyme-QD conjugate a fluorescence calibration study was performed by measuring the fluorescence emission intensity at 655 nm for a number of QD-AP conjugate dilutions (Appendix C). QD-AP batches exhibit variation in fluorescence emission (**Figure 49**) which could be attributed to differences in QD concentration due to dilution during conjugation and handling *e.g.* removal of free AP, but may also be a result of the different degree of conjugation *i.e.* more QDs attached to enzymes. The fluorescence emission intensity of a given volume of each conjugate per millilitre was used to estimate the QD concentration by comparing the fluorescence intensity with the calibration curve obtained using free QDs (Appendix C). In addition an activity assay compared with free enzyme (as described above), was performed for each batch in order to obtain an approximate QD-to-enzyme ratio as described above (see Appendix D). For batch 3 it was estimated that the QD:AP ratio was 2.8:1, assuming an upper concentration limit for AP and that enzymatic activity is unaffected by conjugation to QDs and that the fluorescence emission properties of QDs are unaltered by conjugation. Variations in QD-AP conjugate batch can be illustrated by the degree of conjugation estimated to be 2.8:1 and 13:1 QD:AP for batches 3 and 6 respectively. Batch variation with respect to tracking analysis is discussed in section 7.3.3.

5.11. Summary

Fluorescent labelling of bovine alkaline phosphatase using an organic fluorophore (FITC), proved unsuitable for single molecule tracking. Therefore a bioconjugation method was employed for the covalent attachment of alkaline phosphatase from *E.coli* to fluorescent nano-sized quantum dots. The resulting QD-AP conjugates were characterised by

fluorescence spectroscopy, dynamic light scattering and microscopy techniques to confirm conjugation was successful. An enzymatic activity assay indicated that the enzyme conjugates were active through a colorimetric dephosphorylation reaction. Numerous batches of QD-AP conjugates were prepared throughout the study, these were characterised and compared. Variations between batches were observed which were attributed to differences in environmental and day-to-day conjugation conditions, ultimately resulting in different QD:AP ratios. Dilution of QD-AP during removal of free enzyme and loss of material due to handling *e.g.* filtration, could offer a further explanation to varying fluorescence intensities of QD-AP conjugate solutions. Ultimately if the extent of conjugation could be controlled *i.e.* number of enzymes to QDs, this could offer a potential route to controlling enzymatic activity of conjugates which could be advantageous for enzyme motor applications (see section 7.3.3).

– Chapter 6 –

Biocatalytic self-assembly of phosphatase responsive aromatic peptide amphiphiles – Part 1

6.1. Objectives

In order to develop a self-assembly system for the propulsion of enzyme-QD conjugates, self-assembling substrates were studied, firstly with free enzyme to confirm evidence of supramolecular interactions and conversion to dephosphorylated products with a known concentration of AP (part 1). Secondly, enzyme conjugates were tested for their ability to convert substrates to dephosphorylated fibre- and sphere-assembling products (part 2).

6.2. Introduction

Taking advantage of alkaline phosphatase's ability to dephosphorylate a wide range of phospho-containing substrates, three aromatic dipeptide amphiphiles were chosen for this study, for future investigations for the nanopropulsion of the enzyme, AP. Fmoc-F*p*Y-OH (**1a**)[206–208]; pyrene-*p*YL-OH (**2a**)[203] and Fmoc-*p*YQ-OH (**3a**)[208] have previously been reported as substrates for alkaline phosphatase by dephosphorylation to Fmoc-FY-OH (**1b**); pyrene-YL (**2b**) and Fmoc-YQ-OH (**3b**) respectively (**Figure 50** overleaf).

1b and **2b** are expected to self-assemble into linear fibrous structures,[206,208] whereas it has been shown previously that **3b** forms spherical aggregates.[208] The substrates are investigated as 'fuel' molecules (in Chapter 7) for enzyme nanopropulsion and the resulting self-assembled structures are studied to determine how they influence enzyme motion.

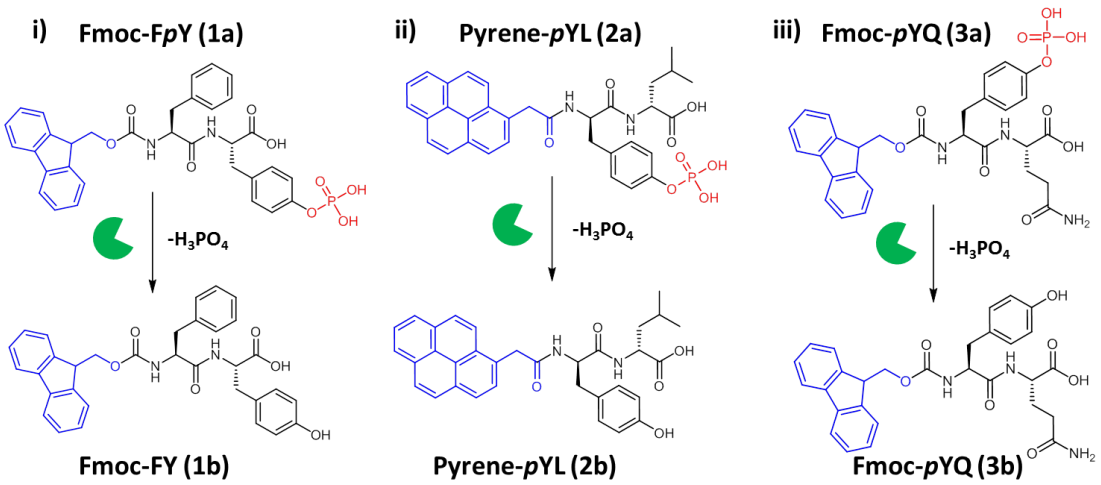

Figure 50 – Structure of aromatic dipeptide amphiphiles studied. (i) Fmoc-F*p*Y (**1a**) is dephosphorylated to Fmoc-FY (**1b**) by alkaline phosphatase. (ii) Pyrene-*p*YL (**2a**) going to pyrene-YL (**2b**) and (iii) Fmoc-*p*YQ (**3a**) going to Fmoc-YQ (**3b**) by the same biocatalytic dephosphorylation reaction. Aromatic groups shown in blue and phospho-containing tyrosine side chain shown in red.

Aromatic dipeptide amphiphiles are discussed in more detail in section 2.8, in summary they are generally short peptide sequences containing both hydrophobic and hydrophilic regions within one molecule. The inbuilt design of the molecule will determine the interactions occurring between molecules, which in turn govern the supramolecular self-assembled structures. A common method to add hydrophobicity to a dipeptide is to functionalise the N-terminus with an aromatic group such as Fmoc or pyrene.[197,202–205] Hydrophilicity can be incorporated within the amino acid sequence, by using charged amino acids such as arginine, lysine, glutamic acid and aspartic acid or phosphate containing groups such as phospho-tyrosine.

As mentioned previously (Section 2.8), aromatic dipeptide amphiphiles are capable of self-assembling into a variety of supramolecular structures. The driving force for self-assembly is thought to be due to a combination of π-stacking interactions between aromatic groups and hydrogen bonding between C=O and N-H groups on neighbouring dipeptide molecules.[172]

In **Figure 50** above, the aromatic dipeptide amphiphiles **1a**, **2a** and **3a** all contain hydrophilic phospho-tyrosine residues (red) and either fluorenyl or pyrene aromatic N-terminal groups (blue). By altering the amino acids within the dipeptide sequence, in this

case, phospho-tyrosine, phenylalanine, leucine or glutamine, the structures in each case will be expected to be different.

6.3. Structure of phosphorylated substrates (1a, 2a, 3a)

1a (Fmoc-F*p*Y-OH) has previously been reported to form micelles with a hydrodynamic radius of 5 nm, in aqueous conditions, above a critical micelle concentration of 5 mM.[207] **1a** molecules are expected to interact in such a way that the aromatic Fmoc groups form the hydrophobic core of micellar structures. The polar phosphate group on the side chain of tyrosine, in combination with the carboxyl C-terminus offers a charged hydrophilic 'head' region, on the surface of the micelle. Similarly, **2a** (pyrene-*p*YL-OH) is expected to form micellar supramolecular structures, as each molecule contains the aromatic pyrene group at the N-terminus and also contains a polar phospho-tyrosine residue. The structure of **3a** is so far unknown; however dynamic light scattering measurements presented in Appendix F, suggest defined structures with average hydrodynamic radius values of 70 nm.

6.4. Structure of dephosphorylated substrates (1b, 2b, 3b)

Addition of phosphatase to **1a**, **2a** and **3a** triggers the dephosphorylation reaction of phospho-tyrosine in each of the sequences, therefore removing the phosphate group and negative charge associated with it (see **Figure 50**). The resulting **1b** and **2b** are expected to then spontaneously self-assemble and extend into fibrous β-sheet structures, by aromatic π-stacking interactions and hydrogen bonding, as previously reported.[203,207] If extensive fibrous networks are achieved these are expected to 'trap' water molecules in a self-supporting hydrogel.

In the case of the dephosphorylated product **3b**, previous reports have shown spherical aggregates rather than networks of fibres.[208] Upon dephosphorylation of **3a** (Fmoc-*p*YQ-OH) by AP to **3b**, it is expected that spherical aggregates will form, as shown with previous studies with alkaline phosphatase[208] and another subtilisin responsive system *i.e.* the self-assembly of Fmoc-YQ-OH (from Fmoc-YQ-OMe).[210] The different morphology observed is

thought to be due to steric effects caused by the glutamine side chain, which prevents stacking into extended fibre structures.[210]

Each of the self-assembled systems were characterised individually using a number of techniques including: fluorescence spectroscopy to indicate changes in the environment of aromatic moieties; HPLC to monitor the enzymatic conversion to corresponding dephosphorylated products; and finally dynamic light scattering to determine size distribution of expected micellar or spherical structures.

6.5. Peptide amphiphile 1a (Fmoc-F*p*Y-OH)

The fluorescence emission spectra of 10mM **1a** being dephosphorylated by AP (0.2mg/mL, 4 U), shows the expected spectroscopic change in the aromatic fluorenyl environment when compared with previous studies[207] (see section 4.1 for further details on fluorescence spectroscopy techniques). Exciting **1a** at 295 nm reveals an emission maximum at 320 nm with a shoulder at 370 nm indicative of micelle structures (**Figure 51 (A)** overleaf - solid line). Upon addition of AP the shoulder at 370 nm diminishes indicating the disassembly of micelle structures. Further to this, the 320 nm fluorenyl peak experiences a red shift and a peak at 450 nm is observed, implying extended fibre formation and π-π interactions involved (**Figure 51 (A)** dashed line).[62]

DLS analysis of a solution of 10mM **1a** revealed structures with average hydrodynamic radius values of 5 nm, as previously reported (see Appendix E).[207] At the concentration measured for **1a** *i.e.* 10mM, this is above the critical micelle concentration of 5mM[207] therefore micelle-like structures are expected.

HPLC was then employed to monitor the enzymatic reaction, as the phosphorylated starting material will have a different retention time compared to the dephosphorylated product. The enzymatic dephosphorylation of **1a** to **1b** by AP monitored by HPLC showed a conversion of 58% after 24 hours (**Figure 51 (B)**). **Figure 51 (B) inset** shows the resulting self-supporting hydrogel of **1b** after 24 hours. This self-assembling system has previously been characterised in more detail, and results expressed here are in line with the previous study.[207]

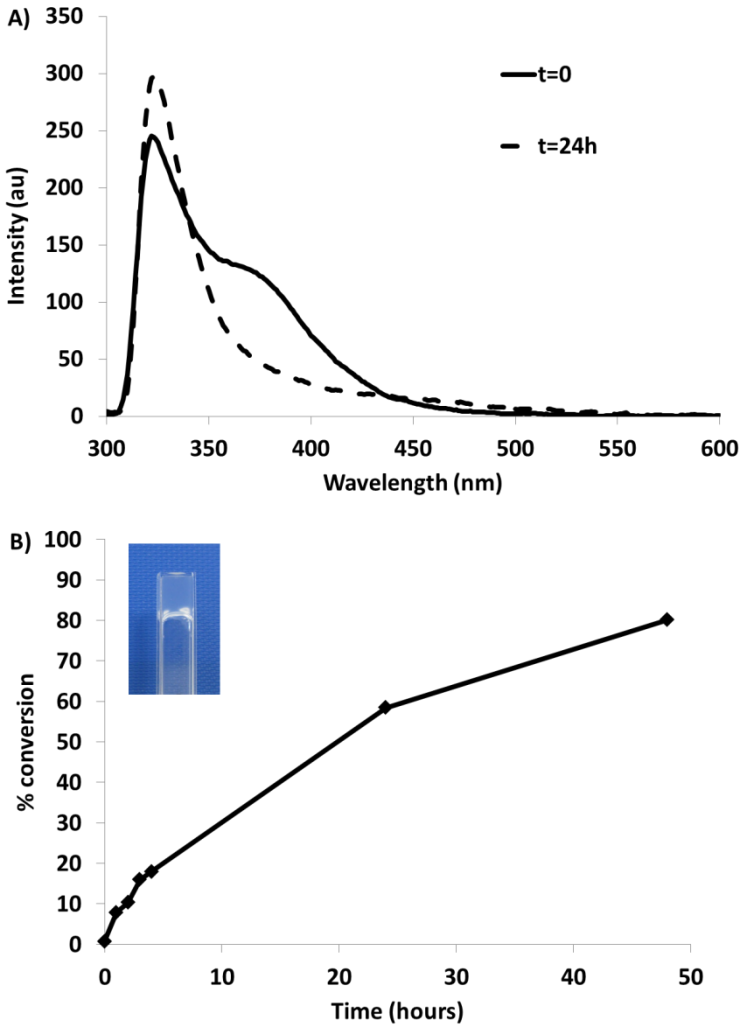

Figure 51 – (A) Fluorescence emission spectra of 10 mM **1a** at t=0 (no enzyme) solid line and t=24h (after addition of 4U AP) dashed line. (B) Percentage conversion of **1a** to **1b** by HPLC. Inset - image of Fmoc-FY gel after 24hours.

6.6. Peptide amphiphile 2a (pyrene-*p*YL-OH)

The fluorescence emission spectra of **2a** reflects the different pyrene aromatic functional group attached to the N-terminus of the dipeptide, compared to the previously discussed Fmoc functionalised system (**Figure 52 (A)** overleaf). Excitation at 334 nm results in a number of peaks in the visible region of the electromagnetic spectrum between 400-550 nm. The most intense peaks are centred at 400 and 470 nm (see section 4.1.2 for a detailed description). With the addition of 4 U AP to a solution of 5mM **2a**, an enhanced fluorescence signal at 400 nm is observed. The fluorescence spectra obtained resemble that of the recently published pyrene-functionalised YL dipeptide.[205]

A solution of 10mM **2a** was analysed by DLS and an average hydrodynamic radius value of 8 nm was determined (Appendix E).

Monitoring the phosphatase responsive dephosphorylation of **2a** to **2b** by HPLC, resulted in a conversion of 55% (t=24 hours) (**Figure 52 (B)**). **Figure 52 (C)** shows the starting solution of **2a** (left) and the resulting self-supporting hydrogel of **2b** after 24 hours (right). The top images show that pyrene fluoresces in the visible region, when excited at 365 nm.

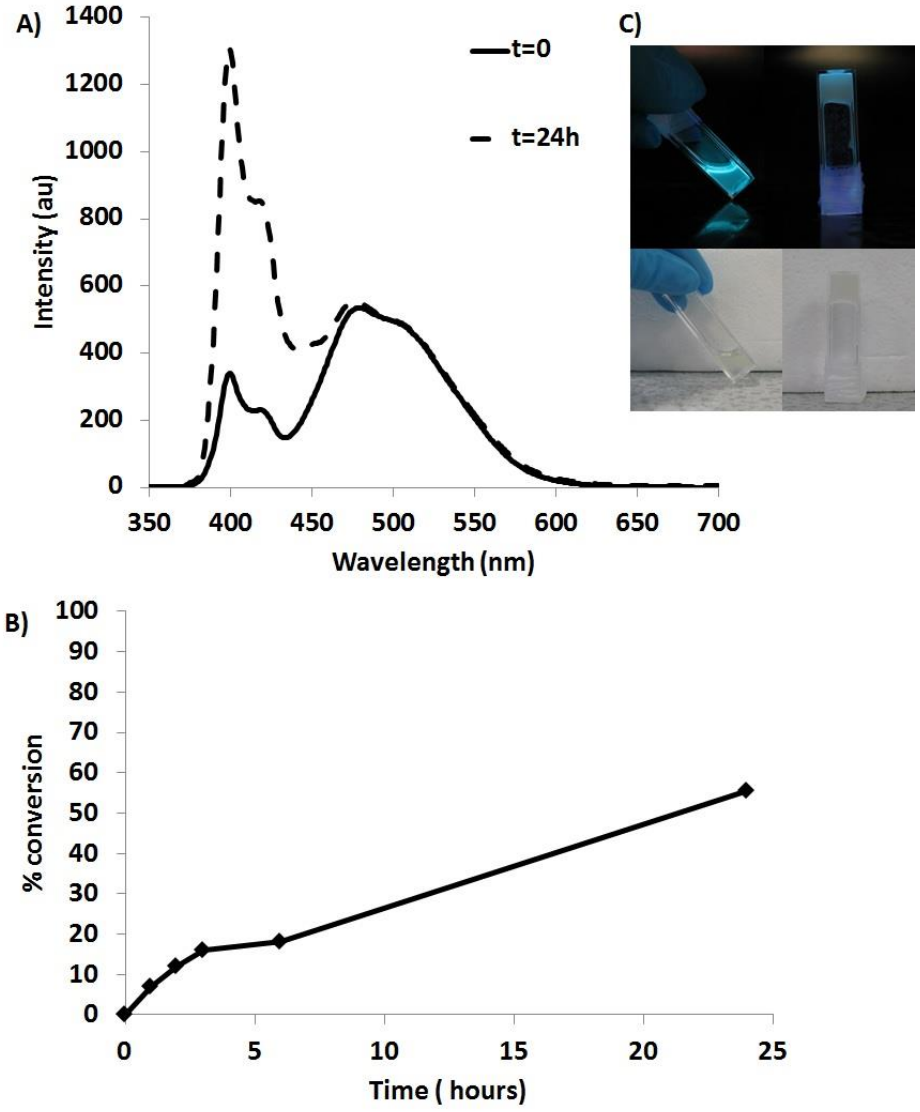

Figure 52 – (A) Fluorescence emission spectra of 5 mM **2a** t=0 (no enzyme) solid line, and t =24h (after addition of 4 U AP) dashed line. (B) Percentage conversion of **2a** to **2b** by HPLC. (C) Images of **2a** solutions (left) and **2b** gel t = 24 hours after addition of AP (right). Top images - samples excited at 365 nm.

6.7. Peptide amphiphile 3a (Fmoc-*p*YQ-OH)

Aromatic dipeptide derivative systems **1a** and **2a** undergo supramolecular transitions from micelle containing solutions to hydrogels composed of fibrous networks by biocatalytic dephosphorylation (see section 2.8.1). **3a** is expected to behave differently due to the hydrophilic nature of glutamine which remains unchanged after enzymatic dephosphorylation of **3a** to **3b**. Fluorescence spectroscopy reveals that the dephosphorylation reaction of **3a** to **3b** shows the opposite spectral response to that of **1a**/**1b**. The shoulder associated with micellar structures at 370 nm is apparent after the addition of AP (0.2mg/mL, 4 U) (**Figure 53 (A)**). The spectral profile of **3b** (t = 24 hours) appears similar to previous reports of the same system,[208] however in this case a red shift of the 320 nm peak was observed compared to the blue shift reported in recent studies.[208]

The Fmoc-*p*YQ-OH/AP system, as well as an analogous system: Fmoc-YQ-OMe/subtilisin[210] result in enzymatic conversion to Fmoc-YQ-OH, which is reported to form spherical aggregates by TEM.[208,210] It is therefore expected that the corresponding dephosphorylated product *i.e.* **3b** (Fmoc-YQ-OH) in this study will form similar spherical aggregates. Dynamic light scattering revealed structures with hydrodynamic radius values of approximately 70 and 34 nm for **3a** and the biocatalytic product **3b** respectively (Appendix F). These results differ from the values obtained for the subtilisin responsive self-assembling system, due to the different enzyme and buffer conditions used in this study.[210]

An HPLC conversion study of **3a** to **3b** shows after 24 hours (of AP addition) 99.9 % conversion was achieved (**Figure 53 (B)**), in line with previous reports.[208] For this system, visually the solution appears unchanged after AP addition and no hydrogelation is observed, as expected.[208] It can be seen in Appendix G that the initial conversion rates are faster for **3a** to **3b** compared to the **1a**/**1b** and **2a**/**2b** systems.

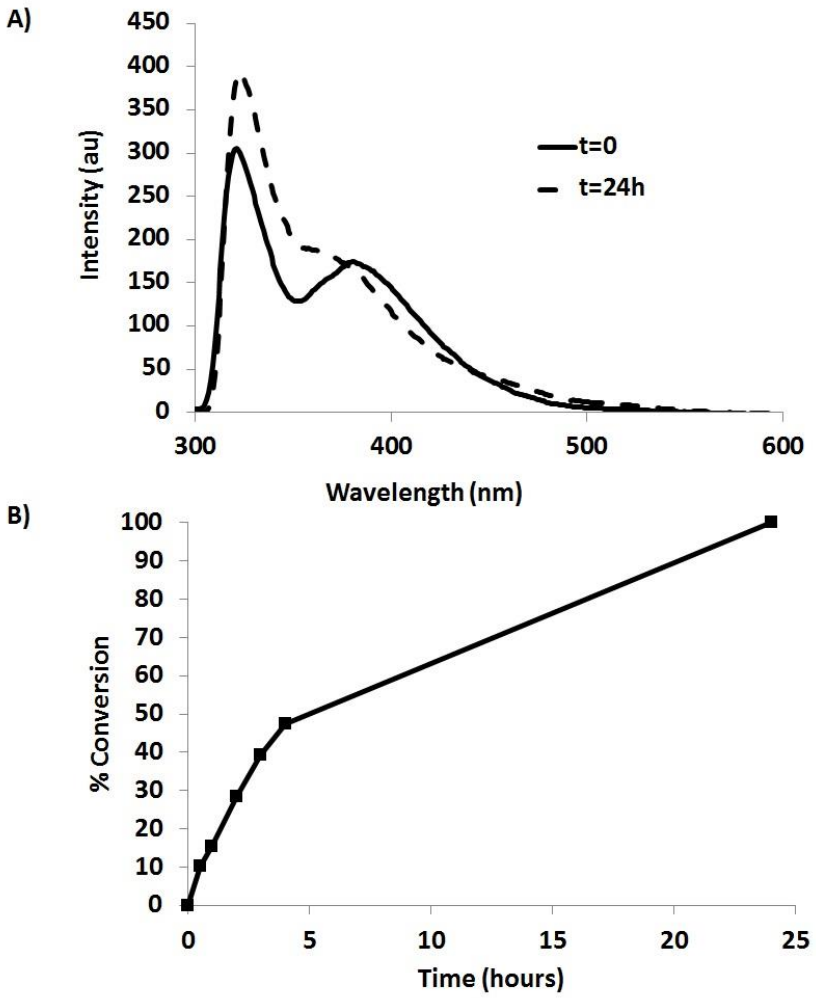

Figure 53 – (A) Fluorescence emission spectra of 10 mM **3a** t=0 (no enzyme) solid line, and t=24h (after addition of AP) dashed line. (B) Percentage conversion of **3a** to **3b** by HPLC.

6.8. Summary

In summary, characterisation by fluorescence spectroscopy, HPLC and DLS show that generally for **1a** and **2a** the dephosphorylation reaction by AP converts supramolecular micelle-like structures to fibrous networks, and above a critical gelation concentration hydrogelation of the bulk solution results. Fluorescence spectroscopy is used in this instance to monitor the environment of the aromatic moieties which enable supramolecular structures to be predicted. HPLC monitors the enzymatic reaction of phospho-starting material to the dephosphorylated product. The self-assembled structures expected to form for **1b** and **2b** are confirmed in section 2.8.

Biocatalytic self-assembly of aromatic peptide amphiphiles by QD-phosphatase conjugates – Part 2

6.9. Introduction

QD-alkaline phosphatase conjugates, prepared as in section 5.6, were investigated for their ability to catalyse the conversion of **1a**, **2a** and **3a** into the corresponding self-assembling species: **1b**, **2b** and **3b** respectively (**Figure 50**). The enzyme, attached to QDs, was confirmed to be active using a *p*-nitrophenyl phosphate activity assay (see section 5.8), however this does not directly determine whether QD-AP conjugates will successfully initiate the micelle-to-fibre or sphere-to-sphere transitions, of the above mentioned aromatic dipeptide amphiphiles. Each dipeptide system was studied individually, using fluorescence spectroscopy and HPLC to monitor the self-assembly and enzymatic conversion by QD-AP. Due to the concentration of enzyme in a given volume of QD-AP is estimated to be nano molar (nM), the conversion for each system is expected to be in line with a nM concentration of free enzyme. Therefore 0.37 nM (upper limit) free AP conversion studies were performed (for **1a** *i.e.* Fmoc-F*p*Y system only) for comparison with QD-AP (concentration determined by an activity assay calibration see section 3.3.16).

6.10. Peptide amphiphile 1a (Fmoc-F*p*Y-OH)

To test the ability of QD-AP to dephosphorylate **1a**, an HPLC time study was performed. 200 µL/mL QD-AP was added to 10 mM **1a** and HPLC samples were obtained at regular time points. No conversion to **1b** was detected up to 5 hours after addition of the conjugate, but after 24 hours, 48 hours and 1 week, percentage conversion values were 0.68, 1.08 and 2.58 % respectively. The solution does not transform into a hydrogel as seen with the free enzyme, due to the lower conversion rates. For the purposes of nanopropulsion, gelation is not desired and localised regions of self-assembly and fibre growth are expected. As a comparison, a conversion study of **1a** to **1b** was performed with free enzyme concentration equal to that estimated for the enzyme concentration in a given volume of QD-AP solution *i.e.* 0.37 nM (see section 5.9) and compared with QD-AP. After the addition of 0.37 nM free AP to 10 mM **1a**, no detectable conversion was observed up to 1 week, but at 2 and 4 week time points, values of 0.93 and 1.04 % conversion to **1b** were recorded by HPLC. These

values were comparable to the same time study performed with ~30 µL/mL QD-AP (volume per mL estimated to have an upper AP concentration of 0.37 nM), where at 2 and 4 week time points, the conversion to **1b** was 0.93 and 1.18 % (compared to no conversion for the negative control with no AP – see Appendix H).

Fluorescence spectroscopy was used to analyse the aromatic interactions occurring between the aromatic dipeptide amphiphile molecules and also to monitor the fluorescence characteristics of the QD-AP conjugates during the reaction. Exciting at 295 nm, the resulting fluorescence emission spectra for **1a** (**Figure 54**) shows the typical 320 nm peak for Fmoc and a shoulder at 370 nm, suggesting micellar structures are present, before addition of QD-AP. Upon addition of QD-AP, the ratio of 320:370 nm peaks increases over time, as the shoulder diminishes slightly. The changes in fluorescence intensity of the fluorenyl groups are subtle and are not easily detected using spectroscopic methods (negative control spectra can be found in Appendix H). The fluorescence signal is dominated by the unconverted material as the QD-AP conversion product yield is low. Therefore it can be concluded that fluorescence spectroscopy is better suited to samples with faster conversion rates and which self-assemble in bulk.

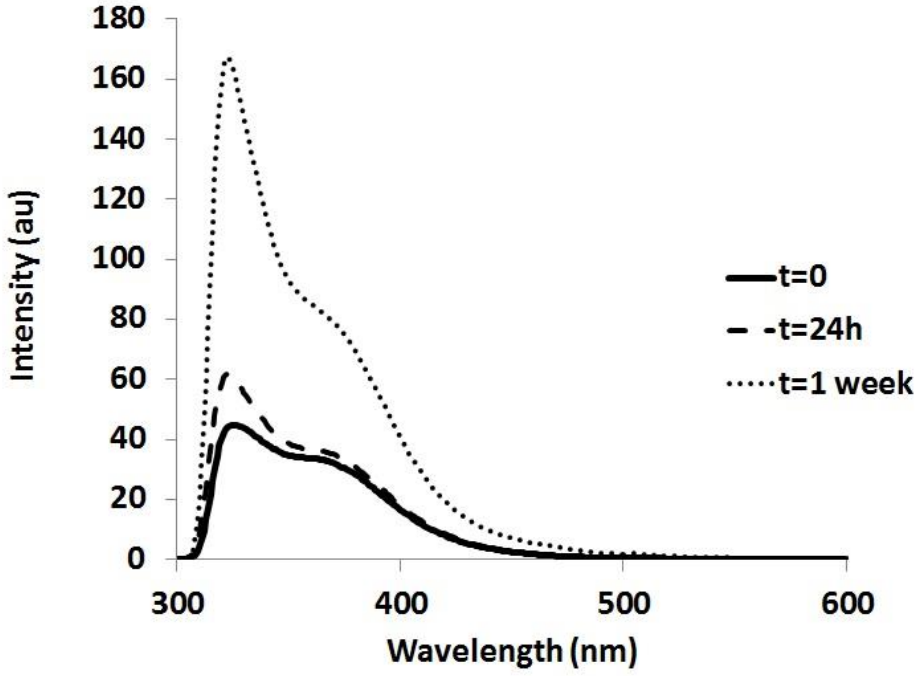

Figure 54 - Fluorescence emission spectra of 10 mM **1a** in the presence of QD-AP, at t=0 (before QD-AP addition); t=24hours (dashed line) and t=1 week (dotted line).

6.10.1. QD-AP fluorescence quenching study

Fluorescence spectroscopy can however, reveal information on the stability of the QD-AP fluorescence as the enzymatic reaction with **1a** proceeds. Exciting at 435 nm, QD-AP fluorescence emission spectra were obtained at regular time points, where t=0 marks the addition of QD-AP. The λ_{max} of the QD-AP fluorescence is reported to be at 655nm, however, over 4 hours a blue shift from 646 nm to 643 nm is observed. The intensity of the QD-AP peak increases initially for the first 5 hours studied but after 24 hours the fluorescence has completely quenched (**Figure 55**). Other possible explanations for the reduction in fluorescence signal at longer times, could be due to settling, however for a typical 1 hour tracking experiment this effect would be minimal.

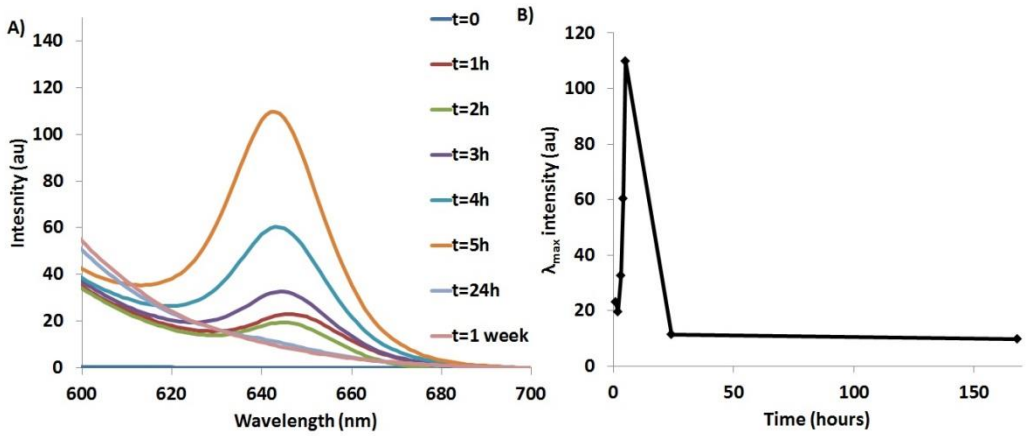

Figure 55 – (A) Fluorescence emission spectra of QD-AP in the presence of 10 mM **1a**. There is a shift in the λ_{max} from 646 nm to 643 nm within 4 hours. (B) Corresponding λ_{max} versus time plot, which shows an initial increase in fluorescence of QD-AP, followed by quenching after 24 hours.

To investigate the fluorescence quenching further, unconjugated QDs (8 nM) and AP were added separately to a 10 mM solution of **1a**, to identify if the fibre formation affects the fluorescence signal of unconjugated QDs (see **Figure 56** overleaf). The λ_{max} of QDs again experiences a blue shift from 649 nm at t=0, to 645 nm after 5 hours. After 24 hours the signal for QDs almost completely quenches and shifts to 631 nm, concluding that free QDs are also quenched when the same enzymatic reaction is occurring.

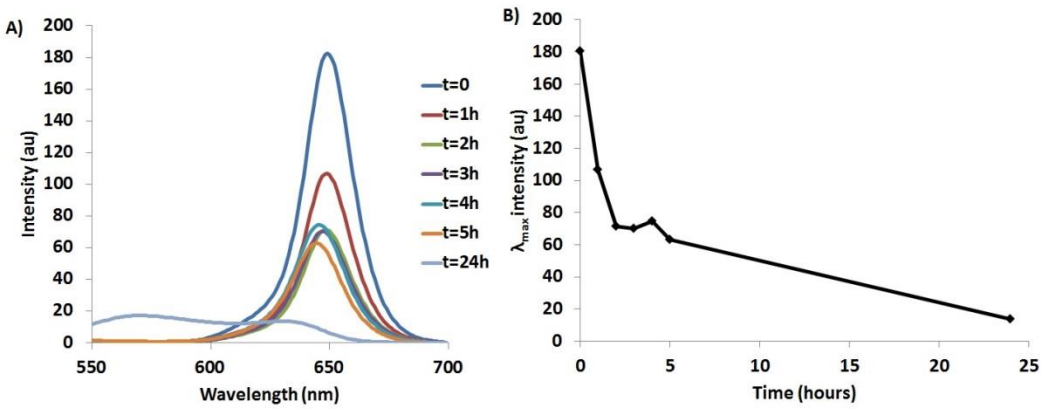

Figure 56 – (A) Fluorescence emission spectra of QDs in the presence of 10 mM **1a** and AP. A blue shift is observed in the $\lambda_{max.}$ (B) Corresponding λ_{max} versus time plot, which shows quenching of QD fluorescence with time.

A previous report, suggests that CdS quantum dots will attach to Fmoc-FF-OH self-assembled fibres producing a red shift in the fluorescence emission of the QDs however no quenching is observed. In the presence of the enzymes glucose oxidase and horseradish peroxidase to the QD/fibre network system, quenching of QDs was attributed to the products of the enzymatic reactions *i.e.* glucose and phenol/hydroquinone respectively.[316] Phenol and hydroquinone groups are thought to act as electron acceptors from QDs, which is turn quenches the QD fluorescence. In this study AP removes the phosphate group of the tyrosine side chain of **1a**, resulting in phenolic tyrosine. The fluorescence quenching of the QDs experienced experimentally for this system, may be as a result of the combination of attachment to fibres and the phenolic functionality of **1b**, (however the conversion to **1b** has been shown previously to be very low compared to free enzyme).

To investigate the apparent phenolic quenching of free QDs, further studies were undertaken. QDs were added to solutions containing potassium phosphate buffer as a negative control; 10 mM **1a** in buffer and a solution containing 4U AP also in buffer. The fluorescence intensity for each scenario shows a 60.2, 29.8 and 8.8% decrease after 24 hours, from the starting intensity value for QD in buffer, 10mM **1a** and AP respectively (**Figure 56**). Quenching of QD fluorescence has been observed by a number of groups and is thought to be due to an electron transfer process, where electrons are transferred from QDs to an electron accepting quencher.[316] Studies have suggested a link between phenol containing substances (as mentioned previously) but also certain amino acids such as asparagine and tryptophan.[316,317]

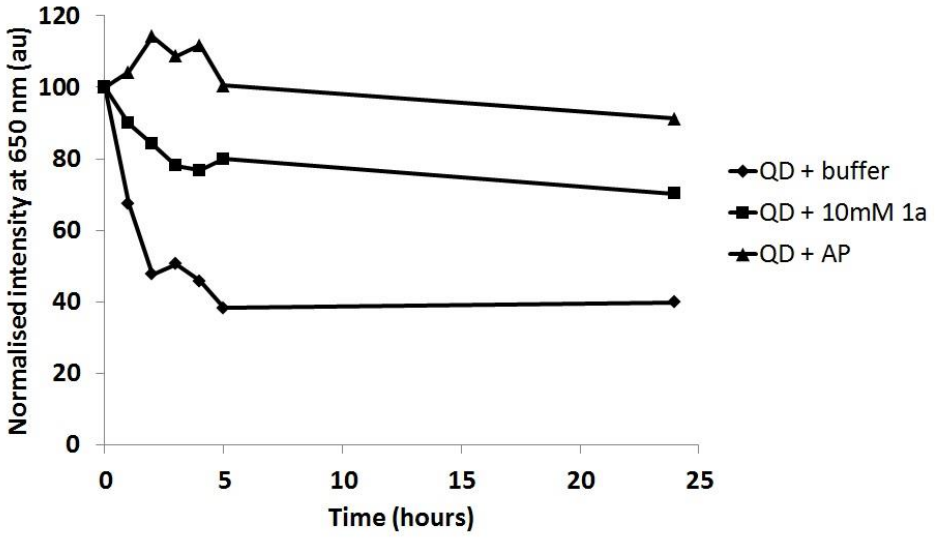

Figure 57 - QD fluorescence intensity over time, in the presence of buffer, 10mM **1a** in buffer and 4 U AP in buffer. Quenching of QD fluorescence emission is observed in all cases, but more so with QDs in buffer.

Another possible source of quenching is the presence of **1b** (*i.e.* converted enzymatically from **1a**). To investigate this, the fluorescence emission intensity of a solution of QDs was monitored over time, exposed to different concentrations of chemically made **1b** (Appendix I). Generally, all samples showed some degree of quenching with time, except 10mM **1b**. Overall the results were erratic, which could be attributed to the low solubility of **1b** in water.

Although quenching is observed in all cases, the extent of quenching has been unpredictable and difficult to draw any conclusions or trends. It can however be concluded that quenching occurs over a time frame of hours, which for nanopropulsion tracking experiments (typically 1 hour) quenching would be minimal and would not affect the ability to track a conjugate within a short period of time. As long as there is sufficient QD-AP fluorescence intensity during the tracking 'window' of one hour, the actual QD-AP intensity value is not important for this study.

6.11. Peptide amphiphile 2a (pyrene-*p*YL-OH)

Fluorescence emission spectra of 5 mM **2a** are shown in **Figure 58** overleaf. Upon the addition of QD-AP the pyrene spectral changes are subtle. However, after 24 hours an enhanced fluorescence signal is observed for peaks in both the 400 and 470 nm regions. As

the dephosphorylation reaction proceeds using QD-AP, the fluorescence emission spectra are expected to follow the trend of the same reaction undertaken by free AP but over a longer time, reflecting the lower (nM) AP concentration available in the conjugate solution.

A fluorescence signal for the QD-AP conjugate can also be simultaneously detected at longer wavelengths, around 650 nm (see arrow in **Figure 58**). It can be seen however that the intensity of QD-AP is considerably lower in comparison to that of a 5mM solution of **2a** (**Figure 58**), leading to difficulties for future tracking experiments (see section 8.6).

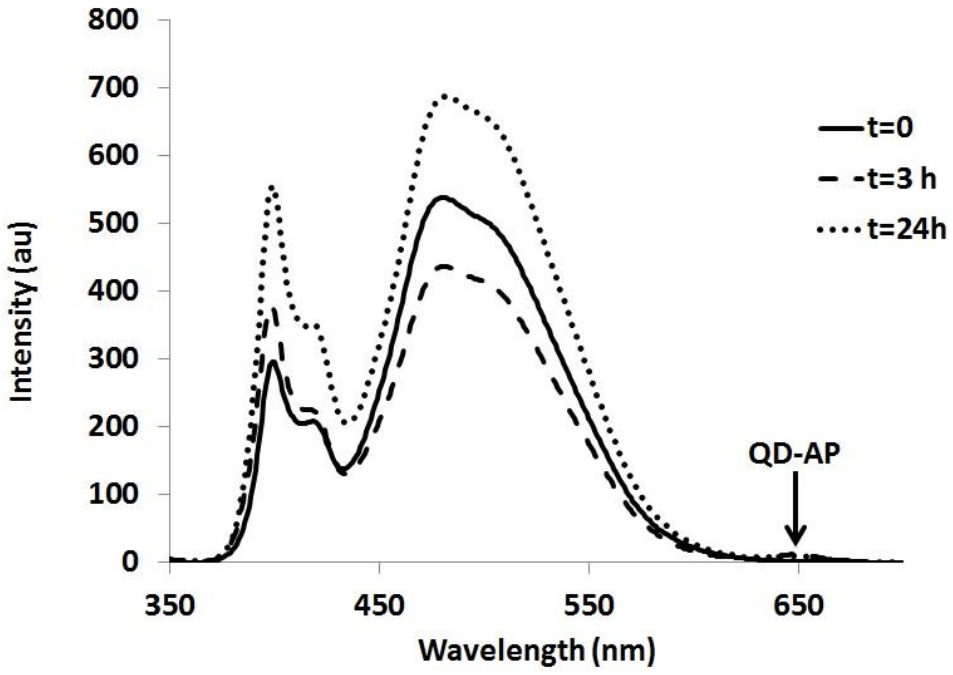

Figure 58 - Fluorescence spectra of 5 mM **2a** before addition of QD-AP (t=0), then 3 and 24 hours after addition.

Biocatalytic conversion of 5mM **2a** to **2b** using QD-AP was determined using HPLC. Conversion to the product (**2b**) can be seen after 2 hours of QD-AP addition and after 24 hours the percentage conversion reaches 3.6, with higher conversion rates compared to **1a** and **3a** reflecting the lower substrate concentration compared to enzyme concentration (see **Table 7** for full time study values). The solution was not expected to form into a self-supporting hydrogel, however visual observations revealed non-uniform opaque regions within the solution after a number of hours, which could signify localised aggregates of fibres.

Table 7 – Percentage conversion of **2a** to **2b** by biocatalytic dephosphorylation using QD-AP.

Time (hours)	Conversion (%)
0	0
1	0
2	1.9
3	1.4
6	2.0
24	3.6

6.12. Peptide amphiphile 3a (Fmoc-*p*YQ-OH)

QD-AP was investigated for the ability to convert **3a** to **3b** by dephosphorylation and initiate self-assembly into spherical aggregates, as shown in previous studies.[208] Fluorescence emission spectra (**Figure 60**) of 10mM **3a** before addition of QD-AP (t=0) and 1 week after addition, shows a similar, yet smaller red shift in the 320 nm peak (compared to a high concentration of free AP *i.e.* 0.2 mg/mL, 4 U – see **Figure 53 (A)**). The peak at around 370 nm changes shape and the intensity diminishes compared to the zero time point. HPLC analysis shows ~1% conversion to **3b**, 24 hours after the addition of QD-AP to 10mM **3a**, confirming the ability of QD-AP to dephosphorylate **3a** with conversion values in line with other dipeptide substrates studied.

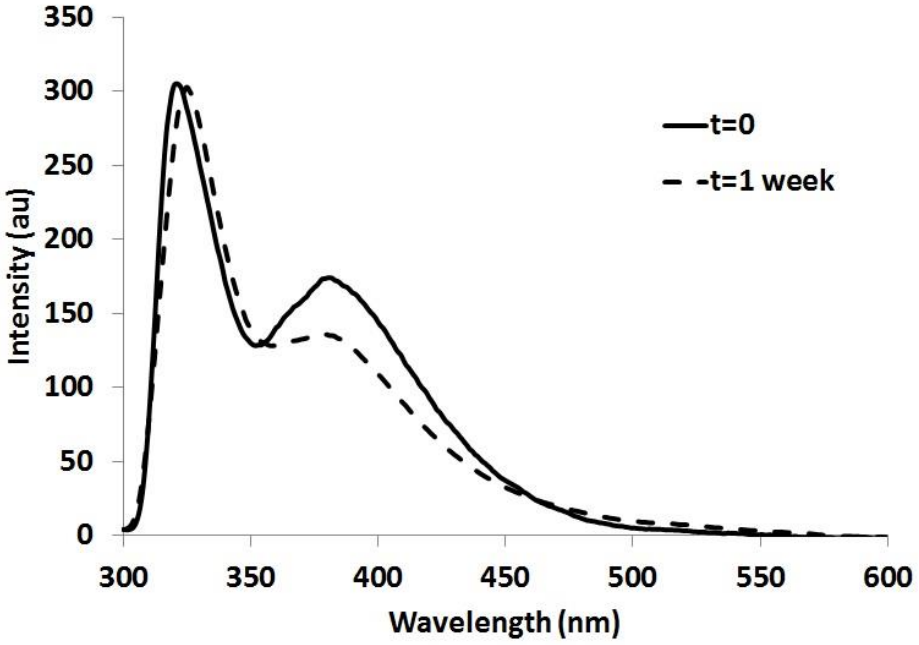

Figure 59 - Fluorescence emission spectra of 10mM **3a** before QD-AP and 1 week after the addition of QD-AP.

6.13. Summary

The biocatalytic conversion and supramolecular self-assembly of aromatic dipeptide amphiphiles were confirmed using free enzyme (AP) and AP conjugated to QDs. Systems were analysed through spectroscopic and chromatographic techniques (see chapter 8 for microscopic evidence of fibre growth). Dephosphorylation and subsequent self-assembly of substrates by QD-AP conjugates proved to have lower conversion rates, in line with a low enzyme concentration ($7x10^{-4}$ U). This finding enables future tracking without hindering QD-AP diffusion, an effect which may be observed if bulk sample gelation occurred, seen with higher free AP concentration (4 U).

Fluorescence quenching of QD-AP conjugates was observed in the presence of **1a**. Studies to underpin the source of quenching proved inconclusive due to fluctuations in fluorescence emission intensity. Complete quenching was generally only observed after a number of hours, therefore for future tracking of QD-AP this effect should be taken into account *i.e.* by only measuring fresh QD-AP samples within a certain time frame *e.g.* 1 hour.

Through studying self-assembly systems such as micelle-to-fibre and sphere-to-sphere transformations, three potential self-assembling 'fuels' for QD-AP propulsion have been

identified: (i) fibre-assembling substrates **1a** and **2a**, (ii) sphere assembling substrate **3a** (and from previous activity assay studies a non-self-assembling substrate (*p*-nitrophenyl phosphate, **4a**).

– Chapter 7 –

Nanopropulsion by biocatalytic self-assembly

7.1. Objectives

The main aim of the project was to induce nanopropulsion by biocatalytic self-assembly therefore this chapter describes tracking analysis of QD-AP conjugates exposed to two fibre-assembling fuels (**1a** and **2a**), a sphere-assembling substrate (**3a**) and non-self-assembling substrate (**4a**). By comparing speed and diffusion coefficient data obtained for each case a comparison can be made between unidirectional self-assembly and non-directional self-assembly (fibres and spheres respectively). Further to this, an additional objective was to develop a means of directional control using a fuel concentration gradient.

7.2. Introduction

Propulsion of the enzyme alkaline phosphatase from *E. coli* is investigated, using biocatalytically induced self-assembly of aromatic peptide amphiphiles Fmoc-F*p*Y$^{206–208}$ (**1a**) and pyrene-*p*YL^{195} (**2a**) – see **Figure 60** overleaf. The amphiphilic nature of both **1a** and **2a** means the phosphorylated molecules exist as spherical micelle structures in water (as mentioned in 6.3). Enzymatic removal of the charged tyrosine phosphate group by alkaline phosphatase leads to the dephosphorylated products **1b** and **2b** respectively (**Figure 60 (C) (i)** and **(ii)**). Phosphate removal results in aromatic and hydrogen bonding interactions inducing the self-assembly of **1b** and **2b** into β-sheet fibre structures. By following the motion of enzymes as they catalyse the conversion of micellar amphiphile structures into fibres, biocatalytic conversion is explored for the capability to propel the enzyme at a rate greater than normal diffusion.

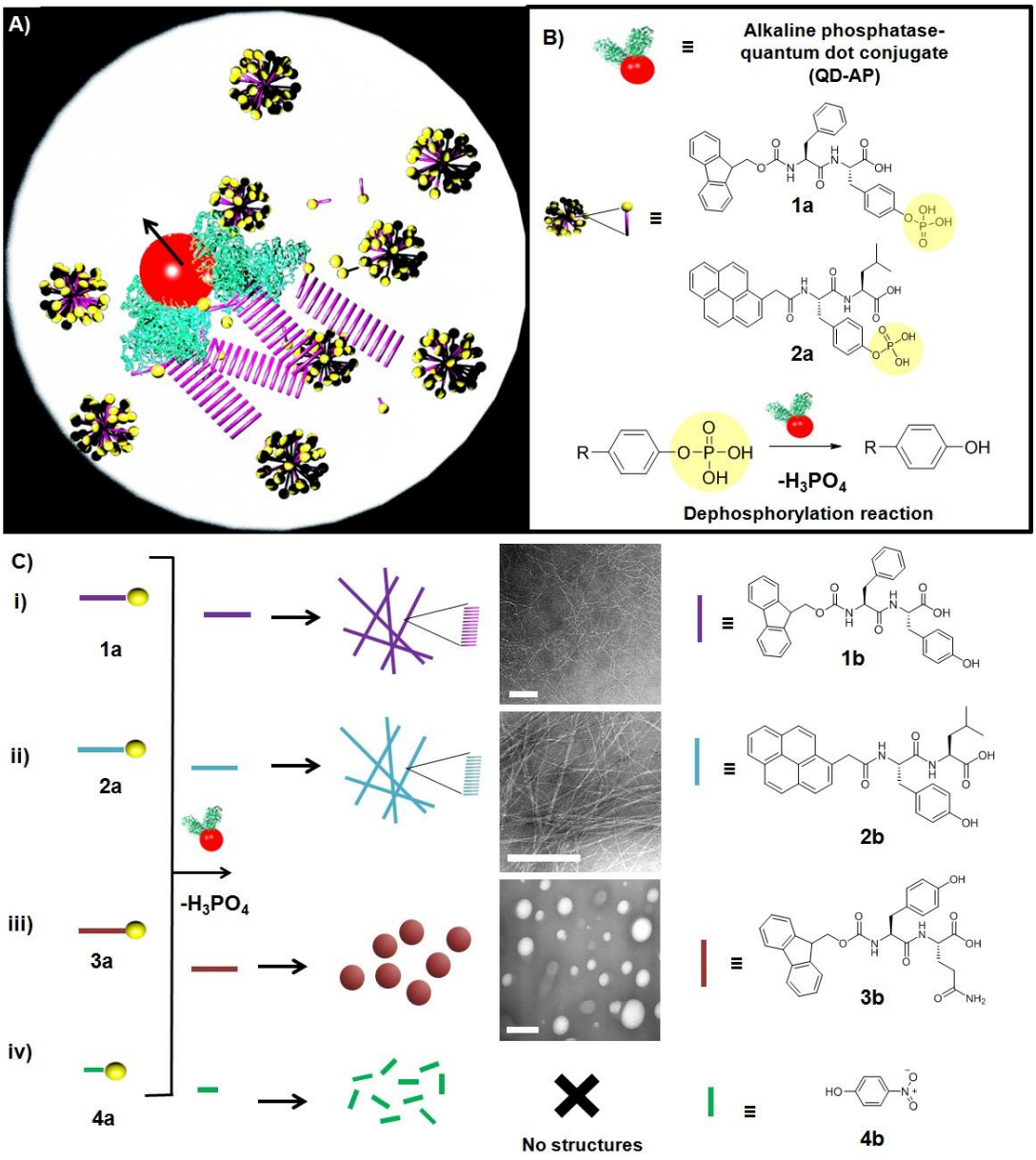

Figure 60 – (A) Scheme illustrating an alkaline phosphatase-quantum dot conjugate propelled by the biocatalytic transformation of micellar fuel molecules of **1a**/**2a** into fibre structures of **1b**/**2b** (scheme not to scale). (B) Key illustrating alkaline phosphatase-QD conjugates and micellar fuel molecules of Fmoc-F*p*Y (**1a**) and pyrene-*p*YL (**2a**), including a general biocatalytic dephosphorylation reaction for all substrates. (C) (i) fibre assembling substrate **1a**; (ii)fibre assembling substrate **2a**; (iii) sphere assembling substrate **3a**, and (iv) non-self-assembling control fuel **4a**, converted by QD-AP to **1b**, **2b**, **3b** and **4b** respectively. TEM images of resulting self-assembled structures *i.e.* fibres and spheres, obtained using free AP (scale bars = 200 nm). *Images of **1b** and **3b** obtained by Meghan Hughes.

The role of biocatalytic self-assembly is explored for propulsion by comparison with no fuel as well as a non-self-assembling molecule, *p*-nitrophenyl phosphate (**4a**) (**Figure 60 (C) (iv)**), a well-known substrate for alkaline phosphatase.[318] Further to this, a non-directional self-

assembling control is investigated: Fmoc-*p*YQ (**3a**) (**Figure 60 (C) (iii)**), which upon dephosphorylation by phosphatase is expected to self-assemble into spherical structures[210] (rather than linear fibres). All fuel systems contain molecules that will be dephosphorylated by phosphatase; however the hypothesis is that only the fibre self-assembling substrates **1a** and **2a** will induce propulsion, as the biocatalytic products (**1b** and **2b**) self-assemble into linear fibres, providing a directional 'impulse' to the motor.

7.3. Enzyme-conjugate tracking analysis

Fluorescence microscopy was used to visualise solutions containing QD-AP conjugates (as described in section 4.3). In order to see and track single particles, an EMCCD camera fitted with a 650/60nm optical filter was employed. QD-AP conjugates were added to a solution of the substrate within a glass bottom dish (see **Figure 30 (C)**). Tracking videos obtained of enzyme-conjugates are composed of a sequence of individual images or 'frames'. As discussed in section 4.3.4, each particle coordinate is determined and the distances travelled by particles between neighbouring frames are analysed by an in-house modified MATLAB program. Data is obtained for individual particles including trajectories, frame-to-frame speed, mean square displacement and angle of trajectory, for the fibre self-assembling fuels (**1a** and **2a**), the sphere-self-assembling control (**3a**), the non-self-assembling substrate (**4a**), and a control with no fuel, which measures free diffusion of the QD-AP conjugate for comparison.

Because transport at the nanoscale is a statistical process where thermal fluctuations are important, it is necessary to obtain a large amount of data for comparing each scenario. We perform a number of experiments (repeats) for each substrate, each experiment consisting of multiple videos. Obtaining adequate data is important as each batch of enzyme-QD conjugates will contain a range of sizes and diffusive motion is inherently a 'random' process. Each video recorded was either 300 or 600 frames in length at a rate of typically 23 frames per second; since particles move in and out of the plane of focus, individual tracks can be of varying length during the video. The number of particles tracked in each video varied from 5 to 200, and each experiment was repeated up to 4 times, with similar data obtained in each repeat. The frame-to-frame speed data for all frames was combined and an overall distribution of speeds and average overall value was obtained. The number of particles tracked is thus a combination of repeated experiments, and the nature of the

experiment allows for specific particles to be counted multiple times as new particles if they leave the focal plane then return at a later time point.

7.3.1. Comparison with free QDs – speed distribution

QD-AP conjugates were tracked (with no fuel present) and frame-to-frame speed distribution data was compared with a solution of free QDs (see **Figure 61**). Due to differing amounts of data obtained in each case, the frequency of particles travelling at each speed is normalised by dividing each data point with the total number of data points. It is clear in **Figure 61**, that free QDs exhibit overall faster particles compared to larger sized conjugates (see DLS size distribution plot in **Figure 43**), as expected. Overall, the average frame-to-frame speed of QDs was found to be 7.2 µm/s (based on 243 particles and 3437 data points), compared to 5.6 µm/s average speed (based on 1075 particles and 17239 data points) for QD-AP conjugate clusters. It is also worth noting that the larger size of conjugate clusters (compared to free QDs) allows for easier visualisation and tracking, which subsequently leads to more data *i.e.* a higher QD:AP ratio as estimated to be 2.8:1.0 and 13.0:1.0 for QD-AP batches 3 and 6, respectively.

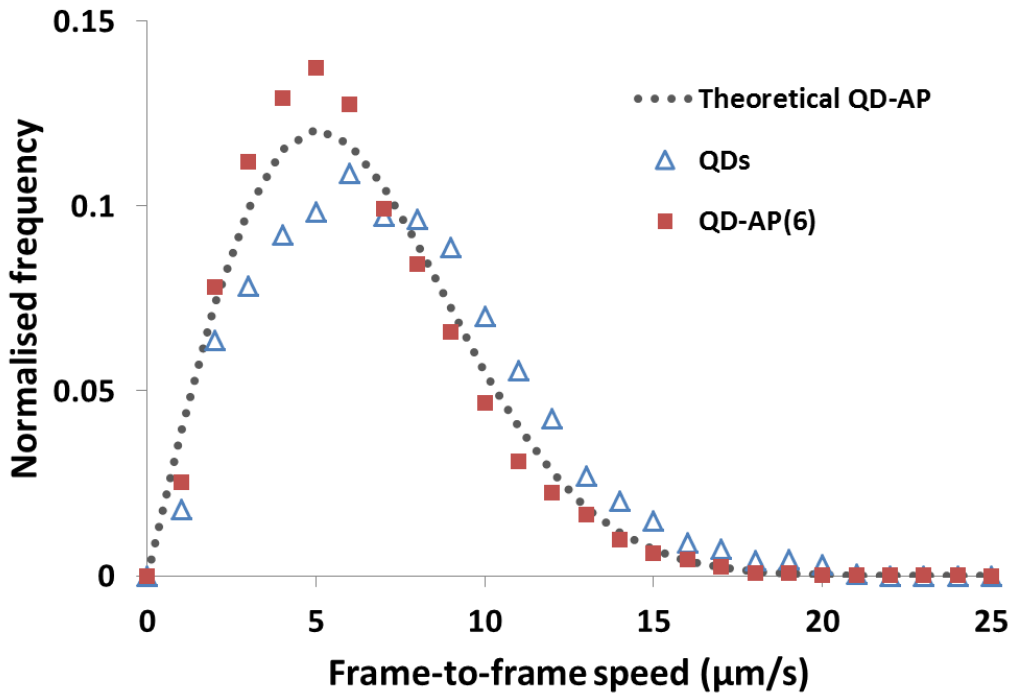

Figure 61 - Frame-to-frame speed distribution data for free QDs and QD-AP (batch 6), excited at 365 nm. Dotted line represents the theoretical distribution of speeds for a particle with an average hydrodynamic radius of 17 nm (as found experimentally for QD-AP by DLS – see **Figure 43**.

The experimentally determined plot for QD-AP conjugate clusters of varying sizes as shown by DLS in **Figure 43**, is compared to a theoretical probability plot calculated using the average hydrodynamic radius of QD-AP conjugates experimentally determined by DLS (17 nm). A diffusion coefficient was determined using the experimentally determined hydrodynamic radius of QD-AP and the Stokes-Einstein equation 1 (see section 1.1):

$$\boldsymbol{D = \frac{k_B T}{6\pi\eta R_H} = \frac{1.38 \times 10^{-23} \times 295.15}{6\pi \times 1.002 \times 10^{-3} \times 1.7 \times 10^{-8}} = 12.7\ \mu m^2/s}$$

The value for diffusion coefficient, *D* (12.7 $\mu m^2/s$), for QD-AP conjugates with a hydrodynamic radius of 17 nm, was used in the following equation with different values of speed (*v*) corresponding to those found experimentally in **Figure 61**:

$$\boldsymbol{P = k.v.\exp(-\frac{v^2}{4D})} \qquad \text{Equation 8}$$

Where *P* is the probability, *k* is a normalising factor, *v* is the speed and *D* is the diffusion coefficient of conjugates with a hydrodynamic radius of 17 nm, calculated as above. The original solution of this 'random walk' diffusion problem was given by Lord Rayleigh in 1880 and is discussed in letters to the journal Nature in 1905.[319,320]

It can be seen in **Figure 61** that the experimental data obtained is in relatively good agreement and fits the calculated plot (dotted line), for a fixed size (of 17 nm hydrodynamic radius), whereas the experimentally found data represents conjugates with a range of sizes.

7.3.2. QD-AP excitation wavelength comparison

The excitation wavelengths chosen for this study were 365 and 435 nm; however a compromise must be made between more efficient excitation of QDs at lower wavelengths and background fluorescence/scattering issues due to the fluorescent nature of the self-assembling fuels in the UV range. **Figure 62** overleaf illustrates the frame-to-frame speed distribution data for the same sample of QD-AP conjugates, excited at 365 nm and 435 nm.

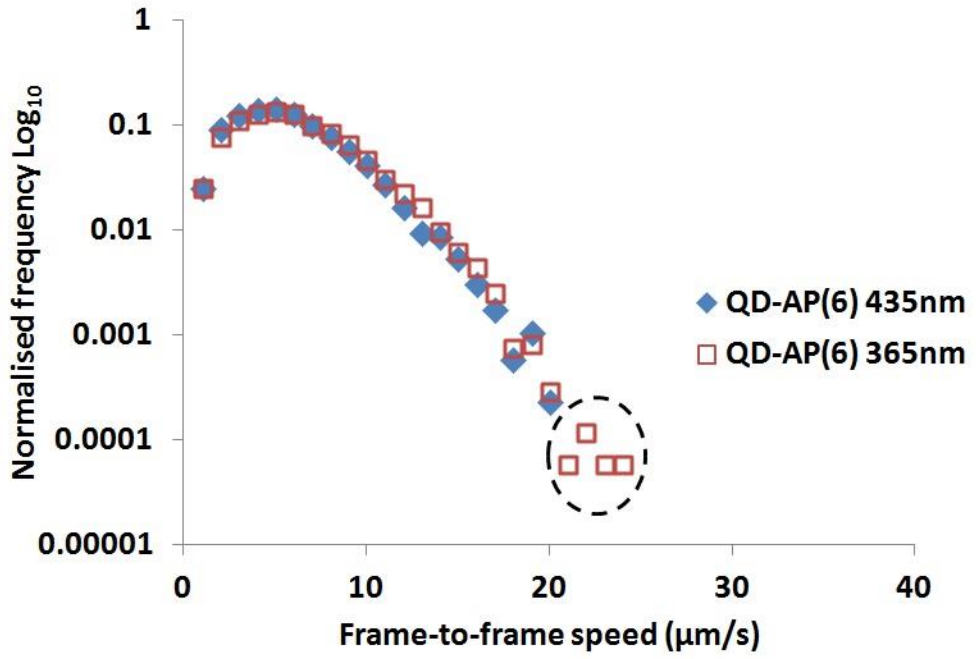

Figure 62 - Frame-to-frame speed distribution of QD-AP conjugates (batch 6) illuminated by 435 nm and 365 nm wavelengths of light.

The frame-to-frame speed distributions, obtained with each wavelength, are similar, however at the lower excitation wavelength (365 nm) we detect a population of conjugates exhibiting higher speeds (see highlighted data points in **Figure 62**). The more effective excitation of conjugates at lower wavelengths (*i.e.* 365 nm) means smaller (and faster) conjugates are more easily detected and tracked. In terms of data obtained with each illumination wavelength, the same sample resulted in different amounts of data obtained *i.e.* for 435 nm illumination 357 particles were detected for a total of 8634 data points, whereas at 365 nm excitation, as many as 1075 particles were tracked (total of 17239 data points). The resulting number of particles tracked is related to how efficiently the conjugates are excited; therefore it is important that the wavelength of illumination is taken into account when comparing results. It is worth noting in **Figure 62** that apart from the small number of faster particles detected with 365 nm illumination, the speed distribution at lower speeds is unaffected by the wavelength used.

7.3.3. Batch variation

A number of batches of QD-AP conjugates were used to accumulate all of the data for this investigation. Batch variations exist due to day-to-day environmental conditions at the time of carrying out the conjugation reaction (see section 5.10 for batch comparison). Individual

experiments are time consuming *i.e.* 3-5 days for a motility assay to final data analysis, and so it is not always possible to measure conjugates under exactly the same conditions. Control data was obtained using all batches and these are compared. The speed distribution data obtained for different batches of QD-AP conjugates (both excited at 435 nm) are compared in **Figure 63**. Batch variation is evident as shown in section 5.10; however this variation can be accounted for, when comparing data for the different substrates, by always comparing results using the same batch.

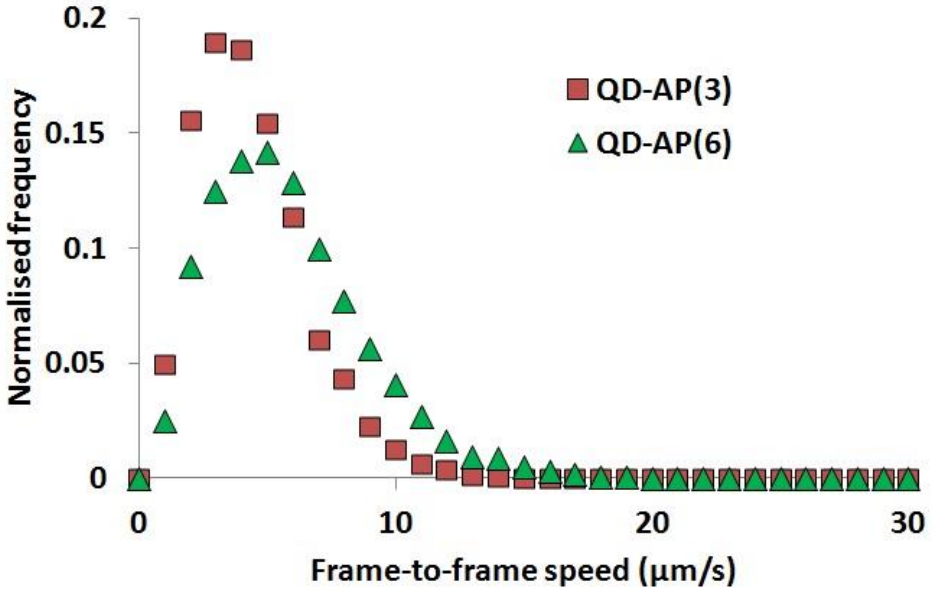

Figure 63 - Speed distribution comparison: batches 3 and 6 of QD-AP conjugates (no fuel), excited at 435 nm.

7.4. Nanopropulsion with fibre-assembling peptide amphiphile (1a)

For this investigation it was originally expected that fibre-assembling substrates **1a** and **2a** would be studied in parallel for their ability to propel the enzyme-QD conjugate. However for reasons explained in section 7.5, the effect of substrates **1a** and **2a** on enzyme-conjugate motion will be discussed separately, firstly comparing fibre-assembling **1a** with controls (no fuel, sphere assembling (**3a**) and non-assembling (**4a**)), followed by a further discussion of the second fibre-assembling fuel (**2a**) (section 7.5).

Example trajectories of tracked conjugates with fibre-assembling substrate **1a**, sphere-assembling (**3a**) and non-self-assembling substrate **4a** are compared along with trajectories with no substrate (**Figure 64**).

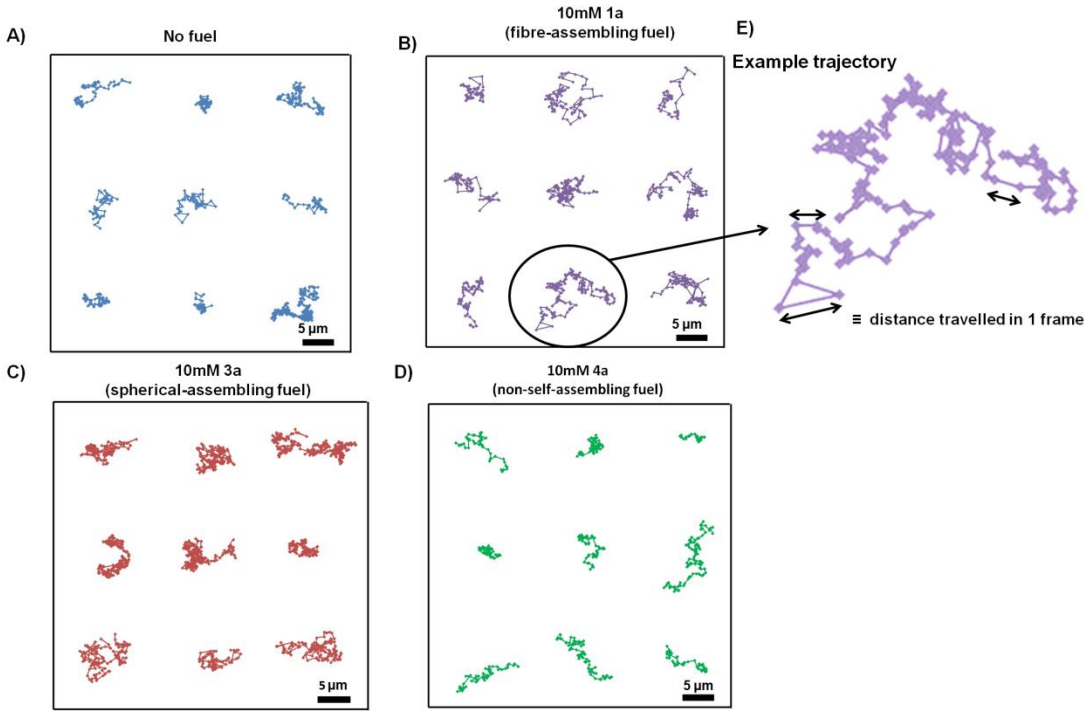

Figure 64 –Composite of example trajectories for (A) QD-AP with no fuel, (B) in the presence of fibre-assembling fuel **1a**, (C) sphere-assembling substrate **3a** and (D) non-self-assembling fuel **4a**. (E) Example trajectory of a single QD-AP conjugate 'fuelled' by 10mM **1a**. Each connected pair of data points represents the distance travelled between subsequent frames. This data is then used to calculate the frame-to-frame speed.

Clearly motion remains diffusive on the length-scale (microns) and time-scale (seconds) observed here as micellar substrate fuel molecules (**1a**) will be encountered at random by the QD-AP conjugates and bursts of motion driven by fibre assembly will be in random directions. However, in the presence of 10 mM fibre-assembling fuel **1a**, QD-AP conjugates exhibit clearly enhanced rate of diffusion (as shown in **Table 8**): with an average frame-to-frame speed of 5.7µm/s (based on 7007 particle trajectories and 4 experiments), compared to the no-fuel control with an average speed of 4.4µm/s (719 particle trajectories and 3 experiments) *i.e.* an enhancement of average frame-to-frame speed of 29%. Additionally the non-self-assembling fuel **4a** has nearly no effect on the speed of the conjugates compared to the no-fuel control (average frame-to-frame speed of 4.0 µm/s for 1139

particles and 2 experiments). Interestingly, conjugates in the presence of the sphere-self-assembling fuel **3a** also show no evidence of enhanced motion (average frame-to-frame speed of 4.6 μm/s based on 1131 particle trajectories and 2 experiments). This implies that indeed *fibre* formation *i.e.* unidirectional self-assembly, by **1a** converting to **1b** is responsible for the enhanced diffusion (see **Table 8** for summary of results).

The average diffusion coefficient values for QD-AP conjugates without fuel and in the presence of 10 mM **1a, 3a** and **4a** were found to be 1.42; 2.71; 1.49 and 1.99 $\mu m^2/s$ respectively, indicating faster diffusion with fibre assembling fuel **1a** (see Appendix N for example MSD plots). For each fuel scenario diffusion coefficients are calculated by obtaining overall average values from individual video diffusion coefficients.

Table 8 - Summary of average speed data, as well as diffusion coefficients, for QD-AP with 10 mM **1a**, **3a**, **4a** and no fuel (**2a** will be discussed separately in section 7.5).

Substrate (10mM)	**Average speed (μm/s)**	**Diffusion coefficient, D ($\mu m^2/s$)**	**Number of particles**
No Fuel	4.4	1.42	719
1a	5.7	2.71	7007
3a	4.6	1.49	1131
4a	4.0	1.99	1139

7.4.1. Speed distribution comparison with control substrates

While average speeds are informative, the DLS analysis of the conjugate clearly revealed a range of conjugate sizes, so within a conjugate population there is a range of rates of motion. In **Figure 65** the frame-to-frame speed distributions are compared, for the self-assembling and non-self-assembling substrates (at 10mM fuel concentration) and the no-fuel control. With self-assembling fuel **1a,** there is a clear and significant population of faster particles compared to the no fuel control, the sphere-self-assembling control (**3a**) and non-self-assembling fuel (**4a**); moreover the peak in the speed distribution is significantly shifted to higher values (see **Figure 65**), further suggesting that biocatalytic self-assembly into fibrous structures drives enhanced motion. QD-AP conjugates from the same preparation method are used in all experiments; hence the distribution of sizes of conjugates and how many enzymes are attached per QD will be statistically similar: if motion were not enhanced by the presence of fuel substrate, we would expect to see overlapping speed distributions for all cases.

We may expect that as a fibre grows from the enzyme-quantum dot surface, the size of the particle would increase with fibre growth, therefore increasing the hydrodynamic drag and rotational time (τ_R), resulting in slower diffusion. Experimentally we observe enhanced diffusion, suggesting that fibres do not stay attached during enzymatic conversion of fuel. A more realistic assumption is that enzymes convert fuel molecules which then diffuse away from the enzyme to allow for the next fuel molecule to be converted; therefore fibre growth does not occur at the enzyme surface.

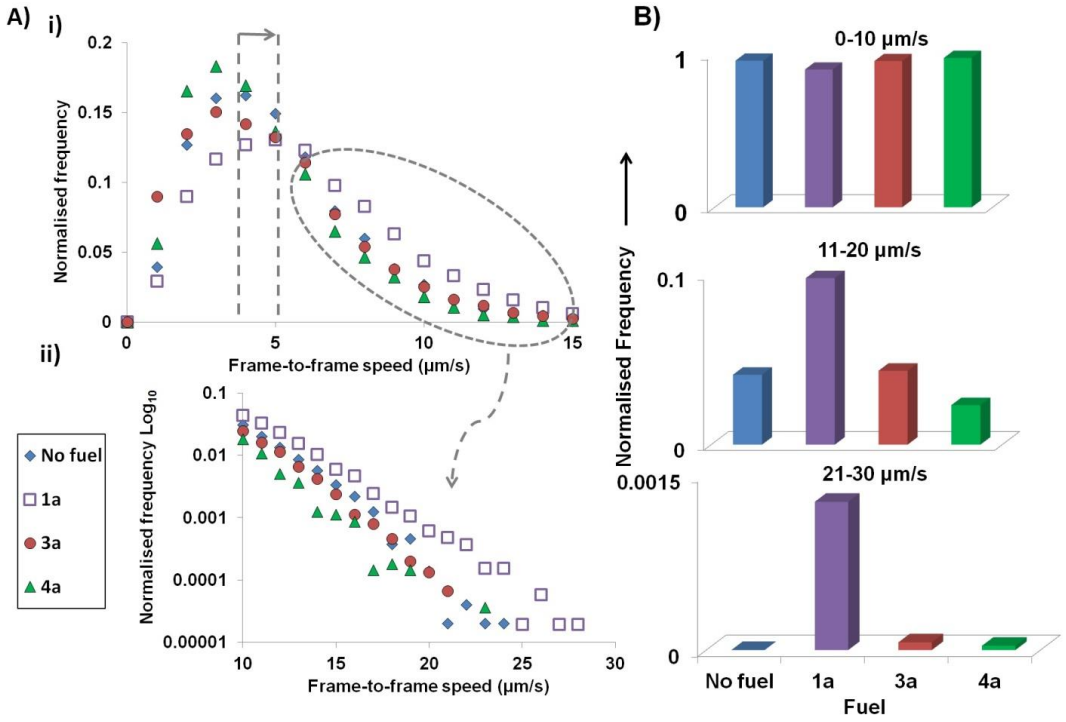

Figure 65 – (A) (i) Frame-to-frame speed distribution of QD-AP conjugates with different fuels and without fuel: **1a** – fibre-assembling fuel, **3a** – spherical self-assembling fuel, **4a** - non-self-assembling fuel (for **2a** – see section 7.5). A significant shift in the population maximum is observed with **1a**, compared to no fuel, **3a** and **4a**, indicative of a faster average frame-to-frame speed. Dotted lines illustrate the peak maxima and shift for QD-AP conjugates with no fuel compared to with **1a**. (ii) Frame-to-frame speed distribution (log scale) illustrating a significant population of conjugates at higher speeds with 10mM **1a**. (B) Histograms representing populations of conjugates for each fuel scenario at speed ranges from 0-10; 11-20 and 21-30 µm/s. With the fibre self-assembling fuel **1a**, there are fewer conjugates moving at the lower speed range (0-10 µm/s), compared to other fuels (and no fuel), while more conjugates display faster frame-to-frame speeds between 11-20 and 21-30 µm/s speed ranges.

7.4.2. Effect of batch variation on speed distribution

The frame-to-frame speed distribution for conjugates in the presence of 10 mM **1a** is compared for two different batches of QD-AP conjugates (**Figure 66** overleaf).

It is evident that batch-to-batch variations exist and result in different speed distributions as well as average speed values of 5.7 and 5.4 µm/s for batches 3 and 6, respectively. This can be related to the variation in activity of the QD-AP conjugates (Appendix D); in which faster conjugates (*i.e.* a greater average frame-to-frame speed) correspond to more active (in terms of *p*-nitrophenyl phosphate turnover) QD-AP conjugates (batch 3). It can be seen in Appendix D that conjugate QD-AP batch 3 is more active compared to batch 6.

This finding could be a step towards controlling conjugate speed by controlling the activity of the enzyme-QD conjugates. Differences in activity are likely due to differences in the degree of conjugation of enzyme to QDs. The more active the enzyme-conjugate, the faster the average frame-to-frame speed is expected to be, therefore engineering better conjugation *i.e.* more enzymes to QDs, is a potential route to further enhancing the propulsion effect.

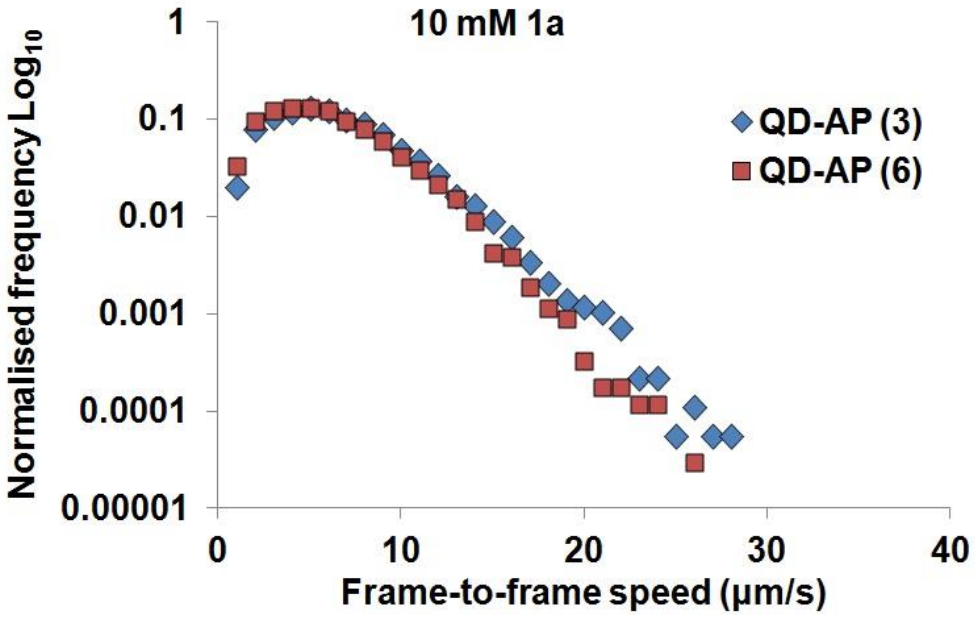

Figure 66 - Effect of QD-AP batch variation on speed distribution.

7.4.3. Experimental repeatability

The speed distributions of the same batch of QD-AP conjugates (with 10mM **1a**), measured at different times, are compared in **Figure 67** overleaf. The distributions are in good agreement with each other. Therefore it can be concluded that the biggest variation in speed data results from batch-to-batch differences as discussed above, and that measurements of a given batch are repeatable giving statistically similar results.

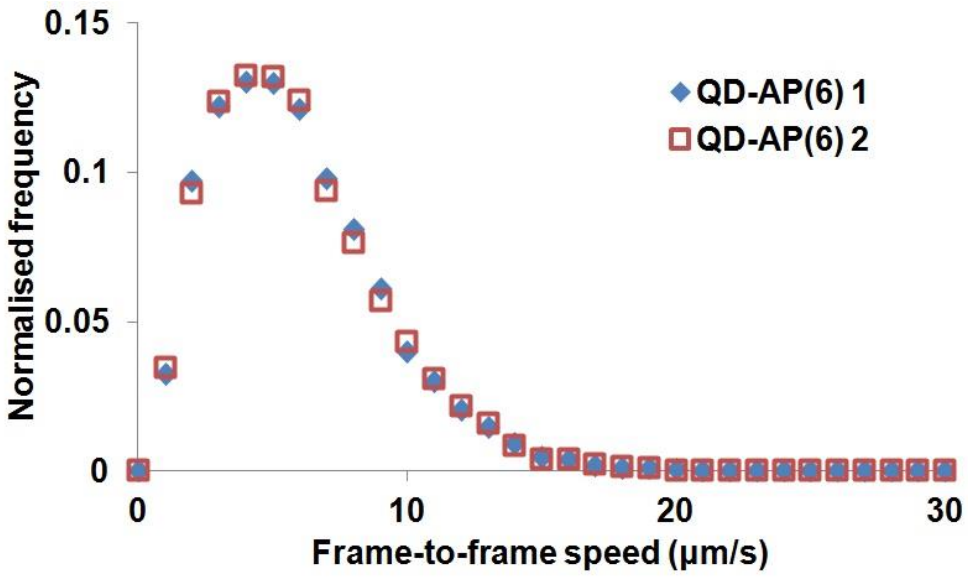

Figure 67 - Day-to-day comparison of speed distribution for the same batch of QD-AP conjugates with 10 mM **1a**, excited at 435 nm with two repeat experiments, 1 and 2 (2284 and 1728 particles tracked respectively).

7.4.4. Effect of 1a concentration on conjugate speed

Conjugate motion is studied with increasing fibre self-assembling fuel (**1a**) concentration. In **Figure 68** a shift in the frame-to-frame speed distribution is observed with increasing fuel concentration (at least up to 10 mM fuel concentration), while with non-self-assembling fuel (**4a**) conjugate speed is independent of fuel concentration.

While there is a clear increase in enhancement of motion with increasing fibre self-assembling fuel (**1a**) concentration between 5mM and 10mM, interestingly at 20mM **1a** the frame-to-frame speed distribution reverts to slower conjugate speeds (**Figure 68** (**E**)). This dependence on fuel concentration is difficult to explain definitively; however it is worth noting that at higher concentrations of **1a** *e.g.* 16mM, Fmoc-F*p*Y self-assembly has been observed to occur *without* catalysis.[213] This would imply that at a higher concentration some proportion of the 'fuel' was unavailable since it had already converted to a self-assembled nano-rod state.

A more detailed investigation of concentration dependence would be an interesting further step. For example, it would be interesting to collect data at concentrations around the critical micelle concentration (CMC), *i.e.* 5 mM of **1a**, to examine whether enhanced motion

is ‘switched on’ near the CMC when the fuel is in the micellar form compared to free dissociated molecules below the CMC.

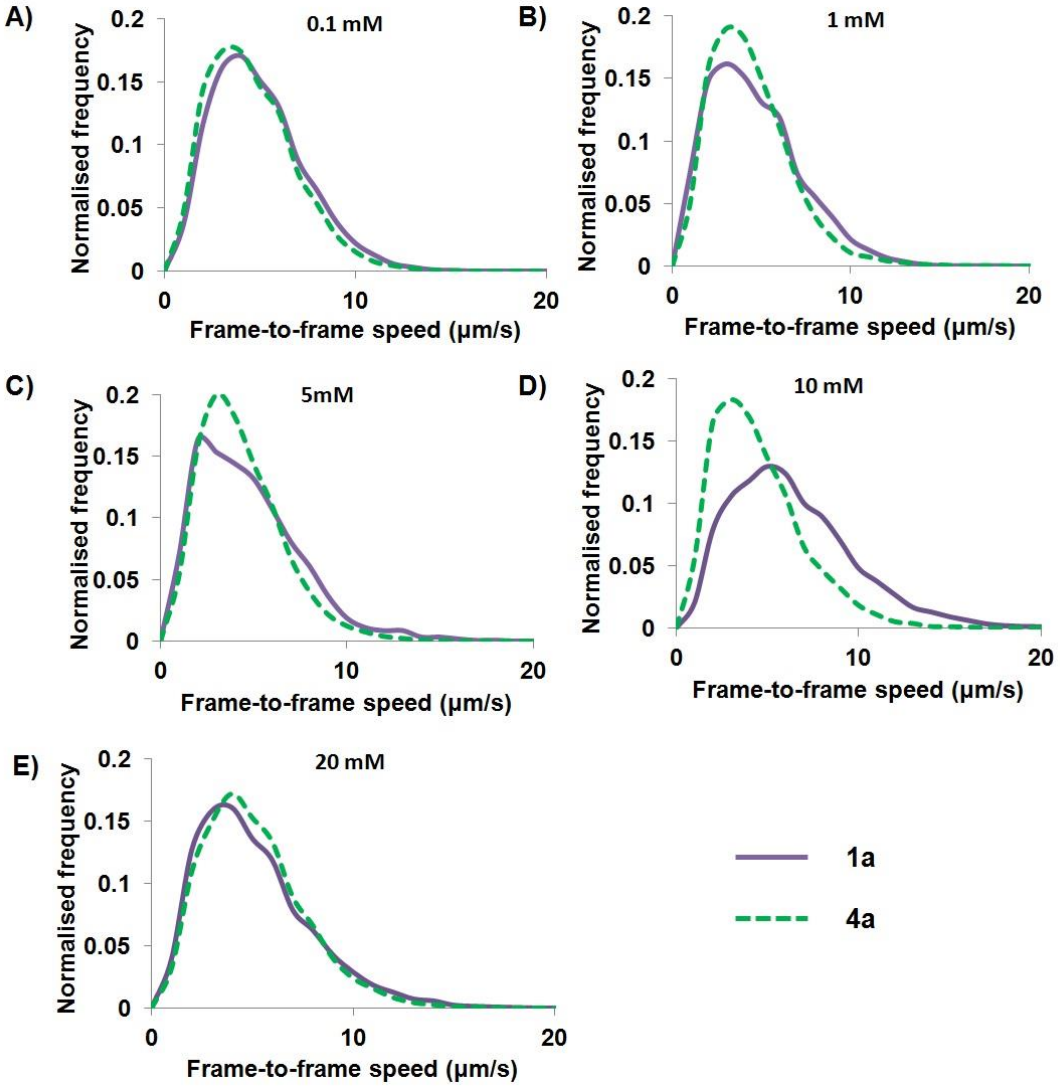

Figure 68 – Frame-to-frame speed distributions of QD-AP conjugates with different concentrations of fibre assembling fuel **1a** (purple solid line) and non-self-assembling substrate **4a** (green dashed line). Separate plots of QD-AP conjugate frame-to-frame speed distributions with different concentrations of **1a** and **4a** are provided in **Appendix K**.

7.5. Nanopropulsion with intrinsically fluorescent fibre-assembling peptide amphiphile 2a

In an effort to further understand the propulsion effect observed with fibre-assembling substrate **1a**, simultaneous visualisation of enzyme-conjugates and self-assembled fibre structures would be beneficial (as discussed in section 8.6). Due to the fluorescence emission of the Fmoc-based fibre system (**1a**) being in the low nanometre range (320 nm), substrate **1a** is not suitable for simultaneous tracking of conjugates and self-assembled structures. Other methods such as AFM cannot easily be used in real time and in solution to visualise fibre growth or particle motion, and often lead to drying- or surface-induced structural effects. Alternative methods to visualise self-assembled structures including intrinsic and extrinsic fluorescent labelling methods, are investigated in sections 8.3 and 8.4.

Pyrene-functionalised aromatic peptide amphiphile pyrene-*p*YL (**2a**) is also investigated for propulsion of QD-AP conjugates by fibre formation, in the hope that a similar speed enhancing effect is observed, along with pyrene as an intrinsic fluorescent probe for visualising self-assembled fibres (as well as QD-AP conjugates). Simultaneous fibre/QD-AP visualisation requires excitation of pyrene-functionalised substrates at wavelengths close to 334 nm. As mentioned previously, quantum dots have broad excitation wavelength ranges (due to the broad absorption band) therefore in this case the excitation wavelength is determined by the molecular fluorophore such as pyrene.

Before simultaneous fibre and QD-AP conjugate visualisation is attempted, first conjugate motion alone in the presence of fibre-assembling substrate **2a** is studied**.** QD-AP conjugates were added to 10 mM **2a** to investigate the effect of biocatalytic self-assembly on conjugate speed (as with peptide amphiphile **1a**, discussed above in section 7.4).

A similar effect of QD-AP frame-to-frame speed enhancement might be expected with **2a**; however problems arise due to the highly fluorescent nature of **2a**, preventing accurate data acquisition for tracking. The fluorescence signal of 10 mM **2a** creates a significant background signal preventing clear visualisation of single QD-AP conjugates and subsequent tracking is not possible. Lower **2a** substrate concentrations were investigated, in order to determine the highest concentration of **2a** capable of inducing an enhanced diffusion, while

low enough to visualise conjugates at a high enough quality to track. A number of fibre-assembling substrate (**2a**) concentrations were studied - 10, 5, 1, 0.1 and 0.01 mM. However only 0.1 and 0.01 mM concentrations exhibited low enough pyrene signal for QD-AP conjugates to be tracked effectively. It can be seen from **Figure 69** that at low concentrations of **2a** *i.e.* 0.01 and 0.1 mM, frame-to-frame speed enhancement is not observed however there is a small population of faster conjugates at 0.1 mM **2a** (compared with 0.01 mM) see **Figure 69 (B)**. The total population of conjugates measured with 0.01 mM is small (*i.e.* 444 particles compared to 1631 for 0.1mM) it is therefore difficult to conclude statistically that speeds are enhanced for 0.1 mM due to the possibility that within the smaller population faster conjugates were present but simply not observed. Example composite trajectories can be found in Appendix L.

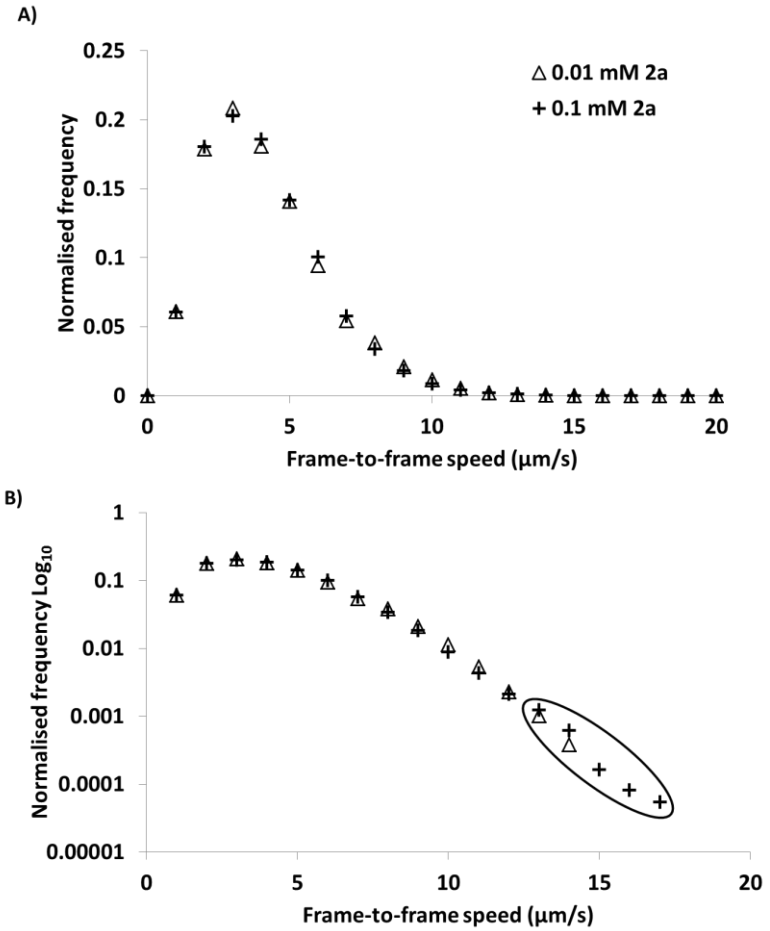

Figure 69 – (A) Frame-to-frame speed distribution of QD-AP with 0.01 mM (triangle) and 0.1 mM (cross) of fibre-assembling substrate **2a**, including the same data shown with a log scale for the normalised frequency (B).

Average frame-to-frame speeds for 0.01 and 0.1 mM **2a** were found to be 3.7 and 3.5 µm/s (based on 444/1631 particle trajectories and 1/3 experiments respectively). These values are compared to the no-fuel control with an average frame-to-frame speed of 4.4 µm/s (719 particle trajectories and 3 experiments). See **Table 9** and **Figure 70** overleaf for a summary and comparison of average frame-to-frame speed for 0.1 mM **2a** compared with no fuel, fibre-assembling substrate **1a** and non-self-assembling substrate **4a** (at a concentration of 0.1 mM). It is evident that at low fibre-assembling substrate concentrations (0.1 mM **2a**), frame-to-frame speed distributions of conjugates are similar to the other fibre-assembling substrate **1a**, as well as the non-self-assembling substrate **4a** and no fuel, and even appear to be slightly slower (**Table 9**). As described previously in section 7.4.4, an enhancement of QD-AP frame-to-frame speed is not observed with lower concentrations of fibre assembling substrate **1a**. It may be possible that at concentrations below the expected critical micelle concentration of **2a**[**] enhancement is not observed due to there being little or no sphere to fibre transformation.

Table 9 - Summary of average speed data, as well as diffusion coefficients, for QD-AP with 0.1 mM **1a**, **2a**, **4a** and no fuel.

Substrate (0.1 mM)	**Average speed (µm/s)**	**Diffusion coefficient, D ($\mu m^2/s$)**	**Number of particles**
No fuel	4.4	1.42	719
1a	4.5	1.17	774
2a	3.5	1.06	1631
4a	3.9	1.24	607

[**] *The CMC of **2a** was not measured here however it is expected to be in the same range as **1a** i.e. around 5 mM or lower due to **2a** being more hydrophobic than **1a**.*

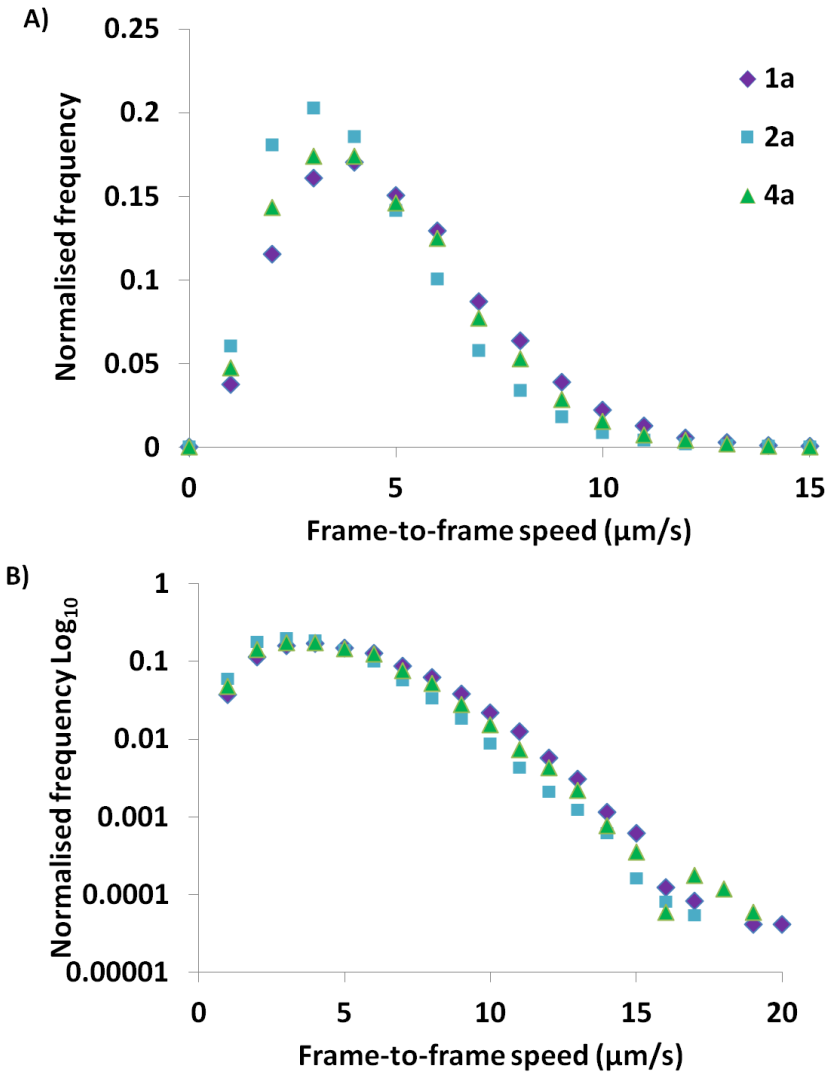

Figure 70 – (A) Frame-to-frame speed distribution of QD-AP with 0.1 mM fibre-assembling substrate **1a** (purple diamonds), fibre-assembling substrate **2a** (blue squares) and non-self-assembling substrate **4a** (green triangle symbols), including the same data shown with a log scale for the normalised frequency (B).

7.6. Summary

In summary it has been shown that the diffusive transport of alkaline phosphatase-quantum dot conjugates is enhanced by the addition of a self-assembling fuel **1a** at high enough fuel concentration. The fibre self-assembling fuel **1a** is dephosphorylated by the enzyme to **1b**, which facilitates fibre formation, which we propose aids the propulsion of alkaline phosphatase-QD conjugates leading to enhanced motion.

Pyrene-functionalised fibre-assembling substrate **2a** may provide a promising route to conjugate propulsion, as well as simultaneous fibre and conjugate visualisation. However,

background fluorescence issues of **2a** at concentrations required for propulsion (*e.g.* 10mM) prevents tracking of conjugates.

In the case of the self-assembling control **3a**, which assembles into spherical aggregates, rather than fibrous structures, enhanced diffusion was not observed, leading to the conclusion that the transformation from micelles to fibres of **1a** to **1b** molecules is essential for the nanopropulsion of QD-AP conjugates. This supports the proposal that linear fibre-assembly provides extra propulsion to enhance the transport of the conjugate. Since a given fibre propulsion 'event' will be in a random direction depending on rotational Brownian motion of the conjugate, the result of many events is increased diffusive transport of the conjugate.

7.7. Towards directional control of QD-AP conjugates

QD-AP conjugates driven by substrate fuel which is dissolved uniformly throughout the motility solution results in enhanced motion with fibre-assembling fuel **1a.** However motion is random as QD-AP conjugates encounter substrate fuel molecules at random as they diffuse in solution, at a rate that does not depend on location. Examples of enhanced but also directional motion have been reported through the incorporation of a fuel concentration gradient into various nanomotor systems.[34,51,321] Directed motion of artificial motors has been demonstrated using fuel saturated gel reservoirs from which the fuel diffuses into the surrounding solution, resulting in a concentration gradient, which the motors travel along in the direction of increasing concentration.[34,51] Additionally enzyme molecules have been shown by DLS to exhibit enhanced motion in response to a substrate concentration gradient created by a microfluidics set-up.[321]

As an initial step towards directional control of QD-AP conjugates, a polyacrylamide gel saturated in fuel substrate is investigated. Fibre-assembling substrates **1a** and **2a**, as well as buffer control (no fuel) and non-self-assembling substrate **4a** are studied for their ability to direct the motion of QD-AP conjugates, along a substrate concentration gradient. This study would require further development and additional controls such as free QDs with and without fuel saturated gel reservoirs.

A gel saturated in 5 mM substrate, then placed in buffer, results in time-dependent diffusion of the substrate from the initially high substrate concentration of the gel to low substrate concentration at distances far from the gel. Diffusion of the substrate from the gel thus creates a time-dependent substrate concentration gradient within the local environment of the motility assay. It is worth noting that although gels are saturated in 5 mM substrate solutions, it is uncertain as to the final concentration of substrate within a given gel, as substrates may be more concentrated in the gel due to differences in hydrophilicity/hydrophobicity.

Polyacrylamide gels saturated with fibre-assembling substrates **1a** and **2a** were monitored by fluorescence spectroscopy to confirm diffusion of the substrate from the gel. Each substrate-saturated gel was added to a known volume of buffer (1 mL) in a cuvette and the fluorescence intensity of **1a** (320 nm) and **2a** (377 nm) was monitored with time (see Appendix J). A local fluorescence emission measurement was obtained at a fixed distance from the gel, *i.e.* where the fluorimeter excitation beam is centred, for both **1a** and **2a** substrates which showed an increase in fluorescence emission intensity with time indicating diffusion of the substrates from the polyacrylamide gel.

A motility assay was designed for directed motion of QD-AP conjugates with gel 'fuel' reservoirs. The assay consists of the same sample holder and conditions as used with previous motility experiments (see section 4.3.3.6.). A square of substrate-saturated gel (4 mm x 4 mm x 1 mm) was added to one quadrant of the sample well (rather than the substrate being present within the entire motility solution), as shown in **Figure 71** overleaf. The objective is focused in the centre of the sample well and as with previous motility experiments, digital videos of the conjugates are recorded at regular time points for a period of time (up to 1 hour).

The videos are analysed and data is obtained for QD-AP conjugate frame-to-frame speeds, MSD, and angle of trajectory. The angle of trajectory in this case, is particularly important to illustrate whether the conjugates are directed or remain randomly diffusive, illustrated by angle of trajectory distributions in a specific range of angle or evenly spread, respectively. Average frame-to-frame speeds (represented by one video per time point), can also offer information on whether the speed is enhanced due to the substrate

concentration gradient and may indicate trends with time due to the time-dependent diffusion of the substrate from the gel reservoir.

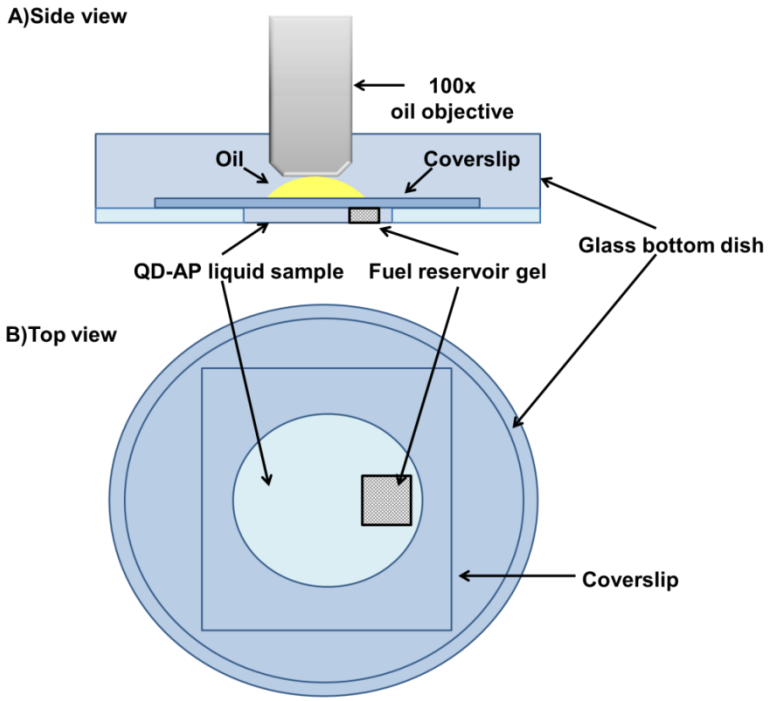

Figure 71 - Fuel reservoir motility assay set up. Glass bottom dish with QD-AP sample secured in a well with glass coverslip, for use with oil immersion objective. The 'fuel' or substrate soaked polyacrylamide gel is placed in a specific segment of the well.

7.7.1. Control reservoir – no fuel

Firstly a control gel was studied, which was saturated in buffer containing no substrate. This ensures that any directional effect observed with substrate saturated gels is truly due to a substrate concentration gradient and not caused by flow. Example composite trajectories for QD-AP with a gel saturated in buffer are shown for the first 15-30 minutes of a motility experiment and also 30-60 minutes (**Figure 72** overleaf). Two time periods were analysed separately due to the time dependent nature of the experiment *i.e.* the concentration gradient changes with time as substrate diffuses from the gel. Trajectories appear non-directional and diffusive at shorter and longer times within the control no fuel experiment, consistent with Brownian motion and minimal effects due to flow.

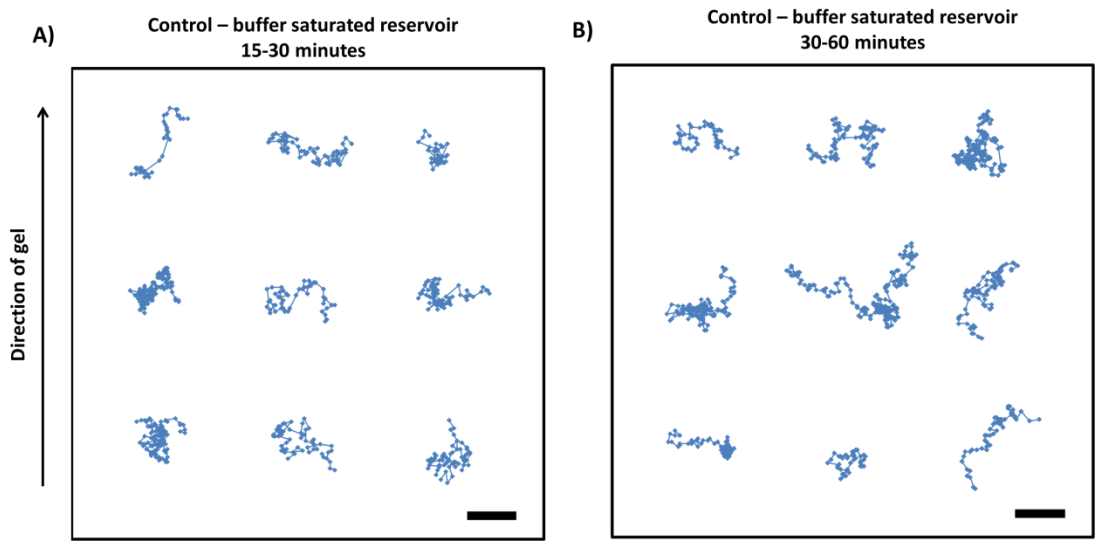

Figure 72 - Composite of trajectory examples of QD-AP with buffer saturated gel (no fuel control) between (A) 15-30 minutes and (B) 30-60 minutes of motility experiment. Arrow represents the general direction of the buffer saturated gel in relation to particles being tracked. Scale bars = 5 µm.

In **Figure 73**, the angle of trajectory of QD-AP conjugates with no fuel without the gel is compared with conjugates in the presence of a buffer saturated gel. Overall the angle of trajectory distributions are similar and represent random motion in both cases *i.e.* a relatively even spread of angles (for time dependent angle of trajectory distribution see Appendix M). Additionally MSD plots indicate Brownian motion as linear plots are observed for a number of example particles (see Appendix N), as opposed to curved MSD plots, indicative of directed motion.

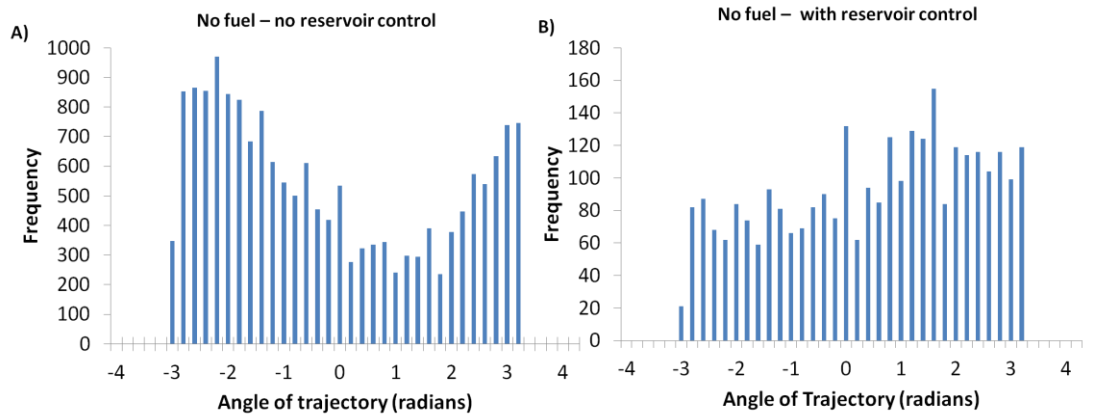

Figure 73 - Angle of trajectory distributions for QD-AP with (A) no fuel and no gel and (B) gel saturated in buffer (no fuel).

The average frame-to-frame speeds of QD-AP conjugates with buffer saturated gel (no fuel) are compared to the overall average speed of QD-AP conjugates in buffer (no fuel, no gel). The average frame-to-frame speed of conjugates with control gel saturated in buffer (no fuel), show some variation between data points but there is no apparent relationship with time (**Figure 74**). The overall average frame-to-frame speed value for QD-AP conjugates with buffer saturated gel is 3.9 µm/s, compared to 4.4 µm/s for control with no fuel and no gel (dotted line in **Figure 74**), based on 1 experiment and 133 particles. See **Table 8** for no gel average frame-to-frame speed value.

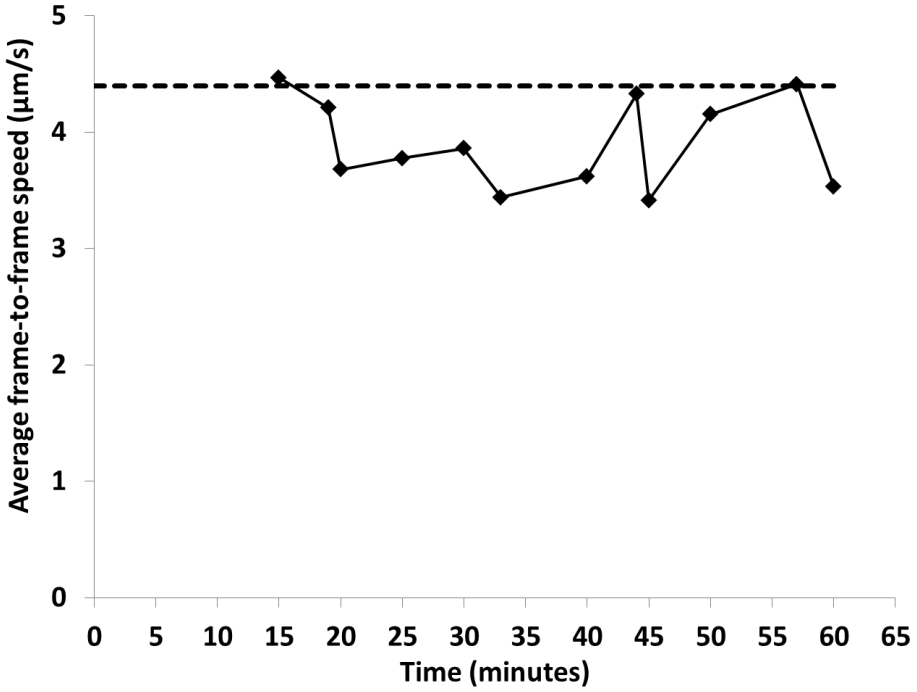

Figure 74 - Average frame-to-frame speed of QD-AP conjugates, as a function of time point, in the presence of buffer saturated gel (control), compared to the average speed of QD-AP conjugates in buffer (no fuel and no gel), shown by the dashed line.

7.7.2. Fibre-assembling substrate reservoir 1a

A gel saturated in fibre-assembling substrate **1a** is studied to investigate directional control of QD-AP conjugates. Example composite trajectories in **Figure 75** overleaf show more linear trajectories (compared to random control trajectories), which are relatively aligned in terms of direction.

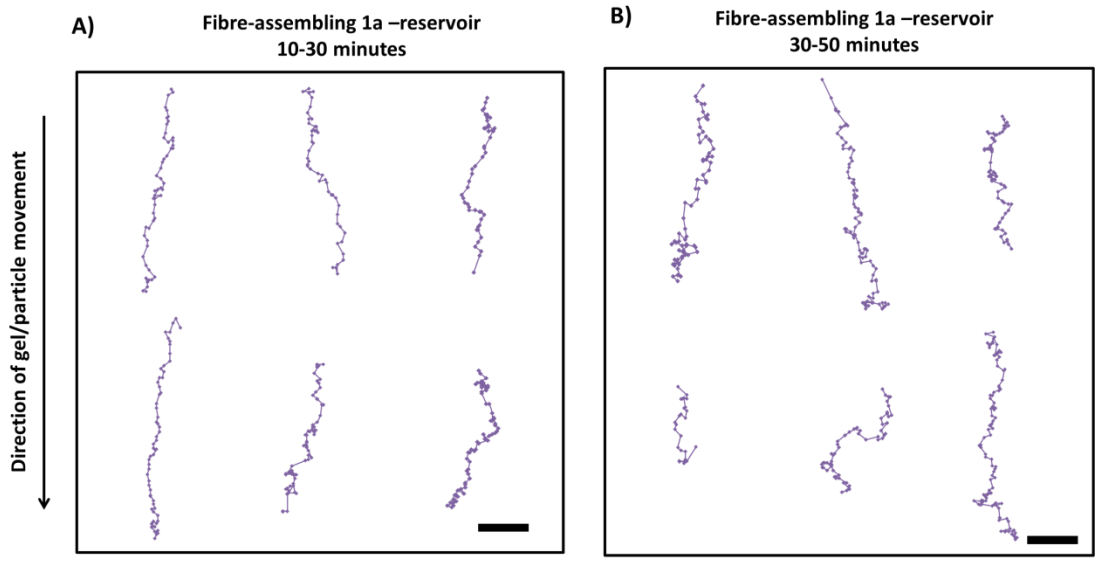

Figure 75 - Composite trajectory examples of QD-AP with gel saturated in fibre-assembling **1a**, between (A) 10-30 minutes and (B) 30-50 minutes of motility experiment. Scale bars represent 5 µm.

Directionality of QD-AP conjugates is further confirmed experimentally as conjugates were seen to move towards the gel reservoir. Further to this in **Figure 76**, angle of trajectory distributions with **1a** saturated gel range between +/-3.14-1.4 radians (**Figure 76 (B)**) (the gel was at approximately +/- 3.14 radians in relation to tracked particles), compared to an evenly spread distribution when fibre-assembling substrate **1a** is present throughout the motility medium (**Figure 76 (A)**).

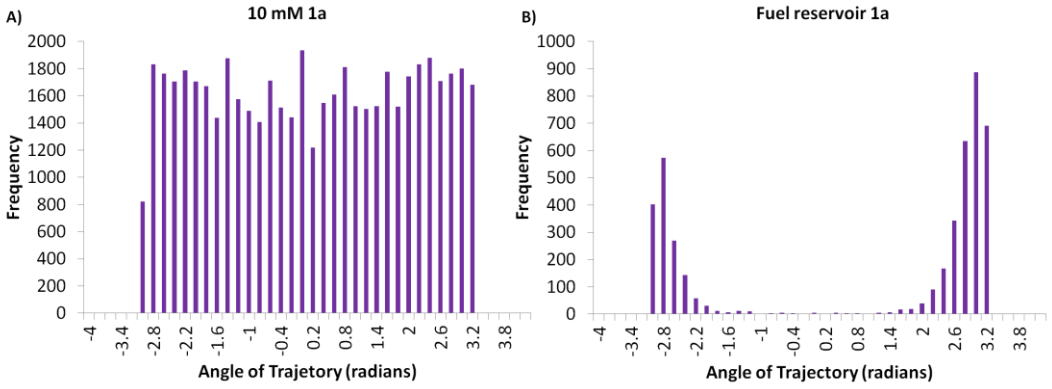

Figure 76 - Angle of trajectory distributions of QD-AP with (A) 10 mM **1a** (fibre-assembling substrate) without gel, and (B) gel saturated in **1a**.

Average frame-to-frame speeds of QD-AP conjugates with a gel reservoir saturated in fibre-assembling substrate **1a** show enhanced diffusion and decreasing speed with time indicative of a substrate concentration gradient (**Figure 77**). This is thought to be due to the substrate concentration gradient becoming less steep over time, as the substrate is more evenly distributed in the surrounding environment.

The initial average frame-to-frame speed of conjugates is 9.1 µm/s (t=10 mins) and by 50 minutes after the addition of the QD-AP conjugates, the speed has reduced to 5.6 µm/s, comparable to the average speed of QD-AP in 10 mM **1a** no gel reservoir (dashed line in **Figure 77**). The overall average frame-to-frame speed of QD-AP conjugates with **1a** saturated gel and gel with no fuel are 7.0 and 3.9 µm/s, respectively (based on 1 experiment and 170 particles). MSD plots are curved consistent with directed motion (see Appendix O), however further control measures would be required to eliminate the possibility of flow within the system

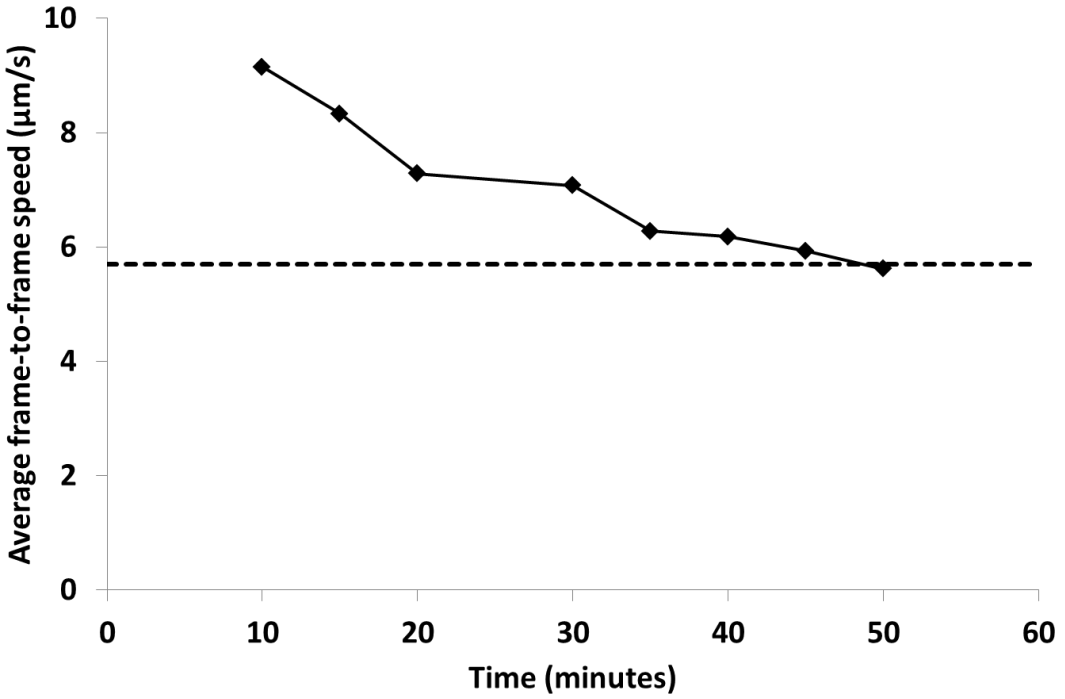

Figure 77 - Average frame-to-frame speed of QD-AP conjugates, as a function of time point, in the presence of **1a** saturated gel, compared to the average speed of QD-AP conjugates in 10 mM **1a** (present throughout the solution) shown by the dashed line.

7.7.3. Fibre-assembling substrate reservoir 2a

A gel saturated in the second fibre-assembling substrate **2a** is similarly studied to investigate directional control of QD-AP conjugates. Example composite trajectories, in **Figure 78** show more linear trajectories (compared to random control trajectories), which are relatively aligned in terms of direction.

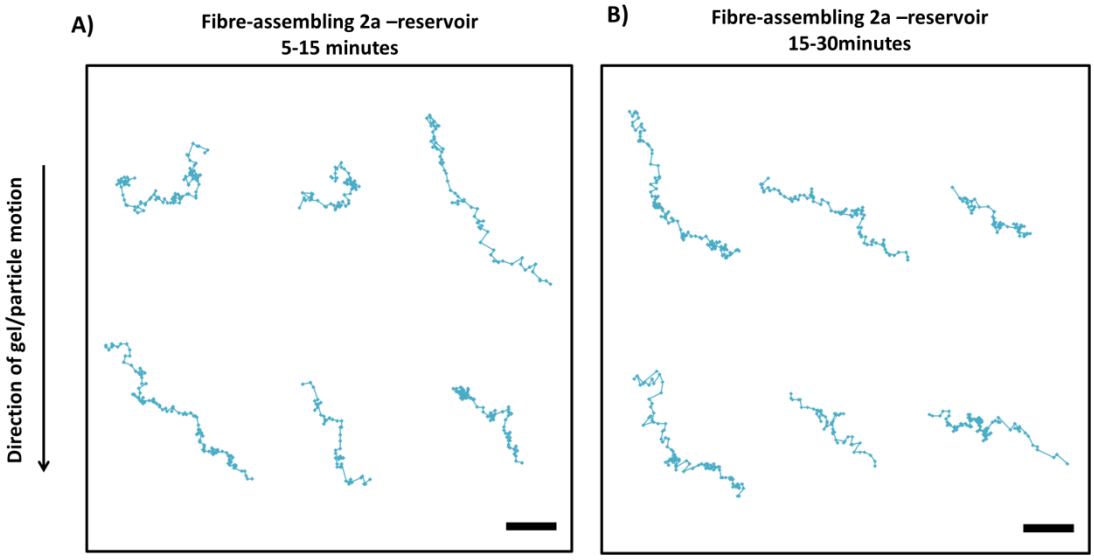

Figure 78 - Composite trajectory examples of QD-AP with gel saturated in fibre-assembling **2a**, between (A) 5-15 minutes and (B) 15-30 minutes of motility experiment. The arrow represents the general direction of the gel and particle motion. Scale bars = 5 µm.

Conjugates were observed experimentally to move towards the gel reservoir, however according to the initial positioning of the gel reservoir the particles appear to move diagonally, this could be due to a shift in the gel position over time but is also dependent on the positioning of the objective *i.e.* where it is focused, in relation to the gel. In **Figure 79**, angle of trajectory distributions of QD-AP conjugates with 0.1 mM **2a** (without gel) are compared to conjugates with gel saturated in **2a**. Previous studies with fibre-assembling **2a** present uniformly throughout the motility solution revealed that above 0.1 mM the fluorescence signal was intense, preventing QD-AP conjugate tracking. Here, the intrinsically fluorescent substrate **2a** is saturated within a gel reservoir at a higher concentration (5mM starting solution). Isolating the fluorescent substrate in a gel reservoir eliminates the fluorescent interference issues observed when the substrate was throughout the solution. The angle of trajectory distribution of QD-AP conjugates with **2a** saturated gel reservoir shows some directionality with an angle of trajectory range between +/-3.14-1.0

radians (gel direction approximately +/- 1.5 radians) (**Figure 79 (B)**), compared to a more evenly spread distribution when fibre-assembling substrate **2a** is present throughout the motility medium (**Figure 79 (A)**.

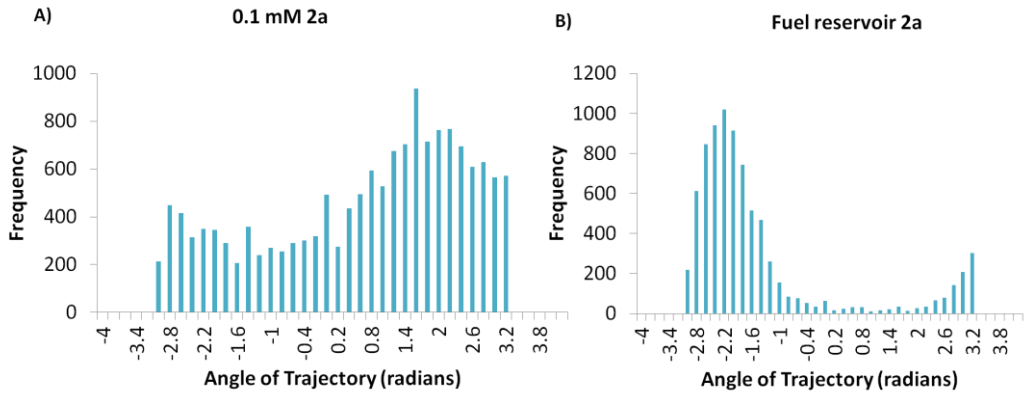

Figure 79 - Angle of trajectory distributions of QD-AP with (A) 0.1 mM **2a** (fibre-assembling substrate) without gel, and (B) gel saturated in **2a**.

Average frame-to-frame speeds of QD-AP conjugates with a gel reservoir saturated in fibre-assembling substrate **2a**, show no apparent dependence with time but vary between data points (**Figure 80** overleaf). This could be due to the hydrophobic nature of **2a** which may compete with diffusion of the substrate into the medium *i.e.* **2a** may interact with polyacrylamide gel rather than diffusing into the surrounding solution, so that the time dependence of the **2a** concentration gradient will be complicated (as indicated in Appendix J). Overall average frame-to-frame speed is enhanced with **2a** saturated gel (5.3 µm/s) compared to control reservoir (3.9 µm/s) and 3.5 µm/s for QD-AP in 0.1 mM **2a** present throughout the solution (see **Table 9**), based on 1 experiment and 271 particles. See Appendix P for example MSD plots.

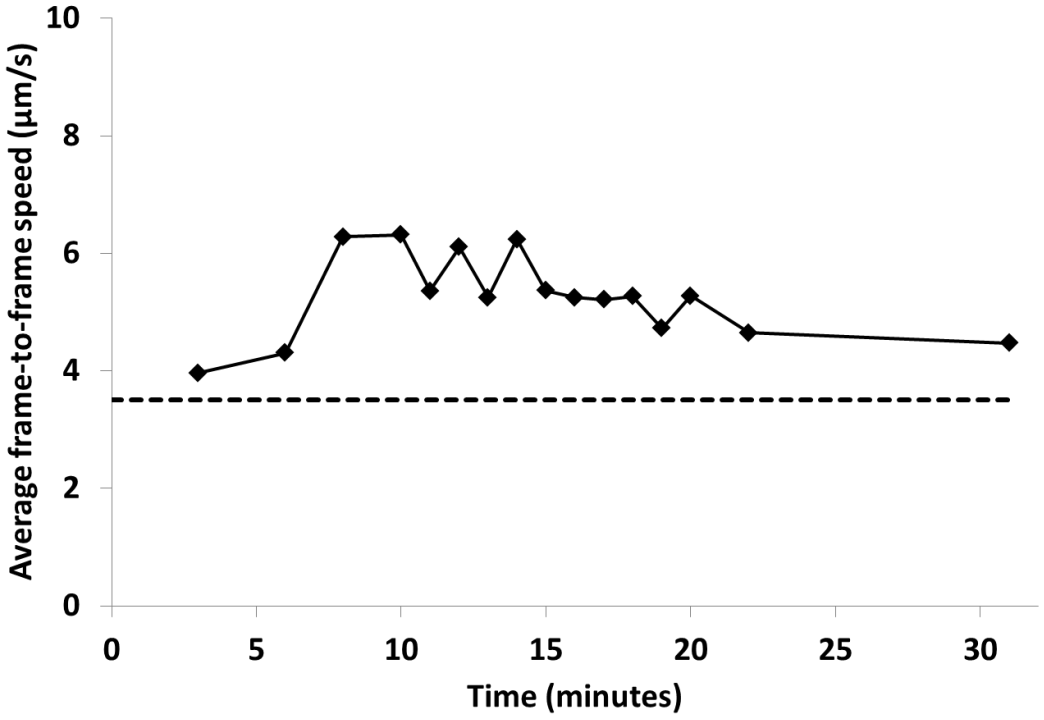

Figure 80 - Average frame-to-frame speed of QD-AP conjugates, as a function of time point, in the presence of **2a** saturated gel, compared to the average speed of QD-AP conjugates in 0.1 mM **2a** (present throughout the solution), shown by the dashed line.

7.7.4. Non-self-assembling substrate reservoir 4a

A gel saturated in the non-self-assembling substrate **4a** is also studied to investigate directional control of QD-AP conjugates. Example composite trajectories in **Figure 81** overleaf show once again more linear trajectories (compared to random control trajectories) which are aligned in terms of direction. Interestingly, differences in trajectories arise with time as trajectories become shorter and more random after 15-25 minutes compared to shorter times (5-15 minutes after addition of QD-AP conjugates). This effect may be due to a diminishing effect of the concentration gradient with time, where at longer times the substrate could have diffused throughout the motility sample until uniformly distributed, and QD-AP conjugates revert to more Brownian motion. Although this trend is not observed with other substrates, this could be consequential of hydrophilicity or size of the substrate, where **4a** is relatively smaller compared to **1a** and **2a** and is likely to be more hydrophilic, therefore may diffuse from the gel at a faster rate.

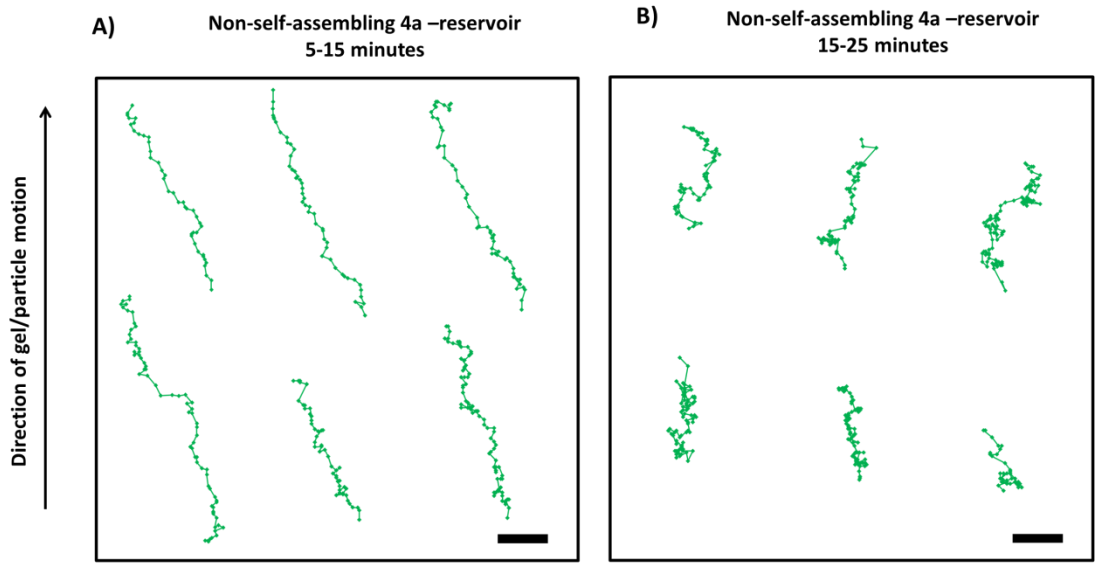

Figure 81 - Composite trajectory examples of QD-AP with gel saturated in non-self-assembling **4a**, between (A) 5-15 minutes and (B) 15-25 minutes of motility experiment. Arrow represents the direction of gel in relation of the tracked particles and also direction of particle motion. Scale bars = 5 µm.

QD-AP conjugates were observed experimentally to move towards the gel reservoir. In **Figure 82** overleaf, the angle of trajectory of QD-AP conjugates with 10 mM **4a** (without gel) is compared to conjugates with gel saturated in **4a**. The angle of trajectory distribution of QD-AP conjugates with **4a** saturated gel reservoir shows directionality with an angle of trajectory range between -1.0-1.4 radians (gel position approximately 0 in relation to tracked particles) (**Figure 82 (B)**), compared to a more evenly spread distribution when non-self-assembling substrate **4a** is present throughout the motility environment (**Figure 82 (A)**). Comparing with the other substrate saturated gel systems (**1a** and **2a**); conjugates with **4a** appear most directional in terms of exhibiting the smallest range of angle of trajectories.

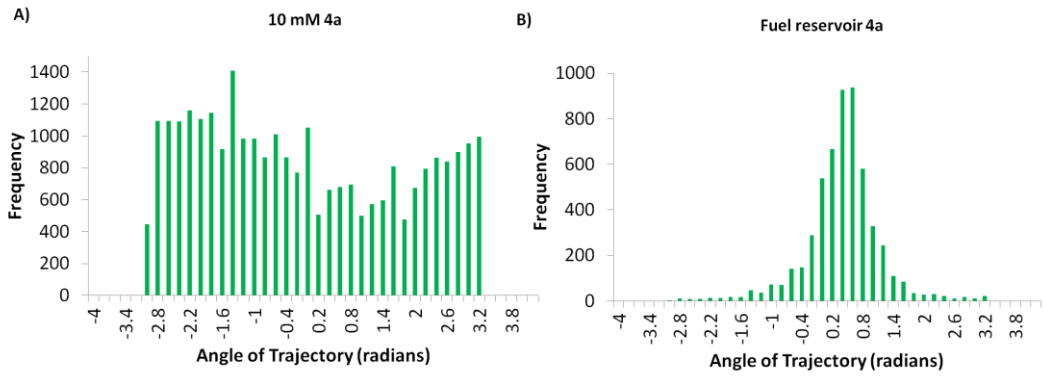

Figure 82 - Angle of trajectory distributions of QD-AP with (A) 10 mM **4a** (non-self-assembling substrate) without gel, and (B) gel saturated in **4a**.

Previous studies of QD-AP conjugates with up to 20 mM non-self-assembling substrate **4a** dissolved throughout the motility solution, did not exhibit enhanced motion. However it is clear from **Figure 83** that QD-AP conjugate average frame-to-frame speed is initially enhanced at values of 11.8 µm/s (t = 5 mins) and by 25 minutes (after the addition of QD-AP conjugates), the speed has reduced to 3.5 µm/s, comparable to the overall average frame-to-frame speed of conjugates in 10 mM **4a** present throughout the solution (4.0 µm/s), see **Table 8**. Overall average frame-to-frame speeds of QD-AP conjugates with **4a** saturated gel, and gel with no fuel are 6.7 and 3.9 µm/s, respectively (based on 1 hour long experiment and 332 particles).

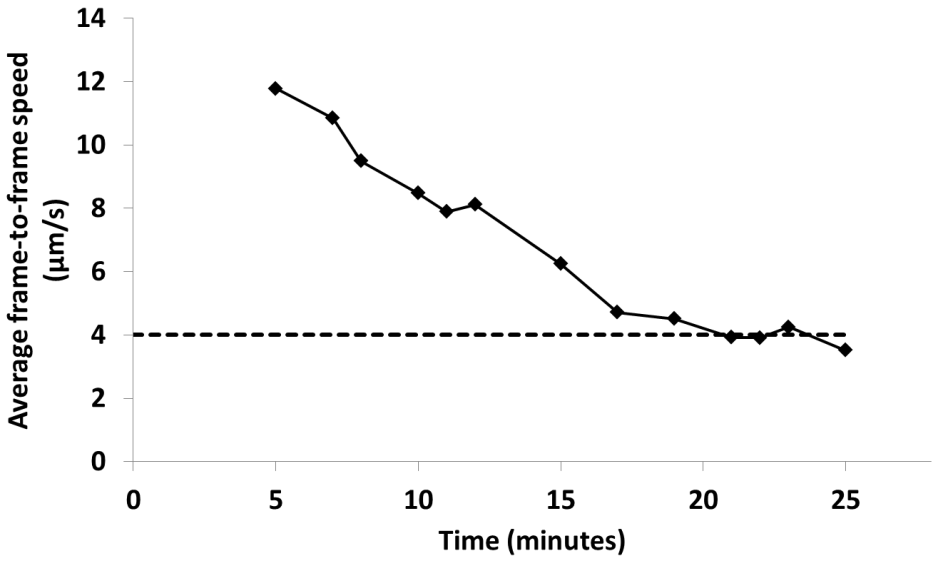

Figure 83 - Average frame-to-frame speed of QD-AP conjugates, as a function of time point, in the presence of **4a** saturated gel, compared to the average speed of QD-AP conjugates in 10 mM **4a** (present throughout the solution), shown by the dashed line.

7.7.5. Summary

In summary, initial demonstration of the directional control of QD-AP conjugates was achieved by isolating the substrate 'fuel' within an acrylamide gel. Diffusion of substrates into the surrounding buffer solution creates a substrate concentration gradient, where substrates **1a**, **2a** and **4a** were shown to direct the motion of QD-AP conjugates, as well as enhance the average frame-to-frame speed at initial time points. The approximate location of the substrate gel reservoirs (in relation to tracked particles) in most cases correlated with the angle of trajectories observed experimentally by the particles, however the gel may be liable to shift during the experiment and the observations are reliant on the positioning of the objective *i.e.* where the objective is focused in relation to the gel reservoir.

Interestingly, in the case of substrate **4a**, QD-AP conjugates, previously showed no enhancement of speed when the substrate was uniformly distributed throughout the motility solution, however when the substrate was released locally from a gel reservoir, conjugate speeds were enhanced compared to the average frame-to-frame speed of conjugates in fuel present throughout the system. Enhanced diffusion of QD-AP was previously only observed with fibre-assembling substrate **1a** at 10 mM concentrations. In contrast preliminary studies with substrate concentration gradients suggest that enhanced and directed diffusion may be possible even in the case of non-self-assembling substrates (**4a**). Interestingly this has also been observed with catalase and urease enzymes in a microfluidic cell using DLS, however these catalytic effects on transport remain to be explained.[321] This effect could be attributed to the presence of a concentration gradient, however at this preliminary stage of the investigation, further control measures would be required to conclusively attribute the enhanced and directed motion to the presence of fuel concentration gradients. As the results stand, without suitable controls, the directed motion observed could be attributed flow in the system.

– Chapter 8 –

Visualisation of self-assembled supramolecular structures

8.1. Objectives

As confirmed by fluorescence microscopy tracking of QD-AP conjugates, there is an enhancement in the diffusion rate of the conjugates in the presence of fibre-assembling substrate **1a** (10 mM). It is proposed that the linear growth of a fibre which is transformed from a spherical micellar structure provides an impulsive force on the enzyme-QD conjugate. Therefore the ultimate aim for this investigation would be to visualise enzyme-QD conjugates and fibres simultaneously in a fluid three-dimensional environment to gain more information about the propulsion mechanism.

8.2. Introduction

Visualisation of supramolecular structures is generally performed by a number of electron microscopy or atomic force microscopy techniques. These methods however involve immobilising or drying the sample to a surface in order to image. Self-assembled fibre structures of **1b** and **2b** (as in **Figure 60**), converted by AP and QD-AP from **1a** and **2a** respectively, were initially confirmed using atomic force microscopy and electron microscopy techniques (TEM and cryo-TEM). See **Figure 84** overleaf for TEM images and Appendix S for additional images of **2b** fibres by AFM.

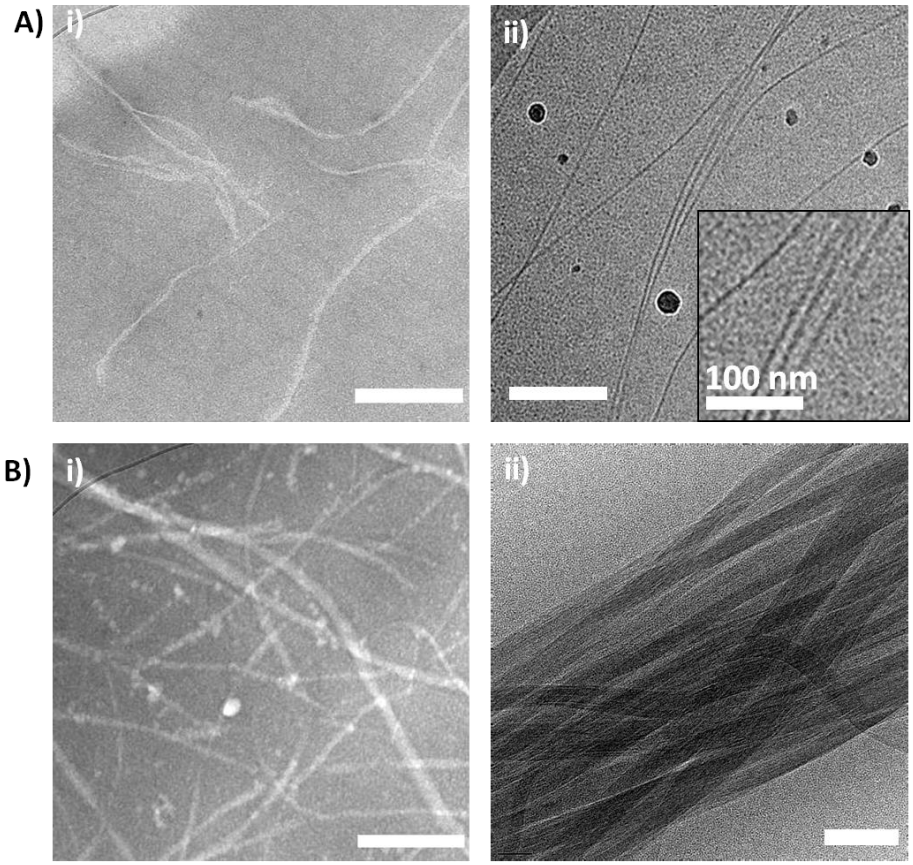

Figure 84 - Transmission electron micrographs (i) and cryo-TEM images (ii) of (A) fibres of **1b** (converted from **1a** by QD-AP) and (B) fibres of **2b** (converted from **2a** by QD-AP). Scale bars represent 200 nm.

Although informative of resulting supramolecular structures, AFM and TEM techniques are not ideal methods for dynamic real-time tracking of fibres and enzyme-QD conjugates simultaneously. Fluorescence microscopy provides a potential route to simultaneous visualisation of the self-assembled fibre structures, as well as QD-AP conjugates, in an effort to gain information about the self-assembly propulsion mechanism of enzyme-quantum dot conjugates (see section 8.6).

Here, two methods of fibre visualisation are investigated: firstly extrinsic fluorescent staining using thioflavin T; and secondly incorporation of an inbuilt intrinsic fluorescence group within the design of the self-assembling 'monomers' (*e.g.* pyrene functionalised fibre assembling substrate **2a**). Initial investigations aim to determine the optimum visualisation technique for fibres made by free alkaline phosphatase, before undertaking similar studies with enzyme-QD conjugates for two-fluorophore simultaneous visualisation.

8.3. Fibre visualisation - Extrinsic fluorescent staining of 1b fibres

Fmoc-functionalised peptide substrates fluoresce in the UV range (320 nm), therefore are not easily compatible with most fluorescence microscopes. Thioflavin T, which emits light at 480 nm in the visible region, can be used as a fluorescent stain for the direct visualisation of biocatalytic self-assembled fibres of for example Fmoc-FY (**1b**), (as ThT fluoresces in the presence of β-sheet assemblies – see section 4.1.3).

The fluorescence microscope was fitted with a 482 nm optical emission filter to capture fluorescence signal from ThT stained fibres (as described in Techniques section 4.3.2.1). A control sample of 10 mM **1a** solution was prepared with the addition of 1 μM ThT and studied in a simple flow cell arrangement by fluorescence microscopy. No fluorescent structures were observed as expected with a **1a** solution consisting of micelles *i.e.* no β-sheet fibrous structures of **1b** are present before phosphatase addition.

With the addition of alkaline phosphatase (4 U), to 10 mM **1a** containing ThT, gel formation of the bulk sample was seen after 24 hours. The gel was placed in a simple flow cell and by fluorescent microscopy fibre-like bundles stained with ThT were observed at the surface of the flow cell. In addition, spherical aggregates were found throughout the three-dimensional sample, indicating the biocatalytic conversion of **1a** to **1b** and the formation of β-rich structures (see **Figure 85** overleaf). The fluorescent spheres observed were in the tens of micron size range and appeared to be immobilised throughout the gel (see **Figure 85**). Individual fibres were not observed, possibly due to low fluorescence emission compared to the highly fluorescent spherulites. Similar spherulitic structures have been observed by β-amyloid fibre forming proteins and peptides[243,322,323] and also with a similar dipeptide system (Fmoc-SF-OMe) which was found to assemble into 100 μm diameter spheres.[179] It may be possible that fibres grow radially from a central point, creating sphere-like structures.

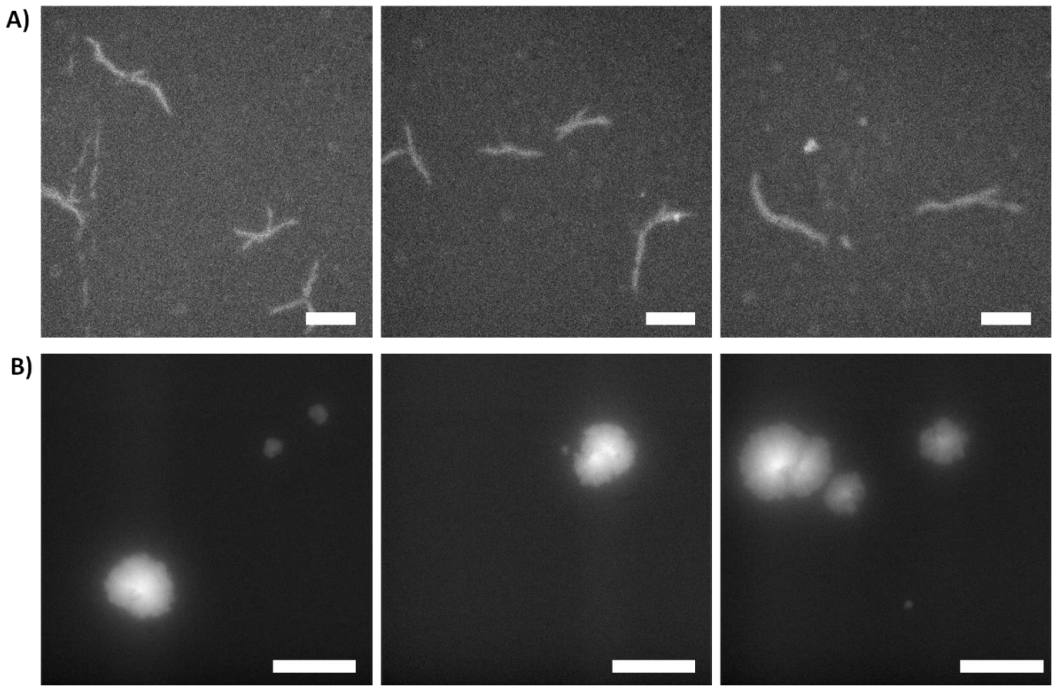

Figure 85 - Thioflavin T stained (A) fibre bundles of **1b** (converted from **1a** by AP) on the surface of a simple flow cell; and (B) spherulitic structures present throughout the flow cell. Scale bar represents 20 µm. No structures were observed at t = 0, before enzyme addition.

A gel made from the conversion of **1a** to **1b** by alkaline phosphatase was dried onto a glass surface to reduce fluorescence interference presented by a three dimensional sample. The fibres were stained with ThT after gel formation, and visualised using fluorescence microscopy. Fibres and fibre bundles were observed dried on a glass surface, but also large aggregates of fibres were apparent, as observed with previous flow cell (3D) observations, suggesting that fibres grow radially from a central point (see **Figure 86** overleaf).

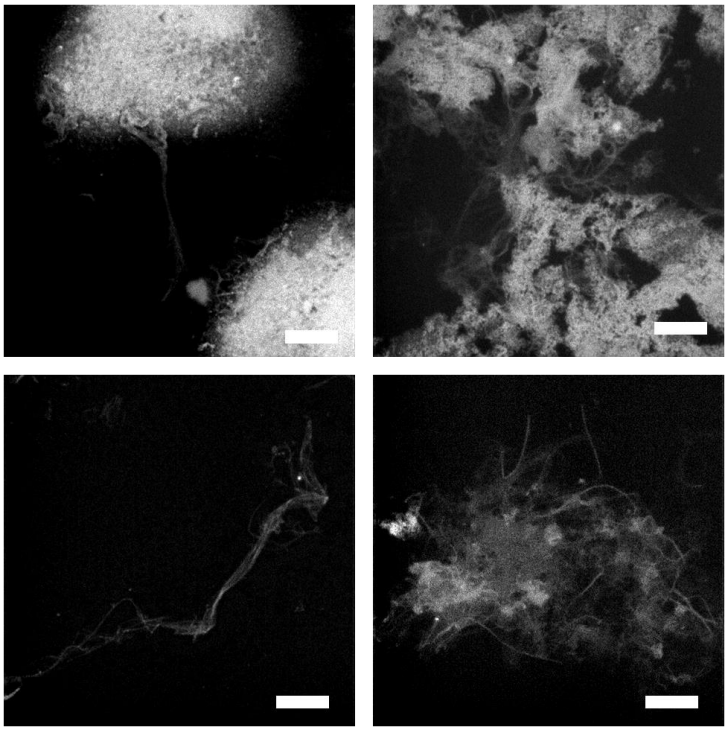

Figure 86 –ThT stained fibre bundles and aggregates of **1b** (converted from **1a** by AP), dried onto glass. Scale bar represents 20 μm.

Visualisation of ThT-stained **1b** fibres, using free alkaline phosphatase, was possible due to the bulk gelation of the sample *i.e.* fibres were present throughout the sample. The fibre growth process in the motility experiments, using alkaline phosphatase conjugated with quantum dots is thought to occur locally, where isolated regions of fibres are expected rather than a gel, due to the low enzyme concentration (upper limit of approximately 7.0 $x10^{-4}$ U). When fluorescently stained with ThT, the localised fibrous regions result in low fluorescent signal not detectable using an EMCCD camera (despite frame averaging and increased camera gain). Therefore for real-time visualisation of localised fibre growth made by QD-AP conjugates, it has been shown that ThT staining is unsuitable and only large aggregates of fibres give intense enough signal to visualise.

8.4. Fibre visualisation - Intrinsically fluorescent 2b fibres

8.4.1. Fluorescence microscopy

While extrinsic staining allowed for the visualisation of Fmoc-containing self-assembled aggregated structures, observation of individual fibres or fibre bundles was only possible when the sample was dried on a two-dimensional surface. As mentioned in section 4.1.2, the inbuilt design of the self-assembling molecule can incorporate a fluorescent group such as pyrene, which fluoresces at a more accessible wavelength for fluorescence microscopy (monomer peaks at 417 nm compared to 320 nm of Fmoc as well as additional fluorescence signals at longer wavelengths indicative of self-assembly). As discussed in section 4.3.2, the microscope can be modified to include specific excitation sources *e.g.* illumination lamps and optical filters, as well as optical filters for the collection of the target fluorescent signal. Pyrene excitation requires UV illumination close to 334 nm using an LED lamp and a 365 nm excitation filter. Additionally, the microscope is fitted with a 417 nm emission optical filter for pyrene detection (see Appendix B for optical filter combination).

Initial visualisation experiments confirmed that fibres of **2b** could be visualised using free AP (4 U) added to a 5mM **2a** solution. Samples were prepared by adding solutions/gels onto a glass slide and drying before observation by fluorescence microscopy. Control images of 5 mM **2a** were obtained to conclude that no fibrous structures were present before addition of enzyme (Appendix T). Fibre growth was studied over time by preparing dried samples of the enzymatic reaction after 1, 2 and 20 hours of the addition of AP (see **Figure 87** overleaf). At the 1 hour time point, only short fibrous structures were observed but after 2 and 20 hours fibre networks and aggregates of fibres were seen. The fully gelled sample at 20 hours displayed a number of fibrous arrangements from bundles and networks to previously observed (with ThT stained **1a**) fibrous spheres, *i.e.* fibres growing from a central point.

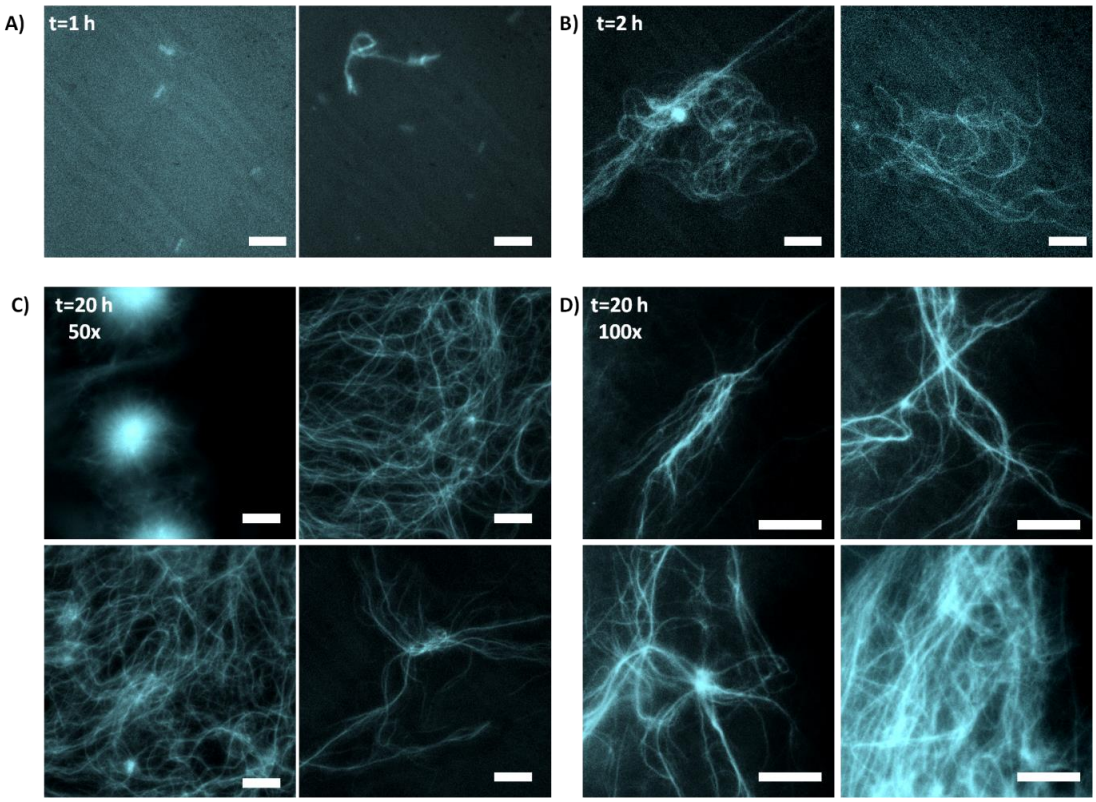

Figure 87 – Fluorescence micrographs of 5mM **2a** with AP at (A) 1 hour, (B) 2 hours, (C) and (D) 20 hours after addition of 4U AP dried onto glass surface. False coloured to represent colour physically observed through microscope binoculars. Scale bars = 20 µm.

A similar time study was performed for 5mM **2a** and AP conjugated to QDs (QD-AP) - as shown in **Figure 88** overleaf. At the shorter time points *e.g.* 1 and 2 hours, no structures were observed. Twenty hours after the addition of QD-AP to **2a** showed localised clusters of short fibrous structures, in line with a slower conversion rate compared to free AP (QD-AP upper limit of 7×10^{-4} U compared to 4 U with AP).

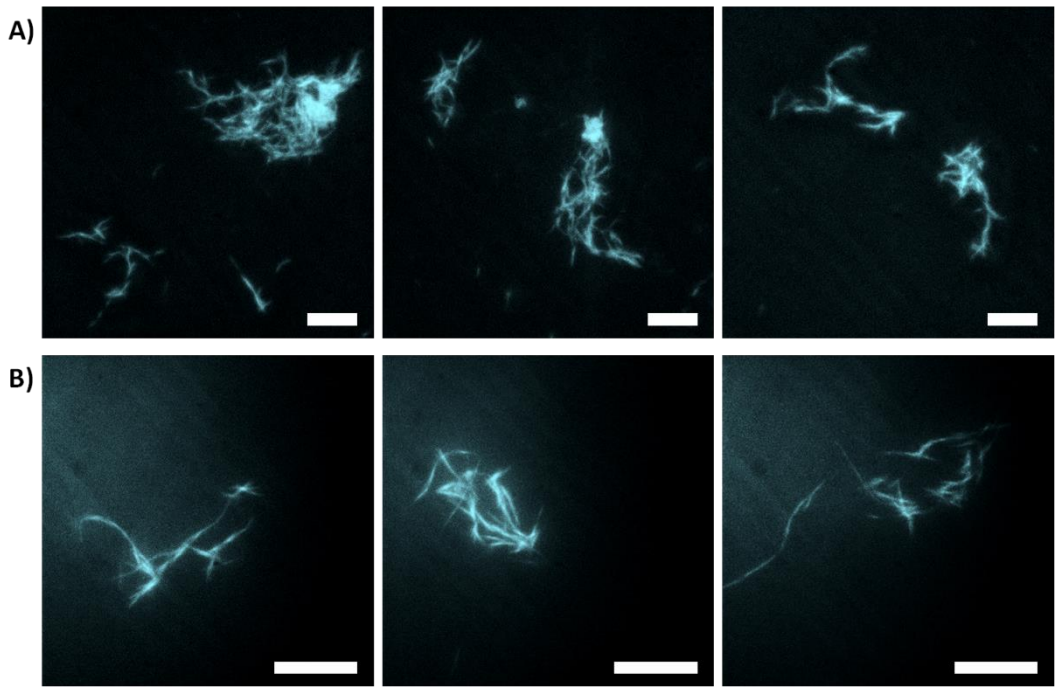

Figure 88 - Fluorescence micrographs of 5 mM **2a** with QD-AP 20 hours after addition, dried onto glass surface, (A) 50x and (B) 100x magnification. False coloured to represent colour physically observed through microscope binoculars. Scale bars = 20 µm.

8.4.2. 2-photon microscopy

Previous fluorescence microscopy methods have proved successful for imaging both extrinsically stained fibres of **1b** and intrinsically fluorescent structures of **2b** dried on a 2D surface. Background fluorescence issues presented by an optically turbid three-dimensional environment (needed for tracking experiments), proved that conventional fluorescence microscopy was not an ideal technique for real-time monitoring of fibre growth.

Two-photon microscopy offers an attractive fluorescence imaging technique for imaging 3-dimensional environments such as cells and tissues. Infrared laser light used to excite the sample minimises the effect of scattering (observed for example with fluorescence microscopy motility experiments of QD-AP in the presence of **2a**). Absorption of light by the sample can be limited to a small volume therefore a lower light dose is experienced by the sample reducing photobleaching (often seen with one photon excitation). Two-photon microscopy can also be used for two-fluorophore systems due to a broad excitation spectrum.[324] See Appendix R for a comparison of one and two photon excitation.

Samples of **2a** were prepared in a simple flow cell arrangement and initial experiments with free AP (4 U) were performed to confirm visualisation of intrinsically fluorescent **2b** fibre structures. Twenty four hours after the addition of AP (to **2a**), fibrous spheres were observed, connected by networks of longer fibres (as seen previously with fluorescence microscopy) – see **Figure 89 (A)**. After 1 week, fibre networks are dense as seen on **Figure 89 (B)**.

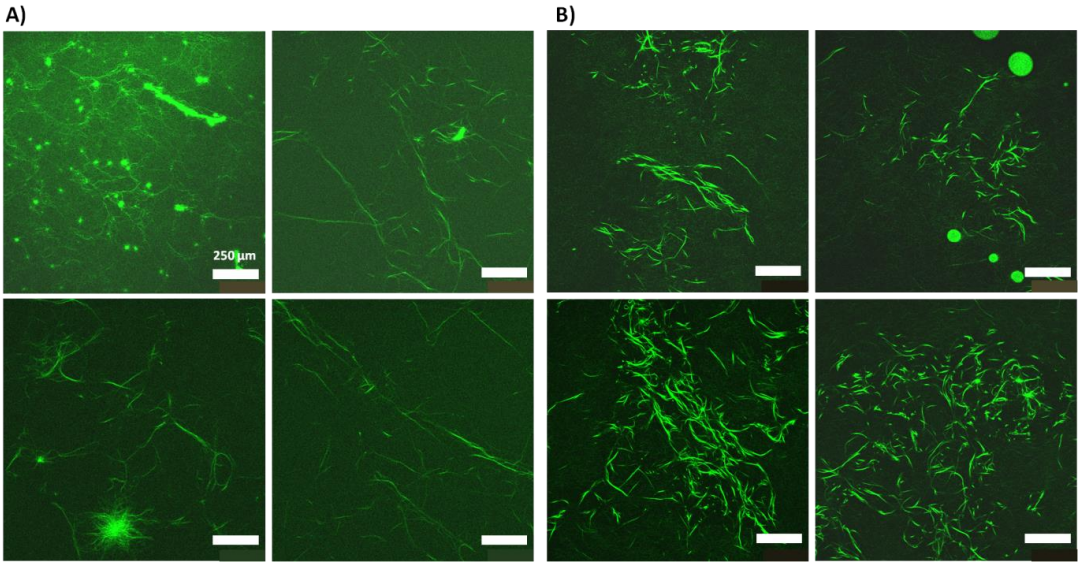

Figure 89 - Two-photon micrographs of 5 mM **2a**: (A) 24 hours and (B) 1 week after the addition of 4 U AP. Samples are imaged in a flow cell environment. Scale bars represent 25 µm, unless stated otherwise.

A similar time study was performed for **2a** and AP ($7x10^{-4}$ U) at the upper AP concentration as calculated for a known volume of QD-AP conjugates - shown in **Figure 90** overleaf. At 24 hours after the addition of AP, short fibres growing from central points in 'star-like' assemblies were observed throughout the sample (compared to long fibres connected in a network arrangement with higher AP concentration). At the 1 week time point localised clusters of fibrous assemblies were observed (**Figure 90 (B)**), in line with the assumption of localised regions of fibrous structures with low enzyme concentrations ($7x10^{-4}$ U AP compared to 4U of AP).

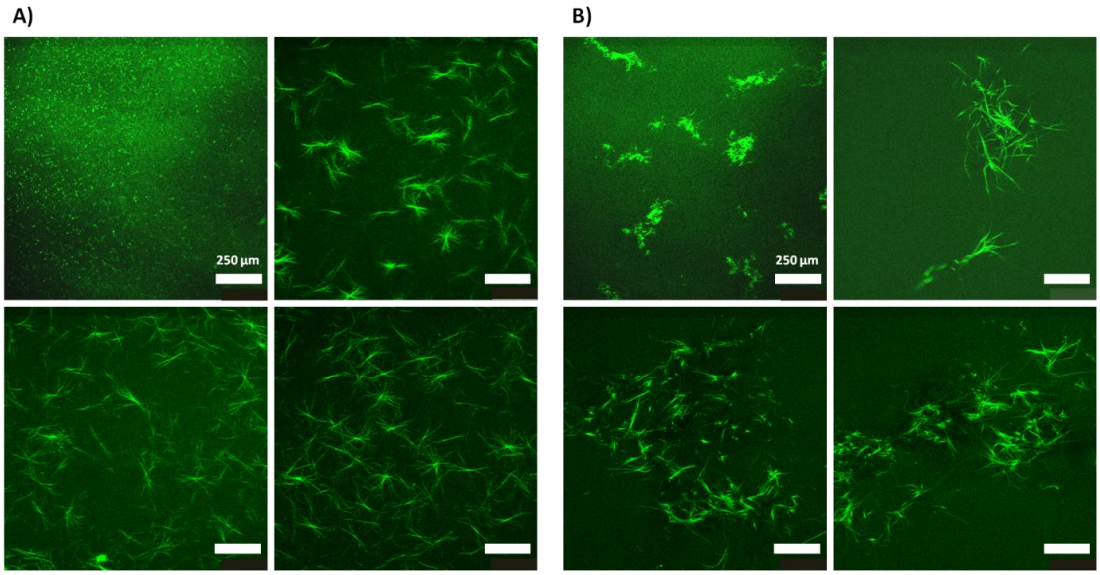

Figure 90 - Two-photon micrographs of 5 mM **2a**: (A) 24 hours and (B) 1 week after the addition of $7x10^{-4}$ U AP. Samples are imaged in a flow cell environment. Scale bars represent 25 µm, unless stated otherwise.

Finally, the same time study was performed for **2a** and QD-AP (estimated AP upper limit of $7x10^{-4}$ U). At 24 hours after the addition of QD-AP, short singular fibres or fibre bundles were seen throughout the sample (compared to fibrous networks and star-like assemblies for AP at 4 and $7x10^{-4}$ U respectively). At the 1 week time point localised dendritic fibrous assemblies were observed (**Figure 91** overleaf). Interestingly the resulting **2b** structures observed with AP conjugated to QDs and non-conjugated AP are considerably different, implying that the fact enzymes are immobilised or conjugated to the QDs has an effect on the self-assembly process. It may therefore be possible to control self-assembled structures of the same starting material by altering the enzyme *e.g.* conjugating to QDs, although further work in this area is beyond the scope of this thesis. This effect could also be due to the fact that there may be numerous QDs per enzyme molecule (*i.e.* estimated QD:enzyme ratios of 2.8:1 or 13:1) which could sterically hinder the biocatalytic reaction and resulting fibre growth, leading to the observed dendritic fibrous structures.

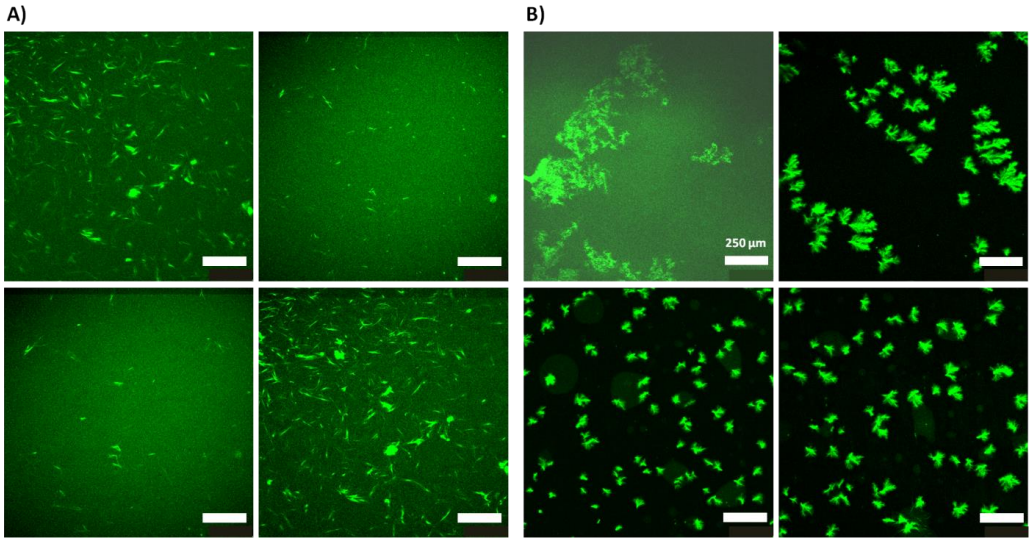

Figure 91 - Two-photon micrographs of 5 mM **2a**: (A) 24 hours and (B) 1 week after the addition of QD-AP. Samples are imaged in a flow cell environment. Scale bars represent 25 µm, unless stated otherwise.

8.5. Towards fibre visualisation by co-assembly with intrinsically fluorescent 2a

In a final attempt to visualise the self-assembled structures of **1b**, free pyrene and pyrene containing **2a** were investigated for fluorescent 'doping' of **1b**. Fluorescent doping involves the addition of small amounts (nM-µM) of a fluorescent probe to a precursor solution of a self-assembling system, for incorporation into the resulting supramolecular structures. Previous spectroscopic studies of **1a** (converted to **1b** by AP) in the presence of molecular pyrene, suggested that pyrene became incorporated, to some extent, within the resulting fibre structures of **1b**.[207] Additionally Xu *et al.* report the fluorescent imaging of non-fluorescent phosphatase responsive self-assembled structures by incorporating a fluorescent dansyl-analogue.[325] Taking advantage of these findings, free pyrene (100 nM) was added to a 10 mM solution of **1a** before adding 4 U of AP. One, two and twenty four hour time points were obtained by drying 25 µL onto a glass slide and drying before observation by fluorescence microscopy. Fibrous structures were not observed, instead only small fluorescent 'spots' were seen (Appendix U).

Further to this, a similar study was performed which involved combining **1a** and **2a** prior to enzyme addition for co-assembly into fibrous structures. Co-assembly of aromatic dipeptides, functionalised by Fmoc and pyrene, has been reported recently.[205] Mixing an

intrinsically fluorescent pyrene-functionalised dipeptide **2a** (emission in the visible range), with an Fmoc-functionalised dipeptide **1a** (emission in the UV range), which both assemble in response to biocatalytic conversion of AP, may provide an alternative method to extrinsic staining for fibre visualisation. Xu *et al.* report doping non-fluorescent (enzyme responsive) self-assembling molecules with fluorescent molecules for visualisation and detection in cells.[325]

Issues which arise from highly fluorescent **2a** at concentrations greater than 1 mM (as described in section 7.5), could also be addressed by altering the ratio of the **1a**:**2a** mixture to ensure pyrene fluorescence does not dominate for future uses with QD-AP tracking. Initial fluorescence microscopy observations of dried samples of 9:1 mM **1a**:**2a**, revealed a number of undefined fluorescent regions on the glass surface (see **Figure 92**). Two-photon microscopy analysis of the same sample, in a 3-dimensional flow cell arrangement, showed a number of non-uniform structures such as sheets, fibres and small spheres which could represent micellar structures. These findings indicate that individual biocatalytic systems (*e.g*. conversion of **1a** and **2a** to **1b** and **2b** respectively), form fibrous self-assembled structures, when combined disruption of the resulting supramolecular structures are seen to take place.

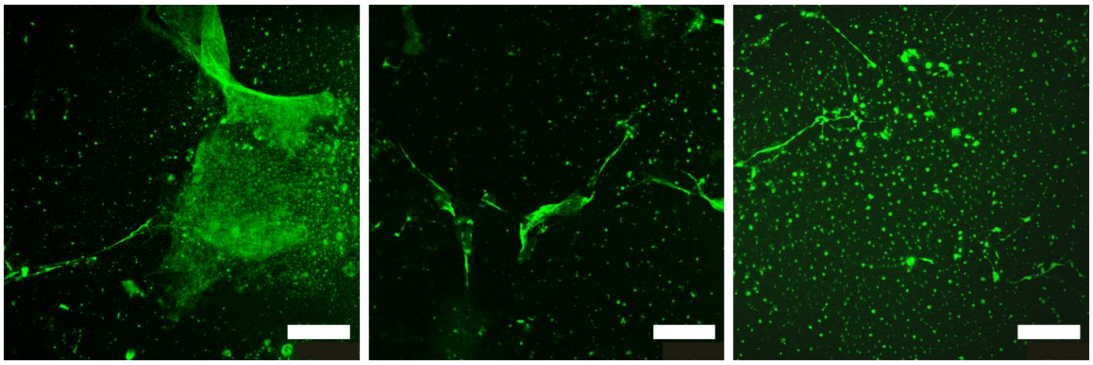

Figure 92 - Two-photon micrographs of 10 mM **1a**/1mM **2a**, 1 week after the addition of 4 U AP. Sample imaged in a flow cell environment. Scale bars represent 25 µm.

8.6. Towards simultaneous fibre and QD-AP conjugate visualisation

As discussed previously, in order to gain information about the apparent self-assembly driven diffusion of QD-AP conjugates with 10 mM **1a** (section 7.4), simultaneous visualisation of the resulting self-assembled structures and QD-AP is required.

Cryo-TEM was used to confirm the presence of fibrous structures using enzymes conjugated to quantum dots (**Figure 93**), however this method does not allow for real time dynamic monitoring of the process. QD-AP conjugates also have a similar appearance to ice crystals which are common artefacts seen with cryo-TEM, therefore making it difficult to distinguish between features.

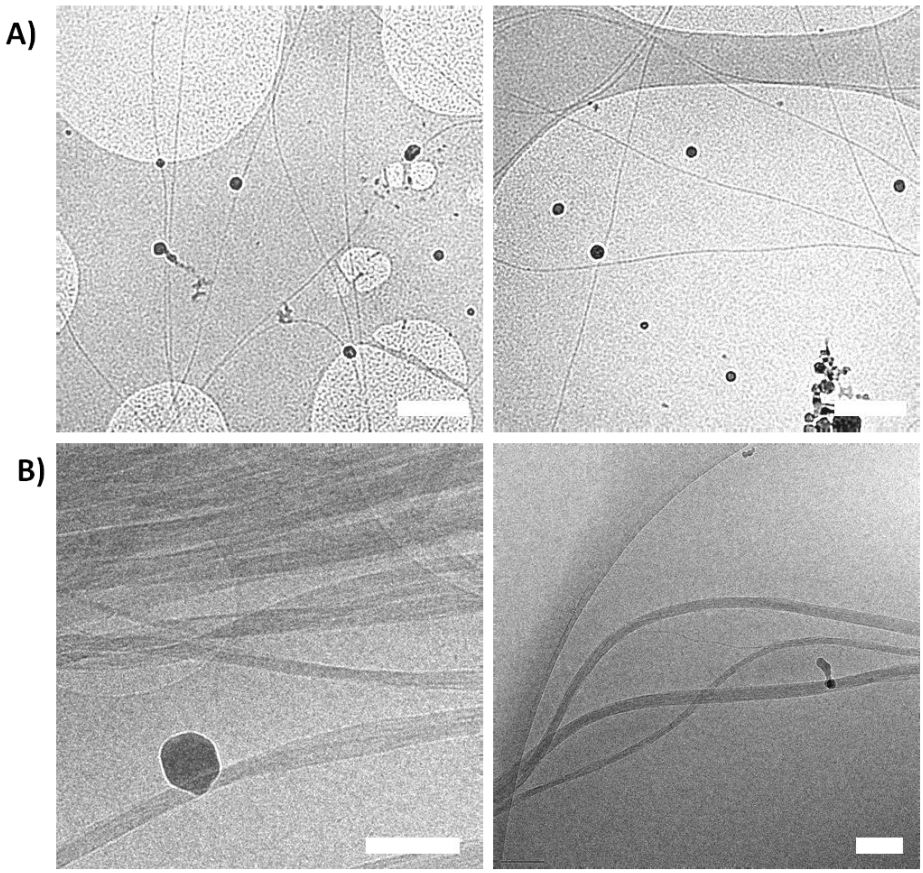

Figure 93 - Cryo-TEM images of (A) 10 mM **1a** (converted to **1b** by QD-AP) and (B) 5 mM **2a** (converted to **2b** by QD-AP). Scale bars represent 200 nm.

In theory, fluorescence microscopy offers a route to simultaneous two-fluorophore visualisation using a combination of optical filters and fluorophores which have the

same/similar excitation wavelengths. Individually, extrinsically stained fibres of **1b** and intrinsically fluorescent **2b** fibres were studied in combination with QD-AP conjugates using appropriate optical filters.

ThT stained fibres of **1b** (made from QD-AP from **1a**) were visualised dried on a glass surface, using the conditions as described previously (section 8.3). Excitation of both ThT and QD-AP conjugates was achieved by 435 nm illumination. **Figure 94** overleaf illustrates ThT stained **1b** fibre visualisation using a 482 nm emission filter (as shown previously with AP system). Switching the filter to 650 nm facilitates the detection of the QD-AP conjugates within the same sample (as shown in **Figure 94 (B)**). A two-camera/optical filter system would allow for real-time simultaneous visualisation of two fluorophores, without the need to switch between filters. The final system requires the detection of multiple wavelengths therefore dichroic filters are not employed, as these generally selectively pass light of a particular wavelength or wavelength range, whereas here we would need to pass multiple wavelengths to the detector. This allows for maximum light to reach the detector (camera) however may play a part in background fluorescence or scattering noise. It can be seen from **Figure 94 (B)**, that although a single band optical filter is in place to capture only QD-AP fluorescence (650/60nm), some noise/scattered light from ThT stained fibres is evident in some cases, as well as signal from the target QD-AP conjugates.

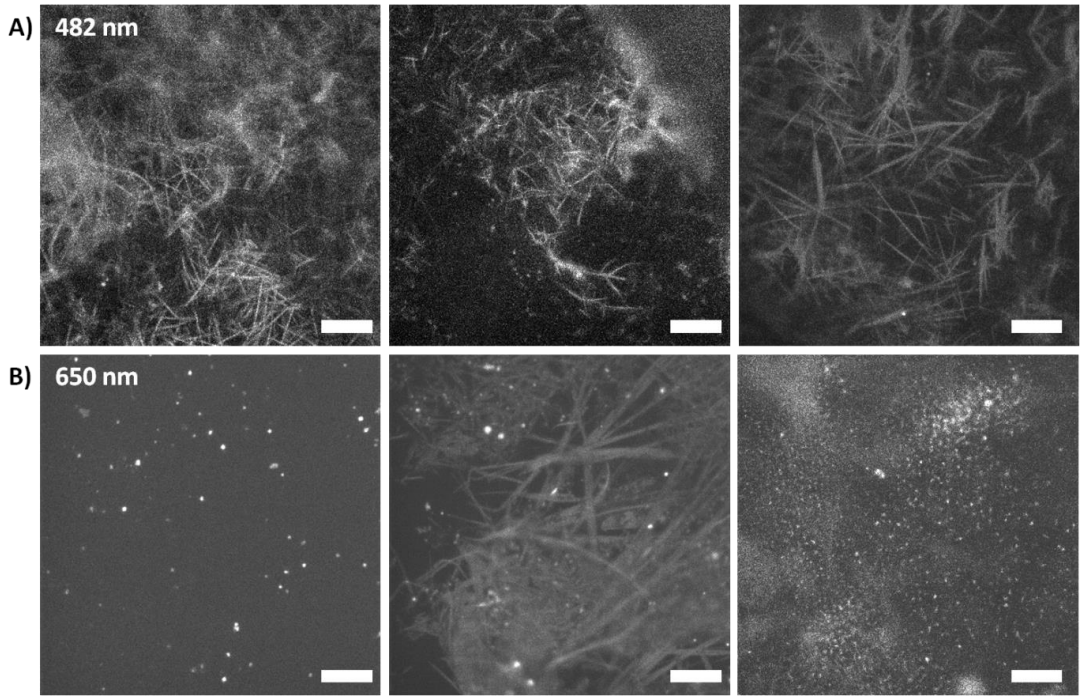

Figure 94 - Fluorescence micrographs of different areas containing dried samples of 10 mM **1a** stained with ThT and the addition of QD-AP (1 week after addition). (A) Detection of ThT stained fibres using 482 nm optical filters and (B) Detection of QD-AP conjugates with 650 nm optical filter. Scale bars = 20 µm.

In an attempt to gain evidence of co-localisation of self-assembled fibres and QD-AP conjugates, the same area of sample was visualised with both excitation filters *i.e.* 482 nm for ThT and 650 nm for QD-AP. **Figure 95**, shows an example of ThT stained **1b** (although no defined fibres were seen) and on the same sample, QD-AP signal was detected by switching excitation filters.

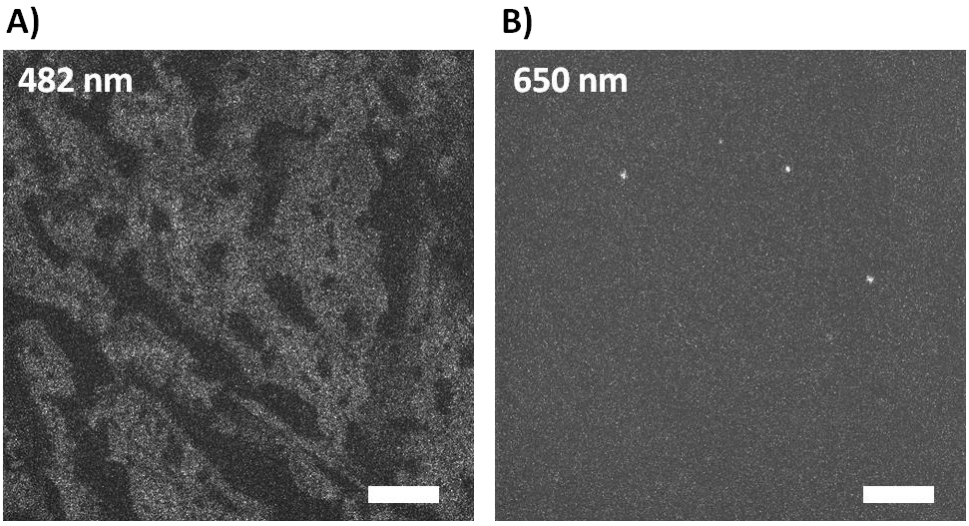

Figure 95 - Fluorescence micrographs of the same area of dried 10 mM **1a** stained with ThT and the addition of QD-AP (1 week after addition). (A) Detection of ThT stained fibres using 482 nm optical filters and (B) Detection of QD-AP conjugates with 650 nm optical filter. Images obtained are of the same area using different detection filters. Scale bars = 20 μm.

Individual observation of the intrinsically fluorescent system **2a**, proved advantageous over extrinsic methods in terms of sample preparation and fluorescence intensity. Therefore simultaneous visualisation of fibre and QD-AP conjugates with **2a** was studied using a combination of optical filters for detection of pyrene (417 nm) and QD-AP (650 nm) – see Appendix B for optical filter combination. Very few QD-AP conjugates were observed however one example is shown in **Figure 96**, which illustrates possible co-localisation of **2b** fibres and a QD-AP conjugate (as shown in the overlaid image – **Figure 96 (C)**). The lack of fluorescent conjugates observed could be attributed to a quenching effect (discussed in section 6.10.1, with **1a**), another explanation could be that the conjugates interact and immobilise onto the glass surface leading to a quenching effect. In an effort to investigate possible quenching but also determine whether QD-AP conjugates can be visualised simultaneously with fibres immobilised on a surface, 'fresh' QD-AP conjugates were added to a slide containing dried fibres of **2b**, prepared previously. Sample video 13 (supplementary material) shows that QD-AP conjugates can be observed (with 650 nm optical filter) despite background noise from fluorescent **2b** fibres. This effect would multiply if fibres were present in all directions of the sample *i.e*. 3D flow cell, preventing the effective tracking of QD-AP conjugates (as found in section 7.5 with **2a** concentrations

greater than 1 mM). Similarly with 2-photon microscopy, **2b** fibre signal is detected in the 'red' QD-AP region even at **2a** concentrations of 1 mM (Appendix V).

It can also be seen in sample video 13 (supplementary material) that QD-AP conjugates appear to 'stick' and immobilise on to the surface and/or fibre structures on the surface, one possible reason for the inability to detect conjugates after a period of time *i.e.* 24 hours.

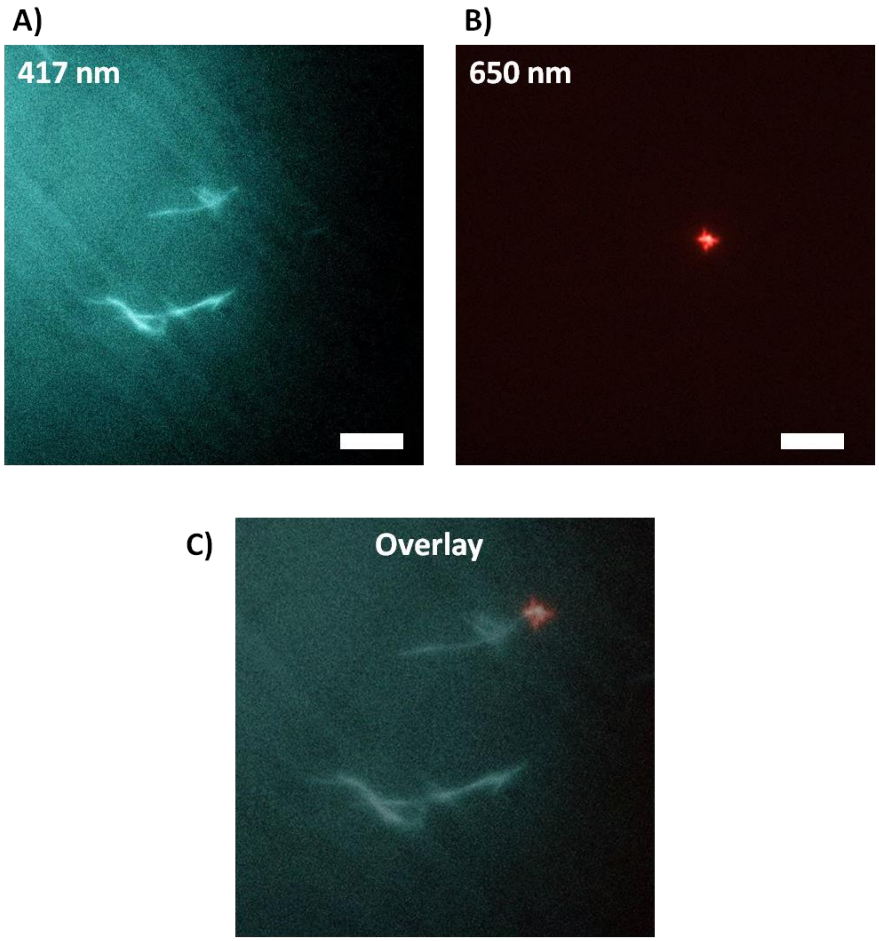

Figure 96 - Fluorescence micrographs of intrinsically fluorescent 5 mM **2a** with QD-AP dried on glass surface (20 hours after addition). (A) Detection of **2a** fibres using 417 nm optical filter and (B) Detection of QD-AP conjugates with 650 nm optical filter. (C) Overlaid images representing observation through microscope binoculars. Images obtained are of the same area using different detection filters. Scale bars = 20 µm.

8.7. Summary

In summary the successful visualisation of biocatalytically induced self-assembled structures of **1b** and **2b** was achieved by extrinsic and intrinsic methods respectively. Two-

photon microscopy proved to be the most promising technique for real-time fibre visualisation in a three-dimensional environment. Supramolecular assemblies observed for **2b** were shown to differ in response to whether the enzyme was conjugated to QDs or not, therefore offering a potential route for the control of resulting biocatalytic self-assembled structures which would be worth further investigations.

Ultimately in order to gain further information about the QD-AP propulsion mechanism, simultaneous fibre and QD-AP conjugate visualisation was attempted. Self-assembled fibres and conjugates were successfully visualised by fluorescence microscopy but only when immobilised on a 2D surface, and there remain significant barriers to an optimised technique that could be used for the simultaneous real time tracking of fibres and QD-AP conjugates. It may, in fact, be impossible technologically at this stage to visualise the self-assembly process of molecules in real time due to the short (nano-second) time-scale at which the interactions occur.

– Chapter 9 –

Towards a multi-enzyme nanomotor system

9.1. Objectives

The objective here is to demonstrate the possibility of using different biocatalytic self-assembling systems to achieve nanopropulsion, for example using different enzymes such as thermolysin or α-chymotrypsin and corresponding substrates. Additionally the potential to use different coloured quantum dots is investigated towards multi-enzyme/QD dual tracking of conjugates.

9.2. Introduction

In previous chapters QD-AP conjugate propulsion was confirmed with fibre-assembling substrate **1a** and directional control of QD-AP conjugates was initially explored by substrate saturated gel reservoirs. Additionally visualisation studies have proved that simultaneous two fluorophore detection is possible with fluorescence microscopy using a combination of optical filters. These findings form a potential route towards demonstrating separate 'nanocontrol' of enzymes in mixtures by self-assembly driven nanopropulsion. Demonstrating this would involve conjugating different enzymes *e.g.* thermolysin and alkaline phosphatase to different coloured quantum dots (red and green emitting) and by combining with 'fuel' reservoirs containing specific enzyme substrates, enzymes may be separated from a mixture.

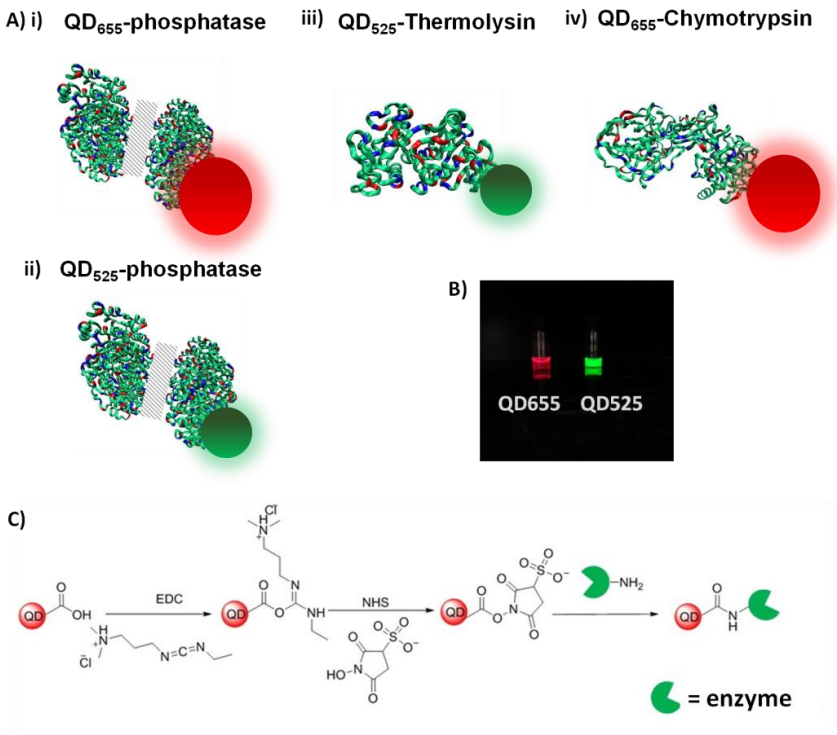

Figure 97 - Scheme of proposed enzyme-QD conjugates. (A) Alkaline phosphatase dimer conjugated to (i) 655 nm and (ii) 525 nm emitting QDs (hashed lines represent interactions between monomer units in an AP dimer); (iii) Thermolysin conjugated to 525 nm emitting QDs and (iv) α-chymotrypsin enzymes conjugated to 655 nm emitting QDs. (B) 655 and 525 nm emitting QDs under UV illumination (365 nm). (C) Bioconjugation reaction *via* an EDC/NHS coupling method.

As described in section 5.6 alkaline phosphatase was conjugated to 655 nm emitting (red) quantum dots. To investigate the possibility of producing AP conjugates with a different colour (and size) of QD, conjugation is performed with 525 nm emitting QDs (green) to make QD_{525}-AP conjugates (**Figure 97 (A)**).

As shown in **Figure 97**, α-chymotrypsin (from bovine pancreas) and thermolysin (from *Bacillus thermoproteolyticus rokko)* are also investigated towards a potential multi-enzyme system for applications in nano-separation of enzymes. Protease enzymes such as α-chymotrypsin and thermolysin are known for their hydrolytic abilities, however here we aim to take advantage of their reverse hydrolysis capabilities for the biocatalytic self-assembly of aromatic dipeptides.

9.3. Alkaline Phosphatase-QD_{525} Bioconjugation

Alkaline phosphatase was conjugated to carboxyl functionalised 525 nm emitting quantum dots *via* EDC/NHS coupling as described in section 5.6. Reagents and excess enzyme were removed by filtration and centrifugation (see section 5.7) and purification was monitored by the colorimetric *p*-nitrophenyl phosphate UV-Vis assay as described in section 5.8, see Appendix W.

An activity assay was performed to confirm activity of QD_{525}-AP and to compare with QD_{655}-AP conjugate (**Table 10**), showing that the QD_{525}-AP is less active than the red QD analogue (QD_{655}-AP), however the activity of QD_{525}-AP is significantly above that of the no enzyme control. Apparent loss of activity could be due to reduced QD concentration through loss of green QDs during handling due to the smaller size compared to 655 nm quantum dots. Filter units used for the preparation of conjugates appeared fluorescent in the green region when observed under UV illumination (365 nm), suggesting that QDs were retained within the filter. Another possible reason as to the reduction in activity could be attributed to the smaller size of green QDs, leading to fewer AP molecules conjugating to QDs compared to the larger 655 nm emitting QDs. Conjugation for this system has not been optimised so further work would be required to improve and control the activity of the conjugates.

Table 10 - Activity assay for QD_{525}-AP with *p*-nitrophenyl phosphate substrate monitored by UV-Vis at 410 nm (ΔA_{410nm}) and compared to the activity of QD_{655}-AP

Sample	ΔA_{410nm}
Control	0.00
QD655-AP (batch 3)	9.6×10^{-3}
QD525-AP	1×10^{-5}

9.3.1. Alkaline Phosphatase-QD_{525} Characterisation

DLS was performed to obtain size distribution information for QD_{525}-AP compared with free QDs (525 nm emitting) and also with QD_{655}-AP conjugates which are expected to be larger in size. **Figure 98** demonstrates that QD_{525}-AP conjugates have a wider size distribution compared to free QDs (525 nm) and a shifted peak giving hydrodynamic radius values of 6.4 nm and 1.2 nm respectively. QD_{525}-AP conjugates (6.4 nm radius) are found to be smaller than QD_{655}-AP which has a hydrodynamic radius value centred around 10.3 nm.

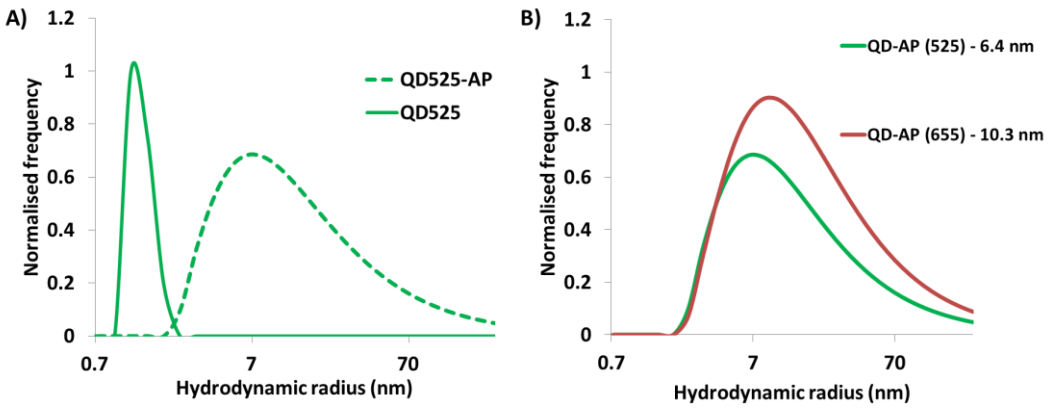

Figure 98 – (A) DLS size distribution of QD_{525} (green solid line) and QD_{525}-AP (green dashed line) and (B) size distribution comparison between QD_{655}-AP (batch 6) and QD_{525}-AP (red and green lines respectively) with average hydrodynamic radius values of 6.4 and 10.3 nm respectively.

The fluorescence emission spectra of QD_{525}-AP conjugates (200 µL/mL) and a sample of 1 nM QDs (525 nm) were compared as shown in **Figure 99**. A small red-shift of the λ_{max} is observed after conjugation, however from a fluorescence microscopy perspective, the shift isn't significant enough to affect observation and tracking, as detection relies on an optical filter which passes light over a wavelength range. It is worth noting that during conjugation a number of wash steps and dilutions are performed therefore the resulting conjugate solution used for all measurement and investigations will contain unknown QD concentrations. An estimate of QD concentration in a given volume of conjugate *i.e.* µL/mL, can be performed by comparison with a known QD concentration, however this assumes that the optical properties of the QDs are unaffected by the conjugation process.

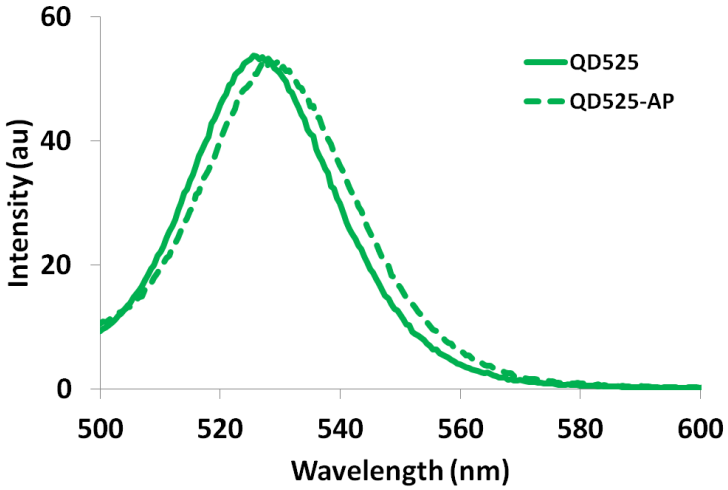

Figure 99 - Fluorescence emission spectra of QD_{525} (solid line) and QD_{525}-AP conjugates (dashed line).

9.3.2. Towards a two-fluorophore system

QD_{525}-AP conjugates were studied by fluorescence microscopy to confirm the ability to track individual conjugates. Under the same conditions as described previously for QD_{655}-AP *i.e.* glass bottom dish, oil immersion objective (section 7.3). QD_{525}-AP conjugates were imaged with 365 nm illumination and detected with a 536/40 nm single band optical filter (see Appendix X for optical filter combination).

Mixed solutions of both free QDs and QD-AP conjugates (525 and 655 nm) were analysed by fluorescence spectroscopy to show the combined fluorescence emission spectrum when excited at 365 nm (**Figure 100**). In terms of fluorescence intensity the 'green' QDs were less intense despite being the same concentration as 655 nm QDs (as quoted by the manufacturer). This effect can be related to the lower extinction coefficient of the green QDs.[229] A more pronounced effect was observed after conjugation with AP despite there being an increased conjugate volume/mL of 200 µL/mL QD_{525}-AP, compared to 50 µL/mL for the QD_{655}-AP. Again this could be attributed to loss of material during conjugation. As mentioned previously volumes of conjugate per millilitre cannot easily be compared due to the unknown QD concentration after conjugation, as each conjugate may be washed and diluted to a different extent.

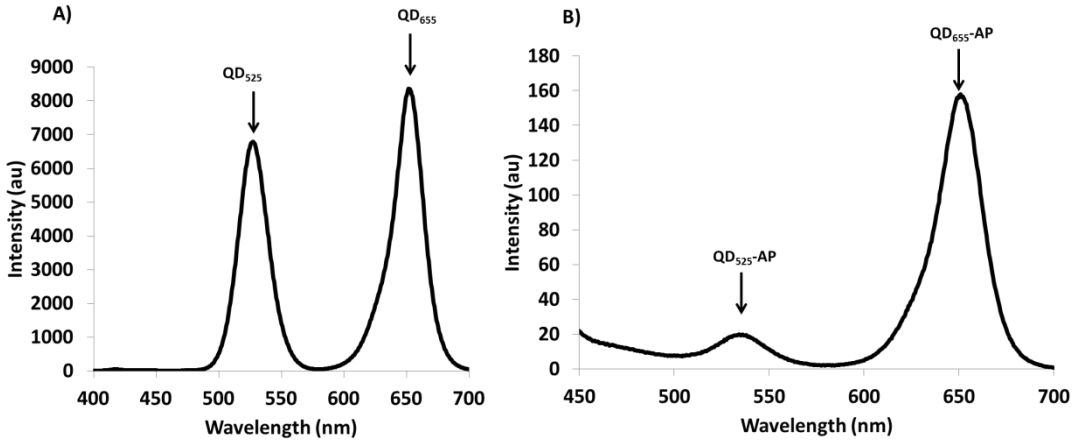

Figure 100 – (A) Fluorescence emission spectrum of a mixed solution containing QD_{525} and QD_{655} (1:1 ratio), illustrating a difference in fluorescence emission intensity with the same concentration of QDs in each case. (B) A mixed solution of QD_{525}-AP (200 µL/mL) and QD_{655}-AP (50 µL/mL), exciting at 365 nm.

A mixed solution of 'red' and 'green' conjugates was then observed and tracked by fluorescence microscopy. Each conjugate was observed individually by switching between emission optical filters: 650/60 nm optical filter for QD_{655}-AP (32 µL/mL) and 536/40 nm optical filter for QD_{525}-AP (300 µL/mL) - see Appendix Y for optical filter combination. Volumes of conjugate per mL were chosen by comparing emission spectra by fluorescence spectroscopy, for samples which gave similar fluorescence intensities *i.e.* more of QD_{525}-AP is required per mL of buffer to achieve fluorescence intensity similar to QD_{655}-AP conjugates. Videos were obtained for each conjugate then tracked using the MATLAB tracking program to obtain frame-to-frame speed data (as described in section 4.3.4).

Frame-to-frame speed distribution plots in **Figure 101**, illustrate the overall faster speeds of smaller (by DLS) QD_{525}-AP conjugates, with an average frame-to-frame speed of 5.9 µm/s (based on 193 particles and 1 experiment). Larger QD_{655}-AP conjugates display an average frame-to-frame speed of 4.5 µm/s (based on 362 particles and 1 experiment).

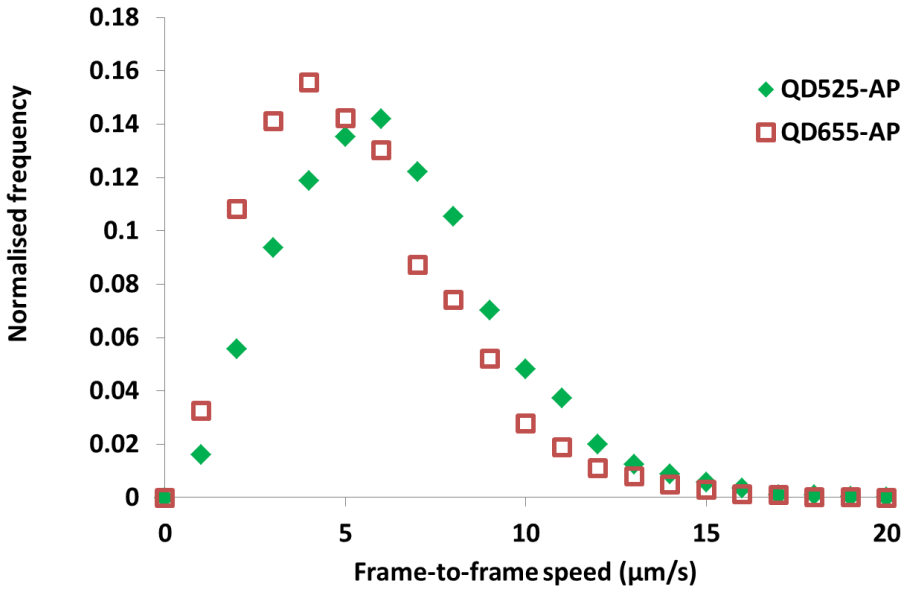

Figure 101 - Frame-to-frame speed distribution plots of a mixture of QD_{525}-AP/QD_{655}-AP without fuel.

9.4. Testing conjugation with other enzymes

Having confirmed the potential to simultaneously track a two QD/fluorophore system *i.e.* QD_{525}-AP/QD_{655}-AP by fluorescence microscopy, the next step towards a multi-enzyme-motor system driven by self-assembly, was to investigate the possibility of conjugating different enzymes to quantum dots.

Thermolysin and α-chymotrypsin are enzymes reported previously for biocatalytic self-assembly of aromatic dipeptide amphiphiles (as discussed in section 2.8).[179,203,211,214] They are investigated here towards the development of a multi-enzyme/multi-QD system by bioconjugation to different coloured QDs *i.e.* red and green.

Thermolysin and chymotrypsin were conjugated to 525 nm and 655 nm emitting quantum dots respectively (see sections 3.3.4 and 3.3.5 for conjugation method). Reagents and unconjugated enzymes were removed by filtration and centrifugation. The purification of each conjugate was analysed separately using activity assay protocols specific for the individual enzyme. QD_{525}-Therm is described in section 3.3.13 and QD_{655}-Chym in section 3.3.14 (see Appendix Z and Appendix AA for UV monitoring).

9.4.1. QD_{525}-Thermolysin characterisation

The activity assay for thermolysin relies on the hydrolysis of casein, monitored by UV-Vis (absorbance at 660 nm) using Folin and Ciocalteu's phenol reagent for the detection of amine groups resulting from enzymatic hydrolysis. The activity assay involves incubation at 37°C with several reagents (see materials and methods, section 3.3.13), before measuring a single absorbance value per sample at 660 nm. **Figure 102** overleaf shows the absorbance values for QD_{525}-Therm compared with free thermolysin (0.15 units/mL), a blank and unconjugated QD_{525} control. It can be confirmed that the activity of the blank, free QDs and QD_{525}-Therm conjugates were similar concluding that QD_{525}-therm conjugates were not active compared to free thermolysin. Although conjugates appear more active compared to free QDs, the method of obtaining the absorbance value involved multiple incubation steps with a number of reagents, followed by filtrations, and only one final absorbance reading is taken which could lead to some discrepancies between no or low levels of activity. Therefore there is a possibility that QD_{525}-therm conjugates have a very low activity that the standard activity assay is not sensitive enough to detect.

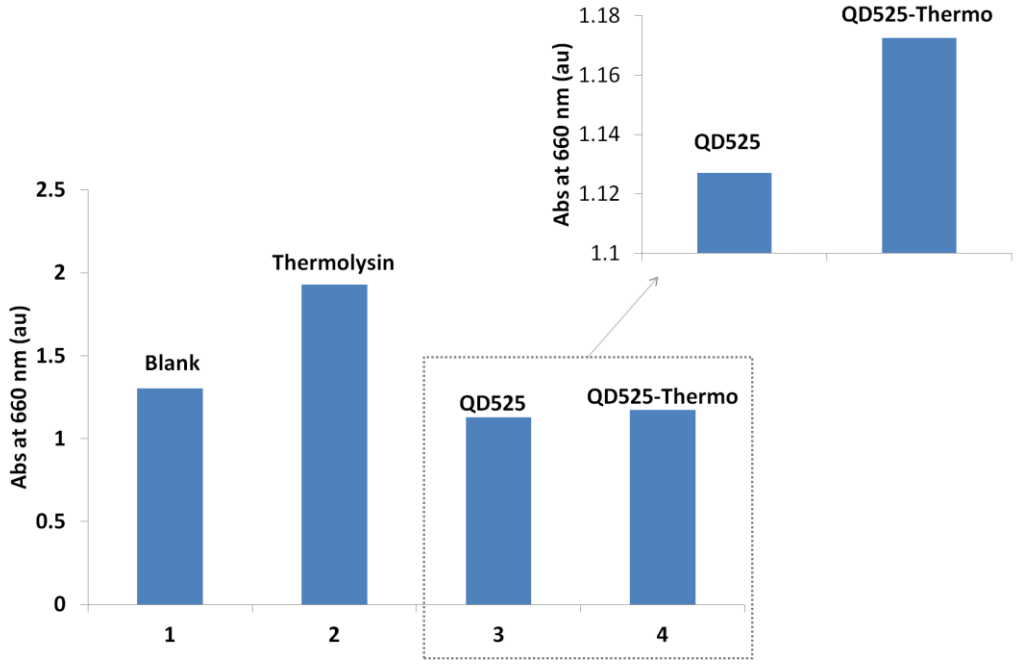

Figure 102 - QD_{525}-Therm activity assay - hydrolysis of casein and monitored at 660 nm.

DLS confirmed a larger size distribution of QD_{525}-Therm conjugates compared to thermolysin and QDs (525 nm emitting). Two populations are observed for QD_{525}-Therm conjugates however, one centred close to that of free QDs with a hydrodynamic radius of 2.4 nm (compared to 1.2 nm for QD_{525}), and the other hydrodynamic radius value centred around 69.8 nm (**Figure 103** overleaf). The presence of two size populations suggests that the solution contains a mixture of free unconjugated QDs as well as conjugates. Removal of free unconjugated enzyme is further confirmed by the absence of a size distribution similar to thermolysin.

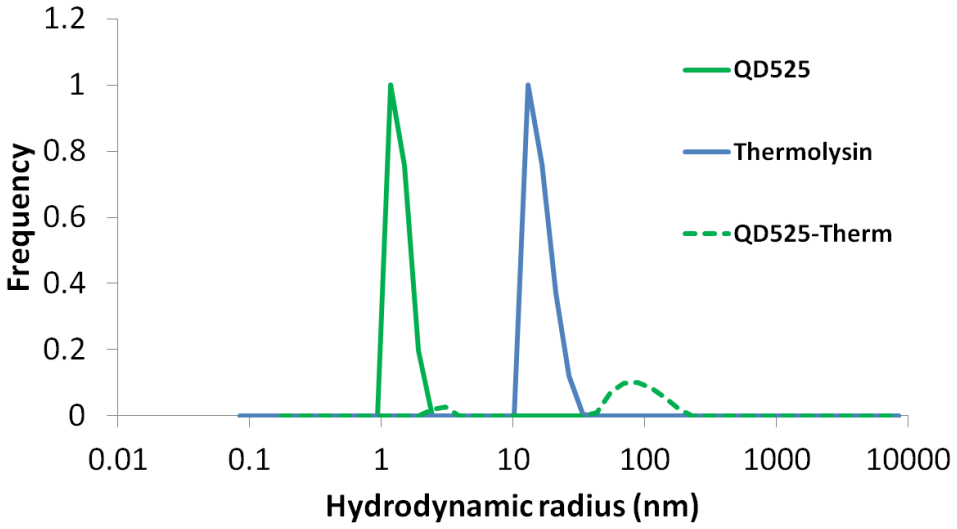

Figure 103 - Size distributions of QD_{525} (green solid line), thermolysin (blue solid line) and QD_{525}-Therm conjugates (green dashed line) measured by DLS. Plot of QD_{525}-Therm is mass unweighted whereas the other plots are mass weighted, hence the difference in scale.

The fluorescence emission spectra of QD_{525}-Therm conjugates and QDs (525 nm) were analysed as shown in **Figure 104**. The emission wavelength remains the same however the shape of the curve is altered after conjugation to thermolysin. The emission spectrum of QD_{525}-Therm appears multi-modal, which suggests the conjugation reaction may have had an effect on the QD structure. Interestingly QD_{525}-AP conjugates did not show the same effect (see **Figure 99**). Fluorescence emission was visibly reduced after conjugation (**Figure 104** inset), a possible result of handling *i.e.* QDs getting trapped in the filtration units, due to the smaller size of QD_{525} compared to QD_{655}, as mentioned previously.

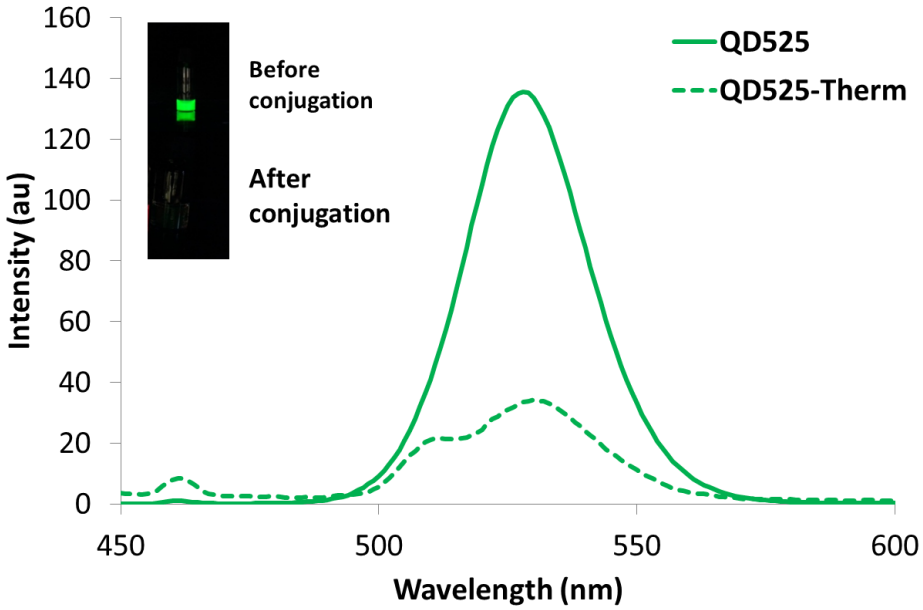

Figure 104 - Fluorescence emission spectra of QD_{525} (solid line) and QD_{525}-Therm (dashed line), excited at 435 nm. Inset shows QD_{525} before conjugation and QD_{525}-Therm after conjugation under UV illumination (365 nm lamp).

9.4.2. Proposed self-assembling substrate 'fuel' for QD_{525}-Thermolysin conjugates

The fuel substrate(s) for QD_{525}-Therm conjugates, for future applications in propulsion, were Fmoc-T-OH and F-OMe (see **Figure 105**). A similar system was reported for Fmoc-S-OH and F-OMe which upon addition of thermolysin underwent condensation (reverse hydrolysis) to Fmoc-SF-OMe which self-assembled into 2-D sheets.[179] Here, Fmoc-T-OH and F-OMe are expected to undergo reverse hydrolysis in the presence of QD_{525}-Therm conjugates, to Fmoc-TF-OMe fibres.[211]

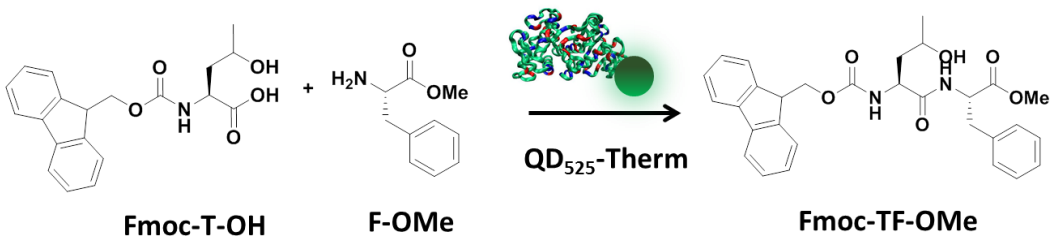

Figure 105 - Proposed substrate fuel system for QD_{525}-Therm. Fmoc-T-OH (10 mM) and F-OMe (40 mM) are reacted with thermolysin (conjugated to QDs) for the reverse hydrolysis to Fmoc-TF-OMe.

The conversion of starting materials (Fmoc-T-OH 10mM:F-OMe 40 mM) was monitored by HPLC in the presence of thermolysin and QD_{525}-Therm conjugates. After 24 hours the percentage converted to Fmoc-TF-OMe was 87 and 0 % by thermolysin and QD_{525}-Therm conjugates respectively (see

Appendix BB for thermolysin conversion).

Overall initial observations of the QD_{525}-Therm conjugates show the sample to be inactive, and the findings result in further questions about the stability of QDs and activity of thermolysin after conjugation.

9.4.3. QD_{655}-Chymotrypsin characterisation

The activity assay for chymotrypsin relies on ester hydrolysis of the substrate benzoyl-L-tyrosine ethyl ester (BTEE) monitored at 256 nm by UV-Vis spectroscopy. The absorbance (at 256 nm) is measured every 30 seconds for 5.5 minutes in order to determine a gradient (rate) ΔA value for comparison. **Table 11** shows the ΔA at 256 nm for QD_{655}-Chym conjugates compared with chymotrypsin (20 μg/mL) and a blank control (here an unconjugated QD_{655} control was not possible due to being highly absorbant at 256 nm). When comparing rates of conversion *i.e.* gradients, it can be seen that QD_{655}-Chym conjugates show activity compared to the negative control sample.

Table 11 - QD_{655}-Chym activity assay - ester hydrolysis of BTEE monitored at 256 nm.

Sample	ΔA(256nm)
Control	0.00000
QD655-Chym	0.00030
Chymotrypsin	0.00116

DLS analysis confirmed a larger size distribution of QD_{655}-Chym conjugates compared to chymotrypsin and QDs (655 nm emitting). As seen with QD_{525}-Therm, two populations are observed for QD_{655}-Chym conjugates, one centred close to that of free QDs with a hydrodynamic radius of 3.9 nm (compared to 3.9 nm for QD_{655}), and the other with a

hydrodynamic radius value centred around 16.5 nm, indicative of a successful conjugation reaction (**Figure 106**). The presence of two size populations suggests that the conjugate solution contains a mixture of free unconjugated QDs as well as conjugates. Removal of free unconjugated enzyme is further confirmed by the absence of a size distribution similar to chymotrypsin.

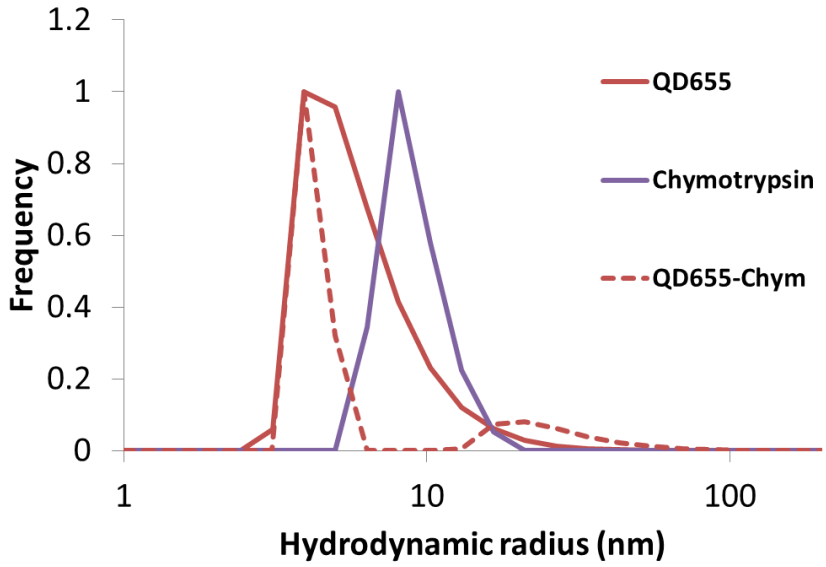

Figure 106 - DLS size distribution plots of QD_{655} (red solid line), chymotrypsin (purple solid line) and QD_{655}-Chym conjugates (red dashed line).

Fluorescence spectroscopy analysis of QD_{655}-Chym conjugates and QDs (655 nm emitting) are shown in **Figure 107**. The emission spectra are symmetrical in appearance and λ_{max} wavelengths are comparable with a slight decrease in intensity after conjugation (attributed to, as above, dilution during filtration) – see **Figure 107** inset.

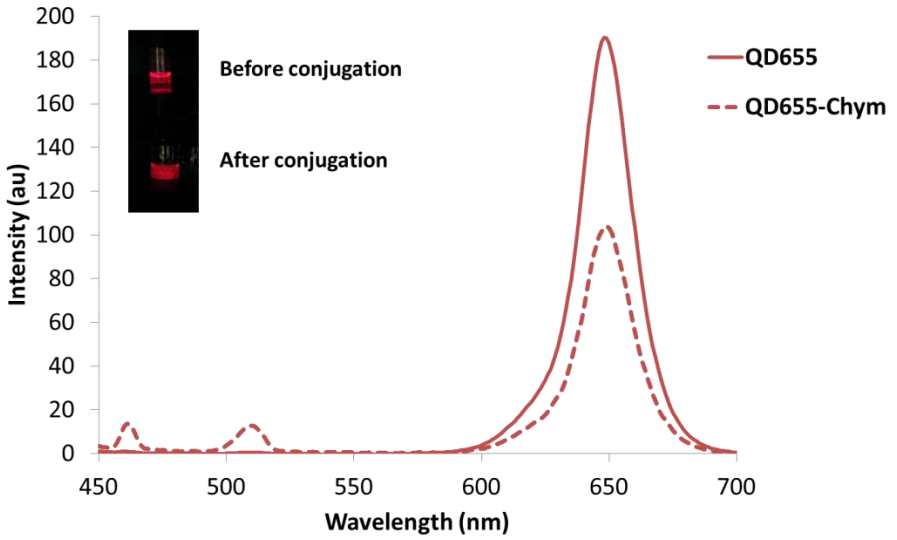

Figure 107 - Fluorescence emission spectra of QD_{655} (solid line) and QD_{655}-Chym (dashed line), excited at 435 nm. Inset shows QD_{655} before conjugation and QD_{655}-Chym after conjugation under UV illumination (365 nm lamp).

9.4.4. Proposed self-assembling substrate 'fuel' for QD_{655}-Chymotrypsin conjugates

The fuel substrate(s) for QD_{655}-Chym conjugates for future applications in propulsion were Pyrene-Y-OMe and Y-NH_2 (see **Figure 108** overleaf). A similar system was reported for Nap-Y-OMe and Y-NH_2 which upon addition of chymotrypsin starting materials were converted to Nap-YY-NH_2 which self-assembles into fibrous structures.[214] The resulting nanofibres diminish over time by the competing amide hydrolysis reaction by the same enzyme. This assembly and disassembly process could be used for a simple dynamically propelled system, similar in concept to actin polymerisation/depolymerisation driven motion. Actin polymerisation relies on the availability of the chemical fuel ATP for the polymerisation of actin at one end of the filament while at the other end depolymerisation occurs more rapidly (see section 2.1). The use of a dissipating system for motion, in which biocatalytic self-assembly initially occurs and the same enzyme is then responsible for performing the opposite reaction to disassemble the structures, could provide a route to a simplified analogue of a dynamic biological system such as that displayed by actin.

Here Pyrene-Y-OMe and Y-NH_2 are expected to convert to Pyrene-YY-NH_2 in the presence of QD_{655}-Chym conjugates. This system would have the advantage of intrinsic fluorescence from pyrene.

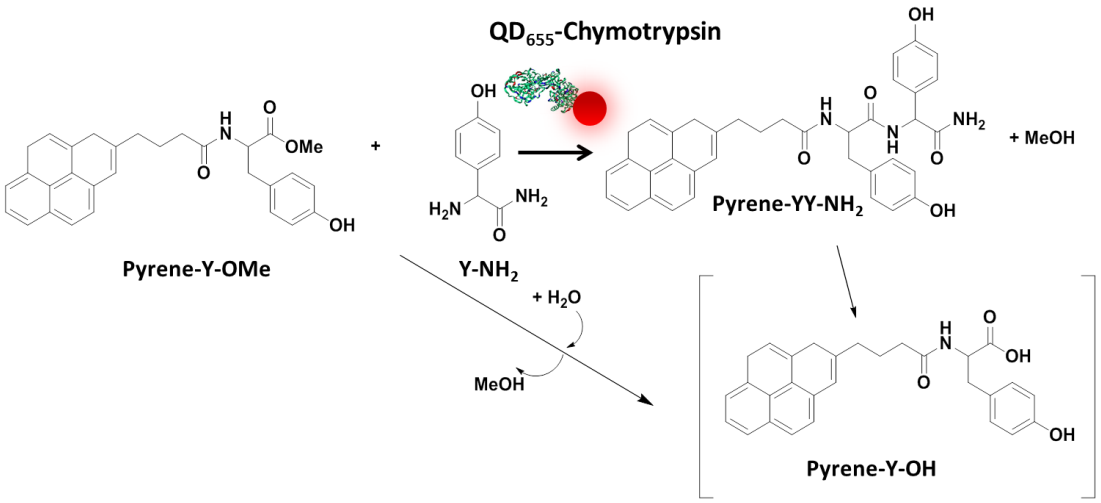

Figure 108 - Proposed substrate fuel system for QD_{655}-Chym conjugates. Pyrene-Y-OMe and Y-NH_2 are combined by catalysis with QD_{655}-Chym to pyrene-YY-NH_2 (and Pyrene-Y-OH side product).

The conversion of starting materials (Pyrene-Y-OMe 20mM: Y-NH_2 20 mM) in the presence of chymotrypsin and QD_{655}-Chym conjugates was followed by HPLC. After 24 hours the percentage converted to Pyrene-YY-NH_2 was 31.8 and 9.5% by chymotrypsin and QD_{655}-Chym conjugates respectively (see **Figure 109**). Conversion to Pyrene-YY-NH_2 by QD_{655}-Chym is considerably higher compared to other enzymatic (conjugate) reactions monitored by HPLC, for example QD_{525}-Therm with <1% conversion to product after 2 weeks.

Longer time points up to 240 hours were analysed for possible hydrolysis of Pyrene-YY-NH_2, however this was not observed by either free chymotrypsin or conjugates. This suggests that unlike the previously reported Nap-Y/Y-NH_2 system, Pyrene-Y/Y-NH_2 is thermodynamically stable. Alternatively there could be a barrier to hydrolysis *e.g.* limited substrate accessibility in the self-assembled state.

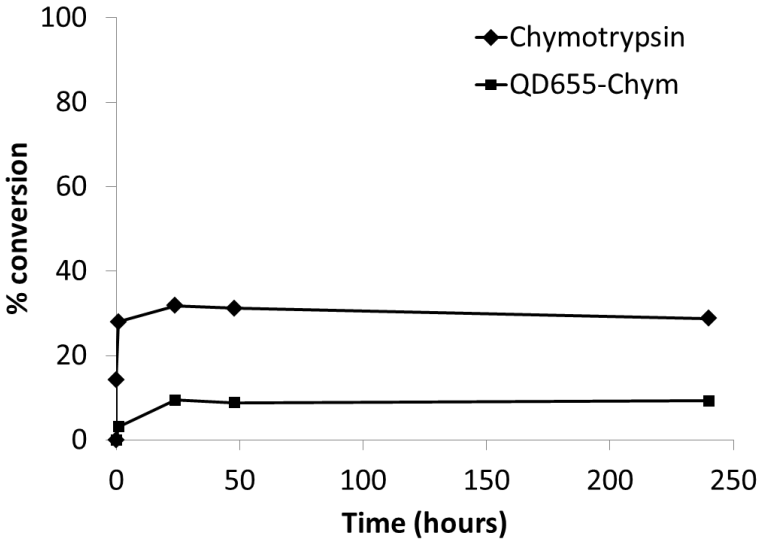

Figure 109 - HPLC conversion of Pyrene-Y-OMe and Y-NH_2 to Pyrene-YY-NH_2 by chymotrypsin and QD_{655}-chym conjugates.

9.4.5. Microscopy and tracking of QD_{655}-Chymotrypsin conjugates

Fluorescence microscopy was used to visualise solutions containing QD_{655}-Chym conjugates (as described in for QD-AP section 7.3). The microscope was fitted with a 650/60nm optical emission filter for QD_{655}-Chym detection and conjugates were excited at 365 nm. QD_{655}-Chym conjugates were added to a glass bottom dish in buffer with no fuel and a series of digital videos were recorded for subsequent tracking *via* MATLAB (as described in section 4.3.4). Here the frame-to-frame speed is analysed in comparison with QD_{655} and QD_{655}-AP with no fuel. Frame-to-frame speed distribution plots in **Figure 110** overleaf illustrate the overall faster speeds of smaller QD_{655}-Chym conjugates with an average frame-to-frame speed of 6.0 µm/s (based on 1084 particles and 1 experiment), compared to QD_{655}-AP conjugates (5.6 µm/s for average frame-to-frame speed, based on 1075 particles and 1 experiment, excited at 365 nm). Additionally these values can be compared to free 655 nm emitting quantum dots in which the average frame-to-frame speed was found to be 7.2 µm/s (based on 243 particles and 1 experiment) as illustrated in **Table 12**.

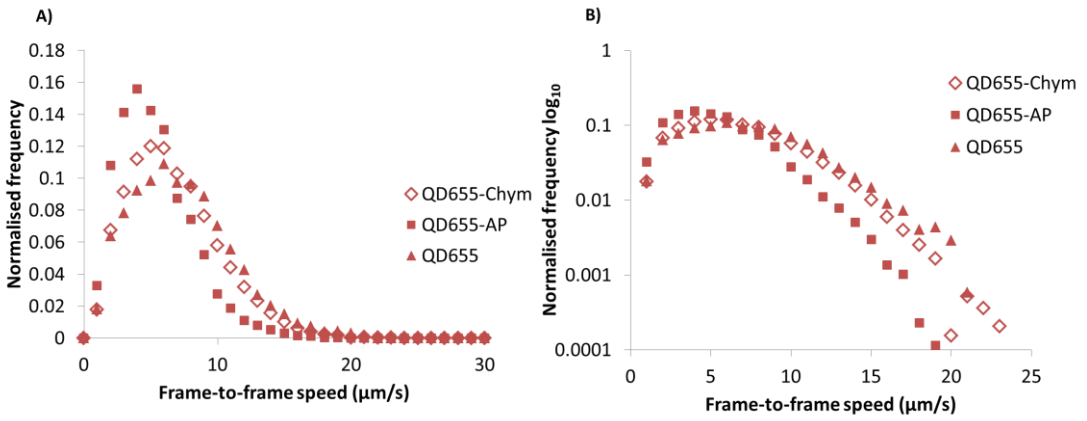

Figure 110 – (A) Frame-to-frame Speed distribution of QD_{655}, QD_{655}-AP and QD_{655}-Chym. (B) Speed distributions with logarithmic frequency scale.

In general, smaller conjugates/particles exhibit faster average speeds as shown in **Table 12**, which summarises average sizes and frame-to-frame speeds of conjugates and QDs. Although QD_{655}-Chym conjugates are larger in terms of average hydrodynamic radius compared to QD_{655}-AP, the presence of a population of smaller particles affects the overall frame-to-frame speed distribution.

Table 12 – Summary of frame-to-frame average speed and hydrodynamic radius values for QD_{655}, QD_{655}-Chym and QD_{655}-AP

	Average frame-to-frame speed (µm/s)	**Average hydrodynamic radius (nm)**
QD_{655}	7.2	3.9
QD_{655}-Chym	6.0	3.9 and 16.5
QD_{655}-AP	5.6	10.3

9.5. Summary

To summarise, the successful conjugation of active alkaline phosphatase and chymotrypsin to different coloured quantum dots was achieved, along with the development of methods to monitor removal of free enzyme in each case. The conjugation of thermolysin to 525 nm QDs was attempted but proved unsuccessful in terms of enzyme activity and fluorescence emission of QDs after conjugation. It can therefore be concluded that conjugation of different enzymes to QDs must be treated and optimised on an individual basis, as enzyme

structure *i.e.* conjugation sites and active site residues will play a key role in the conjugation reaction and resulting conjugate. With optimisation, however, based on the biocatalytic self-assembling systems summarised in **Table 6**, the conjugation of enzymes to quantum dots could lead to potentially many conjugate/self-assembly driven motility combinations.

A multi-QD (fluorophore) system was investigated by imaging and tracking phosphatase conjugated to green and red QDs by fluorescence microscopy showing the possibility of simultaneously tracking different populations. During initial studies optical filters were switched between one camera for alternate QD visualisation, however ideally simultaneous visualisation of red and green conjugates *e.g.* QD_{525}-AP and QD_{655}-Chym could be performed in real-time by utilising a two-camera set-up, where each camera is fitted with an optical filter corresponding to the fluorophores being studied.

These studies are the first steps towards a nano-separation device which uses biocatalytic self-assembly driven nanopropulsion. This idea would incorporate enzyme-specific substrate reservoirs (as seen in section 7.7) which could be used to separate and direct enzyme mixtures along corresponding substrate concentration gradients.

– Chapter 10 –

10.1 Conclusions, outlook and future work

Methods were developed for the conjugation of *Escherichia coli* alkaline phosphatase to 655 nm emitting quantum dots *via* an EDC/NHS coupling. Removal of unconjugated enzyme and reactants was achieved by filtration and centrifugation. A method was developed to monitor enzyme removal utilising a colorimetric enzyme activity assay, followed by UV-Vis spectroscopy.

Enzyme-QD conjugates were characterised by a number of techniques: DLS confirmed an increase in size after conjugation compared to unconjugated QDs and alkaline phosphatase, suggesting successful bioconjugation to QD-AP; TEM and AFM imaging techniques confirmed the formation of larger objects compared to QDs; and the fluorescence emission spectra of QDs conjugated to AP showed a similar spectral response compared to free QDs, in terms of λ_{max} and spectral shape. Differences observed for conjugate fluorescence emission intensity can be attributed to dilution which occurs during the conjugation reaction and subsequent filtration steps, resulting in an unknown QD concentration in the final conjugate suspension.

An activity assay confirmed QD-AP conjugates were active, with a similar activity to an upper limit of 7.0×10^{-4}U of 'free' enzyme. Fluorescence calibration curves of QDs were used to estimate QD:AP ratios of 2.8**:**1.0 and 13.0**:**1.0 for different batches of QD-AP conjugates, assuming enzymatic activity and fluorescence intensity were unaffected by the conjugation reaction. This method was also restricted by the detection limit of QDs at low concentrations by fluorescence spectroscopy.

Batch variation exists in terms of activity and conjugate size, however if investigated further this 'issue' could in fact be advantageous to create conjugate nanomotors by which enzyme activity is initially controlled by the degree of conjugation.

Overall bioconjugation of alkaline phosphatase to semiconductor quantum dots was successful as the conjugated enzyme exhibited phosphatase activity, the 'particle' size increased after conjugation as shown by DLS and microscopy techniques (TEM and AFM) and the QD-AP fluorescence emission spectral shape was comparable to unconjugated QDs.

A number of phosphatase responsive aromatic dipeptide self-assembling substrates were investigated towards the nanopropulsion of QD-AP conjugates. Initial studies confirmed the enzymatic conversion of substrate starting materials to self-assembling products, with unconjugated AP. Two previously reported fibre assembling substrates (**1a** and **2a**) and one aromatic dipeptide substrate (**3a**) which reportedly self-assembles into spheres in response to AP were studied by spectroscopic techniques to confirm supramolecular interactions. Substrates **1a** and **2a** exist as micellar structures and upon addition of AP are converted to fibrous assemblies of **1b** and **2b**. The enzymatic reactions of **1a**, **2a** and **3a** to corresponding dephosphorylated products were followed by HPLC. X-ray diffraction techniques could potentially be used to confirm the suspected β-sheet conformations of the fibre forming systems **1b** and **2b**, and determine spacing between sheets.[326]

Conversion studies were also performed for QD-AP responsive self-assembly, by which conversion to dephosphorylated products (**1b**, **2b** and **3b**) was confirmed by HPLC to be in line with a 7.0 $x10^{-4}$U 'free' enzyme conversion.

The enzyme-QD conjugates (in the presence of self-assembling substrates) were successfully observed and tracked in motion by fluorescence microscopy using an EMCCD camera and a combination of optical filters corresponding to the excitation and emission wavelengths of the conjugates (435 and 650 nm respectively). As well as two fibre-assembling (**1b** and **2b**) and one sphere-assembling substrate (**3b**), an additional non-self-assembling substrate (**4b**) was studied as a control. Videos were obtained for QD-AP conjugates with different substrates and analysed by a custom modified MATLAB programme to obtain data of individual 'particles' such as trajectories, frame-to-frame speed, MSD, diffusion coefficient and angle of trajectory. Large quantities of data were gathered giving results with significant statistical stability.

For this study we focus on the frame-to-frame average speed to detect enhancement in diffusion characteristic with different fuel substrates, however further data analysis could be performed to calculate the rotational diffusion coefficient and diffusion time (τ_R) for the data obtained here.

QD-AP conjugates were found to exhibit enhanced diffusion with 10 mM fibre-assembling substrate **1a** compared to non-self-assembling and sphere-assembling substrates, indicative that the micelle to fibre transformation causes a propulsive effect. Intrinsically fluorescent

pyrene-functionalised substrate **2a** resulted in background fluorescence issues at concentrations required for propulsion preventing tracking of conjugates.

Additionally, a shift in the frame-to-frame speed distribution is observed with increasing fibre-assembling substrate **1a** (at least up to 10 mM fuel concentration), while with the non-self-assembling substrate (**4a**) conjugate speed was independent of fuel concentration.

Our original assumption that fibres stay attached to and push along the enzyme linearly, seems less likely given the results. A more likely explanation is that the fuel substrates are converted by the enzyme conjugates, diffuse away from the active site and form fibres independent of the conjugates. It can therefore be assumed that the biocatalytic transformation from spherical micellar fuel to monomeric fuel (and subsequent self-assembled fibre structures), leads to the enhanced motion observed here for 10 mM **1a**.

Further experiments to investigate this could take advantage of fluorescence resonance energy transfer (FRET). FRET relies on the emission spectrum of a donor molecule overlapping with the absorption spectrum of an acceptor molecule for energy transfer.[327] Therefore by labelling the peptide and enzyme with donor and acceptor molecules the molecular interactions between substrate molecules and the enzyme during biocatalysis could be investigated. This technique could give an indication of whether fibre growth occurs independently of the enzyme-conjugates or whether the fibre grows at or near to the conjugate surface.

The potential for directional control of QD-AP conjugates was tested by isolating the substrate 'fuel' within an acrylamide gel. A concentration gradient results as substrates diffuse into the surrounding medium. Substrates **1a**, **2a** and **4a** were shown to direct the motion of QD-AP conjugates towards the substrate saturated gel, as well as enhance the average frame-to-frame speed. Interestingly this effect is observed with the non-self-assembling substrate **4a**, despite having no enhancement on conjugate speeds when present throughout the entire motility medium, suggesting at this stage that a flow could be responsible. Future control experiments, for example, unconjugated QDs in gel reservoir systems with and without fuel, are required to conclude true directional control with fuel saturated reservoirs and eliminate the possibility of flow within the system.

An attractive feature for a self-propelled motor is the ability to start and stop motion.[44,328] A possible strategy to 'start' and 'stop' an enzymatic system such as QD-AP could be achieved

using a reversible inhibiter. Vanadate is a competitive inhibitor for alkaline phosphatase, with complete reversal by EDTA or dilution.[329] Experiments could be designed for repeated 'start/stop' motion of QD-AP conjugates, by the addition of vanadate to revert to slower diffusion rates consistent with a no fuel system, and addition of EDTA would 'restart' motility *e.g.* QD-AP conjugates would exhibit enhanced motion in the presence of fibre-assembling substrate **1a**.

A biocatalytically propelled system could be used for applications such as cargo transportation, nano-separation of enzymes and also potentially allows information to be gained on enzyme motion and forces during catalysis. Initial conjugation methods could be developed to further control the conjugation and minimise batch variation of conjugation. On the other hand, if precise control over the degree of conjugation could be achieved, this would lead to a method of controlling the overall speed of the conjugates *e.g.* more enzymes to QDs, results in a higher catalytic activity and subsequently faster conjugates.

Visualisation of biocatalytically induced self-assembled fibres of **1b** and **2b** was achieved by extrinsic and intrinsic methods respectively. Extrinsic fluorescence methods utilised Thioflavin T for the fluorescent staining of **1b** fibres. Fibres of **2b** were visualised by the intrinsically fluorescent aromatic group pyrene.

Two-photon microscopy proved to be the most promising technique for real-time fibre visualisation in a three-dimensional environment. Fibres made by QD-AP were dendritic in appearance compared to fibrous networks by AP. Fibrous assembles made with low AP concentrations (7.0×10^{-4} U) and QD-AP conjugates resulted in regions of localised fibre formation compared to extensive networks observed for 4 U of AP. Supramolecular assemblies observed for **2b** were shown to differ depending on whether the enzyme was conjugated to QDs or not. The dendritic fibrous structures of **2b** made by AP conjugated to QDs, suggests that supramolecular structures could be influenced by initially controlling the conjugation *e.g.* the degree of conjugation of AP and QDs.

Simultaneous fibre and QD-AP conjugate visualisation was successful by fluorescence microscopy, using both extrinsic staining methods and intrinsically fluorescent substrates, but only when samples of fibre-assembling substrates containing QD-AP conjugates were immobilised on a 2D glass surface.

Alternative fluorescent probes for visualisation of β-sheet fibrous structures could be investigated. Nile Red is an alternative extrinsic dye that has an affinity for hydrophobic surfaces of proteins and has therefore been used for the detection of protein aggregations in such cases as fibril formation.[330–333] In an aqueous environment Nile Red exhibits little or no fluorescence but upon binding with a hydrophobic surface an intense fluorescence emission between 610-623 nm is observed, when excited at 560 nm.[330] This system may not be suitable in conjunction with 655 nm QDs as the excitation maxima values are relatively close and the excitation wavelength may be unsuitable for simultaneous QD and fibre-dye excitation, however other QD wavelengths could be investigated.

Congo red is an extrinsic protein stain used for the detection of amyloid fibrils.[334–336] Upon illumination with polarised light, Congo red-stained fibrils exhibit a green birefringence which could be utilised for microscopy purposes.[240,243,247,337] Congo red staining is thought to be more difficult to perform and analyse than Thioflavin T, however it would be useful to use a variety of methods to determine the best technique for the system being studied.

Ultimately the simultaneous and real-time visualisation of supramolecular fibres during nano-propulsion of enzyme-QD conjugates would be advantageous to gain more information about the propulsion mechanism. Questions still remain as to how enzyme-conjugates are propelled by fibre growth and how the micelle to fibre transformation of **1a** to **1b** provides an extra propulsive force compared to non-self-assembling substrates and sphere-to-sphere transformation. Stochastic Optical Reconstruction Microscopy (STORM) confocal microscopy could offer a potential route for real-time visualisation of supramolecular aromatic dipeptide fibre formation.[338]

Alkaline phosphatase and chymotrypsin were successfully conjugated to different coloured quantum dots *e.g.* 525 and 655 nm emitting QDs. For each enzyme-conjugate activity assays were developed to monitor the removal of unconjugated enzyme and determine enzymatic activity of the final conjugate. The method described in this thesis for the bioconjugation of enzymes with QDs could be applied to a variety of enzymes. However this study has shown that each system must be treated individually, illustrated by the unsuccessful conjugation of thermolysin to 525 nm emitting QDs. Combining enzyme-QD conjugates with biocatalytic self-assembly there is potentially a vast array of enzyme conjugate/self-assembly driven motility combinations available to study.

A multi-QD system was successfully imaged and tracked by fluorescence microscopy by switching between optical filters. Simultaneous visualisation of red and green conjugates *e.g.* QD_{525}-AP and QD_{655}-Chym could be performed in real-time by utilising a two-camera set-up, and optical filters corresponding to the two fluorophores being studied.

The preparation of multiple enzyme conjugates with different coloured QDs, could lead to the development of a nano-separation device. This idea would incorporate enzyme-specific substrate reservoirs used to separate and direct enzyme-QD conjugate mixtures along corresponding substrate concentration gradients. Additionally a two-camera/optical filter set-up could be employed for simultaneous visualisation of different coloured enzyme-QD conjugates.

Designing different peptide substrate-enzyme motor combinations, in which enzyme-QD motors have affinity to different molecular or particulate cargo, systems of highly selective driven nanoscale transport could be achieved. Dynamically unstable enzyme-peptide systems such as the chymotrypsin/NapYY-NH_2 system,[214] could lead to a potential 'recharging' of fuel for a simple analogue of actin polymerisation driven motion.

10.1.1. Summary

Overall the successful conjugation of alkaline phosphatase to fluorescent QDs allowed for the visualisation of nano-sized conjugates in a three-dimensional environment. Upon the addition of fibre assembling substrates, QD-AP exhibited enhanced motion, which we suggest is due to one dimensional fibre growth. It was initially proposed that fibre propulsion would result in linear and directed conjugate motion, however conjugates continued to display random albeit faster motion. More realistically it seems that conjugates experience short 'bursts' of propulsion caused by transformation of micelles to one-dimensional fibre structures which occurs at a very short timescale (nano seconds). Between bursts, conjugates rotate due to Brownian motion, hence the direction of different bursts is random. As shown with examples of micro- and nano-sized motors, asymmetry seems to be important in achieving ballistic or linear motion. However we propose that self-assembly driven enzyme-conjugate motors only experience short periods of symmetry breakage by the release of products, in this case fibres, from the conjugate surface.

To the best of our knowledge this is the first example of enhanced motion driven by the self-assembly of aromatic peptide amphiphiles into supramolecular fibre structures. Previous examples show enhanced motion of enzymes or artificial motors using fuel concentration gradients.

The findings provided here offer the next steps towards understanding fundamental principles in biocatalytic self-assembly, as well as a method to monitor enzyme motion during catalysis, towards future applications in biocatalytic self-assembly driven nano-construction, transportation and separation devices.

References

(1) Norde, W. *Colloids and Interfaces in Life Sciences and Bionanotechnology, Second Edition*; CRC Press, 2011.

(2) Haw, M. D. Colloidal Suspensions, Brownian Motion, Molecular Reality: A Short History. *J. Phys. Condens. Matter* **2002**, *14*, 7769.

(3) Hunter, R. J. *Foundations of Colloid Science*; Second Edition.; Oxford University Press, 2000.

(4) Horiike, K.; Tojo, H.; Yamano, T.; Nozaki, M. Interpretation of the Stokes Radius of Macromolecules Determined by Gel Filtration Chromatography. *J. Biochem. (Tokyo)* **1983**, *93*, 99–106.

(5) Mazo, R. M. *Brownian Motion: Fluctuations, Dynamics, and Applications*; OUP Oxford, 2008.

(6) Howse, J. R.; Jones, R. A. L.; Ryan, A. J.; Gough, T.; Vafabakhsh, R.; Golestanian, R. Self-Motile Colloidal Particles: From Directed Propulsion to Random Walk. *Phys. Rev. Lett.* **2007**, *99*, 048102.

(7) De Bruin, K.; Ruthardt, N.; von Gersdorff, K.; Bausinger, R.; Wagner, E.; Ogris, M.; Brauchle, C. Cellular Dynamics of EGF Receptor-Targeted Synthetic Viruses. *Mol Ther* **2007**, *15*, 1297–1305.

(8) Dunderdale, G.; Ebbens, S.; Fairclough, P.; Howse, J. Importance of Particle Tracking and Calculating the Mean-Squared Displacement in Distinguishing Nanopropulsion from Other Processes. *Langmuir ACS J. Surf. Colloids* **2012**, *28*, 10997–11006.

(9) Lee, K.-C.; Liu, A. J. New Proposed Mechanism of Actin-Polymerization-Driven Motility. *Biophys. J.* **2008**, *95*, 4529–4539.

(10) Pratt, C. W. *Essential Biochemistry.*; John Wiley: [S.l.], 2013.

(11) Schwartz, I. M.; Ehrenberg, M.; Bindschadler, M.; McGrath, J. L. The Role of Substrate Curvature in Actin-Based Pushing Forces. *Curr. Biol. CB* **2004**, *14*, 1094–1098.

(12) McCullough, B. R.; Grintsevich, E. E.; Chen, C. K.; Kang, H.; Hutchison, A. L.; Henn, A.; Cao, W.; Suarez, C.; Martiel, J.-L.; Blanchoin, L.; *et al.* Cofilin-Linked Changes in Actin Filament Flexibility Promote Severing. *Biophys. J.* **2011**, *101*, 151–159.

(13) Atkinson, S. J.; Hosford, M. A.; Molitoris, B. A. Mechanism of Actin Polymerization in Cellular ATP Depletion. *J. Biol. Chem.* **2004**, *279*, 5194–5199.

(14) Pantarotto, D.; Browne, W. R.; Feringa, B. L. Autonomous Propulsion of Carbon Nanotubes Powered by a Multienzyme Ensemble. *Chem. Commun.* **2008**, 1533–1535.

(15) Schmidt, C.; Vogel, V. Molecular Shuttles Powered by Motor Proteins: Loading and Unloading Stations for Nanocargo Integrated into One Device. *Lab. Chip* **2010**, *10*, 2195–2198.

(16) Soong, R. K.; Bachand, G. D.; Neves, H. P.; Olkhovets, A. G.; Craighead, H. G.; Montemagno, C. D. Powering an Inorganic Nanodevice with a Biomolecular Motor. *Science* **2000**, *290*, 1555–1558.

(17) Cooper, G. M. *The Cell*; 2nd ed.; Sinauer Associates, 2000.

(18) Hiratsuka, Y.; Miyata, M.; Tada, T.; Uyeda, T. Q. P. A Microrotary Motor Powered by Bacteria. *Proc. Natl. Acad. Sci.* **2006**, *103*, 13618–13623.

(19) Ismagilov, R. F.; Schwartz, A.; Bowden, N.; Whitesides, G. M. Autonomous Movement and Self-Assembly. *Angew. Chem. Int. Ed.* **2002**, *41*, 652–654.

(20) Gibbs, J. G.; Zhao, Y.-P. Autonomously Motile Catalytic Nanomotors by Bubble Propulsion. *Appl. Phys. Lett.* **2009**, *94*, 163104–163104 – 3.

(21) Sanchez, S.; Solovev, A. A.; Schulze, S.; Schmidt, O. G. Controlled Manipulation of Multiple Cells Using Catalytic Microbots. *Chem. Commun.* **2010**, *47*, 698–700.
(22) Zacharia, N. S.; Sadeq, Z. S.; Ozin, G. A. Enhanced Speed of Bimetallic Nanorod Motors by Surface Roughening. *Chem. Commun.* **2009**, 5856–5858.
(23) Kanti Dey, K.; Ranjan Panda, B.; Paul, A.; Basu, S.; Chattopadhyay, A. Catalytic Gold Nanoparticle Driven pH Specific Chemical Locomotion. *J. Colloid Interface Sci.* **2010**, *348*, 335–341.
(24) Fattah, Z.; Loget, G.; Lapeyre, V.; Garrigue, P.; Warakulwit, C.; Limtrakul, J.; Bouffier, L.; Kuhn, A. Straightforward Single-Step Generation of Microswimmers by Bipolar Electrochemistry. *Electrochimica Acta* **2011**, *56*, 10562–10566.
(25) Solovev, A. A.; Mei, Y.; Schmidt, O. G. Catalytic Microstrider at the Air–Liquid Interface. *Adv. Mater.* **2010**, *22*, 4340–4344.
(26) Sanchez, S.; Solovev, A. A.; Harazim, S. M.; Schmidt, O. G. Microbots Swimming in the Flowing Streams of Microfluidic Channels. *J. Am. Chem. Soc.* **2011**, *133*, 701–703.
(27) Li, J.-X.; Lu, B.-R.; Shen, Z.; Xu, Z.; Li, H.; Wen, J.; Li, Z.; Qu, X.-P.; Chen, Y.; Mei, Y.; *et al.* Magnetic and Meniscus-Effect Control of Catalytic Rolled-up Micromotors. *Microelectron. Eng.* **2011**, *88*, 1792–1794.
(28) Sanchez, S.; Ananth, A. N.; Fomin, V. M.; Viehrig, M.; Schmidt, O. G. Superfast Motion of Catalytic Microjet Engines at Physiological Temperature. *J. Am. Chem. Soc.* **2011**, *133*, 14860–14863.
(29) Manesh, K. M.; Cardona, M.; Yuan, R.; Clark, M.; Kagan, D.; Balasubramanian, S.; Wang, J. Template-Assisted Fabrication of Salt-Independent Catalytic Tubular Microengines. *ACS Nano* **2010**, *4*, 1799–1804.
(30) Gao, W.; Sattayasamitsathit, S.; Orozco, J.; Wang, J. Highly Efficient Catalytic Microengines: Template Electrosynthesis of Polyaniline/Platinum Microtubes. *J. Am. Chem. Soc.* **2011**, *133*, 11862–11864.
(31) Wang, S.; Wu, N. Selecting the Swimming Mechanisms of Colloidal Particles: Bubble Propulsion versus Self-Diffusiophoresis. *Langmuir* **2014**, *30*, 3477–3486.
(32) Moran, J. L.; Wheat, P. M.; Posner, J. D. Locomotion of Electrocatalytic Nanomotors due to Reaction Induced Charge Auto-Electrophoresis. *Phys. Rev. E* **2010**, *81*.
(33) Laocharoensuk, R.; Burdick, J.; Wang, J. Carbon-Nanotube-Induced Acceleration of Catalytic Nanomotors. *ACS Nano* **2008**, *2*, 1069–1075.
(34) Hong, Y.; Blackman, N. M. K.; Kopp, N. D.; Sen, A.; Velegol, D. Chemotaxis of Nonbiological Colloidal Rods. *Phys. Rev. Lett.* **2007**, *99*, 178103.
(35) Gibbs, J. G.; Fragnito, N. A.; Zhao, Y. Asymmetric Pt/Au Coated Catalytic Micromotors Fabricated by Dynamic Shadowing Growth. *Appl. Phys. Lett.* **2010**, *97*, 253107.
(36) Ibele, M. E.; Lammert, P. E.; Crespi, V. H.; Sen, A. Emergent, Collective Oscillations of Self-Mobile Particles and Patterned Surfaces under Redox Conditions. *ACS Nano* **2010**, *4*, 4845–4851.
(37) Wang, Y.; Hernandez, R. M.; Bartlett, D. J.; Bingham, J. M.; Kline, T. R.; Sen, A.; Mallouk, T. E. Bipolar Electrochemical Mechanism for the Propulsion of Catalytic Nanomotors in Hydrogen Peroxide Solutions†. *Langmuir* **2006**, *22*, 10451–10456.
(38) Ibele, M.; Mallouk, T. E.; Sen, A. Schooling Behavior of Light-Powered Autonomous Micromotors in Water. *Angew. Chem. Int. Ed Engl.* **2009**, *48*, 3308–3312.
(39) Paxton, W. F.; Kistler, K. C.; Olmeda, C. C.; Sen, A.; St. Angelo, S. K.; Cao, Y.; Mallouk, T. E.; Lammert, P. E.; Crespi, V. H. Catalytic Nanomotors: Autonomous Movement of Striped Nanorods. *J. Am. Chem. Soc.* **2004**, *126*, 13424–13431.

(40) Kline, T. R.; Paxton, W. F.; Mallouk, T. E.; Sen, A. Catalytic Nanomotors: Remote-Controlled Autonomous Movement of Striped Metallic Nanorods. *Angew. Chem.* **2005**, *117*, 754–756.
(41) Sanchez, S.; Solovev, A. A.; Mei, Y.; Schmidt, O. G. Dynamics of Biocatalytic Microengines Mediated by Variable Friction Control. *J. Am. Chem. Soc.* **2010**, *132*, 13144–13145.
(42) Mano, N.; Heller, A. Bioelectrochemical Propulsion. *J. Am. Chem. Soc.* **2005**, *127*, 11574–11575.
(43) Burdick, J.; Laocharoensuk, R.; Wheat, P. M.; Posner, J. D.; Wang, J. Synthetic Nanomotors in Microchannel Networks: Directional Microchip Motion and Controlled Manipulation of Cargo. *J. Am. Chem. Soc.* **2008**, *130*, 8164–8165.
(44) Calvo-Marzal, P.; Manesh, K. M.; Kagan, D.; Balasubramanian, S.; Cardona, M.; Flechsig, G.-U.; Posner, J.; Wang, J. Electrochemically-Triggered Motion of Catalytic Nanomotors. *Chem. Commun.* **2009**, 4509–4511.
(45) Zhou, B.; Han, S.; Raja, R.; Somorjai, G. A. *Nanotechnology in Catalysis 3: Vol. 3*; Springer, 2007.
(46) Kovtyukhova, N. I. Toward Understanding of the Propulsion Mechanism of Rod-Shaped Nanoparticles That Catalyze Gas-Generating Reactions. *J. Phys. Chem. C* **2008**, *112*, 6049–6056.
(47) Liu, R.; Sen, A. Autonomous Nanomotor Based on Copper–Platinum Segmented Nanobattery. *J. Am. Chem. Soc.* **2011**, *133*, 20064–20067.
(48) Moon, J.-S.; Park, K.-K.; Kim, J.-H.; Seo, G. The Reduction Reaction of Dissolved Oxygen in Water by Hydrazine over Platinum Catalyst Supported on Activated Carbon Fiber. *Appl. Catal. Gen.* **1999**, *184*, 41–48.
(49) Shankaran, D. R.; Shim, Y.-B. An Amperometric Sensor for Hydrogen Peroxide Based on a (3-Mercaptopropyl)trimethoxysilane Self-Assembled Layer Containing Hydrazine. *Electroanalysis* **2002**, *14*, 704–707.
(50) ISHIDA, K.; NAGASE, M.; UETAKE, N.; ANAZAWA, K.; NAKAMURA, F.; AIZAWA, M.; YOSHIKAWA, H. Low Corrosive Chemical Decontamination Method Using pH Control, (II). *J. Nucl. Sci. Technol.* **2002**, *39*, 941–949.
(51) Pavlick, R. A.; Sengupta, S.; McFadden, T.; Zhang, H.; Sen, A. A Polymerization-Powered Motor. *Angew. Chem. Int. Ed.* **2011**, *50*, 9374–9377.
(52) Sundararajan, S.; Lammert, P. E.; Zudans, A. W.; Crespi, V. H.; Sen, A. Catalytic Motors for Transport of Colloidal Cargo. *Nano Lett.* **2008**, *8*, 1271–1276.
(53) Gao, W.; Pei, A.; Wang, J. Water-Driven Micromotors. *ACS Nano* **2012**, *6*, 8432–8438.
(54) Gao, W.; Feng, X.; Pei, A.; Gu, Y.; Li, J.; Wang, J. Seawater-Driven Magnesium Based Janus Micromotors for Environmental Remediation. *Nanoscale* **2013**, *5*, 4696.
(55) Hong, Y.; Diaz, M.; Córdova-Figueroa, U. M.; Sen, A. Light-Driven Titanium-Dioxide-Based Reversible Microfireworks and Micromotor/Micropump Systems. *Adv. Funct. Mater.* **2010**, *20*, 1568–1576.
(56) Volpe, G.; Buttinoni, I.; Vogt, D.; Kümmerer, H.-J.; Bechinger, C. Microswimmers in Patterned Environments. *Soft Matter* **2011**, *7*, 8810–8815.
(57) Abid, J.-P.; Frigoli, M.; Pansu, R.; Szeftel, J.; Zyss, J.; Larpent, C.; Brasselet, S. Light-Driven Directed Motion of Azobenzene-Coated Polymer Nanoparticles in an Aqueous Medium. *Langmuir* **2011**, *27*, 7967–7971.
(58) Sen, A.; Ibele, M.; Hong, Y.; Velegol, D. Chemo and Phototactic Nano/microbots. *Faraday Discuss.* **2009**, *143*, 15–27; discussion 81–93.
(59) Magdanz, V.; Stoychev, G.; Ionov, L.; Sanchez, S.; Schmidt, O. G. Stimuli-Responsive Microjets with Reconfigurable Shape. *Angew. Chem. Int. Ed.* **2014**, *53*, 2673–2677.

(60) Krishna Kumar, R.; Yu, X.; Patil, A. J.; Li, M.; Mann, S. Cytoskeletal-like Supramolecular Assembly and Nanoparticle-Based Motors in a Model Protocell. *Angew. Chem. Int. Ed.* **2011**, *50*, 9343–9347.
(61) Manesh, K. M.; Balasubramanian, S.; Wang, J. Nanomotor-Based "writing" of Surface Microstructures. *Chem. Commun.* **2010**, *46*, 5704–5706.
(62) Yang, Z.; Gu, H.; Fu, D.; Gao, P.; Lam, J. K.; Xu, B. Enzymatic Formation of Supramolecular Hydrogels. *Adv. Mater.* **2004**, *16*, 1440–1444.
(63) Wu, Y.; Wu, Z.; Lin, X.; He, Q.; Li, J. Autonomous Movement of Controllable Assembled Janus Capsule Motors. *ACS Nano* **2012**, *6*, 10910–10916.
(64) Wilson, D. A.; Nolte, R. J. M.; van Hest, J. C. M. Autonomous Movement of Platinum-Loaded Stomatocytes. *Nat. Chem.* **2012**, *4*, 268–274.
(65) Godoy, J.; Vives, G.; Tour, J. M. Toward Chemical Propulsion: Synthesis of ROMP-Propelled Nanocars. *ACS Nano* **2011**, *5*, 85–90.
(66) Zhang, H.; Duan, W.; Liu, L.; Sen, A. Depolymerization-Powered Autonomous Motors Using Biocompatible Fuel. *J. Am. Chem. Soc.* **2013**, *135*, 15734–15737.
(67) Balasubramanian, S.; Kagan, D.; Manesh, K. M.; Calvo-Marzal, P.; Flechsig, G.-U.; Wang, J. Thermal Modulation of Nanomotor Movement. *Small* **2009**, *5*, 1569–1574.
(68) Dong, B.; Zhou, T.; Zhang, H.; Li, C. Y. Directed Self-Assembly of Nanoparticles for Nanomotors. *ACS Nano* **2013**, *7*, 5192–5198.
(69) Zhao, G.; Pumera, M. Magnetotactic Artificial Self-Propelled Nanojets. *Langmuir ACS J. Surf. Colloids* **2013**, *29*, 7411–7415.
(70) Zhao, G.; Sanchez, S.; Schmidt, O. G.; Pumera, M. Micromotors with Built-in Compasses. *Chem. Commun.* **2012**, *48*, 10090.
(71) García, M.; Orozco, J.; Guix, M.; Gao, W.; Sattayasamitsathit, S.; Escarpa, A.; Merkoçi, A.; Wang, J. Micromotor-Based Lab-on-Chip Immunoassays. *Nanoscale* **2013**, *5*, 1325–1331.
(72) Wang, W.; Castro, L. A.; Hoyos, M.; Mallouk, T. E. Autonomous Motion of Metallic Microrods Propelled by Ultrasound. *ACS Nano* **2012**, *6*, 6122–6132.
(73) Lins, U.; Farina, M.; Kachar, B. Membrane Vesicles in Magnetotactic Bacteria. *Microbiol. Res.* **2003**, *158*, 317–320.
(74) Xuan, M.; Shao, J.; Lin, X.; Dai, L.; He, Q. Self-Propelled Janus Mesoporous Silica Nanomotors with Sub-100 Nm Diameters for Drug Encapsulation and Delivery. *Chemphyschem Eur. J. Chem. Phys. Phys. Chem.* **2014**.
(75) Wu, Z.; Wu, Y.; He, W.; Lin, X.; Sun, J.; He, Q. Self-Propelled Polymer-Based Multilayer Nanorockets for Transportation and Drug Release. *Angew. Chem. Int. Ed.* **2013**, *52*, 7000–7003.
(76) Fan, J.; Yin, J.-J.; Ning, B.; Wu, X.; Hu, Y.; Ferrari, M.; Anderson, G. J.; Wei, J.; Zhao, Y.; Nie, G. Direct Evidence for Catalase and Peroxidase Activities of Ferritin–platinum Nanoparticles. *Biomaterials* **2011**, *32*, 1611–1618.
(77) Switala, J.; Loewen, P. C. Diversity of Properties among Catalases. *Arch. Biochem. Biophys.* **2002**, *401*, 145–154.
(78) Vicario, J.; Eelkema, R.; Browne, W. R.; Meetsma, A.; Crois, R. M. L.; Feringa, B. L. Catalytic Molecular Motors: Fuelling Autonomous Movement by a Surface Bound Synthetic Manganese Catalase. *Chem. Commun.* **2005**, 3936–3938.
(79) Heuvingh, J.; Franco, M.; Chavrier, P.; Sykes, C. ARF1-Mediated Actin Polymerization Produces Movement of Artificial Vesicles. *Proc. Natl. Acad. Sci. U. S. A.* **2007**, *104*, 16928–16933.
(80) Van Oudenaarden, A.; Theriot, J. A. Cooperative Symmetry-Breaking by Actin Polymerization in a Model for Cell Motility. *Nat. Cell Biol.* **1999**, *1*, 493–499.

(81) Orozco, J.; García-Gradilla, V.; D'Agostino, M.; Gao, W.; Cortés, A.; Wang, J. Artificial Enzyme-Powered Microfish for Water-Quality Testing. *ACS Nano* **2013**, *7*, 818–824.
(82) Jeng, R. L.; Goley, E. D.; D'Alessio, J. A.; Chaga, O. Y.; Svitkina, T. M.; Borisy, G. G.; Heinzen, R. A.; Welch, M. D. A Rickettsia WASP-like Protein Activates the Arp2/3 Complex and Mediates Actin-Based Motility. *Cell. Microbiol.* **2004**, *6*, 761–769.
(83) Suetsugu, S.; Miki, H.; Yamaguchi, H.; Obinata, T.; Takenawa, T. Enhancement of Branching Efficiency by the Actin Filament-Binding Activity of N-WASP/WAVE2. *J. Cell Sci.* **2001**, *114*, 4533–4542.
(84) Cameron, L. A.; Footer, M. J.; Oudenaarden, A. van; Theriot, J. A. Motility of ActA Protein-Coated Microspheres Driven by Actin Polymerization. *Proc. Natl. Acad. Sci.* **1999**, *96*, 4908–4913.
(85) Kang, H.; Perlmutter, D. S.; Shenoy, V. B.; Tang, J. X. Observation and Kinematic Description of Long Actin Tracks Induced by Spherical Beads. *Biophys. J.* **2010**, *99*, 2793–2802.
(86) Gucht, J. van der; Paluch, E.; Plastino, J.; Sykes, C. Stress Release Drives Symmetry Breaking for Actin-Based Movement. *Proc. Natl. Acad. Sci.* **2005**, *102*, 7847–7852.
(87) Upadhyaya, A.; van Oudenaarden, A. Actin Polymerization: Forcing Flat Faces Forward. *Curr. Biol. CB* **2004**, *14*, R467–R469.
(88) Yarar, D.; To, W.; Abo, A.; Welch, M. D. The Wiskott-Aldrich Syndrome Protein Directs Actin-Based Motility by Stimulating Actin Nucleation with the Arp2/3 Complex. *Curr. Biol. CB* **1999**, *9*, 555–558.
(89) Fournier-Bidoz, S.; Arsenault, A. C.; Manners, I.; Ozin, G. A. Synthetic Self-Propelled Nanorotors. *Chem. Commun.* **2005**, 441–443.
(90) Ebbens, S.; Jones, R. A. L.; Ryan, A. J.; Golestanian, R.; Howse, J. R. Self-Assembled Autonomous Runners and Tumblers. *Phys. Rev. E* **2010**, *82*, 015304.
(91) He, Y.; Wu, J.; Zhao, Y. Designing Catalytic Nanomotors by Dynamic Shadowing Growth. *Nano Lett.* **2007**, *7*, 1369–1375.
(92) Qin, L.; Banholzer, M. J.; Xu, X.; Huang, L.; Mirkin, C. A. Rational Design and Synthesis of Catalytically Driven Nanorotors. *J. Am. Chem. Soc.* **2007**, *129*, 14870–14871.
(93) Wang, Y.; Fei, S.; Byun, Y.-M.; Lammert, P. E.; Crespi, V. H.; Sen, A.; Mallouk, T. E. Dynamic Interactions between Fast Microscale Rotors. *J. Am. Chem. Soc.* **2009**, *131*, 9926–9927.
(94) Ghosh, A.; Fischer, P. Controlled Propulsion of Artificial Magnetic Nanostructured Propellers. *Nano Lett.* **2009**, *9*, 2243–2245.
(95) Zhang, L.; Petit, T.; Lu, Y.; Kratochvil, B. E.; Peyer, K. E.; Pei, R.; Lou, J.; Nelson, B. J. Controlled Propulsion and Cargo Transport of Rotating Nickel Nanowires near a Patterned Solid Surface. *ACS Nano* **2010**, *4*, 6228–6234.
(96) Noji, H.; Yasuda, R.; Yoshida, M.; Kinosita, K. Direct Observation of the Rotation of F1-ATPase. *Nature* **1997**, *386*, 299–302.
(97) Delius, M. von; Leigh, D. A. Walking Molecules. *Chem. Soc. Rev.* **2011**, *40*, 3656–3676.
(98) Bath, J.; Green, S. J.; Turberfield, A. J. A Free-Running DNA Motor Powered by a Nicking Enzyme. *Angew. Chem. Int. Ed.* **2005**, *44*, 4358–4361.
(99) Yin, P.; Yan, H.; Daniell, X. G.; Turberfield, A. J.; Reif, J. H. A Unidirectional DNA Walker That Moves Autonomously along a Track. *Angew. Chem. Int. Ed.* **2004**, *43*, 4906–4911.

(100) Tian, Y.; He, Y.; Chen, Y.; Yin, P.; Mao, C. A DNAzyme That Walks Processively and Autonomously along a One-Dimensional Track. *Angew. Chem. Int. Ed.* **2005**, *44*, 4355–4358.
(101) Liu, H.; Liu, D. DNA Nanomachines and Their Functional Evolution. *Chem. Commun.* **2009**, 2625–2636.
(102) Kelly, T. R. Molecular Motors: Synthetic DNA-Based Walkers Inspired by Kinesin. *Angew. Chem. Int. Ed.* **2005**, *44*, 4124–4127.
(103) Sherman, W. B.; Seeman, N. C. A Precisely Controlled DNA Biped Walking Device. *Nano Lett.* **2004**, *4*, 1203–1207.
(104) Shin, J.-S.; Pierce, N. A. A Synthetic DNA Walker for Molecular Transport. *J. Am. Chem. Soc.* **2004**, *126*, 10834–10835.
(105) Turberfield, A. J.; Mitchell, J. C.; Yurke, B.; Mills, A. P., Jr; Blakey, M. I.; Simmel, F. C. DNA Fuel for Free-Running Nanomachines. *Phys. Rev. Lett.* **2003**, *90*, 118102.
(106) Sherman, W. Building a Better Nano-Biped. *Science* **2009**, *324*, 46–47.
(107) Wang, C.; Ren, J.; Qu, X. A Stimuli Responsive DNA Walking Device. *Chem. Commun.* **2011**, *47*, 1428–1430.
(108) Arsenault, M. E.; Sun, Y.; Bau, H. H.; Goldman, Y. E. Using Electrical and Optical Tweezers to Facilitate Studies of Molecular Motors. *Phys. Chem. Chem. Phys.* **2009**, *11*, 4834–4839.
(109) Takatsuki, H.; Tanaka, H.; Rice, K. M.; Kolli, M. B.; Nalabotu, S. K.; Kohama, K.; Famouri, P.; Blough, E. R. Transport of Single Cells Using an Actin Bundle-Myosin Bionanomotor Transport System. *Nanotechnology* **2011**, *22*, 245101.
(110) Månsson, A.; Sundberg, M.; Balaz, M.; Bunk, R.; Nicholls, I. A.; Omling, P.; Tågerud, S.; Montelius, L. In Vitro Sliding of Actin Filaments Labelled with Single Quantum Dots. *Biochem. Biophys. Res. Commun.* **2004**, *314*, 529–534.
(111) Mansson, A.; Sundberg, M.; Bunk, R.; Balaz, M.; Nicholls, I. A.; Omling, P.; Tegenfeldt, J. O.; Tagerud, S.; Montelius, L. Actin-Based Molecular Motors for Cargo Transportation in Nanotechnology #8212; Potentials and Challenges. *IEEE Trans. Adv. Packag.* **2005**, *28*, 547–555.
(112) Debold, E. P.; Beck, S. E.; Warshaw, D. M. Effect of Low pH on Single Skeletal Muscle Myosin Mechanics and Kinetics. *Am. J. Physiol. Cell Physiol.* **2008**, *295*, C173–C179.
(113) Suzuki, H.; Oiwa, K.; Yamada, A.; Sakakibara, H.; Nakayama, H.; Mashiko, S. Linear Arrangement of Motor Protein on a Mechanically Deposited Fluoropolymer Thin Film. *Jpn. J. Appl. Phys.* **1995**, *34*, 3937–3941.
(114) Sundberg, M.; Balaz, M.; Bunk, R.; Rosengren-Holmberg, J. P.; Montelius, L.; Nicholls, I. A.; Omling, P.; Tågerud, S.; Månsson, A. Selective Spatial Localization of Actomyosin Motor Function by Chemical Surface Patterning. *Langmuir ACS J. Surf. Colloids* **2006**, *22*, 7302–7312.
(115) Jaber, J. A.; Chase, P. B.; Schlenoff, J. B. Actomyosin-Driven Motility on Patterned Polyelectrolyte Mono- and Multilayers. *Nano Lett.* **2003**, *3*, 1505–1509.
(116) Gordon, A. M.; LaMadrid, M. A.; Chen, Y.; Luo, Z.; Chase, P. B. Calcium Regulation of Skeletal Muscle Thin Filament Motility in Vitro. *Biophys. J.* **1997**, *72*, 1295–1307.
(117) Regnier, M.; Martyn, D. A.; Chase, P. B. Calmidazolium Alters Ca2+ Regulation of Tension Redevelopment Rate in Skinned Skeletal Muscle. *Biophys. J.* **1996**, *71*, 2786–2794.
(118) Byun, K.-E.; Choi, D. S.; Kim, E.; Seo, D. H.; Yang, H.; Seo, S.; Hong, S. Graphene–Polymer Hybrid Nanostructure-Based Bioenergy Storage Device for Real-Time Control of Biological Motor Activity. *ACS Nano* **2011**, *5*, 8656–8664.

(119) Mihajlović, G.; Brunet, N. M.; Trbović, J.; Xiong, P.; Molnár, S. von; Chase, P. B. All-Electrical Switching and Control Mechanism for Actomyosin-Powered Nanoactuators. *Appl. Phys. Lett.* **2004**, *85*, 1060–1062.
(120) Bunk, R.; Sundberg, M.; Månsson, A.; Nicholls, I. A.; Omling, P.; Tågerud, S.; Montelius, L. Guiding Motor-Propelled Molecules with Nanoscale Precision through Silanized Bi-Channel Structures. *Nanotechnology* **2005**, *16*, 710.
(121) Byun, K.-E.; Kim, M.-G.; Chase, P. B.; Hong, S. Selective Assembly and Guiding of Actomyosin Using Carbon Nanotube Network Monolayer Patterns. *Langmuir ACS J. Surf. Colloids* **2007**, *23*, 9535–9539.
(122) Albet-Torres, N.; O'Mahony, J.; Charlton, C.; Balaz, M.; Lisboa, P.; Aastrup, T.; Månsson, A.; Nicholls, I. A. Mode of Heavy Meromyosin Adsorption and Motor Function Correlated with Surface Hydrophobicity and Charge. *Langmuir ACS J. Surf. Colloids* **2007**, *23*, 11147–11156.
(123) Albet-Torres, N.; Gunnarsson, A.; Persson, M.; Balaz, M.; Höök, F.; Månsson, A. Molecular Motors on Lipid Bilayers and Silicon Dioxide: Different Driving Forces for Adsorption. *Soft Matter* **2010**, *6*, 3211–3219.
(124) Nicolau, D. V.; Solana, G.; Kekic, M.; Fulga, F.; Mahanivong, C.; Wright, J.; Ivanova, E. P.; dos Remedios, C. G. Surface Hydrophobicity Modulates the Operation of Actomyosin-Based Dynamic Nanodevices. *Langmuir ACS J. Surf. Colloids* **2007**, *23*, 10846–10854.
(125) Uyeda, T. Q.; Kron, S. J.; Spudich, J. A. Myosin Step Size. Estimation from Slow Sliding Movement of Actin over Low Densities of Heavy Meromyosin. *J. Mol. Biol.* **1990**, *214*, 699–710.
(126) Catlett, N. L.; Weisman, L. S. The Terminal Tail Region of a Yeast Myosin-V Mediates Its Attachment to Vacuole Membranes and Sites of Polarized Growth. *Proc. Natl. Acad. Sci. U. S. A.* **1998**, *95*, 14799–14804.
(127) Kron, S. J.; Spudich, J. A. Fluorescent Actin Filaments Move on Myosin Fixed to a Glass Surface. *Proc. Natl. Acad. Sci. U. S. A.* **1986**, *83*, 6272–6276.
(128) Homsher, E.; Wang, F.; Sellers, J. R. Factors Affecting Movement of F-Actin Filaments Propelled by Skeletal Muscle Heavy Meromyosin. *Am. J. Physiol.* **1992**, *262*, C714–C723.
(129) Riveline, D.; Ott, A.; Jülicher, F.; Winkelmann, D. A.; Cardoso, O.; Lacapère, J. J.; Magnúsdóttir, S.; Viovy, J. L.; Gorre-Talini, L.; Prost, J. Acting on Actin: The Electric Motility Assay. *Eur. Biophys. J. EBJ* **1998**, *27*, 403–408.
(130) Hutchins, B. M.; Platt, M.; Hancock, W. O.; Williams, M. E. Directing Transport of CoFe2O4-Functionalized Microtubules with Magnetic Fields. *Small Weinh. Bergstr. Ger.* **2007**, *3*, 126–131.
(131) Hutchins, B. M.; Platt, M.; Hancock, W. O.; Williams, M. E. Motility of CoFe/sub 2/O/sub 4/ Nanoparticle-Labelled Microtubules in Magnetic Fields. *IET Micro Nano Lett.* **2006**, *1*, 47–52.
(132) Hess, H.; Bachand, G. D. Biomolecular Motors. *Mater. Today* **2005**, *8*, 22–29.
(133) Malcos, J. L.; Hancock, W. O. Engineering Tubulin: Microtubule Functionalization Approaches for Nanoscale Device Applications. *Appl. Microbiol. Biotechnol.* **2011**, *90*, 1–10.
(134) Hess, H.; Vogel, V. Molecular Shuttles Based on Motor Proteins: Active Transport in Synthetic Environments. *Rev. Mol. Biotechnol.* **2001**, *82*, 67–85.
(135) Spetzler, D.; York, J.; Dobbin, C.; Martin, J.; Ishmukhametov, R.; Day, L.; Yu, J.; Kang, H.; Porter, K.; Hornung, T.; *et al.* Recent Developments of Bio-Molecular Motors as on-Chip Devices Using Single Molecule Techniques. *Lab. Chip* **2007**, *7*, 1633–1643.
(136) Hess, H. Self-Assembly Driven by Molecular Motors. *Soft Matter* **2006**, *2*, 669–677.

(137) Bottier, C.; Fattaccioli, J.; Tarhan, M. C.; Yokokawa, R.; Morin, F. O.; Kim, B.; Collard, D.; Fujita, H. Active Transport of Oil Droplets along Oriented Microtubules by Kinesin Molecular Motors. *Lab. Chip* **2009**, *9*, 1694–1700.
(138) Uppalapati, M.; Huang, Y.-M.; Aravamuthan, V.; Jackson, T. N.; Hancock, W. O. "Artificial Mitotic Spindle" Generated by Dielectrophoresis and Protein Micropatterning Supports Bidirectional Transport of Kinesin-Coated Beads. *Integr. Biol. Quant. Biosci. Nano Macro* **2011**, *3*, 57–64.
(139) Doot, R. K.; Hess, H.; Vogel, V. Engineered Networks of Oriented Microtubule Filaments for Directed Cargo Transport. *Soft Matter* **2007**, *3*, 349–356.
(140) Korten, T.; Diez, S. Setting up Roadblocks for Kinesin-1: Mechanism for the Selective Speed Control of Cargo Carrying Microtubules. *Lab. Chip* **2008**, *8*, 1441–1447.
(141) Beeg, J.; Klumpp, S.; Dimova, R.; Gracià, R. S.; Unger, E.; Lipowsky, R. Transport of Beads by Several Kinesin Motors. *Biophys. J.* **2008**, *94*, 532–541.
(142) Herold, C.; Leduc, C.; Stock, R.; Diez, S.; Schwille, P. Long-Range Transport of Giant Vesicles along Microtubule Networks. *Chemphyschem Eur. J. Chem. Phys. Phys. Chem.* **2012**, *13*, 1001–1006.
(143) Ruhnow, F.; Zwicker, D.; Diez, S. Tracking Single Particles and Elongated Filaments with Nanometer Precision. *Biophys. J.* **2011**, *100*, 2820–2828.
(144) Tarhan, M. C.; Yokokawa, R.; Bottier, C.; Collard, D.; Fujita, H. A Nano-Needle/microtubule Composite Gliding on a Kinesin-Coated Surface for Target Molecule Transport. *Lab. Chip* **2010**, *10*, 86–91.
(145) Hiyama, S.; Moritani, Y.; Gojo, R.; Takeuchi, S.; Sutoh, K. Biomolecular-Motor-Based Autonomous Delivery of Lipid Vesicles as Nano- or Microscale Reactors on a Chip. *Lab. Chip* **2010**, *10*, 2741–2748.
(146) Rahim, M. K. A.; Fukaminato, T.; Kamei, T.; Tamaoki, N. Dynamic Photocontrol of the Gliding Motility of a Microtubule Driven by Kinesin on a Photoisomerizable Monolayer Surface. *Langmuir* **2011**, *27*, 10347–10350.
(147) Uppalapati, M.; Huang, Y.-M.; Jackson, T. N.; Hancock, W. O. Enhancing the Stability of Kinesin Motors for Microscale Transport Applications. *Lab. Chip* **2008**, *8*, 358–361.
(148) Du, Y.-Z.; Hiratsuka, Y.; Taira, S.; Eguchi, M.; Uyeda, T. Q. P.; Yumoto, N.; Kodaka, M. Motor Protein Nano-Biomachine Powered by Self-Supplying ATP. *Chem. Commun. Camb. Engl.* **2005**, 2080–2082.
(149) Clemmens, J.; Hess, H.; Doot, R.; Matzke, C. M.; Bachand, G. D.; Vogel, V. Motor-Protein "Roundabouts": Microtubules Moving on Kinesin-Coated Tracks through Engineered Networks. *Lab. Chip* **2004**, *4*, 83–86.
(150) Diehl, M. R.; Zhang, K.; Lee, H. J.; Tirrell, D. A. Engineering Cooperativity in Biomotor-Protein Assemblies. *Science* **2006**, *311*, 1468–1471.
(151) Clemmens, J.; Hess, H.; Lipscomb, R.; Hanein, Y.; Böhringer, K. F.; Matzke, C. M.; Bachand, G. D.; Bunker, B. C.; Vogel, V. Mechanisms of Microtubule Guiding on Microfabricated Kinesin-Coated Surfaces: Chemical and Topographic Surface Patterns. *Langmuir* **2003**, *19*, 10967–10974.
(152) Reuther, C.; Hajdo, L.; Tucker, R.; Kasprzak, A. A.; Diez, S. Biotemplated Nanopatterning of Planar Surfaces with Molecular Motors. *Nano Lett.* **2006**, *6*, 2177–2183.
(153) Dinu, C. Z.; Opitz, J.; Pompe, W.; Howard, J.; Mertig, M.; Diez, S. Parallel Manipulation of Bifunctional DNA Molecules on Structured Surfaces Using Kinesin-Driven Microtubules. *Small Weinh. Bergstr. Ger.* **2006**, *2*, 1090–1098.

(154) Nitzsche, B.; Ruhnow, F.; Diez, S. Quantum-Dot-Assisted Characterization of Microtubule Rotations during Cargo Transport. *Nat. Nanotechnol.* **2008**, *3*, 552–556.
(155) Korten, T.; Birnbaum, W.; Kuckling, D.; Diez, S. Selective Control of Gliding Microtubule Populations. *Nano Lett.* **2012**, *12*, 348–353.
(156) Diez, S.; Reuther, C.; Dinu, C.; Seidel, R.; Mertig, M.; Pompe, W.; Howard, J. Stretching and Transporting DNA Molecules Using Motor Proteins. *Nano Lett.* **2003**, *3*, 1251–1254.
(157) Kerssemakers, J.; Ionov, L.; Queitsch, U.; Luna, S.; Hess, H.; Diez, S. 3D Nanometer Tracking of Motile Microtubules on Reflective Surfaces. *Small* **2009**, *5*, 1732–1737.
(158) Hirabayashi, M.; Taira, S.; Kobayashi, S.; Konishi, K.; Katoh, K.; Hiratsuka, Y.; Kodaka, M.; Uyeda, T. Q. P.; Yumoto, N.; Kubo, T. Malachite Green-Conjugated Microtubules as Mobile Bioprobes Selective for Malachite Green Aptamers with Capturing/releasing Ability. *Biotechnol. Bioeng.* **2006**, *94*, 473–480.
(159) Fischer, T.; Agarwal, A.; Hess, H. A Smart Dust Biosensor Powered by Kinesin Motors. *Nat. Nanotechnol.* **2009**, *4*, 162–166.
(160) Van den Heuvel, M. G. L.; Butcher, C. T.; Lemay, S. G.; Diez, S.; Dekker, C. Electrical Docking of Microtubules for Kinesin-Driven Motility in Nanostructures. *Nano Lett.* **2005**, *5*, 235–241.
(161) Kabir, A. M. R.; Inoue, D.; Kakugo, A.; Kamei, A.; Gong, J. P. Prolongation of the Active Lifetime of a Biomolecular Motor for in Vitro Motility Assay by Using an Inert Atmosphere. *Langmuir* **2011**, *27*, 13659–13668.
(162) Kotake, H.; Yokokawa, R.; Kanno, I.; Kotera, H. Selective Kinesin and Dynein Immobilizaton and Electrical Microtubule Manipulation for Bidirectional Microtubule Motility. In *2011 IEEE 24th International Conference on Micro Electro Mechanical Systems (MEMS)*; 2011; pp. 1373–1376.
(163) Dujovne, I.; van den Heuvel, M.; Shen, Y.; de Graaff, M.; Dekker, C. Velocity Modulation of Microtubules in Electric Fields. *Nano Lett.* **2008**, *8*, 4217–4220.
(164) Hiyama, S.; Takeuchi, S.; Gojo, R.; Shima, T.; Sutoh, K. Biomolecular Motor-Based Cargo Transporters with Loading/unloading Mechanisms on a Micro-Patterned DNA Array. In *IEEE 21st International Conference on Micro Electro Mechanical Systems, 2008. MEMS 2008*; 2008; pp. 144–147.
(165) Brunner, C.; Wahnes, C.; Vogel, V. Cargo Pick-up from Engineered Loading Stations by Kinesin Driven Molecular Shuttles. *Lab. Chip* **2007**, *7*, 1263–1271.
(166) Bromley, E. H. C.; Channon, K.; Moutevelis, E.; Woolfson, D. N. Peptide and Protein Building Blocks for Synthetic Biology: From Programming Biomolecules to Self-Organized Biomolecular Systems. *ACS Chem. Biol.* **2008**, *3*, 38–50.
(167) Reches, M.; Gazit, E. Molecular Self-Assembly of Peptide Nanostructures: Mechanism of Association and Potential Uses. *Curr. Nanosci.* **2006**, *2*, 105–111.
(168) Yanlian, Y.; Ulung, K.; Xiumei, W.; Horii, A.; Yokoi, H.; Shuguang, Z. Designer Self-Assembling Peptide Nanomaterials. *Nano Today* **2009**, *4*, 193–210.
(169) Fairman, R.; Åkerfeldt, K. S. Peptides as Novel Smart Materials. *Curr. Opin. Struct. Biol.* **2005**, *15*, 453–463.
(170) Černý, J.; Hobza, P. Non-Covalent Interactions in Biomacromolecules. *Phys. Chem. Chem. Phys.* **2007**, *9*, 5291.
(171) Beer, P. D.; Gale, P. A.; Smith, D. K. *Supramolecular Chemistry*; Oxford University Press: Oxford ; New York, 1999.
(172) Steed, J. W.; Turner, D. R.; Wallace, K. *Core Concepts in Supramolecular Chemistry and Nanochemistry*; John Wiley & Sons, 2007.
(173) Jones, R. A. L. *Soft Condensed Matter*; Oxford University Press, 2002.

(174) Reches, M.; Gazit, E. Designed Aromatic Homo-Dipeptides: Formation of Ordered Nanostructures and Potential Nanotechnological Applications. *Phys. Biol.* **2006**, *3*, S10–S19.
(175) Zhao, X. Design of Self-Assembling Surfactant-like Peptides and Their Applications. *Curr. Opin. Colloid Interface Sci.* **2009**, *14*, 340–348.
(176) Woolfson, D. N.; Ryadnov, M. G. Peptide-Based Fibrous Biomaterials: Some Things Old, New and Borrowed. *Curr. Opin. Chem. Biol.* **2006**, *10*, 559–567.
(177) Mason, J. M.; Arndt, K. M. Coiled Coil Domains: Stability, Specificity, and Biological Implications. *Chembiochem Eur. J. Chem. Biol.* **2004**, *5*, 170–176.
(178) Cui, H.; Muraoka, T.; Cheetham, A. G.; Stupp, S. I. Self-Assembly of Giant Peptide Nanobelts. *Nano Lett.* **2009**, *9*, 945–951.
(179) Hughes, M.; Xu, H.; Frederix, P. W. J. M.; Smith, A. M.; Hunt, N. T.; Tuttle, T.; Kinloch, I. A.; Ulijn, R. V. Biocatalytic Self-Assembly of 2D Peptide-Based Nanostructures. *Soft Matter* **2011**, *7*, 10032–10038.
(180) Nagai, A.; Nagai, Y.; Qu, H.; Zhang, S. Dynamic Behaviors of Lipid-like Self-Assembling Peptide A 6D and A 6K Nanotubes. *J. Nanosci. Nanotechnol.* **2007**, *7*, 2246–2252.
(181) Adler-Abramovich, L.; Reches, M.; Sedman, V. L.; Allen, S.; Tendler, S. J. B.; Gazit, E. Thermal and Chemical Stability of Diphenylalanine Peptide Nanotubes: Implications for Nanotechnological Applications. *Langmuir* **2006**, *22*, 1313–1320.
(182) Collier, J. H.; Hu, B. H.; Ruberti, J. W.; Zhang, J.; Shum, P.; Thompson, D. H.; Messersmith, P. B. Thermally and Photochemically Triggered Self-Assembly of Peptide Hydrogels. *J. Am. Chem. Soc.* **2001**, *123*, 9463–9464.
(183) Zhao, Y.; Tanaka, M.; Kinoshita, T.; Higuchi, M.; Tan, T. Nanofibrous Scaffold from Self-Assembly of B-Sheet Peptides Containing Phenylalanine for Controlled Release. *J. Controlled Release* **2010**, *142*, 354–360.
(184) Khoe, U.; Yang, Y.; Zhang, S. Self-Assembly of Nanodonut Structure from a Cone-Shaped Designer Lipid-like Peptide Surfactant†. *Langmuir* **2009**, *25*, 4111–4114.
(185) Zha, R. H.; Sur, S.; Stupp, S. I. Self-Assembly of Cytotoxic Peptide Amphiphiles into Supramolecular Membranes for Cancer Therapy. *Adv. Healthc. Mater.* **2013**, *2*, 126–133.
(186) Dasgupta, A.; Mondal, J. H.; Das, D. Peptide Hydrogels. *RSC Adv.* **2013**, *3*, 9117.
(187) Zhou, M.; Smith, A. M.; Das, A. K.; Hodson, N. W.; Collins, R. F.; Ulijn, R. V.; Gough, J. E. Self-Assembled Peptide-Based Hydrogels as Scaffolds for Anchorage-Dependent Cells. *Biomaterials* **2009**, *30*, 2523–2530.
(188) Shome, A.; Debnath, S.; Das, P. K. Head Group Modulated pH-Responsive Hydrogel of Amino Acid-Based Amphiphiles: Entrapment and Release of Cytochrome c and Vitamin B12. *Langmuir ACS J. Surf. Colloids* **2008**, *24*, 4280–4288.
(189) Qiu, Y.; Park, K. Environment-Sensitive Hydrogels for Drug Delivery. *Adv. Drug Deliv. Rev.* **2001**, *53*, 321–339.
(190) Zhou, X.-R.; Ge, R.; Luo, S.-Z. Self-Assembly of pH and Calcium Dual-Responsive Peptide-Amphiphilic Hydrogel. *J. Pept. Sci.* **2013**, *19*, 737–744.
(191) Sahoo, J. K.; Nalluri, S. K. M.; Javid, N.; Webb, H.; Ulijn, R. Biocatalytic Amide Condensation and Gelation Controlled by Light. *Chem. Commun.* **2014**.
(192) Bardelang, D.; Camerel, F.; Margeson, J. C.; Leek, D. M.; Schmutz, M.; Zaman, M. B.; Yu, K.; Soldatov, D. V.; Ziessel, R.; Ratcliffe, C. I.; *et al.* Unusual Sculpting of Dipeptide Particles by Ultrasound Induces Gelation. *J. Am. Chem. Soc.* **2008**, *130*, 3313–3315.

(193) Wang, Y.; Zhan, C.; Fu, H.; Li, X.; Sheng, X.; Zhao, Y.; Xiao, D.; Ma, Y.; Ma, J. S.; Yao, J. Switch from Intra- to Intermolecular H-Bonds by Ultrasound: Induced Gelation and Distinct Nanoscale Morphologies. *Langmuir* **2008**, *24*, 7635–7638.
(194) Ke, D.; Zhan, C.; Li, A. D. Q.; Yao, J. Morphological Transformation between Nanofibers and Vesicles in a Controllable Bipyridine–Tripeptide Self-Assembly. *Angew. Chem. Int. Ed.* **2011**, *50*, 3715–3719.
(195) Roy, S.; Javid, N.; Sefcik, J.; Halling, P. J.; Ulijn, R. V. Salt-Induced Control of Supramolecular Order in Biocatalytic Hydrogelation. *Langmuir* **2012**, *28*, 16664–16670.
(196) Yang, Z.; Liang, G.; Wang, L.; Xu, B. Using a Kinase/Phosphatase Switch to Regulate a Supramolecular Hydrogel and Forming the Supramolecular Hydrogel in Vivo. *J. Am. Chem. Soc.* **2006**, *128*, 3038–3043.
(197) Roy, S.; Ulijn, R. V. Exploiting Biocatalysis in the Synthesis of Supramolecular Polymers. In *Enzymatic Polymerisation*; Palmans, A. R. A.; Heise, A., Eds.; Advances in Polymer Science; Springer Berlin Heidelberg, 2011; pp. 127–143.
(198) Williams, R. J.; Mart, R. J.; Ulijn, R. V. Exploiting Biocatalysis in Peptide Self-Assembly. *Pept. Sci.* **2010**, *94*, 107–117.
(199) Yang, Z.; Liang, G.; Xu, B. Enzymatic Hydrogelation of Small Molecules. *Acc. Chem. Res.* **2008**, *41*, 315–326.
(200) Gao, Y.; Yang, Z.; Kuang, Y.; Ma, M.-L.; Li, J.; Zhao, F.; Xu, B. Enzyme-Instructed Self-Assembly of Peptide Derivatives to Form Nanofibers and Hydrogels. *Biopolymers* **2010**, *94*, 19–31.
(201) Zelzer, M.; Todd, S. J.; Hirst, A. R.; McDonald, T. O.; Ulijn, R. V. Enzyme Responsive Materials: Design Strategies and Future Developments. *Biomater. Sci.* **2012**, *1*, 11–39.
(202) Tang, C.; Ulijn, R. V.; Saiani, A. Self-Assembly and Gelation Properties of Glycine/leucine Fmoc-Dipeptides. *Eur. Phys. J. E* **2013**, *36*, 1–11.
(203) Bai, S.; Debnath, S.; Gibson, K.; Schlicht, B.; Bayne, L.; Zagnoni, M.; Ulijn, R. V. Biocatalytic Self-Assembly of Nanostructured Peptide Microparticles Using Droplet Microfluidics. *Small* **2014**, *10*, 285–293.
(204) Fleming, S.; Debnath, S.; Frederix, P. W. J. M.; Tuttle, T.; Ulijn, R. V. Aromatic Peptide Amphiphiles: Significance of the Fmoc Moiety. *Chem. Commun.* **2013**, *49*, 10587–10589.
(205) Fleming, S.; Debnath, S.; Frederix, P. W. J. M.; Hunt, N. T.; Ulijn, R. V. Insights into the Co-Assembly of Hydrogelators and Surfactants Based on Aromatic Peptide Amphiphiles. *Biomacromolecules* **2014**.
(206) Abul-Haija, Y. M.; Roy, S.; Frederix, P. W. J. M.; Javid, N.; Jayawarna, V.; Ulijn, R. V. Biocatalytically Triggered Co-Assembly of Two-Component Core/Shell Nanofibers. *Small* **2013**, n/a – n/a.
(207) Sadownik, J. W.; Leckie, J.; Ulijn, R. V. Micelle to Fibre Biocatalytic Supramolecular Transformation of an Aromatic Peptide Amphiphile. *Chem. Commun. Camb. Engl.* **2011**, *47*, 728–730.
(208) Hughes, M.; Debnath, S.; Knapp, C. W.; Ulijn, R. V. Antimicrobial Properties of Enzymatically Triggered Self-Assembling Aromatic Peptide Amphiphiles. *Biomater. Sci.* **2013**, *1*, 1138–1142.
(209) Das, A. K.; Collins, R.; Ulijn, R. V. Exploiting Enzymatic (Reversed) Hydrolysis in Directed Self-Assembly of Peptide Nanostructures. *Small* **2008**, *4*, 279–287.
(210) Hughes, M.; Birchall, L. S.; Zuberi, K.; Aitken, L. A.; Debnath, S.; Javid, N.; Ulijn, R. V. Differential Supramolecular Organisation of Fmoc-Dipeptides with Hydrophilic

Terminal Amino Acid Residues by Biocatalytic Self-Assembly. *Soft Matter* **2012**, *8*, 11565–11574.
(211) Hughes, M.; Frederix, P. W. J. M.; Raeburn, J.; Birchall, L. S.; Sadownik, J.; Coomer, F. C.; Lin, I.-H.; Cussen, E. J.; Hunt, N. T.; Tuttle, T.; *et al.* Sequence/structure Relationships in Aromatic Dipeptide Hydrogels Formed under Thermodynamic Control by Enzyme-Assisted Self-Assembly. *Soft Matter* **2012**, *8*, 5595–5602.
(212) Wang, W.; Yang, Z.; Patanavanich, S.; Xu, B.; Chau, Y. Controlling Self-Assembly within Nanospace for Peptide Nanoparticle Fabrication. *Soft Matter* **2008**, *4*, 1617–1620.
(213) Wang, W.; Chau, Y. Self-Assembled Peptide Nanorods as Building Blocks of Fractal Patterns. *Soft Matter* **2009**, *5*, 4893–4898.
(214) Debnath, S.; Roy, S.; Ulijn, R. V. Peptide Nanofibers with Dynamic Instability through Nonequilibrium Biocatalytic Assembly. *J. Am. Chem. Soc.* **2013**, *135*, 16789–16792.
(215) Chronopoulou, L.; Lorenzoni, S.; Masci, G.; Dentini, M.; Togna, A. R.; Togna, G.; Bordi, F.; Palocci, C. Lipase-Supported Synthesis of Peptidic Hydrogels. *Soft Matter* **2010**, *6*, 2525.
(216) Hirst, A. R.; Roy, S.; Arora, M.; Das, A. K.; Hodson, N.; Murray, P.; Marshall, S.; Javid, N.; Sefcik, J.; Boekhoven, J.; *et al.* Biocatalytic Induction of Supramolecular Order. *Nat. Chem.* **2010**, *2*, 1089–1094.
(217) Yang, Z.; Xu, B. A Simple Visual Assay Based on Small Molecule Hydrogels for Detecting Inhibitors of Enzymes. *Chem. Commun.* **2004**, 2424.
(218) Wang, Q.; Yang, Z.; Gao, Y.; Ge, W.; Wang, L.; Xu, B. Enzymatic Hydrogelation to Immobilize an Enzyme for High Activity and Stability. *Soft Matter* **2008**, *4*, 550–553.
(219) Thornton, K.; Abul-Haija, Y. M.; Hodson, N.; Ulijn, R. V. Mechanistic Insights into Phosphatase Triggered Self-Assembly Including Enhancement of Biocatalytic Conversion Rate. *Soft Matter* **2013**, *9*, 9430–9439.
(220) Thornton, K.; Smith, A. M.; Merry, C. L. R.; Ulijn, R. V. Controlling Stiffness in Nanostructured Hydrogels Produced by Enzymatic Dephosphorylation. *Biochem. Soc. Trans.* **2009**, *37*, 660.
(221) Smith, A. M.; Williams, R. J.; Tang, C.; Coppo, P.; Collins, R. F.; Turner, M. L.; Saiani, A.; Ulijn, R. V. Fmoc-Diphenylalanine Self Assembles to a Hydrogel via a Novel Architecture Based on Π–π Interlocked B-Sheets. *Adv. Mater.* **2008**, *20*, 37–41.
(222) Chen, L.; Morris, K.; Laybourn, A.; Elias, D.; Hicks, M. R.; Rodger, A.; Serpell, L.; Adams, D. J. Self-Assembly Mechanism for a Naphthalene−Dipeptide Leading to Hydrogelation. *Langmuir* **2010**, *26*, 5232–5242.
(223) Ryan, D. M.; Nilsson, B. L. Self-Assembled Amino Acids and Dipeptides as Noncovalent Hydrogels for Tissue Engineering. *Polym. Chem.* **2012**, *3*, 18.
(224) Yan, X.; Cui, Y.; He, Q.; Wang, K.; Li, J.; Mu, W.; Wang, B.; Ou-yang, Z. Reversible Transitions between Peptide Nanotubes and Vesicle-Like Structures Including Theoretical Modeling Studies. *Chem. – Eur. J.* **2008**, *14*, 5974–5980.
(225) Yan, X.; He, Q.; Wang, K.; Duan, L.; Cui, Y.; Li, J. Transition of Cationic Dipeptide Nanotubes into Vesicles and Oligonucleotide Delivery. *Angew. Chem. Int. Ed.* **2007**, *46*, 2431–2434.
(226) Matsui, H.; Holtman, C. Organic Nanotube Bridge Fabrication by Controlling Molecular Self-Assembly Processes between Spherical and Tubular Formations. *Nano Lett.* **2002**, *2*, 887–889.
(227) Ulijn, R. V.; Smith, A. M. Designing Peptide Based Nanomaterials. *Chem. Soc. Rev.* **2008**, *37*, 664–675.

(228) Gao, J.; Zheng, W.; Kong, D.; Yang, Z. Dual Enzymes Regulate the Molecular Self-Assembly of Tetra-Peptide Derivatives. *Soft Matter* **2011**, *7*, 10443–10448.
(229) Invitrogen. Qdot ITK Carboxyl Quantum Dots, 2007.
(230) Zheng, Q.; Juette, M. F.; Jockusch, S.; Wasserman, M. R.; Zhou, Z.; Altman, R. B.; Blanchard, S. C. Ultra-Stable Organic Fluorophores for Single-Molecule Research. *Chem. Soc. Rev.* **2014**, *43*, 1044–1056.
(231) Song, B.; Wei, H.; Wang, Z.; Zhang, X.; Smet, M.; Dehaen, W. Supramolecular Nanofibers by Self-Organization of Bola-Amphiphiles through a Combination of Hydrogen Bonding and Π–π Stacking Interactions. *Adv. Mater.* **2007**, *19*, 416–420.
(232) Kang, H. K.; Kang, D. E.; Boo, B. H.; Yoo, S. J.; Lee, J. K.; Lim, E. C. Existence of Intramolecular Triplet Excimer of Bis(9-Fluorenyl)methane: Phosphorescence and Delayed Fluorescence Spectroscopic and Ab Initio Studies. *J. Phys. Chem. A* **2005**, *109*, 6799–6804.
(233) Miller, E.; Jóźwik-Styczyńska, D. Stability of Pyrene-1-Carboxylic Acid and Other Pyrene Derivatives Immobilized on Silane Gels. *Spectrochim. Acta. A. Mol. Biomol. Spectrosc.* **2009**, *72*, 312–321.
(234) Buruiana, E. C.; Buruiana, T.; Hahui, L. Preparation and Characterization of New Optically Active poly(N-Acryloyl Chloride) Functionalized with (S)-Phenylalanine and Pendant Pyrene. *J. Photochem. Photobiol. Chem.* **2007**, *189*, 65–72.
(235) Bains, G. K.; Kim, S. H.; Sorin, E. J.; Narayanaswami, V. The Extent of Pyrene Excimer Fluorescence Emission Is a Reflector of Distance and Flexibility: Analysis of the Segment Linking the LDL Receptor-Binding and Tetramerization Domains of Apolipoprotein E3. *Biochemistry (Mosc.)* **2012**, *51*, 6207–6219.
(236) Basu Ray, G.; Chakraborty, I.; Moulik, S. P. Pyrene Absorption Can Be a Convenient Method for Probing Critical Micellar Concentration (cmc) and Indexing Micellar Polarity. *J. Colloid Interface Sci.* **2006**, *294*, 248–254.
(237) Dominguez, A.; Fernandez, A.; Gonzalez, N.; Iglesias, E.; Montenegro, L. Determination of Critical Micelle Concentration of Some Surfactants by Three Techniques. *J. Chem. Educ.* **1997**, *74*, 1227.
(238) Sabaté, R.; Saupe, S. J. Thioflavin T Fluorescence Anisotropy: An Alternative Technique for the Study of Amyloid Aggregation. *Biochem. Biophys. Res. Commun.* **2007**, *360*, 135–138.
(239) Wu, C.; Biancalana, M.; Koide, S.; Shea, J.-E. Binding Modes of Thioflavin-T to the Single-Layer Beta-Sheet of the Peptide Self-Assembly Mimics. *J. Mol. Biol.* **2009**, *394*, 627–633.
(240) Biancalana, M.; Koide, S. Molecular Mechanism of Thioflavin-T Binding to Amyloid Fibrils. *Biochim. Biophys. Acta* **2010**, *1804*, 1405–1412.
(241) Khurana, R.; Coleman, C.; Ionescu-Zanetti, C.; Carter, S. A.; Krishna, V.; Grover, R. K.; Roy, R.; Singh, S. Mechanism of Thioflavin T Binding to Amyloid Fibrils. *J. Struct. Biol.* **2005**, *151*, 229–238.
(242) Groenning, M.; Olsen, L.; van de Weert, M.; Flink, J. M.; Frokjaer, S.; Jørgensen, F. S. Study on the Binding of Thioflavin T to Beta-Sheet-Rich and Non-Beta-Sheet Cavities. *J. Struct. Biol.* **2007**, *158*, 358–369.
(243) Krebs, M. R. H.; Bromley, E. H. C.; Donald, A. M. The Binding of Thioflavin-T to Amyloid Fibrils: Localisation and Implications. *J. Struct. Biol.* **2005**, *149*, 30–37.
(244) LeVine, H., 3rd. Thioflavine T Interaction with Synthetic Alzheimer's Disease Beta-Amyloid Peptides: Detection of Amyloid Aggregation in Solution. *Protein Sci. Publ. Protein Soc.* **1993**, *2*, 404–410.

(245) Wolfe, L. S.; Calabrese, M. F.; Nath, A.; Blaho, D. V.; Miranker, A. D.; Xiong, Y. Protein-Induced Photophysical Changes to the Amyloid Indicator Dye Thioflavin T. *Proc. Natl. Acad. Sci.* **2010**.
(246) Voropai, E. S.; Samtsov, M. P.; Kaplevskii, K. N.; Maskevich, A. A.; Stepuro, V. I.; Povarova, O. I.; Kuznetsova, I. M.; Turoverov, K. K.; Fink, A. L.; Uverskii, V. N. Spectral Properties of Thioflavin T and Its Complexes with Amyloid Fibrils. *J. Appl. Spectrosc.* **2003**, *70*, 868–874.
(247) Hawe, A.; Sutter, M.; Jiskoot, W. Extrinsic Fluorescent Dyes as Tools for Protein Characterization. *Pharm. Res.* **2008**, *25*, 1487–1499.
(248) Hudson, S. A.; Ecroyd, H.; Kee, T. W.; Carver, J. A. The Thioflavin T Fluorescence Assay for Amyloid Fibril Detection Can Be Biased by the Presence of Exogenous Compounds. *FEBS J.* **2009**, *276*, 5960–5972.
(249) Jamieson, T.; Bakhshi, R.; Petrova, D.; Pocock, R.; Imani, M.; Seifalian, A. M. Biological Applications of Quantum Dots. *Biomaterials* **2007**, *28*, 4717–4732.
(250) Smith, A. M.; Duan, H.; Mohs, A. M.; Nie, S. Bioconjugated Quantum Dots for in Vivo Molecular and Cellular Imaging. *Adv. Drug Deliv. Rev.* **2008**, *60*, 1226–1240.
(251) Alivisatos, A. P.; Gu, W.; Larabell, C. Quantum Dots as Cellular Probes. *Annu. Rev. Biomed. Eng.* **2005**, *7*, 55–76.
(252) Shaner, N. C.; Steinbach, P. A.; Tsien, R. Y. A Guide to Choosing Fluorescent Proteins. *Nat. Methods* **2005**, *2*, 905–909.
(253) Straight, A. F. Fluorescent Protein Applications in Microscopy. *Methods Cell Biol.* **2007**, *81*, 93–113.
(254) Brandenburg, B.; Zhuang, X. Virus Trafficking – Learning from Single-Virus Tracking. *Nat. Rev. Microbiol.* **2007**, *5*, 197–208.
(255) Panchuk-Voloshina, N.; Haugland, R. P.; Bishop-Stewart, J.; Bhalgat, M. K.; Millard, P. J.; Mao, F.; Leung, W. Y.; Haugland, R. P. Alexa Dyes, a Series of New Fluorescent Dyes That Yield Exceptionally Bright, Photostable Conjugates. *J. Histochem. Cytochem. Off. J. Histochem. Soc.* **1999**, *47*, 1179–1188.
(256) Gonçalves, M. S. T. Fluorescent Labeling of Biomolecules with Organic Probes. *Chem. Rev.* **2009**, *109*, 190–212.
(257) Maeda, H.; Ishida, N.; Kawauchi, H.; Tuzimura, K. Reaction of Fluorescein-Isothiocyanate with Proteins and Amino Acids: I. Covalent and Non-Covalent Binding of Fluorescein-Isothiocyanate and Fluorescein to Proteins. *J. Biochem. (Tokyo)* **1969**, *65*, 777–783.
(258) Pierobon, P.; Cappello, G. Quantum Dots to Tail Single Bio-Molecules inside Living Cells. *Adv. Drug Deliv. Rev.* **2012**, *64*, 167–178.
(259) Nan, X.; Sims, P. A.; Xie, X. S. Organelle Tracking in a Living Cell with Microsecond Time Resolution and Nanometer Spatial Precision. *Chemphyschem Eur. J. Chem. Phys. Phys. Chem.* **2008**, *9*, 707–712.
(260) Biebricher, A.; Wende, W.; Escudé, C.; Pingoud, A.; Desbiolles, P. Tracking of Single Quantum Dot Labeled EcoRV Sliding along DNA Manipulated by Double Optical Tweezers. *Biophys. J.* **2009**, *96*, L50–L52.
(261) Zhu, H.; Srivastava, R.; Brown, J. Q.; McShane, M. J. Combined Physical and Chemical Immobilization of Glucose Oxidase in Alginate Microspheres Improves Stability of Encapsulation and Activity. *Bioconjug. Chem.* **2005**, *16*, 1451–1458.
(262) Wang, L.; Cole, K. D.; Gaigalas, A. K.; Zhang, Y.-Z. Fluorescent Nanometer Microspheres as a Reporter for Sensitive Detection of Simulants of Biological Threats Using Multiplexed Suspension Arrays. *Bioconjug. Chem.* **2005**, *16*, 194–199.

(263) Meng, Q.; Li, Z.; Li, G.; Zhang, X.; An, Y.; Zhu, X. X. Aggregation of Biotinylated Polymeric Microspheres Induced by Interaction with Avidin. *Pure Appl. Chem.* **2007**, *79*.
(264) Phadtare, S.; Vinod, V. P.; Mukhopadhyay, K.; Kumar, A.; Rao, M.; Chaudhari, R. V.; Sastry, M. Immobilization and Biocatalytic Activity of Fungal Protease on Gold Nanoparticle-Loaded Zeolite Microspheres. *Biotechnol. Bioeng.* **2004**, *85*, 629–637.
(265) Sowa, Y.; Steel, B. C.; Berry, R. M. A Simple Backscattering Microscope for Fast Tracking of Biological Molecules. *Rev. Sci. Instrum.* **2010**, *81*, 113704.
(266) Maysinger, D.; Lovrić, J.; Eisenberg, A.; Savić, R. Fate of Micelles and Quantum Dots in Cells. *Eur. J. Pharm. Biopharm. Off. J. Arbeitsgemeinschaft Für Pharm. Verfahrenstechnik EV* **2007**, *65*, 270–281.
(267) Green, M.; O'Brien, P. Recent Advances in the Preparation of Semiconductors as Isolated Nanometric Particles: New Routes to Quantum Dots. *Chem. Commun.* **1999**, 2235–2241.
(268) Parak, W. J.; Pellegrino, T.; Plank, C. Labelling of Cells with Quantum Dots. *Nanotechnology* **2005**, *16*, R9.
(269) Lakhtakia, A. *Handbook of Nanotechnology: Nanometer Structure Theory, Modeling, and Simulation*; American Society of Mechanical Engineers, 2004.
(270) Chestnoy, N.; Harris, T. D.; Hull, R.; Brus, L. E. Luminescence and Photophysics of Cadmium Sulfide Semiconductor Clusters: The Nature of the Emitting Electronic State. *J. Phys. Chem.* **1986**, *90*, 3393–3399.
(271) Chan, W. C. .; Maxwell, D. J.; Gao, X.; Bailey, R. E.; Han, M.; Nie, S. Luminescent Quantum Dots for Multiplexed Biological Detection and Imaging. *Curr. Opin. Biotechnol.* **2002**, *13*, 40–46.
(272) Jaiswal, J. K.; Simon, S. M. Potentials and Pitfalls of Fluorescent Quantum Dots for Biological Imaging. *Trends Cell Biol.* **2004**, *14*, 497–504.
(273) Byers, R. J.; Hitchman, E. R. Quantum Dots Brighten Biological Imaging. *Prog. Histochem. Cytochem.* **2011**, *45*, 201–237.
(274) Gao, X.; Yang, L.; Petros, J. A.; Marshall, F. F.; Simons, J. W.; Nie, S. In Vivo Molecular and Cellular Imaging with Quantum Dots. *Curr. Opin. Biotechnol.* **2005**, *16*, 63–72.
(275) McHale, K.; Berglund, A. J.; Mabuchi, H. Quantum Dot Photon Statistics Measured by Three-Dimensional Particle Tracking. *Nano Lett.* **2007**, *7*, 3535–3539.
(276) Medintz, I. L.; Uyeda, H. T.; Goldman, E. R.; Mattoussi, H. Quantum Dot Bioconjugates for Imaging, Labelling and Sensing. *Nat. Mater.* **2005**, *4*, 435–446.
(277) Sapsford, K. E.; Tyner, K. M.; Dair, B. J.; Deschamps, J. R.; Medintz, I. L. Analyzing Nanomaterial Bioconjugates: A Review of Current and Emerging Purification and Characterization Techniques. *Anal. Chem.* **2011**, *83*, 4453–4488.
(278) Liu, H.; Liu, Y.; Liu, S.; Pang, D.-W.; Xiao, G. Clathrin-Mediated Endocytosis in Living Host Cells Visualized through Quantum Dot Labeling of Infectious Hematopoietic Necrosis Virus. *J. Virol.* **2011**, *85*, 6252–6262.
(279) Ishihama, Y.; Funatsu, T. Single Molecule Tracking of Quantum Dot-Labeled mRNAs in a Cell Nucleus. *Biochem. Biophys. Res. Commun.* **2009**, *381*, 33–38.
(280) Tsuji, T.; Kawai-Noma, S.; Pack, C.-G.; Terajima, H.; Yajima, J.; Nishizaka, T.; Kinjo, M.; Taguchi, H. Single-Particle Tracking of Quantum Dot-Conjugated Prion Proteins inside Yeast Cells. *Biochem. Biophys. Res. Commun.* **2011**, *405*, 638–643.
(281) Liu, S.-L.; Zhang, Z.-L.; Sun, E.-Z.; Peng, J.; Xie, M.; Tian, Z.-Q.; Lin, Y.; Pang, D.-W. Visualizing the Endocytic and Exocytic Processes of Wheat Germ Agglutinin by Quantum Dot-Based Single-Particle Tracking. *Biomaterials* **2011**, *32*, 7616–7624.

(282) Fruk, L.; Rajendran, V.; Spengler, M.; Niemeyer, C. M. Light-Induced Triggering of Peroxidase Activity Using Quantum Dots. *ChemBioChem* **2007**, *8*, 2195–2198.
(283) Hild, W. A.; Breunig, M.; Goepferich, A. Quantum Dots - Nano-Sized Probes for the Exploration of Cellular and Intracellular Targeting. *Eur. J. Pharm. Biopharm. Off. J. Arbeitsgemeinschaft Für Pharm. Verfahrenstechnik EV* **2008**, *68*, 153–168.
(284) Ipe, B. I.; Shukla, A.; Lu, H.; Zou, B.; Rehage, H.; Niemeyer, C. M. Dynamic Light-Scattering Analysis of the Electrostatic Interaction of Hexahistidine-Tagged Cytochrome P450 Enzyme with Semiconductor Quantum Dots. *Chemphyschem Eur. J. Chem. Phys. Phys. Chem.* **2006**, *7*, 1112–1118.
(285) Gilroy, K. L.; Cumming, S. A.; Pitt, A. R. A Simple, Sensitive and Selective Quantum-Dot-Based Western Blot Method for the Simultaneous Detection of Multiple Targets from Cell Lysates. *Anal. Bioanal. Chem.* **2010**, *398*, 547–554.
(286) Carrillo-Carrión, C.; Simonet, B. M.; Valcárcel, M. Colistin-Functionalised CdSe/ZnS Quantum Dots as Fluorescent Probe for the Rapid Detection of Escherichia Coli. *Biosens. Bioelectron.* **2011**, *26*, 4368–4374.
(287) Pereira, M.; Lai, E. P. Capillary Electrophoresis for the Characterization of Quantum Dots after Non-Selective or Selective Bioconjugation with Antibodies for Immunoassay. *J. Nanobiotechnology* **2008**, *6*, 10.
(288) Jackeray, R.; Abid, C. K. V. Z.; Singh, G.; Jain, S.; Chattopadhyaya, S.; Sapra, S.; Shrivastav, T. G.; Singh, H. Selective Capturing and Detection of Salmonella Typhi on Polycarbonate Membrane Using Bioconjugated Quantum Dots. *Talanta* **2011**, *84*, 952–962.
(289) Prapainop, K.; Wentworth, P., Jr. A Shotgun Proteomic Study of the Protein Corona Associated with Cholesterol and Atheronal-B Surface-Modified Quantum Dots. *Eur. J. Pharm. Biopharm. Off. J. Arbeitsgemeinschaft Für Pharm. Verfahrenstechnik EV* **2011**, *77*, 353–359.
(290) Paul, A. S.; Pollard, T. D. Energetic Requirements for Processive Elongation of Actin Filaments by FH1FH2-Formins. *J. Biol. Chem.* **2009**, *284*, 12533–12540.
(291) Sigot, V.; Arndt-Jovin, D. J.; Jovin, T. M. Targeted Cellular Delivery of Quantum Dots Loaded on and in Biotinylated Liposomes. *Bioconjug. Chem.* **2010**, *21*, 1465–1472.
(292) Yoo, J.; Kambara, T.; Gonda, K.; Higuchi, H. Intracellular Imaging of Targeted Proteins Labeled with Quantum Dots. *Exp. Cell Res.* **2008**, *314*, 3563–3569.
(293) Vicente, G.; Colón, L. A. Separation of Bioconjugated Quantum Dots Using Capillary Electrophoresis. *Anal. Chem.* **2008**, *80*, 1988–1994.
(294) Mansur, H. S.; González, J. C.; Mansur, A. A. P. Biomolecule-Quantum Dot Systems for Bioconjugation Applications. *Colloids Surf. B Biointerfaces* **2011**, *84*, 360–368.
(295) Bobyr, E.; Lassila, J. K.; Wiersma-Koch, H. I.; Fenn, T. D.; Lee, J. J.; Nikolic-Hughes, I.; Hodgson, K. O.; Rees, D. C.; Hedman, B.; Herschlag, D. High-Resolution Analysis of Zn2+ Coordination in the Alkaline Phosphatase Superfamily by EXAFS and X-Ray Crystallography. *J. Mol. Biol.* **2012**, *415*, 102–117.
(296) Levi, V.; Gratton, E. Three-Dimensional Particle Tracking in a Laser Scanning Fluorescence Microscope. In *Single Particle Tracking and Single Molecule Energy Transfer*; Bräuchle, C.; Lamb, D. C.; Michaelis, J., Eds.; Wiley-VCH Verlag GmbH & Co. KGaA, 2009; pp. 1–24.
(297) Petty, H. R. Fluorescence Microscopy: Established and Emerging Methods, Experimental Strategies, and Applications in Immunology. *Microsc. Res. Tech.* **2007**, *70*, 687–709.
(298) Http://zeiss-Campus.magnet.fsu.edu/articles/basics/resolution.html.

(299) Schmid, B.; Shah, G.; Scherf, N.; Weber, M.; Thierbach, K.; Campos, C. P.; Roeder, I.; Aanstad, P.; Huisken, J. High-Speed Panoramic Light-Sheet Microscopy Reveals Global Endodermal Cell Dynamics. *Nat. Commun.* **2013**, *4*.

(300) Crocker, J. C.; Grier, D. G. Methods of Digital Video Microscopy for Colloidal Studies. *J. Colloid Interface Sci.* **1996**, *179*, 298–310.

(301) Whyte, M. P.; Landt, M.; Ryan, L. M.; Mulivor, R. A.; Henthorn, P. S.; Fedde, K. N.; Mahuren, J. D.; Coburn, S. P. Alkaline Phosphatase: Placental and Tissue-Nonspecific Isoenzymes Hydrolyze Phosphoethanolamine, Inorganic Pyrophosphate, and Pyridoxal 5'-Phosphate. Substrate Accumulation in Carriers of Hypophosphatasia Corrects during Pregnancy. *J. Clin. Invest.* **1995**, *95*, 1440–1445.

(302) Imhof, A.; Megens, M.; Engelberts, J. J.; de Lang, D. T. N.; Sprik, R.; Vos, W. L. Spectroscopy of Fluorescein (FITC) Dyed Colloidal Silica Spheres. *J. Phys. Chem. B* **1999**, *103*, 1408–1415.

(303) Bradshaw, R. A.; Cancedda, F.; Ericsson, L. H.; Neumann, P. A.; Piccoli, S. P.; Schlesinger, M. J.; Shriefer, K.; Walsh, K. A. Amino Acid Sequence of Escherichia Coli Alkaline Phosphatase. *Proc. Natl. Acad. Sci. U. S. A.* **1981**, *78*, 3473–3477.

(304) Flock, T.; Venkatakrishnan, A. J.; Vinothkumar, K. R.; Babu, M. M. Deciphering Membrane Protein Structures from Protein Sequences. *Genome Biol.* **2012**, *13*, 160.

(305) Zhang, L.; Buchet, R.; Azzar, G. Phosphate Binding in the Active Site of Alkaline Phosphatase and the Interactions of 2-Nitrosoacetophenone with Alkaline Phosphatase-Induced Small Structural Changes. *Biophys. J.* **2004**, *86*, 3873–3881.

(306) Csopak, H.; Garellick, G.; Hallberg, B. Purification of Escherichia Coli Alkaline Phosphatase. Improved Growth Conditions for the Bacteria, Modified Methods of Preparation of the Enzyme. *Acta Chem. Scand.* **1972**, *26*, 2401–2411.

(307) Zappa, S.; Boudrant, J.; Kantrowitz, E. R. Pyrococcus Abyssi Alkaline Phosphatase: The Dimer Is the Active Form. *J. Inorg. Biochem.* **2004**, *98*, 575–581.

(308) Hehir, M. J.; Murphy, J. E.; Kantrowitz, E. R. Characterization of Heterodimeric Alkaline Phosphatases from Escherichia Coli: An Investigation of Intragenic Complementation. *J. Mol. Biol.* **2000**, *304*, 645–656.

(309) Yang, K.; Metcalf, W. W. A New Activity for an Old Enzyme: Escherichia Coli Bacterial Alkaline Phosphatase Is a Phosphite-Dependent Hydrogenase. *Proc. Natl. Acad. Sci. U. S. A.* **2004**, *101*, 7919–7924.

(310) O'Brien, P. J.; Lassila, J. K.; Fenn, T. D.; Zalatan, J. G.; Herschlag, D. Arginine Coordination in Enzymatic Phosphoryl Transfer: Evaluation of the Effect of Arg166 Mutations in Escherichia Coli Alkaline Phosphatase,. *Biochemistry (Mosc.)* **2008**, *47*, 7663–7672.

(311) Park, T.; Lee, J. H.; Kim, H. K.; Hoe, H. S.; Kwon, S. T. Nucleotide Sequence of the Gene for Alkaline Phosphatase of Thermus Caldophilus GK24 and Characteristics of the Deduced Primary Structure of the Enzyme. *FEMS Microbiol. Lett.* **1999**, *180*, 133–139.

(312) Manes, T.; Hoylaerts, M. F.; Müller, R.; Lottspeich, F.; Hölke, W.; Millán, J. L. Genetic Complexity, Structure, and Characterization of Highly Active Bovine Intestinal Alkaline Phosphatases. *J. Biol. Chem.* **1998**, *273*, 23353–23360.

(313) Boulanger, R. R., Jr; Kantrowitz, E. R. Characterization of a Monomeric Escherichia Coli Alkaline Phosphatase Formed upon a Single Amino Acid Substitution. *J. Biol. Chem.* **2003**, *278*, 23497–23501.

(314) Holtz, K. M.; Stec, B.; Kantrowitz, E. R. A Model of the Transition State in the Alkaline Phosphatase Reaction. *J. Biol. Chem.* **1999**, *274*, 8351–8354.

(315) López-Alonso, J. P.; Diez-García, F.; Font, J.; Ribó, M.; Vilanova, M.; Scholtz, J. M.; González, C.; Vottariello, F.; Gotte, G.; Libonati, M.; *et al.* Carbodiimide EDC Induces Cross-Links That Stabilize RNase A C-Dimer against Dissociation: EDC Adducts Can Affect Protein Net Charge, Conformation, and Activity. *Bioconjug. Chem.* **2009**, *20*, 1459–1473.
(316) Kim, J. H.; Lim, S. Y.; Nam, D. H.; Ryu, J.; Ku, S. H.; Park, C. B. Self-Assembled, Photoluminescent Peptide Hydrogel as a Versatile Platform for Enzyme-Based Optical Biosensors. *Biosens. Bioelectron.* **2011**, *26*, 1860–1865.
(317) Siegberg, D.; Herten, D.-P. Fluorescence Quenching of Quantum Dots by DNA Nucleotides and Amino Acids1. *Aust. J. Chem.* **2011**, *64*, 512–516.
(318) Breslow, R.; Katz, I. Relative Reactivities of P-Nitrophenyl Phosphate and Phosphorothioate toward Alkaline Phosphatase and in Aqueous Hydrolysis. *J. Am. Chem. Soc.* **1968**, *90*, 7376–7377.
(319) Pearson, K. The Problem of the Random Walk. *Nature* **1905**, *72*, 294.
(320) Rayleigh. The Problem of the Random Walk. *Nature* **1905**, *72*, 318.
(321) Sengupta, S.; Dey, K. K.; Muddana, H. S.; Tabouillot, T.; Ibele, M. E.; Butler, P. J.; Sen, A. Enzyme Molecules as Nanomotors. *J. Am. Chem. Soc.* **2013**, *135*, 1406–1414.
(322) Yagi, H.; Ban, T.; Morigaki, K.; Naiki, H.; Goto, Y. Visualization and Classification of Amyloid Beta Supramolecular Assemblies. *Biochemistry (Mosc.)* **2007**, *46*, 15009–15017.
(323) Chaudhary, N.; Nagaraj, R. Self-Assembly of Short Amyloidogenic Peptides at the Air-Water Interface. *J. Colloid Interface Sci.* **2011**, *360*, 139–147.
(324) Diaspro, A.; Chirico, G.; Collini, M. Two-Photon Fluorescence Excitation and Related Techniques in Biological Microscopy. *Q. Rev. Biophys.* **2005**, *38*, 97–166.
(325) Gao, Y.; Berciu, C.; Kuang, Y.; Shi, J.; Nicastro, D.; Xu, B. Probing Nanoscale Self-Assembly of Nonfluorescent Small Molecules inside Live Mammalian Cells. *ACS Nano* **2013**, *7*, 9055–9063.
(326) Jarvis, J. A.; Craik, D. J.; Wilce, M. C. J. X-Ray-Diffraction Studies of Fibrils Formed from Peptide Fragments of Transthyretin. *Biochem. Biophys. Res. Commun.* **1993**, *192*, 991–998.
(327) Lakowicz, J. R. *Principles of Fluorescence Spectroscopy*; Springer Science & Business Media, 2007.
(328) Ebbens, S. J.; Howse, J. R. In Pursuit of Propulsion at the Nanoscale. *Soft Matter* **2010**, *6*, 726–738.
(329) Huyer, G.; Liu, S.; Kelly, J.; Moffat, J.; Payette, P.; Kennedy, B.; Tsaprailis, G.; Gresser, M. J.; Ramachandran, C. Mechanism of Inhibition of Protein-Tyrosine Phosphatases by Vanadate and Pervanadate. *J. Biol. Chem.* **1997**, *272*, 843–851.
(330) Demeule, B.; Gurny, R.; Arvinte, T. Detection and Characterization of Protein Aggregates by Fluorescence Microscopy. *Int. J. Pharm.* **2007**, *329*, 37–45.
(331) Sackett, D. L.; Knutson, J. R.; Wolff, J. Hydrophobic Surfaces of Tubulin Probed by Time-Resolved and Steady-State Fluorescence of Nile Red. *J. Biol. Chem.* **1990**, *265*, 14899–14906.
(332) Greenspan, P.; Mayer, E. P.; Fowler, S. D. Nile Red: A Selective Fluorescent Stain for Intracellular Lipid Droplets. *J. Cell Biol.* **1985**, *100*, 965–973.
(333) Sutter, M.; Oliveira, S.; Sanders, N. N.; Lucas, B.; van Hoek, A.; Hink, M. A.; Visser, A. J. W. G.; De Smedt, S. C.; Hennink, W. E.; Jiskoot, W. Sensitive Spectroscopic Detection of Large and Denatured Protein Aggregates in Solution by Use of the Fluorescent Dye Nile Red. *J. Fluoresc.* **2007**, *17*, 181–192.

(334) Styren, S. D.; Hamilton, R. L.; Styren, G. C.; Klunk, W. E. X-34, a Fluorescent Derivative of Congo Red: A Novel Histochemical Stain for Alzheimer's Disease Pathology. *J. Histochem. Cytochem. Off. J. Histochem. Soc.* **2000**, *48*, 1223–1232.
(335) Puchtler, H.; Sweat, F.; Levine, M. On the Binding of Congo Red by Amyloid. *J. Histochem. Cytochem.* **1962**, *10*, 355–364.
(336) Khurana, R.; Uversky, V. N.; Nielsen, L.; Fink, A. L. Is Congo Red an Amyloid-Specific Dye? *J. Biol. Chem.* **2001**, *276*, 22715–22721.
(337) Van Rijswijk, M. H.; van Heusden, C. W. The Potassium Permanganate Method. A Reliable Method for Differentiating Amyloid AA from Other Forms of Amyloid in Routine Laboratory Practice. *Am. J. Pathol.* **1979**, *97*, 43–58.
(338) Albertazzi, L.; van der Zwaag, D.; Leenders, C. M. A.; Fitzner, R.; van der Hofstad, R. W.; Meijer, E. W. Probing Exchange Pathways in One-Dimensional Aggregates with Super-Resolution Microscopy. *Science* **2014**, *344*, 491–495.

Table of Figures

Supplementary material

Supplementary material (available on disc) includes sample videos of enzyme-conjugates with different fuel scenarios, and raw data files for all of the tracking experiments included in this thesis.

Example videos

QD-AP no fuel

QD-AP 10 mM **1a**

QD-AP 10 mM **3a**

QD-AP 10 mM **4a**

QD-AP 0.1 mM **2a**

QD-AP control reservoir

QD-AP **1a** reservoir

QD-AP **2a** reservoir

QD-AP **4a** reservoir

QD-AP (525/655 mixed) 536 EM

QD-AP (525/655 mixed) 650 EM

QD655-Chym no fuel

QD-AP added to **2a** fibres on surface

Raw data files

QD655

QD-AP no fuel

QD-AP 0.1 mM **1a**

QD-AP 1 mM **1a**

QD-AP 5 mM **1a**

QD-AP 10 mM **1a**

QD-AP 20 mM **1a**

QD-AP 0.1 mM **2a**

QD-AP 10 mM **3a**

QD-AP 0.1 mM **4a**

QD-AP 1 mM **4a**

QD-AP 5 mM **4a**

QD-AP 10 mM **4a**

QD-AP 20 mM **4a**

QD-AP no fuel control reservoir

QD-AP **1a** reservoir

QD-AP **2a** reservoir

QD-AP **4a** reservoir

QD-AP 525/655 mixed sample no fuel

QD655-Chym no fuel

Appendices

Appendix A

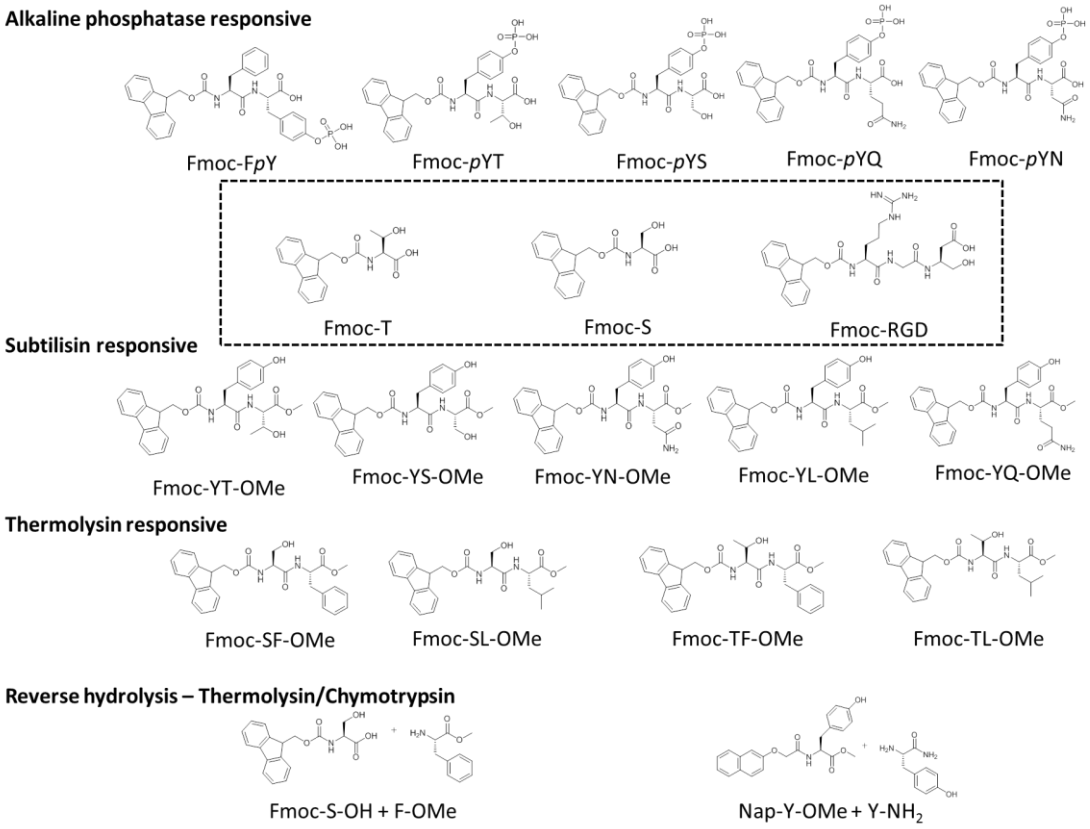

Figure 111 - Full chemical structures of biocatalytic self-assembling aromatic dipeptide amphiphiles in **Table 6**. Dotted line represents those used in conjunction with Fmoc-F*p*Y and alkaline phosphatase for co-assembly.

Appendix B

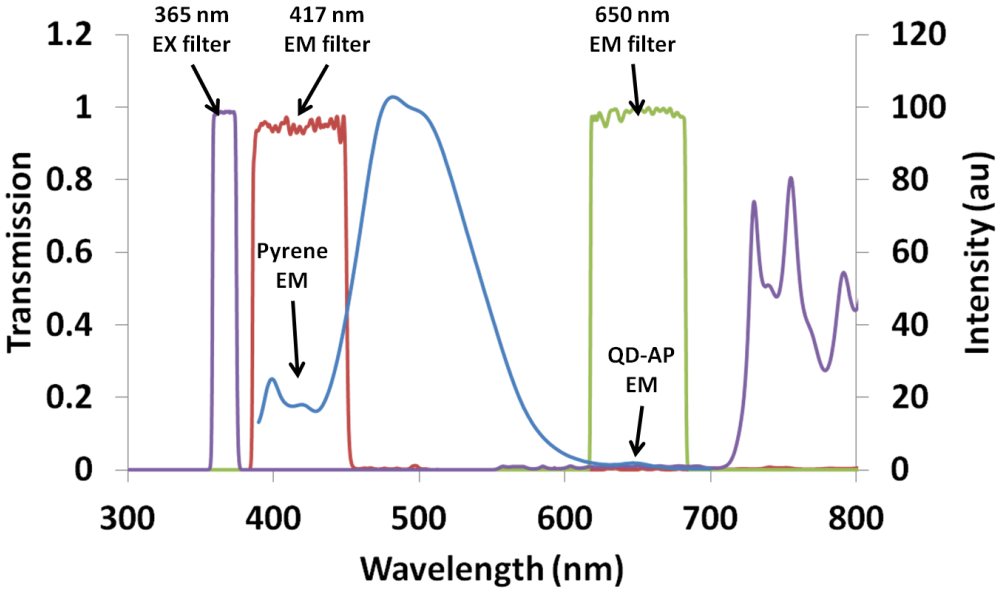

Figure 112 - Example plot of optical filter combination required to capture fluorescence signal for a two fluorophore system of 655 nm emitting QDs in QD-AP and intrinsically fluorescent **2b** fibres (pyrene). EX = excitation and EM = emission.

Appendix C

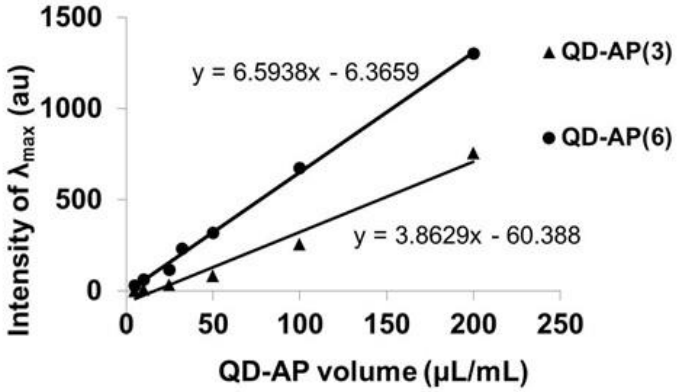

Figure 113 - Calibration curve to estimate the concentration of QD-AP (batches 3 and 6) in an unknown conjugate solution. Lines do not always pass through zero due to the fluorescence detection limit at low QD concentrations as discussed in section 5.9.

Appendix D

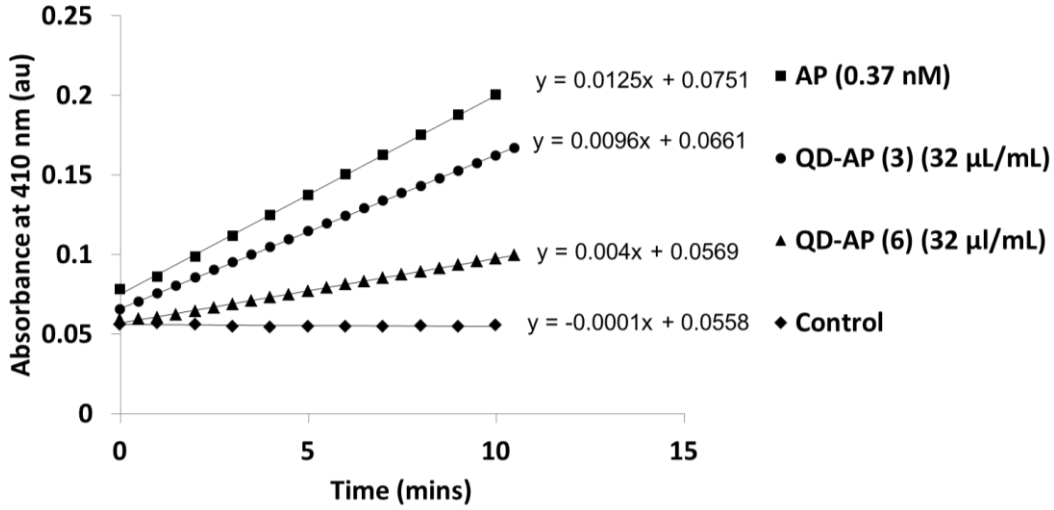

Figure 114 - Calibration for the estimation of enzyme concentration of QD-AP conjugate solutions batches 3 and 6 (32 µl/mL) and AP (7.0 x10^{-4}U).

Appendix E

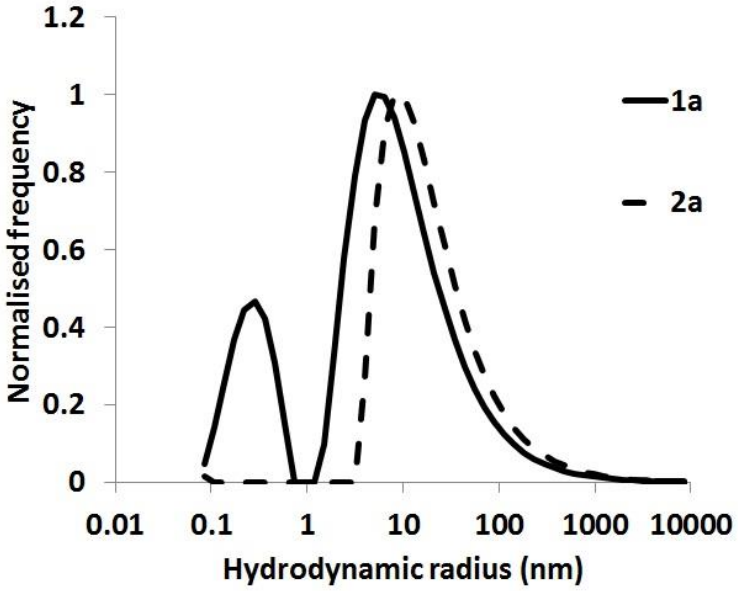

Figure 115 - DLS size distribution plot for 10 mM **1a** and **2a**. The size distribution plots are centred at 5 and 8 nm respectively. Peaks observed below 1 nm are artefacts of the DLS instrument.

Appendix F

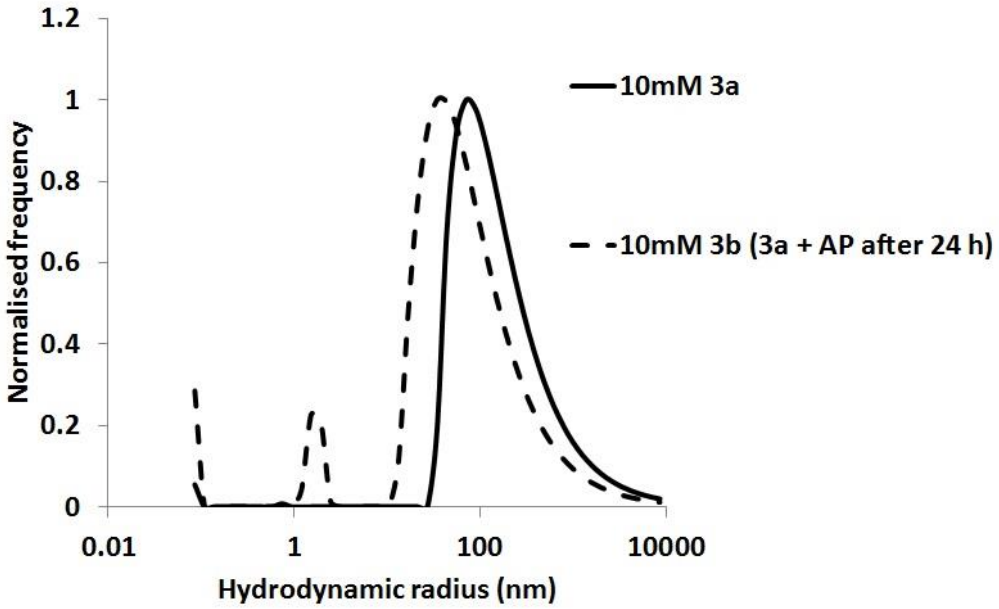

Figure 116 - DLS size distribution plot for 10 mM **3a** and **3b**, where **3b** is implied after the addition of AP to **3a** (t=24hours). The size distribution plots are centred at around 70 and 34 nm respectively. Peaks observed below 1 nm are artefacts of the DLS instrument.

Appendix G

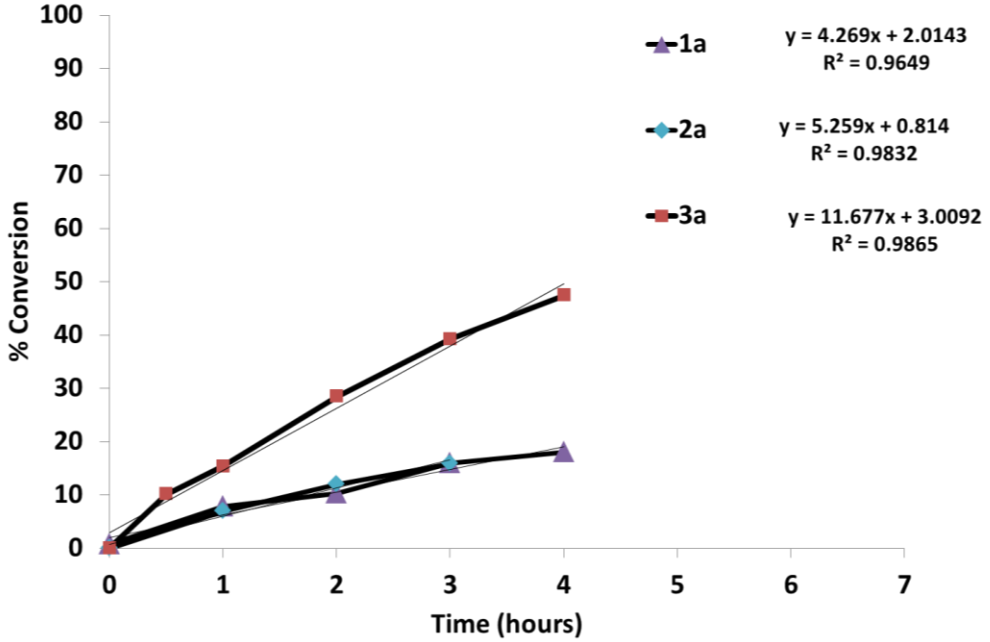

Figure 117 - Comparison of the initial conversion rates of **1a**/**2a**/**3a** to **1b**/**2b**/**3b** respectively by AP.

Appendix H

a)

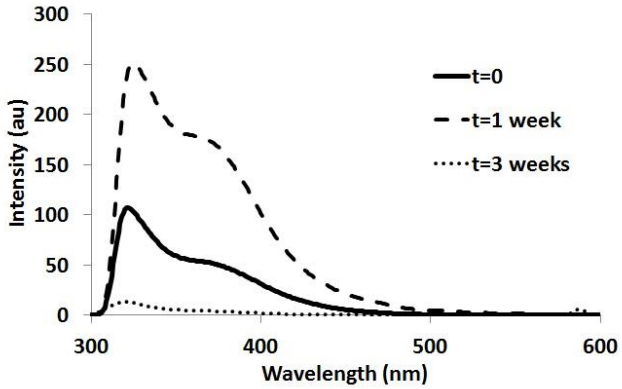

b)

Time (hours)	% conversion
0	0.6
24	0.6
48	0.5
72	0.4
96	0.3
168	0.3
336	0
504	0

Figure 118 – Negative control: Fluorescence emission spectra (a) and HPLC conversion study (b) of 10mM **1a** in buffer without enzyme.

Appendix I

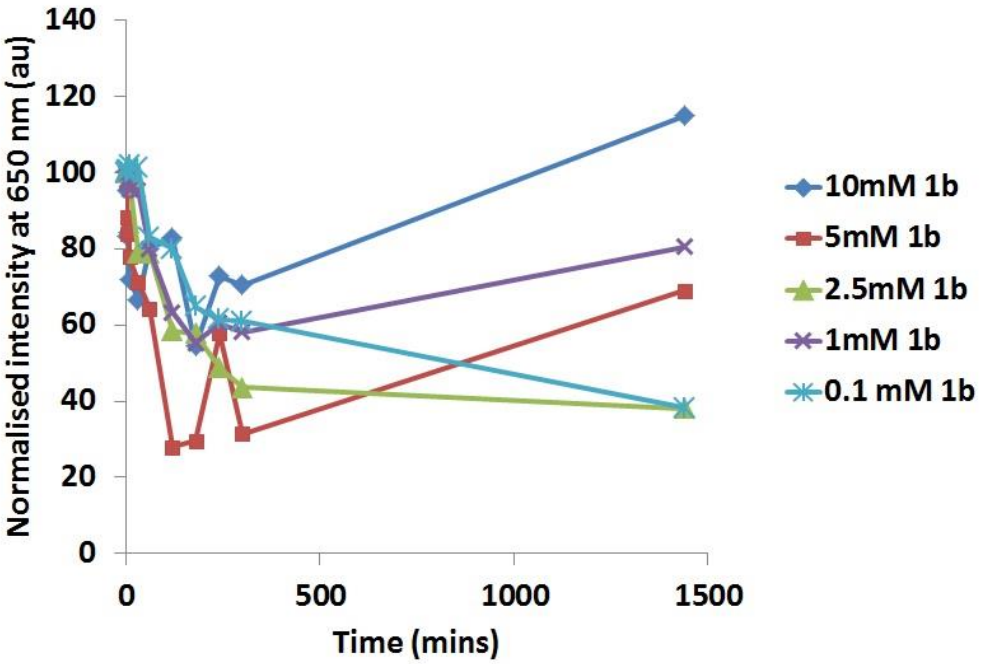

Figure 119 - Fluorescence quenching study for QD-AP in the presence of different concentration of chemically synthesised **1b**.

Appendix J

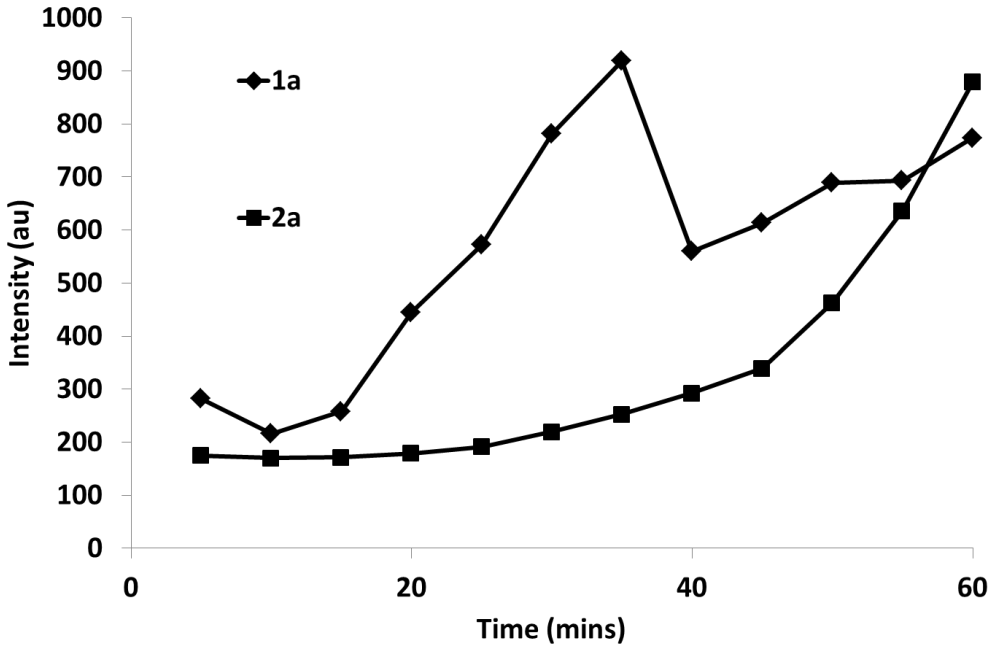

Figure 120 - Diffusion study for polyacrylamide gels saturated in fibre assembling substrates **1a** and **2a**, measured by fluorescence spectroscopy. Fluorescence intensity of **1a** and **2a** measured at 320 and 377 nm respectively over a period of 60 minutes.

Appendix K

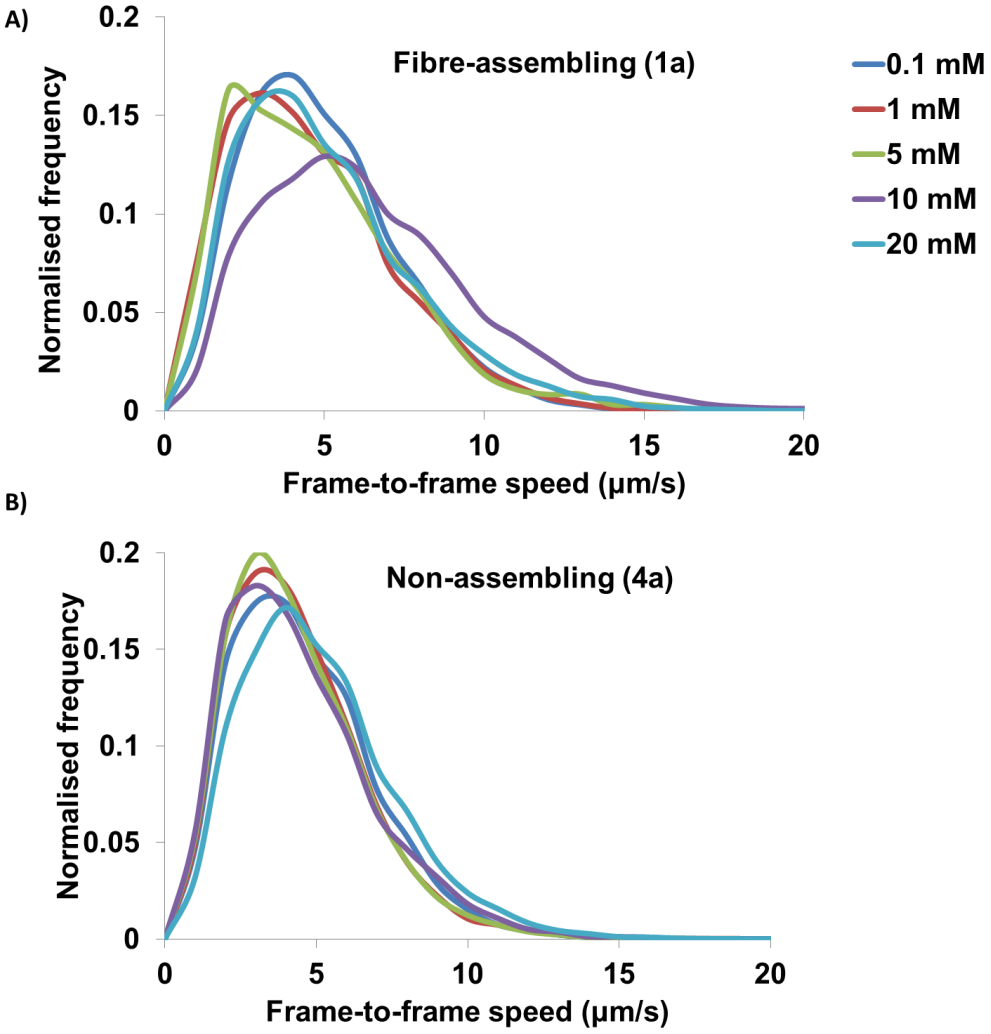

Figure 121 - Frame-to-frame speed distribution of QD-AP with different concentrations of (A) **1a** and (B) **4a**, fibre assembling and non-assembling substrates, respectively.

Appendix L

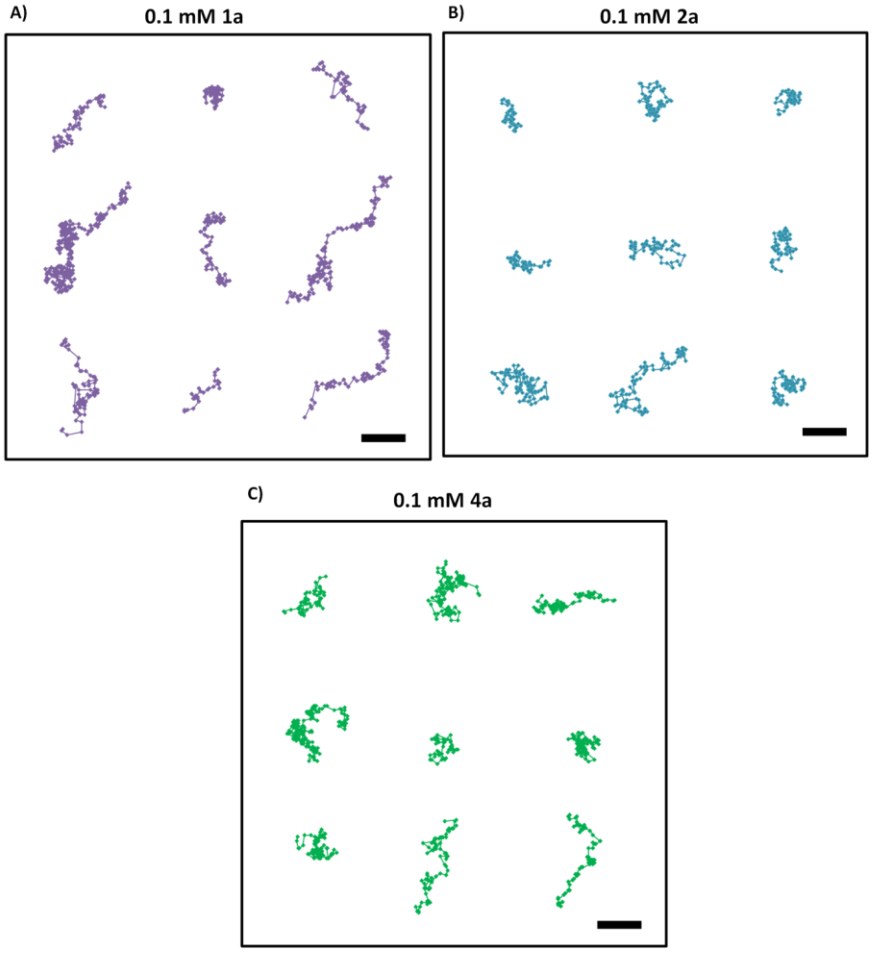

Figure 122 - Example composite trajectories of QD-AP with (A) 0.1 mM fibre-assembling substrate **1a**, (B) 0.1 mM fibre-assembling substrate **2a** and (C) non-self-assembling substrate **4a**. Scale bar = 5µm.

Appendix M

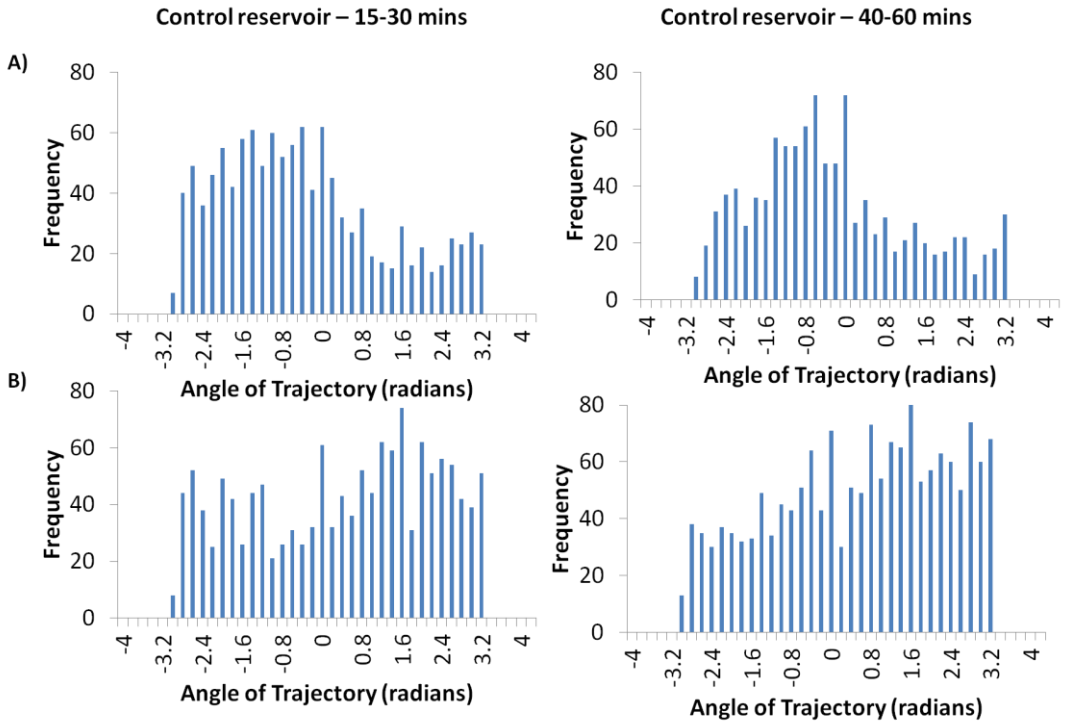

Figure 123 - Angle of trajectory distributions of QD-AP with gel saturated in buffer (no fuel). (A) Experiment 1 angle of trajectory distributions from 15-30 minutes and 45-60 minutes of time study; and the same for experiment 2 (B).

Appendix N

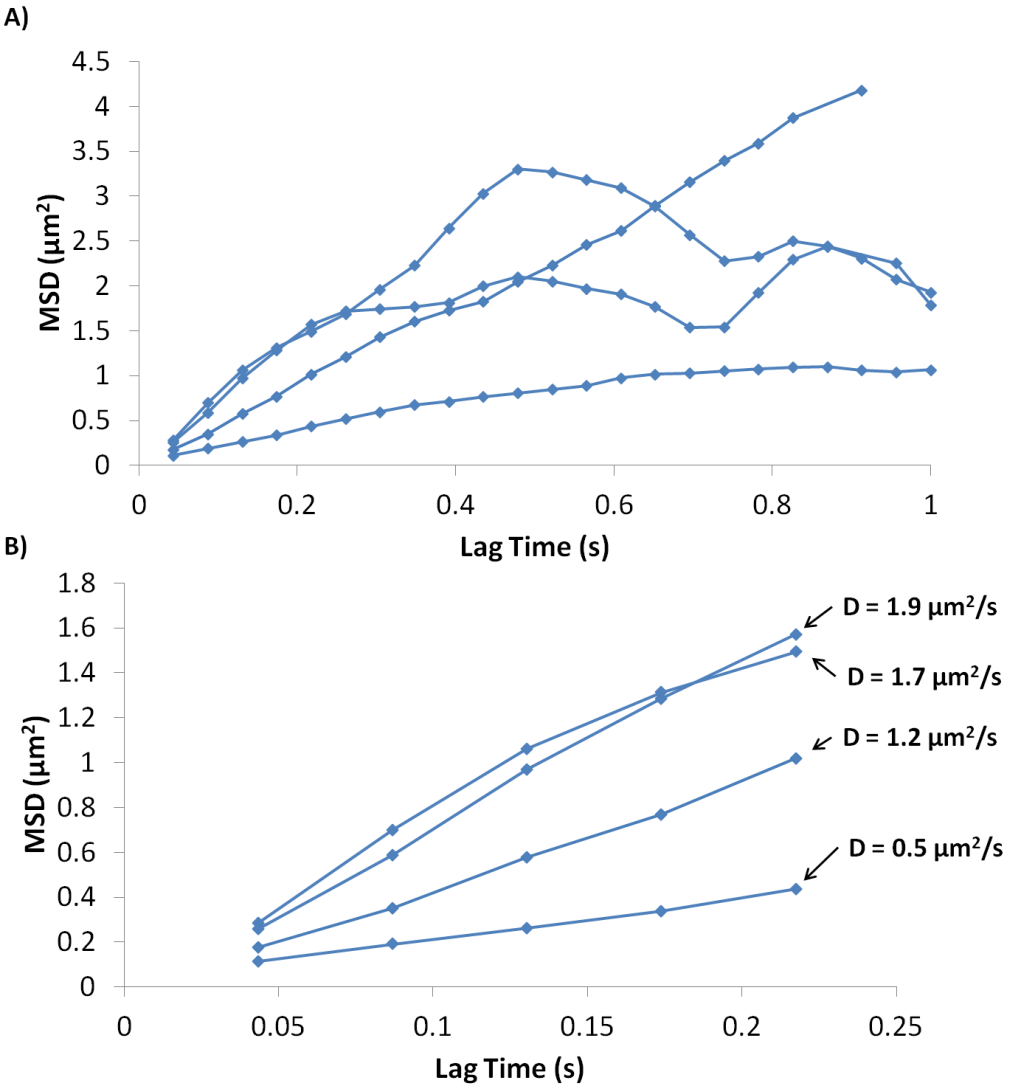

Figure 124 - Mean square displacement versus lag time for example particles with buffer saturated gel (no fuel), up to lag times of (A) 1 second and (B) 0.2 seconds, including example diffusion coefficient, D, values for each particle.

Appendix O

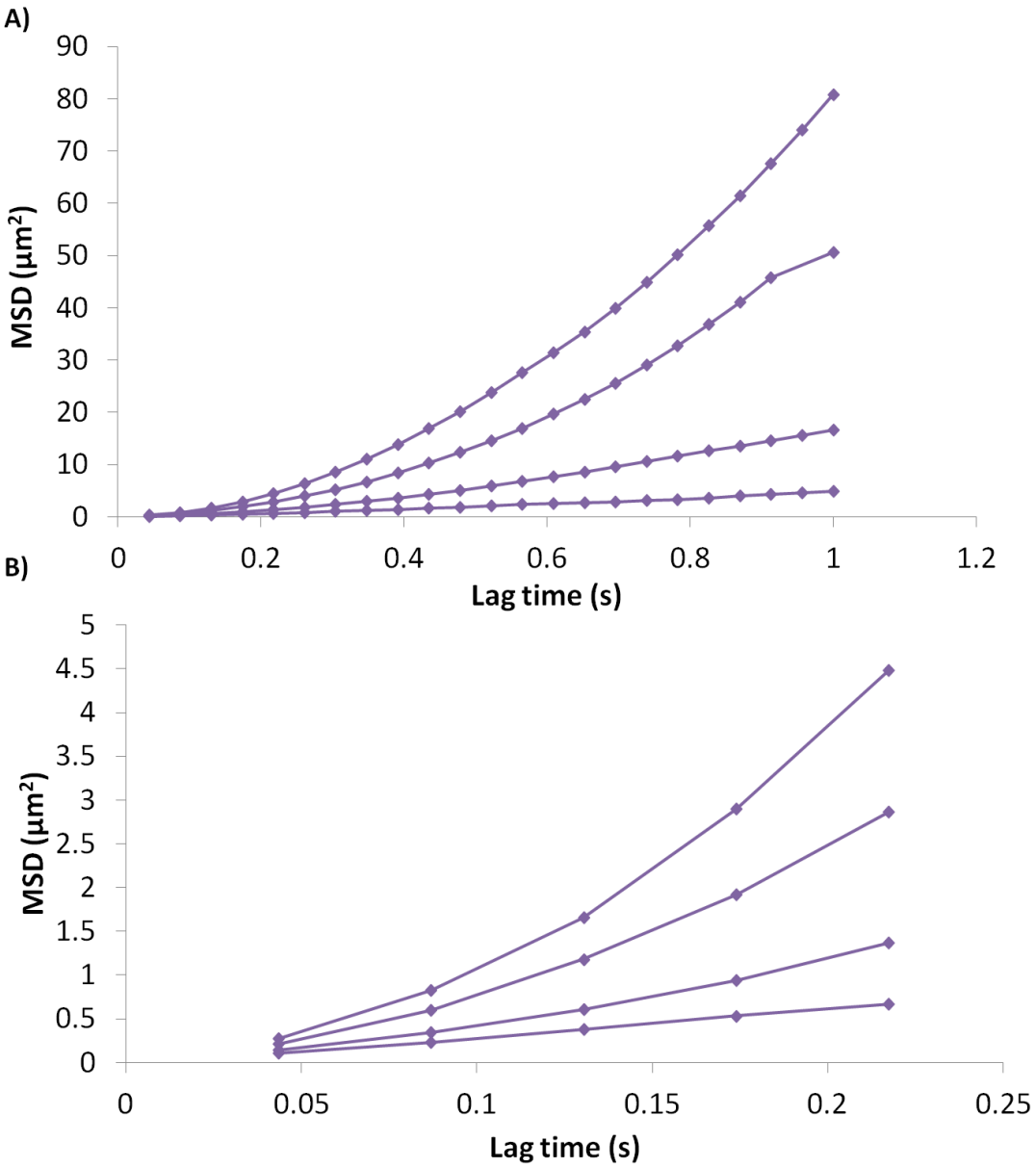

Figure 125 - Mean square displacement versus lag time for example particles with **1a** saturated gel reservoir, up to lag times of (A) 1 second and (B) 0.2 seconds.

Appendix P

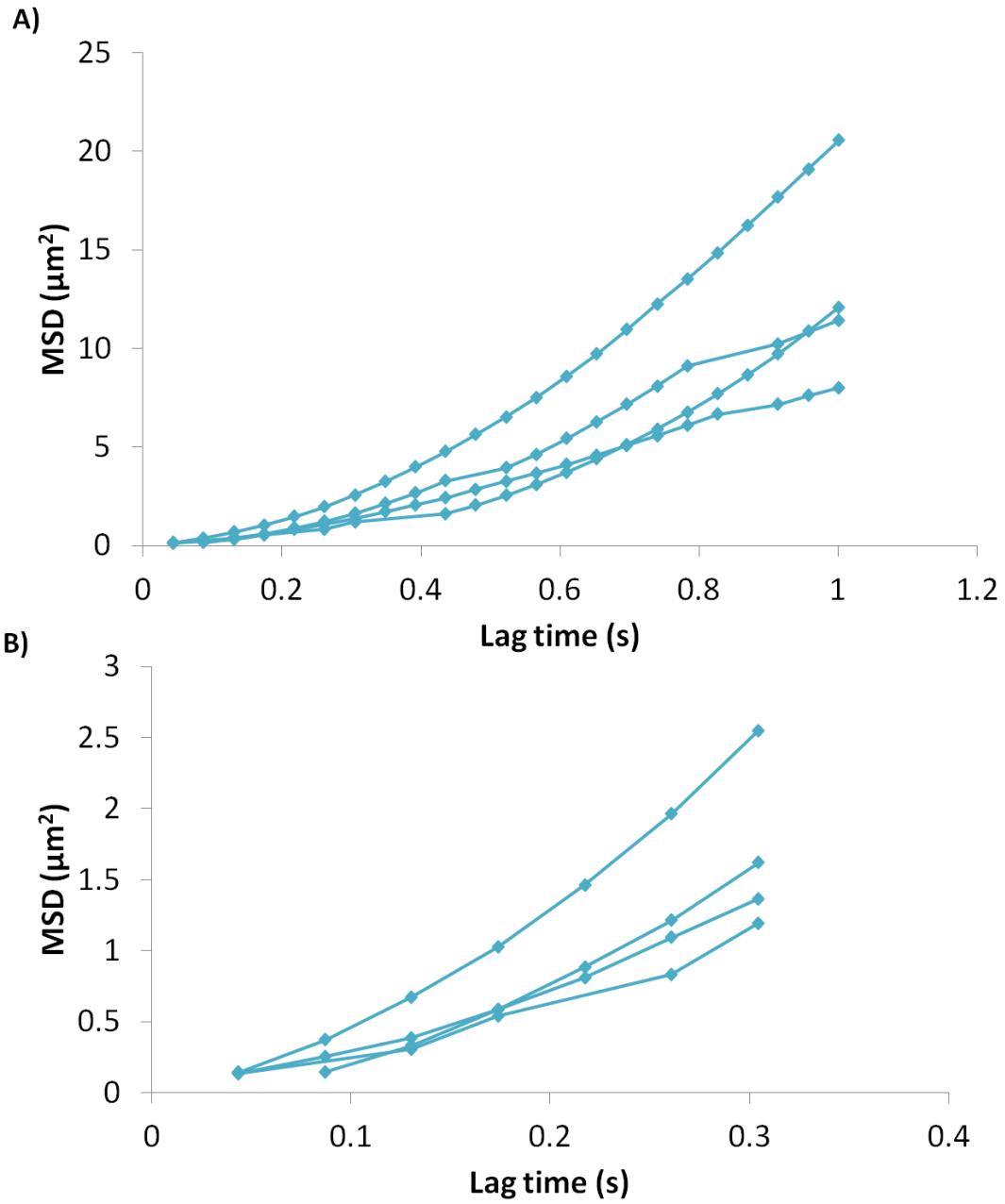

Figure 126 - Mean square displacement versus lag time for example particles with **2a** saturated gel reservoir, up to lag times of (A) 1 second and (B) 0.2 seconds.

Appendix Q

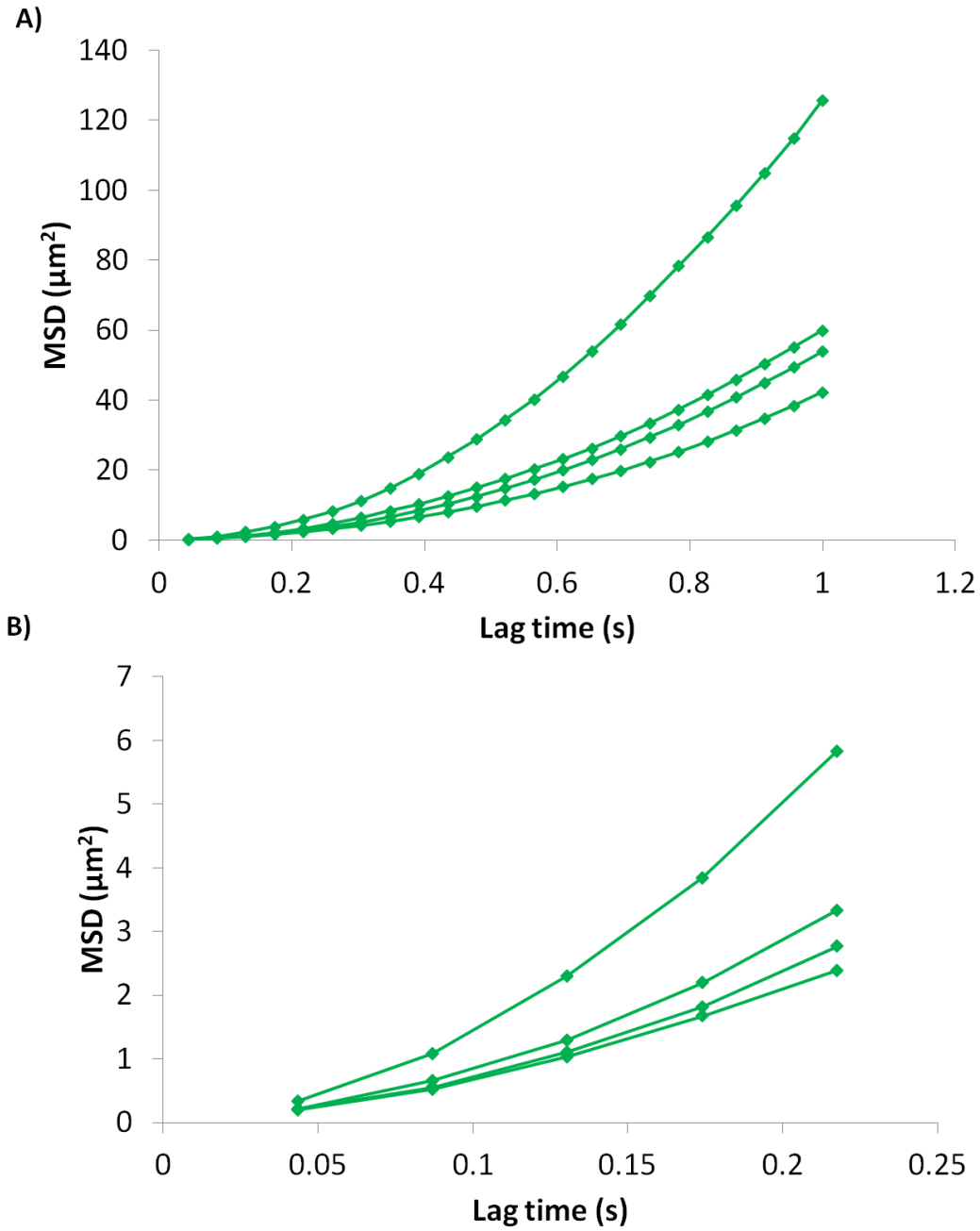

Figure 127 - Mean square displacement versus lag time for example particles with non-self-assembling substrate **4a** saturated gel reservoir, up to lag times of (A) 1 second and (B) 0.2 seconds.

Appendix R

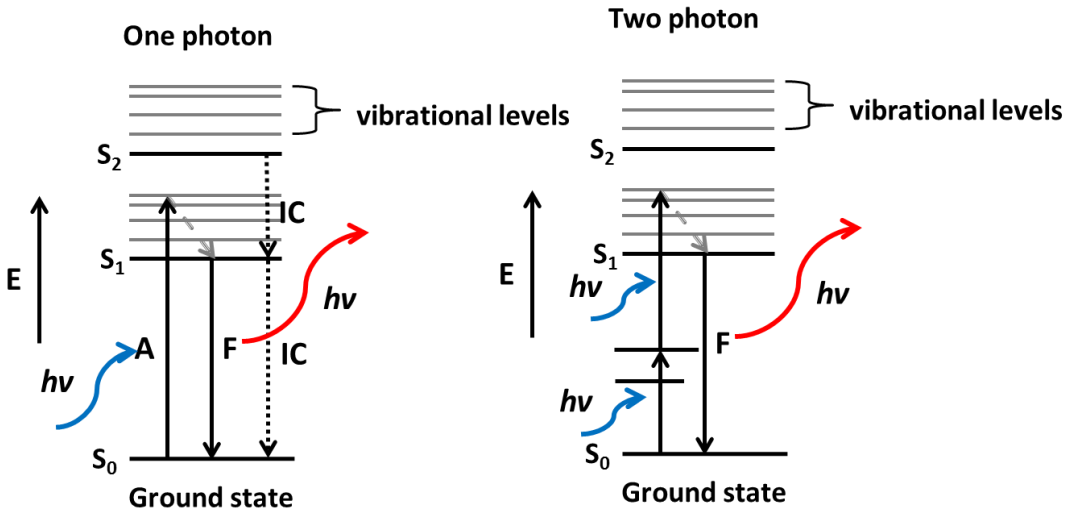

Figure 128 – One and two-photon Jablonski energy diagram.

Appendix S

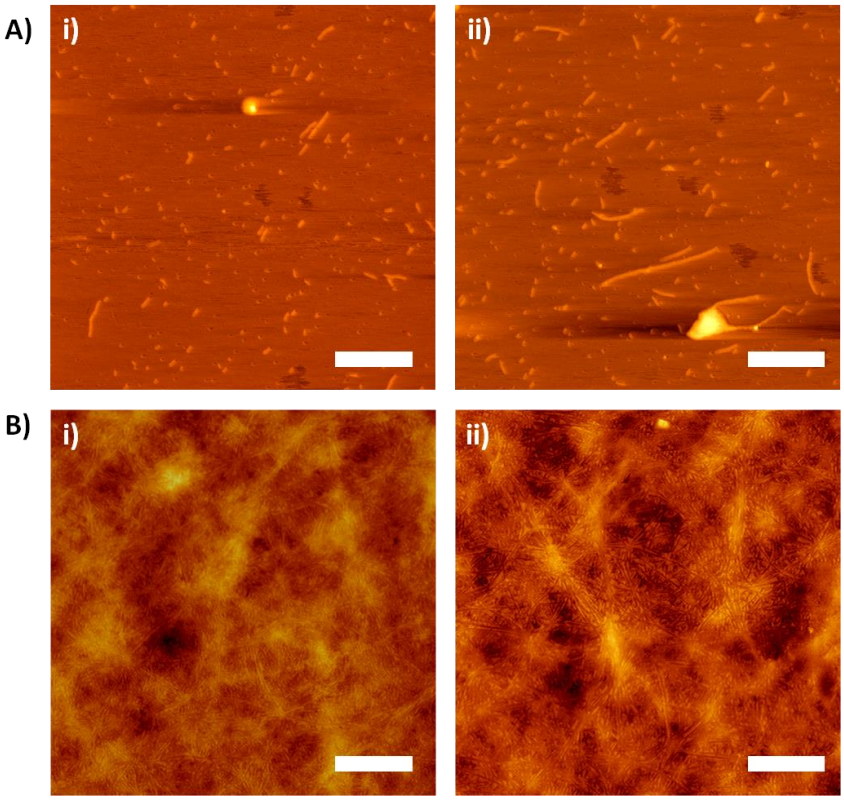

Figure 129 - Atomic force micrographs of **2b** fibres (converted from **2a**) with (A) QD-AP and (B) AP. Scale bars = 2µm.

Appendix T

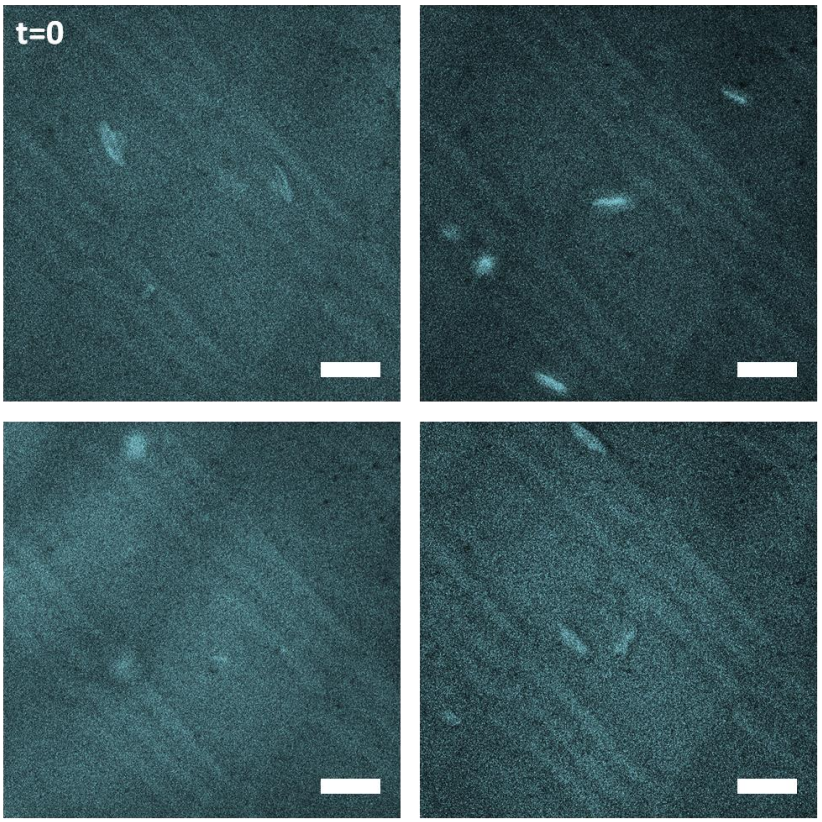

Figure 130 - 5mM **2a** no enzyme or QD-AP (t=0) control fluorescence micrographs. Scale bars represent 20µm.

Appendix U

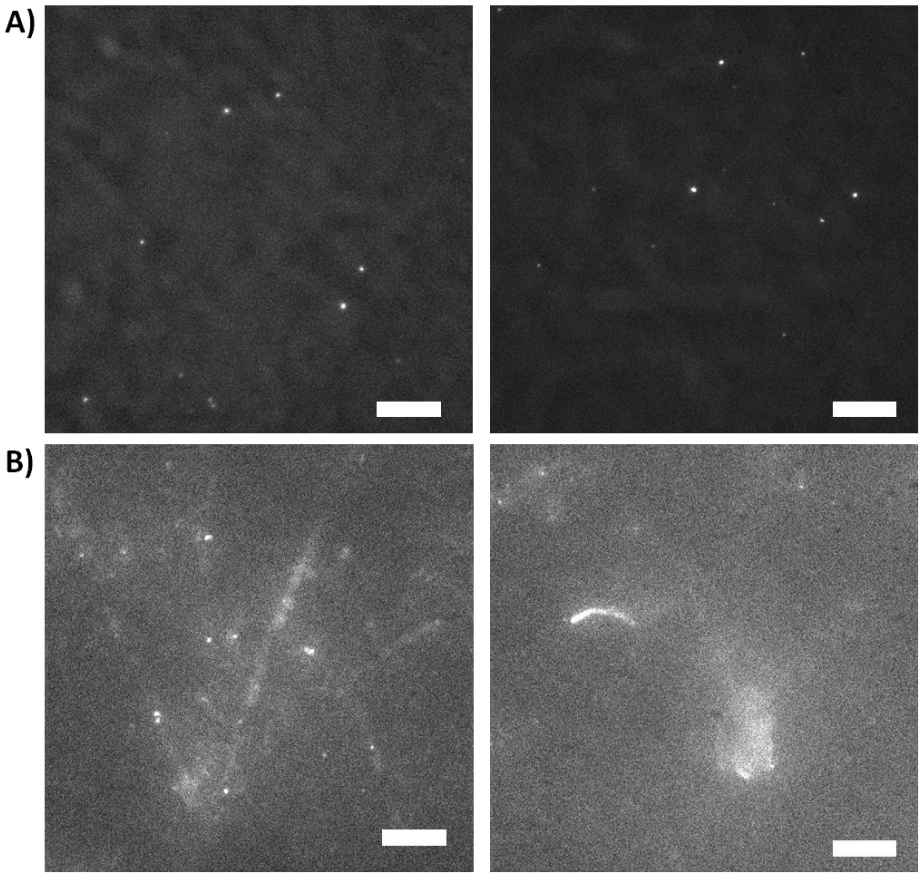

Figure 131 – (A) 10 mM **1a** doped with pyrene dried onto a glass surface, 24 hours after the addition of 4U AP (B) 10 mM **1a** and 1mM **2a** dried onto a glass surface, 24 hours after the addition of 4U AP. Scale bars represent 20 µm.

Appendix V

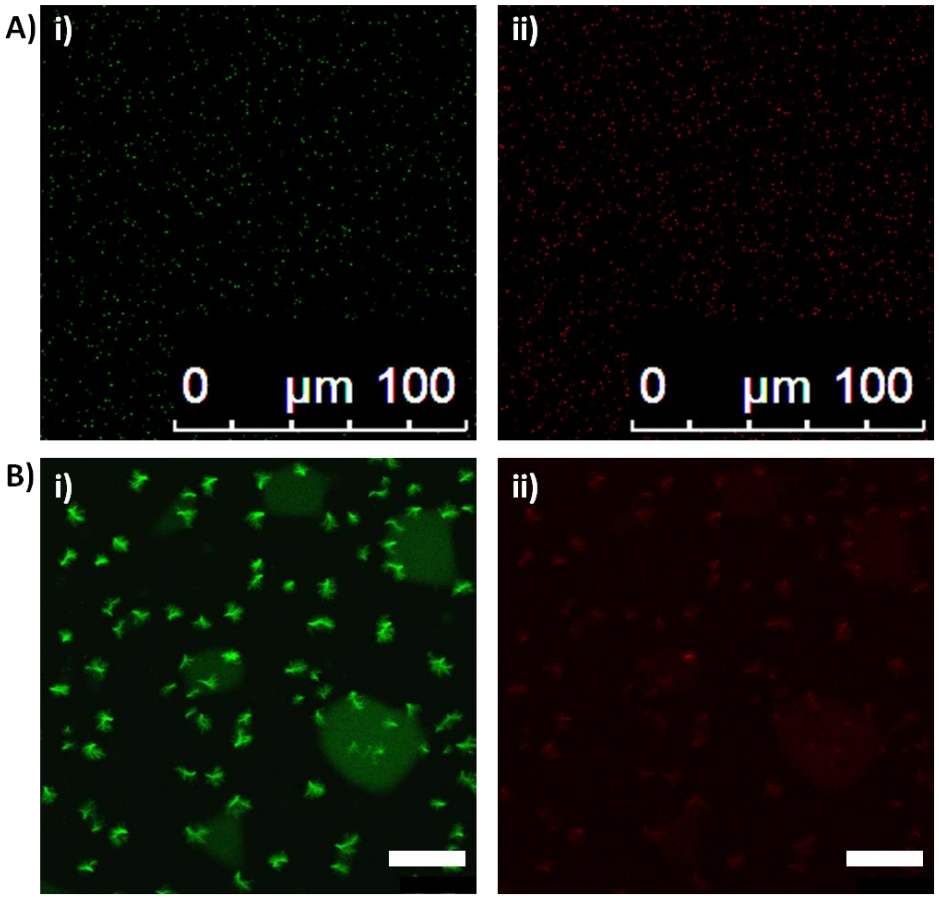

Figure 132 - Two-photon micrographs of (A) 1 mM **2a** with QD-AP and (B) 5 mM **2a** with QD-AP. Both samples were visualised at two wavelength ranges: (i) 400-550 nm for pyrene and (ii) 600-700 nm for QD-AP conjugates. Both samples were imaged 1 week after the addition of QD-AP and were in a flow cell environment. Scale bars represent 25 µm unless otherwise stated.

Appendix W

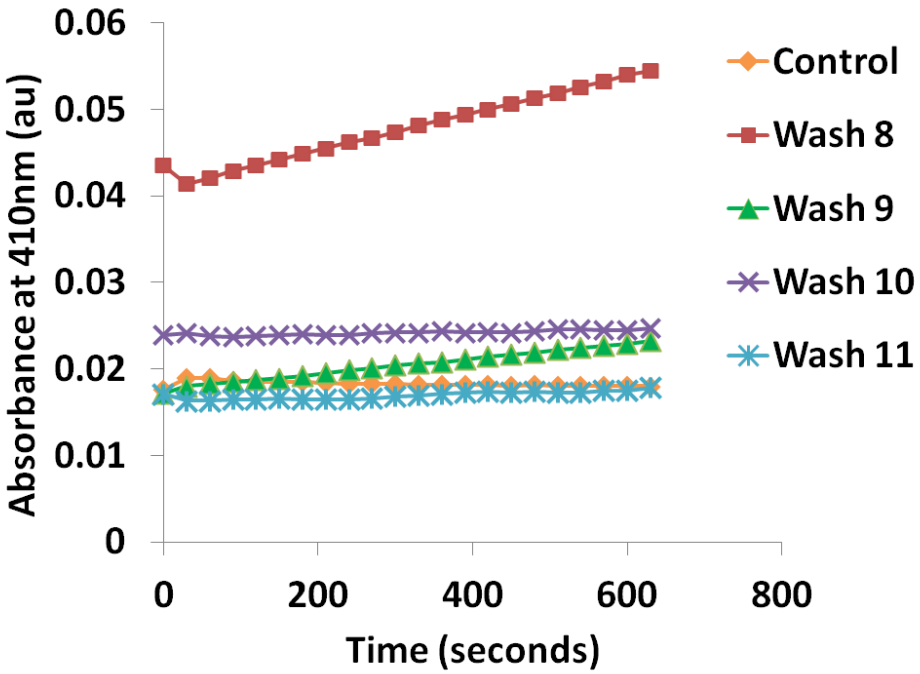

Figure 133 - QD_{525}-AP conjugation analysis, each filtration/centrifugation wash was analysed by UV-Vis in the presence of *p*-nitrophenyl phosphate. The absorbance at 410 nm was monitored over time for each wash, revealing that the absorbance at 410 nm had reduced to the negative control after wash 11 therefore indicating that all free (unconjugated) AP had been washed away.

Appendix X

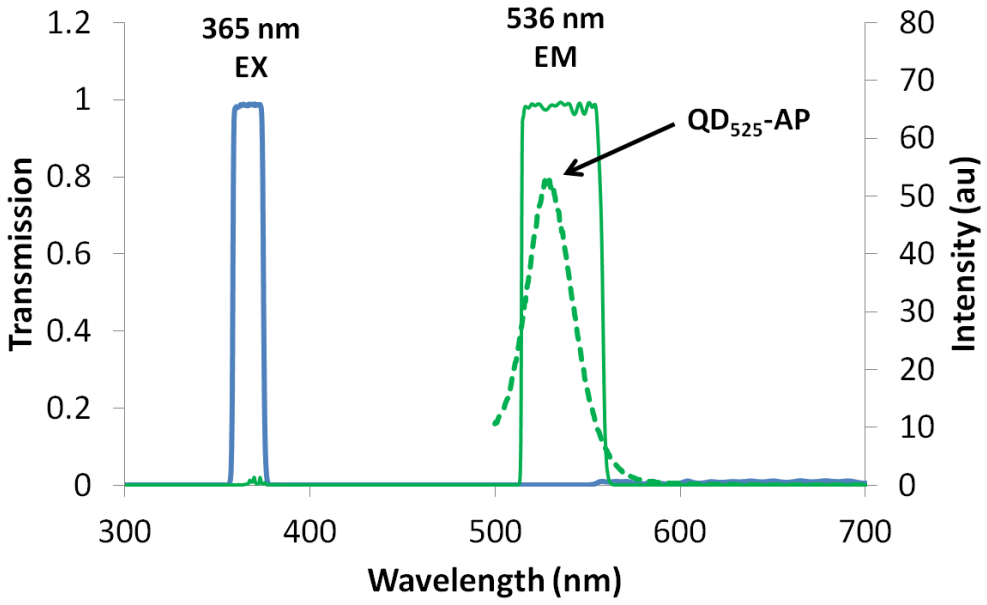

Figure 134 - Optical filter combination for QD_{525}-AP. Excitation optical filter: 365 nm; Emission filter 536 nm for the detection of QD_{525}-AP fluorescence emission (green dashed line - secondary axis).

Appendix Y

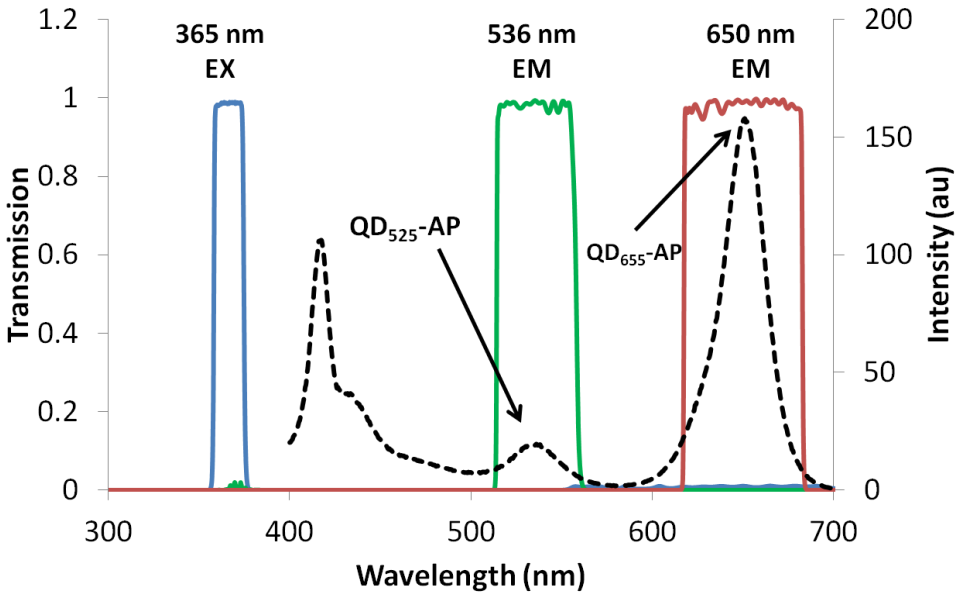

Figure 135 - Optical filter combination of for QD_{525}-AP/QD_{655}-AP mixture. Excitation optical filter: 365 nm; Emission filters 536 nm for the detection of QD_{525}-AP and 650 nm for the detection of QD_{655}-AP. Fluorescence emission spectrum of the QD_{525}-AP/QD_{655}-AP mixture (dashed line - secondary axis).

Appendix Z

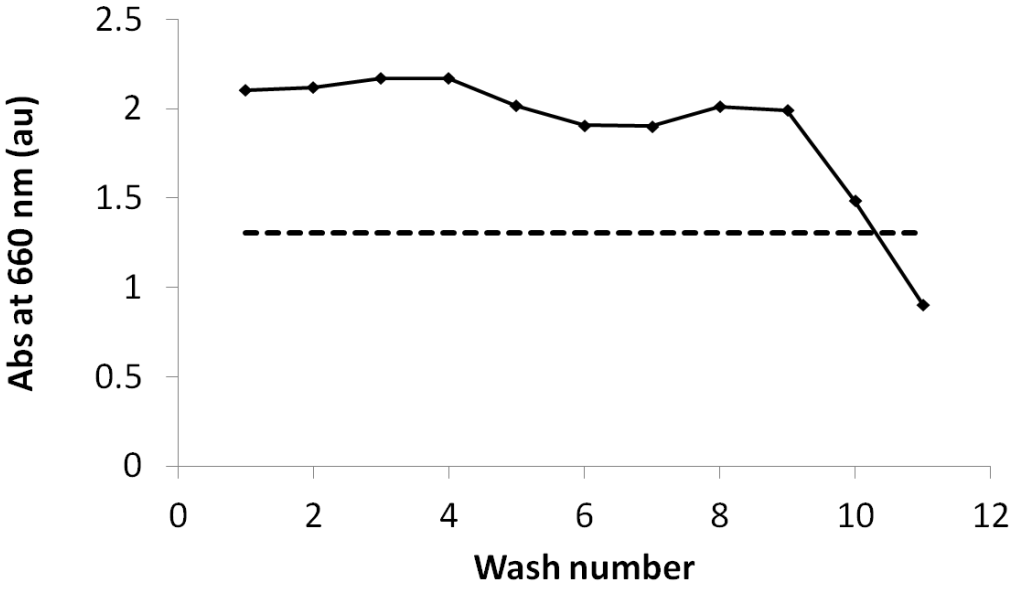

Figure 136 – Conjugate purification analysis of QD_{525}-Therm. Each filtration/wash was analysed by the thermolysin activity assay involving the hydrolysis of casein in the presence of amine detecting Folin and Ciocalteu's phenol reagent and monitored at 660 nm by UV-Vis spectroscopy. Dotted line represents a blank sample *i.e.* negative control, therefore after wash 11 the absorbance value of the wash was below the blank indicating removal of unconjugated thermolysin.

Appendix AA

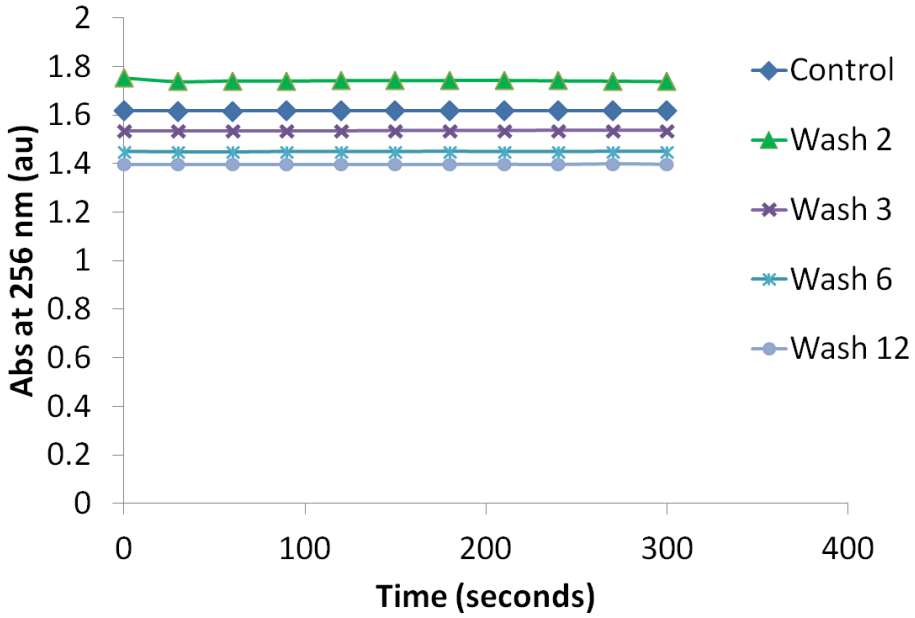

Figure 137 - Conjugate purification analysis of QD_{655}-Chym. Each filtration/wash was analysed by the BTTE activity assay at 256 nm by UV-Vis spectroscopy. Each analysis consisted of monitoring the absorbance over a period of 5.5 mins every 30 seconds to ensure unconjugated enzyme was fully removed from the conjugate.

Appendix BB

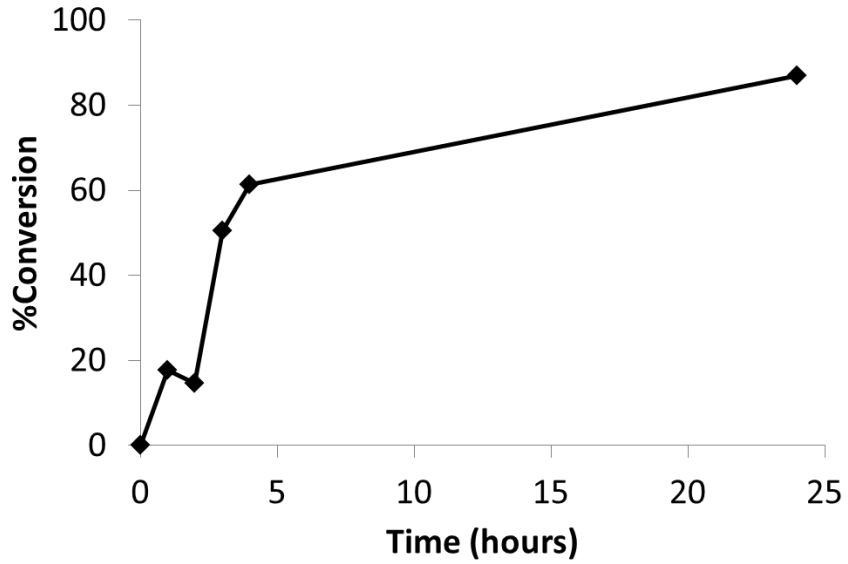

Figure 138 - HPLC conversion of Fmoc-T-OH and F-OMe to Fmoc-TF-OMe by thermolysin.